

Study of the effect of lateral inhomogeneities on the  
propagation of Rayleigh waves in an elastic medium

by

Ali Nasser-Moghaddam

A thesis

presented to the University of Waterloo

in fulfillment of the

thesis requirement for the degree of

Doctor of Philosophy in

Civil Engineering

Waterloo, Ontario, Canada 2006

©Ali Nasser-Moghaddam, 2006

I hereby declare that I am the sole author of this thesis. This is a true copy of the thesis, including any required final revisions, as accepted by my examiners.

I understand that my thesis may be electronically available to the public

Ali Nasser-Moghaddam

## Abstract

The use of geophysical testing methods has considerable potential to be a cost effective and accurate technique to assess near-surface soil conditions. Multi channel analysis of surface waves (MASW) test is a geophysical non-intrusive test that uses the dispersive characteristic of Rayleigh waves to estimate low strain shear modulus and damping coefficient of near-surface soil. Also, this technique is used to detect underground voids. Recently, MASW technique has gained more attention, partly because of its ease of use and partly because of the significant improvements in data acquisition systems. The theories of MASW test consider the effect of horizontal soil layering, though the effect of lateral inhomogeneities (i.e. cavities and voids), inclined layering and inverse layering (i.e. a layered system in which the top layers are stiffer than the bottom ones) are not addressed properly in these theories.

The objective of this dissertation is to investigate the effect of lateral inhomogeneities on the propagation of Rayleigh waves in an elastic half-space excited by a transient loading. The results can be applied to locate underground cavities using MASW test and to improve the MASW analysis techniques. In lieu of theoretical solutions, two and three dimensional numerical models are constructed to simulate the MASW test. To assure the quality of the obtained data, numerical models are calibrated with Lamb solution. Voids with different sizes and embedment depths are inserted in the medium. Responses along the surface as well as inside the medium are recorded and analyzed in time, frequency, spatial and frequency-wave number domains. Different material types and sources are used to generalize the results. Afterwards, the combined effect of void and layered systems on the surface responses are studied. To verify the results, experimental field and laboratory data are presented and the trends are compared to the numerical results.

It is found that the void starts to vibrate in response to the Rayleigh wave excitation. Due to the vibration of the void energy partitioning occurs. Part of the incident energy is reflected in the form of Rayleigh wave. Another part is converted to body waves, and spread into the medium. The transferred part of the energy is attenuated and has smaller amplitudes. Finally, a part of energy is trapped in the void region and bounces back and forth between the void boundaries, until it damps. The trapped energy is associated to higher modes of Rayleigh waves and excited Lamb waves. The effect of trapped energy is seen as a region in the vicinity of the

void with concentrated energy, in frequency domain. The extents of this region depends on the void size, and the frequency content of the incident energy. Thus, in some cases it is possible to correspond the size of the model to the extents of the region with energy concentration.

A new technique is proposed to determine the location of a void, and estimate its embedment depth. The technique is called Attenuation Analysis of Rayleigh Waves (AARW), and is based on the observed damping effect of the void on the surface responses. For verification, the results are compared to experimental field and laboratory data. The observations are in good agreement with the observed numerical results. Further, the AARW technique showed to be a promising tool for void detection.

## Acknowledgements

The development and completion of this work would not have been possible without the support, encouragement and understandings of many individuals to whom I am deeply in gratitude. First, I would like to sincerely thank my supervisor Dr. Giovanni Cascante for his valuable insights, enthusiasm, support and encouragements. I greatly appreciate the time that he spent and his efforts for guiding me through this research work and providing me with invaluable feedbacks and comments. Further, I should thank Dr. Leo Rothenburg, my co-supervisor, whose in depth knowledge in the geotechnical engineering field was a valuable asset during my research work at the University of Waterloo.

My grateful acknowledgement extends to the circle of expert professionals in my examining committee:

- Dr. C. B. Park from Kansas Geological Survey;
- Dr. Anthony Endres from Earth Sciences Department, University of Waterloo;
- Dr. G. W. Brodland from Civil Engineering Department, University of Waterloo;
- Dr. D. E. Grierson from Civil Engineering Department, University of Waterloo

Their valuable feedbacks and enthusiastic questions gave me a better insight into the quality of this work and my future plans for further developing it.

Several organizations and companies provided me the funding and support for my research work. My gratitude goes to Natural Sciences and Engineering Research Council of Canada (NSERC), Centre for Research in Earth and Space Technology (CRESTech), the Canadian Foundation for Innovation (CFI), INCO Limited, and Dillon Consulting.

My special thanks to administrative staff of the Civil Engineering Department: Ken Bowman, Sandra Machan, Donna Armborst, and Kevin Rampersad were always helpful. As a graduate student, I should specially thank Marguarite Knechtel, administrative Co-ordinator of graduate studies. Also, Colin Campbell helped me with learning and working with SWP. His patience in debugging my files and fixing them is really appreciated.

My fellow graduate students were quite instrumental in advancement of this work. I would like to thank all of them, especially Anwar Majid, Zahid H. Khan, Yanjun Yang, Fernando

Tallavo, and Simone Berube. During my study, I always had a chance to discuss my technical problems with them, and of course coming up with an appropriate solution. I wish all the best for them in their study, career, and personal life.

I am forever indebted to my parents for their understanding, endless patience and encouragement when they were most required. I believe that no work can be regarded as a pay off of their enduring loves, thus I can simply say thank you. My sister Sima, and my brother Siavoush were always encouraging and full of useful advises for their younger brother. Without their love, I would not have the endurance to finish this work. My gratitude should extend to my in laws, my niece and my nephews who shared with me their loves. During my Ph.D. works, I had the chance to hear the good news that one of my nephews, Hossein, took civil engineering as his major at UCLA. I do really look forward to see him as a colleague and a professional fellow. My special thanks should go to my wife's parents and family members, whom were always understanding and encouraging.

I am very blessed that I had all the supports and love of my wonderful wife, Parisa, during our mutual life, and specially during my Ph.D. studies. Without her understandings, encouragements, and patience this work was not possible. She is such a joy in my life, specially these days that we are expecting our first baby.

Finally, I want to dedicate this work to all the people whom I love, and to my forever beloved mother land, Iran.

# Contents

<b>1</b>	<b>Foreword</b>	<b>1</b>
1.1	Introduction . . . . .	1
1.2	Methodology and organization . . . . .	3
<b>2</b>	<b>Mechanical-wave propagation in elastic media</b>	<b>6</b>
2.1	Introduction . . . . .	6
2.2	Development of governing dynamic equilibrium equations and their solutions . . . . .	7
2.2.1	General elasticity equations . . . . .	7
2.2.2	Waves in unbounded media . . . . .	12
2.2.3	Waves in homogeneous semi-infinite media . . . . .	13
2.2.4	Dispersion curves, group and phase velocities . . . . .	18
2.3	Seismic waves: characteristics and behavior . . . . .	19
2.3.1	Body waves . . . . .	19
2.3.2	Surface waves . . . . .	20
2.4	Damping and attenuation in seismic waves . . . . .	26
2.4.1	Geometrical damping . . . . .	27
2.4.2	Reflection, transmission and scattering at interfaces . . . . .	28
2.4.3	Intrinsic damping . . . . .	29
2.4.4	Total attenuation . . . . .	32
2.5	Forced vibration of an elastic semi infinite media . . . . .	32
<b>3</b>	<b>Signal processing techniques</b>	<b>35</b>
3.1	Time domain analysis . . . . .	35

3.2	Frequency domain analysis . . . . .	37
3.2.1	Properties of Fourier transform . . . . .	39
3.3	System: definition and characteristics . . . . .	39
3.4	Processing of discrete signals . . . . .	42
3.5	Signal analysis in frequency-wavenumber domain . . . . .	47
3.5.1	Two dimensional (2D) signals: characteristics and representation . . . . .	47
3.5.2	2D Fourier transform - FK transform . . . . .	49
3.5.3	Calculation technique . . . . .	51
<b>4</b>	<b>Geophysical exploration techniques</b>	<b>54</b>
4.1	Introduction . . . . .	54
4.2	Resistivity method . . . . .	58
4.3	MASW method . . . . .	64
4.3.1	Development of the technique and related theories . . . . .	64
<b>5</b>	<b>Numerical modeling of Rayleigh wave propagation</b>	<b>75</b>
5.1	Introduction . . . . .	75
5.2	Principles of finite differences method . . . . .	76
5.2.1	Derivative approximations . . . . .	77
5.2.2	Difference form of equation of motion for homogeneous medium . . . . .	77
5.2.3	Difference form of equation of motion for non-homogeneous medium . . . . .	78
5.2.4	Boundary and initial conditions . . . . .	79
5.2.5	Description of finite differences program FLAC . . . . .	89
<b>6</b>	<b>Behavior of Rayleigh waves in the presence of lateral and vertical inhomogeneities</b>	<b>92</b>
6.1	Introduction . . . . .	92
6.1.1	Background . . . . .	92
6.1.2	Statement of the problem . . . . .	94
6.2	Numerical experimental methodology . . . . .	96
6.2.1	Model description . . . . .	97



6.2.2	Recording points and analysis parameters . . . . .	100
6.2.3	Normalization and characteristic wavelength . . . . .	103
6.3	Time responses . . . . .	105
6.3.1	Surface responses . . . . .	105
6.3.2	Responses inside the medium . . . . .	108
6.4	Frequency responses . . . . .	115
6.4.1	Surface responses . . . . .	115
6.4.2	Responses along vertical lines inside the medium . . . . .	116
6.5	2D Fourier transforms . . . . .	121
6.6	Discussions . . . . .	124
6.7	Summary of the conclusions . . . . .	128
<b>7</b>	<b>Effect of cavity properties on surface responses</b>	<b>134</b>
7.1	Introduction . . . . .	134
7.2	Effect of width of the void (case 1) . . . . .	135
7.3	Effect of depth of the void (case 2) . . . . .	142
7.4	Effect of medium with two layers - Natural layering: Soft layer overlying bedrock (case 3) . . . . .	148
7.4.1	Time responses . . . . .	151
7.4.2	Frequency responses . . . . .	155
7.4.3	2D Fourier spectrum . . . . .	158
7.5	Effect of medium with two layers - Inverse layering: Stiff layer overlying soft layer (case 4) . . . . .	161
7.6	Effect of lateral dimension of the void - 3D effect of the cavity (case 5) . . . . .	169
7.6.1	Model description . . . . .	169
7.6.2	Effect of out of plain dimension of the void on surface responses . . . . .	179
7.6.3	Effect of void offset on the surface responses . . . . .	182
7.7	Summary of the conclusions . . . . .	186
<b>8</b>	<b>Attenuation Analysis of Rayleigh Waves Method</b>	<b>187</b>
8.1	Introduction . . . . .	187

8.2	Development of the method . . . . .	188
8.3	Proposed method for detecting a void . . . . .	197
8.4	Proposed method for estimating the embedment depth of a void . . . . .	200
8.5	Summary of the Attenuation Analysis of Rayleigh Waves (AARW) . . . . .	203
<b>9</b>	<b>Verification of the results with experimental data</b>	<b>205</b>
9.1	Introduction . . . . .	205
9.2	Abandoned mine detection at INCO mine site . . . . .	205
9.2.1	Site description . . . . .	205
9.2.2	Experimental methodology . . . . .	207
9.2.3	Experimental results . . . . .	210
9.3	Sandbox prototype . . . . .	217
9.3.1	Prototype description . . . . .	217
9.3.2	Experimental methodology . . . . .	220
9.3.3	Experimental results . . . . .	220
9.4	Summary and conclusions . . . . .	225
<b>10</b>	<b>Conclusions and Recommendations</b>	<b>226</b>
10.1	Conclusions . . . . .	226
10.2	Recommendations for future works . . . . .	229
<b>A</b>	<b>Selected closed form solutions</b>	<b>244</b>
<b>B</b>	<b>Developed MathCAD<sup>®</sup> work sheets</b>	<b>246</b>
<b>C</b>	<b>Selected FLAC<sup>®</sup> input files</b>	<b>260</b>
C.1	FLAC input file for model S00_02: . . . . .	260
C.2	FLAC input file for model S03_01 (Three dimensional model): . . . . .	269

# List of Tables

2.1	Relations between the various elastic constants . . . . .	10
2.2	typical p-wave velocities in earth materials . . . . .	19
2.3	Amplitude distance relations in Lamb’s problem (Bath 1984) . . . . .	33
4.1	Geophysical methods, the physical property that they are based on, and their main applications [1] . . . . .	56
4.2	Sources of noise that affect different geophysical methods [1] . . . . .	58
4.3	Resistivity values and ranges for common geological materials [1]. . . . .	59
4.4	Historical development of MASW test . . . . .	66
6.1	Model types used in this study . . . . .	96
6.2	Material properties used in model type S00 . . . . .	102
7.1	Embedment depth of the void in different studies . . . . .	142
7.2	Model types used in this study . . . . .	150
7.3	Frequencies below which are filtered from models . . . . .	155
7.4	Reflection and transmission ratios between the materials used in model type S02	164
7.5	Boundary conditions assigned to different boundary plains in model type S03 . .	170
A.1	Definition of the parameters used in the closed form solutions . . . . .	244
A.2	Model properties and loading conditions for the studied cases . . . . .	245
A.3	Surface displacements for the studied cases . . . . .	245

# List of Figures

2-1	Components of strain and stress . . . . .	8
2-2	Incident and reflected wave system . . . . .	15
2-3	p- and s- wave displacements . . . . .	20
2-4	Love wave surface deformation . . . . .	21
2-5	Graphical solution of the dispersion of Love waves . . . . .	22
2-6	Love waves propagation modes . . . . .	23
2-7	Rayleigh surface deformation . . . . .	24
2-8	Variation of Rayleigh wave displacements with depth. . . . .	25
2-9	Cummulative energy flux of Rayleigh wave with depth . . . . .	27
2-10	Lamb solution for forced vibration of a semi-infinite medium. . . . .	34
3-1	Aliasing . . . . .	36
3-2	Effect of reflection on the frequency response of a signal. . . . .	40
3-3	Cross correlation of two signals . . . . .	44
3-4	Energy leakage due to truncation of signals. . . . .	45
3-5	Definition of Half-Power Bandwidth. . . . .	47
3-6	Representation of signals in wiggle and contour plots. . . . .	48
3-7	Signals in t-d domain and the correspong spectrum in FK domain. . . . .	50
3-8	Schematic of the effect of optical transform on the FK data. . . . .	53
4-1	General electrode configuration in a resistivity survey. . . . .	60
4-2	Variation of apparent ressitivity curve with electrode seperation . . . . .	62
4-3	Pseudosections to interpret the resistivity data . . . . .	63

4-4	Schematic of the field layout of MASW test. . . . .	69
4-5	Schematics of different geometries of MASW test. . . . .	70
4-6	Calculated wrapped and unwrapped phases for a set of data. . . . .	71
5-1	A portion of the spatial grid near a curved boundary (after [2]) . . . . .	81
5-2	a) Typical infinite system b) Typical equivalent bounded model (after [3]) . . .	82
5-3	Dispersion curve for non dimensional s-wave phase velocity. . . . .	88
5-4	Basic explicit calculation cycle . . . . .	89
5-5	a) Overlaid quadrilateral elements used in FLAC b) Typical triangular element with velocity vectors c) Nodal force vector (after Itasca 2000 [4] with modifica- tions) . . . . .	90
6-1	Model numbers and main characteristics of each model. . . . .	97
6-2	Geometry and dimensions of the basic finite differences model used in this chapter. . . . .	98
6-3	Representation of used Lamb source in time and frequency domains. . . . .	99
6-4	General geometry of a model with void. . . . .	100
6-5	Location of recording points . . . . .	101
6-6	Variation of the cumulative energy of the applied source, and the first receiver responses with wavelength. . . . .	104
6-7	Time responses at the surface of model S00-01. . . . .	107
6-8	Time responses along the surface of model S00_05 . . . . .	111
6-9	Group velocities measured at the surface of the models. . . . .	112
6-10	Normalized time responses along vertical lines inside the medium. . . . .	113
6-11	Normalized time responses (in z direction) along arcs inside the medium. . . . .	114
6-12	Frequency spectra at the surface of the medium. . . . .	117
6-13	Cummulative energy verses normalized depth . . . . .	118
6-14	Frequency spectra of the responses along vertical lines inside the medium. . . . .	120
6-15	2D Fourier amplitudes of surface responses . . . . .	123
6-16	Time responses recorded around and imaginary boundary (S00_01) and a void (S00_09). . . . .	126
6-17	Frequency responses around the void. . . . .	127

6-18	Surface displacements and void deformations at times $t = 0.11s$ to $t = 0.12s$ . . .	129
6-19	Surface displacements and void deformations at times $t = 0.1225s$ to $t = 0.13s$ . . .	131
6-20	Surface displacements and void deformations at times $t = 0.1325s$ to $t = 0.14s$ . . .	132
6-21	Surface displacements and void deformations at times $t = 0.1425s$ to $t = 0.15s$ . . .	133
7-1	Effect of the void width on the surface responses. . . . .	139
7-2	Effect of the width of the void on the frequency content of surface responses. . .	140
7-3	Effect of the width of the void on the frequency content of surface responses. . .	141
7-4	Effect of the void depth on the time responses at the medium surface. . . . .	144
7-5	Effect of the void depth on the time responses at the medium surface. . . . .	145
7-6	Effect of the void depth on the frequency content of the vertical displacements at the medium surface. . . . .	146
7-7	Effect of the void depth on the frequency content of the vertical displacements at the medium surface. . . . .	147
7-8	The numbering system for model type S01 along with the characteristics of each model. . . . .	149
7-9	The cumulative energy verses wavelength for models with a soft layer overlying a stiff layer (model S01_XX). The effect of filtration of low frequencies in models with shallow elastic layer is observed in the plots. . . . .	150
7-10	Contour plots of the vertical displacements recorded at the surface of model type S01. . . . .	153
7-11	Contour plots of the vertical displacements at the surface of model type S01. . .	154
7-12	Contour plots of the spectrum of layered models. . . . .	156
7-13	Contour plots of the spectrum of layered models with void. . . . .	157
7-14	2D Fourier responses of layered models (Type S01) with no void. . . . .	159
7-15	2D Fourier responses of layered models (Type S01) with void. . . . .	160
7-16	The numbering system for model type S02 along with the characteristics of each model. . . . .	162
7-17	The numbering system for model type S02 along with the characteristics of each model. . . . .	163

7-18	The cumulative energy verses wavelength for models with a stiff layer overlying a soft layer (model S02_XX). The effect of filtration of low frequencies in models with shallow elastic layer is observed in the plots. . . . .	165
7-19	Contour plots of the vertical displacements at the surface of model type S02. . .	166
7-20	Spectrum of the vertical displacements at the surface of model type S02. . . . .	168
7-21	Description of 3D models developed in this study (Study S03). . . . .	172
7-22	Description of 3D models developed in this study (Study S03). The basic model is S03_00, which consists of two regions. Region 1 consists of uniform grids in x-direction and nonuniform grids in y- and z- directions. Region 2 has non uniform grids in all the three dimensions. The geometry of thevoids considered in each study is presented in the associated figure. at the bottom of the figure views of the models in y-z and x-z plains are shown. . . . .	173
7-23	Representation of the source applied to model type S03. . . . .	174
7-24	Comparison between the time responses of 3D models and 2D axisymmetric models.	176
7-25	Comparison between the spectra of 3D models and 2D axisymmetric models. . .	177
7-26	Cumulative energy verse wavelength in 3D models. . . . .	178
7-27	Effect of out of plain dimension of the void on surface responses in time domain.	180
7-28	Effect of out of plain dimension of the void on surface responses in frequency domain. . . . .	181
7-29	Effect of void offset in time domain. . . . .	184
7-30	Effect of void offset in frequency domain. . . . .	185
8-1	Displacement field in a two layered medium, and a void at different times. Due to interaction of the main R-wave event with the void, energy partitioning occurs. Thus, the transmitted energy is attenuated. . . . .	190
8-2	Displacement field in a two layered medium, and a void at different times. Due to interaction of the main R-wave event with the void, energy partitioning occurs. Thus, the transmitted energy is attenuated. . . . .	191
8-3	Displacement field in a two layered medium, and a void at different times. Due to interaction of the main R-wave event with the void, energy partitioning occurs. Thus, the transmitted energy is attenuated. . . . .	192

8-4	Displacement field in a two layered medium, and a void at different times. Due to interaction of the main R-wave event with the void, energy partitioning occurs. Thus, the transmitted energy is attenuated. . . . .	193
8-5	Frequency responses at the surface of two models. . . . .	194
8-6	Calculated LD values for three different models, and two different locations. . . . .	196
8-7	Logarithmic decrement (LD) contour for model S00_09. . . . .	198
8-8	Representation of the gain function, original signal and the signal magnified by the gain function. . . . .	199
8-9	Variation of NED parameter with distance from source. . . . .	201
8-10	CALD values obtained from vertical and horizontal components of the surface responses. . . . .	203
9-1	Schematic of a typical crown pillar. . . . .	206
9-2	Crown pillar failure . . . . .	207
9-3	Aerial map of the investigated mine site . . . . .	208
9-4	Recorded responses over crown pillar 1. . . . .	211
9-5	Recorded responses over crown pillar 2. . . . .	212
9-6	Spectrum of the responses over crown pillars. . . . .	215
9-7	Variation of NED with distance, over crown pillar 1. . . . .	216
9-8	Picture of the sandbox used for the test. . . . .	218
9-9	Sketch of the sand box prototype . . . . .	219
9-10	Cummulative energy at the location of first receiver along line 2. . . . .	221
9-11	Contours of the surface responses of the sand box. . . . .	223
9-12	Spectrum of the surface responses of the sand box. . . . .	224
9-13	Application of AARW method to the sand box data. . . . .	225



# Nomenclature

$\alpha$  = wave number in vertical direction;

damping coefficient

general coefficient

$\beta$  = wave number in vertical direction

$\delta_{kl}$  = Kronecker delta function, is equal to 1 when  $k = l$  and 0 otherwise

$\delta A$  = cross section area

$\delta f$  = sampling frequency

$\delta L$  = length

$\delta R$  = resistance

$\delta t$  sampling time

$\epsilon_{ij}$  = strain component, where  $i$  is the direction of the axis perpendicular to the plain of the strain, and  $j$  is the direction of the strain

$\sigma_{ij}$  = strain component, where  $i$  is the direction of the axis perpendicular to the plain of the stress, and  $j$  is the direction of the stress

$\nu$  = Poisson ratio

$\rho$  = mass density of the body

resistivity of a block of material with cross section  $\delta A$

$\lambda$  = Lamé constant;

wavelength

$\lambda_{ch}$  = characteristic wavelength

$\kappa$  = ratio between p-wave and s-wave velocities

$\xi, \zeta$  = wavenumbers in horizontal direction

$\omega$  = circular frequency =  $\frac{2\pi}{f}$

$\xi$  = damping ratio

$\mu$  = Lamé constant

$\eta$  = viscosity parameter

$\theta$ : angle that the wave makes with horizontal

$\phi(\omega)$  = phase spectrum

$\phi(f)$  = phase difference for frequency  $f$

$\psi$  = Lamb source constant parameter

$\Delta$  = dialation, which is the increment of volume per volume  
receiver spacing

$\Delta_t$  = logarithmic decrement with respect to time

$\Delta_x$  = logarithmic decrement with respect to distance

$\Delta t$  = sampling rate in time domain

$\Delta t_{crit}$  = critical time step

$\Delta x$  = sampling rate in spatial domain  
grid spacing in x direction

$\Delta y$  = grid spacing in y direction

$\Delta z$  = grid spacing in z direction

$\Omega_{ij}$  = rigid-body rotation

$\nabla$  = Laplacian operator

$\Phi, \Psi$  = potential functions

$a$  = height of the void in numerical models

$a_i$  = component of acceleration in  $i$  direction

$b$  = width of the void in numerical models

$c$  = phase velocity =  $\frac{\omega}{k}$

$d$  = size of the inclusion

$d_z$  = distance between receiver number  $z$  and first receiver

$f$  = frequency

$f_{cu}$  = cut off frequency

$f_s$  = sampling frequency

$f_{Nyquist}$  = Nyquist frequency

$f_u$  = frequency at point  $u$

$g_z$  = value of the gain function at location  $z$

$h$  = embedment depth of the void in numerical models

$i$  =  $\sqrt{-1}$

$k$  = wave number =  $\frac{2\pi}{\lambda}$

$k_{Nyq}$  = Nyquist wave number  
 $q_p$  = ratio between the numerical phase velocity and true phase velocity for p-wave  
 $q_s$  = ratio between the numerical phase velocity and true phase velocity for s-wave  
 $r_1, r_2$  = distance between source and points 1 and 2  
 $s(t, x)$  = set of data in time-distance domain  
 $t_{ch}$  = characteristic time  
 $t_{max}$  = maximum dynamic time (running time) in the numerical model  
 $t_{near}$  = arrival time of the reflections from near boundary of the void  
 $t_{far}$  = arrival time of the reflections from far boundary of the void  
 $t(f)$  = time delay for frequency  $f$   
 $u_i$  = particle displacement in direction  $i$   
 $\ddot{u}_i$  = particle acceleration in direction  $i$   
 $w_i$  = window function  
 $x_i$  = unit vector in direction  $i$   
     amplitude of the recorded signal at time  $i$   
 $x(t)$  = general functions of time  
 $y(t)$  = general functions of time  
 $z$  = acoustic impedance  
  
 $A$  = area of the triangle in the F.D. scheme  
 $A_1, A_2$  = amplitude of particle motion  
 $AARW$  = Attenuation Analysis of Rayleigh waves  
 $ALD_j$  = Amplified Logarithmic Decrement value at frequency  $f_j$   
 $C_p$  = p-wave velocity  
 $C_s$  = s-wave velocity  
 $C_R$  = Rayleigh wave velocity  
 $C_L$  = Love wave velocity  
 $CALD_j$  = Cumulative Amplified Logarithmic Decrement value at frequency  $f_j$   
 $CE_d$  = cumulative energy above depth  $d$   
 $D$  = offset value - distance between the first receiver and the source  
 $E$  = Young's modulus of elasticity

$E_z$  = signal energy at location  $z$   
 $F_b$  = Lamb source constant parameter  
 $F_i$  = body forces  
 $F(x)$  = general function  
 $F(\omega)$  = amplitude spectrum  
 $G$  = shear modulus of soil  
 $G(x)$  = general function  
 $G(\omega)$  = amplitude spectrum  
 $H(\omega)$  = gain of the system  
 $I$  = current  
 $K$  = bulk modulus of soil  
     geometric factor  
 $L_x$  = array length in  $x$  direction, in numerical models  
 $MASW$  = Multi Channel Analysis of Surface Waves  
 $N$  = total number of records in time  
 $NED_z$  = Normalized-Energy-Distance parameter at distance  $z$   
 $Q_i$  = external forces  
 $Q(\omega)$  = quality factor  
 $R$  = resistance  
 $R_{a \rightarrow b}$  = reflection coefficient from material  $a$  to  $b$   
 $R1, R2, \dots$  = recording point number in the numerical models  
 $SASW$  = Spectral Analysis of Surface Waves  
 $S(\omega, k)$  = set of data in frequency-wave number domain  
 $T$  = transmission factor;  
     period of excitation  
     system operator  
     length of records in time  
 $T_{a \rightarrow b}$  = transmission coefficient from material  $a$  to  $b$   
 $X_u$  = Fourier amplitude at frequency  $f_u$   
 $U$  = group velocity =  $\frac{d\omega}{dk}$

$V$  = potential

$V1, V2, \dots$  = recording point number in the numerical models

$V_L$  = Lamb wave velocity

$V_R$  = phase velocity

$W$  = total stored energy per volume per cycle of vibration

$\Delta W$  = dissipated energy per volume per cycle of vibration

# Chapter 1

## Foreword

### 1.1 Introduction

Detecting underground cavities beneath construction sites and urban areas is a crucial task for many engineering projects. Each year, subsidence and surface soil failure due to underground voids cause substantial damage around the world. Most of the seismic methods currently used for cavity detection can successfully locate a void but not its embedment depth. In spite of successful case histories, void detection is still a challenging problem because of the lack of a standard, quantitative void-detection technique. In addition, existing non-destructive techniques do not consider the effect of lateral inhomogeneities, i.e., cavities, in the wave propagation. Thus, the detection of underground cavities needs further study.

Each year, ground surface failure and subsidence due to underground cavities cause major problems around the world by damaging buildings, foundations and infrastructure. Underground voids can be created naturally by karst solution processes resulting in caves in carbonate rocks or by tunnelling and mining processes. Abandoned mines are of particular concern as maps indicating the location of underground excavations are generally not available, and few organizations take responsibility for assessing the physical stability of abandoned mine works. Turney [5] reports that subsidence over abandoned coal mines pose a potential hazard for approximately 13,000 people and 5,000 houses along the Front Range Urban Corridor, Colorado. Vlcko [6] indicates that the major cause of historical heritage damage is mass movements of earth caused by subsidence into abandoned excavations or natural cavities. Yaoru et al. [7]

discuss the damage to structures and dams due to deformation of karstic cavities in China. In general, the detection of cavities on construction sites is a priority in karst prone regions or areas with subsurface excavation histories.

Engineering assessment of the stability of caverns depends upon successful cavity detection and characterization, which is achieved by various intrusive tests (i.e., drilling, test pits, or trenching) or by non-destructive tests (NDT) using geophysical methods. Hutchinson et al. [8] provides a comparison of various geophysical approaches for void detection. With the recent advances in equipment and data acquisition systems, the use of NDT has proven to be successful in many cases and has gained greater acceptance in the industry [9].

Geophysical testing methods have considerable potential to provide cost effective and accurate techniques to assess near-surface soil conditions. Most of these techniques are non-intrusive, i.e. they do not alter the characteristics of the medium that they are being applied to. In comparison to conventional boring methods, geophysical techniques provide information about a large area in a short time. Among these techniques the multi-channel analysis of surface waves (MASW) test has gained attention in recent years. This attention is partly because of its ease of use and partly because of the significant improvements in data acquisition systems.

The MASW test is a geophysical seismic technique that uses the dispersive characteristic of Rayleigh waves to estimate low strain shear modulus and damping coefficient of near-surface soil. Also, this technique is used to detect underground cavities. In the conventional MASW test a number of geophones (or accelerometers) are deployed in a line along the surface, and the ground is excited by a mechanical source, at the surface. The responses are recorded in time domain, and transformed to frequency domain. The Rayleigh wave velocity profile of the medium (Rayleigh wave velocity verses depth) is then inverted from the frequency data (dispersion curve). Theoretical expressions are available that relate the Rayleigh-wave velocity to shear-wave velocity, shear modulus, and consequently to elastic modulus and damping ratio of the medium. Thus, the low strain mechanical properties of the soil are estimated from the MASW test.

The theory of the MASW test was originated in 1960's, and further developed in 1980's and 1990's. This theory is based on the stiffness matrices developed for mechanical excitations propagating in an elastic homogeneous and isotropic material. The system is assumed to be

horizontally layered, and normally layered (top layers have smaller stiffness than the bottom ones). In the application of this theory to soil, the above assumptions are valid only to some limits. Soil is elastic at very low strains (in the order of  $10^{-5}$  or less), and is not homogeneous. In general, soil layers (boundaries with distinct changes in mechanical properties) are not horizontal. Very often, inverse layering is observed in soil systems, specially in clayey deposits. Further, lateral inhomogeneities such as cavities might be present in the soil layers. All the mentioned shortcomings introduce difficulties in the interpretation of MASW test data.

The objective of this dissertation is to investigate the effect of lateral inhomogeneities on the propagation of Rayleigh waves in an elastic medium. In general, the results of this investigation can be used to interpret the MASW test results and to improve the analysis techniques associated to the test. Specific application of the conducted study is in locating underground cavities using the MASW test and estimating their boundaries.

## 1.2 Methodology and organization

The research methodology selected for this study is based on developing numerical models to investigate the behavior of Rayleigh waves in the presence of lateral inhomogeneities, and to verify the results with field and laboratory scale prototypes. The numerical modelling starts with a homogeneous half-space that has rectangular voids inserted in them to model the lateral inhomogeneities. The effect of the depth and size of the void on the surface responses are investigated by varying the void size and embedment depths. The next step consists of introducing a void in layered systems. Two types of layering is considered. natural layering, in which the top layer has a smaller stiffness than the bottom layer, and inverse layering, where the stiffness of the top layer is higher than the bottom one. In both cases the void is located in the top layer. Three dimensional models are developed in the next stage to investigate the effect of lateral dimensions of the cavity on the surface responses. Finally, the field results over two crown pillars, and the results obtained from a laboratory scale prototype, are utilized to verify the observations and conclusions.

This thesis contains 10 chapters and is organized hereafter in the following order:

**Chapter 2** begins with the theoretical examination of mechanical wave generation with



the focus on Rayleigh waves. It discusses the governing dynamic equations, and the effect of bounded and unbounded media on the propagation of mechanical energy. The concepts of dispersion curves and phase velocities are introduced, and different types of damping and attenuation are discussed. Finally, the Lamb problem is introduced and the details of its solution is investigated.

**Chapter 3** examines the signal processing methods used for analysis of the data. Time and frequency domain techniques are discussed. The concept of Nyquist frequency is explained and the effect of discretization on the signals are investigated. A detail review of the two-dimensional Fourier transforms are provided. Details of the computational methods used for evaluating the 2D-Fourier transforms are presented at the end.

**Chapter 4** reviews the general principles of geophysical methods and their pros and cons in comparison to conventional soil assessment techniques. The techniques that are commonly used in the detection of underground cavities are introduced and the resistivity method is discussed in more detail, as a representative. In-depth study of the MASW method is introduced in this chapter. Details of the method and its historical development from 1930's to present are presented.

**Chapter 5** reviews the principles of the finite differences technique that is used in this study. Related concepts, such as stability, consistency, and artificial boundaries are introduced in this chapter. The basic concepts of the numerical code (FLAC) that is used throughout this investigation are presented. Lastly, the basics of the developed basic model are introduced and the procedure followed to assure its stability and accuracy are presented.

**Chapter 6** explains the results obtained from simulations of half-space in the presence of a void and excited by a source applied to the surface. The surface responses, along with the responses around the void, and along vertical lines and arcs inside the medium are studied in time and frequency domains. The 2D Fourier transforms of the surface responses are also presented. In each case, the responses are compared to the corresponding responses in a homogeneous half-space (without void).

**Chapter 7** presents the studies conducted to investigate the effect of width and embedment depth of the void on surface responses. This chapter continues with the results of the investigation of the combined effect of void and layered medium on the surface responses. The

three dimensional models are introduced next and the obtained results are discussed in detail.

**Chapter 8** shows the details of a developed method for detecting a void and estimating its embedment depth. The method is called Attenuation Analysis of Rayleigh Waves (AARW), and is based on the damping effect of cavities on the surface responses. The validity of the technique is investigated through its application to various models.

**Chapter 9** explains the verification procedure used in this study. The real data collected over two crown pillars in Sudbury, Ontario, are presented and the observations are explained with reference to the results obtained from this study. Moreover, the results obtained from a laboratory scale prototype are presented. These results are used to verify the applicability of the AARW technique and the conclusions made in the previous chapters.

**Chapter 10** summarizes the conclusions of this study. Further, recommendations for further studies and researches are provided in this chapter.

Most of the contour and image plots presented in this study are in black and white format. The corresponding figures in colored format and additional figures are presented in a compact disk (CD) that is attached to this dissertation. Throughout the text, this CD is referred to as Appendix CD.

## Chapter 2

# Mechanical-wave propagation in elastic media

### 2.1 Introduction

The study of the propagation of mechanical-waves (stress-waves) in elastic media goes back hundreds of years, when the concern was mostly with musical instruments and water waves. The related modern theories were developed in 19th century as an extension of theory of elasticity to the problem of vibrating bodies. Due to its application in the field of geophysics, the interest in the study of waves in elastic media gained momentum in the latter part of 19<sup>th</sup> century. The profound contributions of Rayleigh, Lamb, Love and others gave a significant advancement to the field in this era. At the beginning of 20<sup>th</sup> century, this field of study was disregarded partly because of the interests in the new fields of physics, i.e. atomic physics, and partly since the available theories at the time were far more advanced than the available experimental techniques. The development of advanced electronic equipment and the application of the theories in characterizing of the material has increased the interest in the theories of mechanical-wave propagation in elastic, inelastic and imperfectly elastic materials. These theories have applications in seismology, mechanical and civil engineering to practices such as detection of nuclear explosions, nondestructive testing of materials, detection of buried objects, pile driving and etc. Recent activities in this field are mostly concerned with the development of vibration theories for plates and shells, analysis of situations with transient loadings, pulse propagation

in half-space and propagation of waves in inhomogeneities materials. In rigid dynamics, it is assumed that when a point of a body is subjected to a force, the result would be an instant motion in all the points of the body. This force produces a linear acceleration of the body along with an angular acceleration about its center of gravity (Newton's laws of motion). On the other hand, in theory of elasticity the body is assumed to be in a state of static equilibrium and elastic deformations occur in the whole body. A combination of these two approaches leads to the subject of propagation of mechanical-waves. This method of analysis should be utilized when the load is applied in a short period of time or changes rapidly during the observation time with respect to the natural vibration frequencies of the body. In general, when a solid body is disturbed, body waves in the forms of dilatational waves (p-waves) and distortional waves (s-waves) are produced. Shear waves (s-waves) cannot propagate in a liquid. At the surface of a solid, two other types of waves can be generated: Rayleigh and Love waves. This chapter introduces the basic governing equations, and the principles of the formation and propagation of the fore mentioned waves, which will be referred throughout this dissertation. For conciseness, some of the formulations are stated in two dimensional form, yet it will not affect the generality of the discussions and results. Also, a brief discussion of energy dissipation mechanisms in elastic solids is introduced. Unless otherwise stated, the coverage of this chapter is based on the works presented in [10, 11, 12, 13].

## 2.2 Development of governing dynamic equilibrium equations and their solutions

### 2.2.1 General elasticity equations

In the theory of elasticity, the change in the relative position of adjacent points in a body is called strain and is defined as:

$$\epsilon_{ij} = \frac{1}{2} \left( \frac{\partial u_i}{\partial x_j} + \frac{\partial u_j}{\partial x_i} + \frac{\partial u_k}{\partial x_i} \frac{\partial u_l}{\partial x_j} \delta_{kl} \right) \quad (2.1)$$

where  $u_i$  stands for particle displacement in the direction  $i$ ,  $x_i$  is the unit vector in the direction  $i$ ,  $\delta_{kl}$  is the Kroneker delta function, which is equal to 1 when  $k = l$  and 0 otherwise, and  $\epsilon_{ij}$

is the strain where the first subscript indicates the direction of the axis perpendicular to the plane in question and the second indicates the direction of the strain. In most of the engineering applications, small deformations are prevalent i.e. the magnitudes of the unit elongations and strains are in the order of  $10^{-3}$  or less. For small strains the second order terms in equation 2.1 are negligible. Thus, by disregarding the last term in equation 2.1 the general equation which is applicable throughout this dissertation will be in the following form:

$$\epsilon_{ij} = \frac{1}{2} \left( \frac{\partial u_i}{\partial x_j} + \frac{\partial u_j}{\partial x_i} \right) \quad (2.2)$$

Figure 2-1 represents, the components of stress and strain in a solid in the general form. Also the displacements of any point “p” may be resolved parallel to the axes 1, 2 and 3 into components  $u_1$ ,  $u_2$  and  $u_3$ . In case of linear strains, it is assumed that a line element remains a straight line

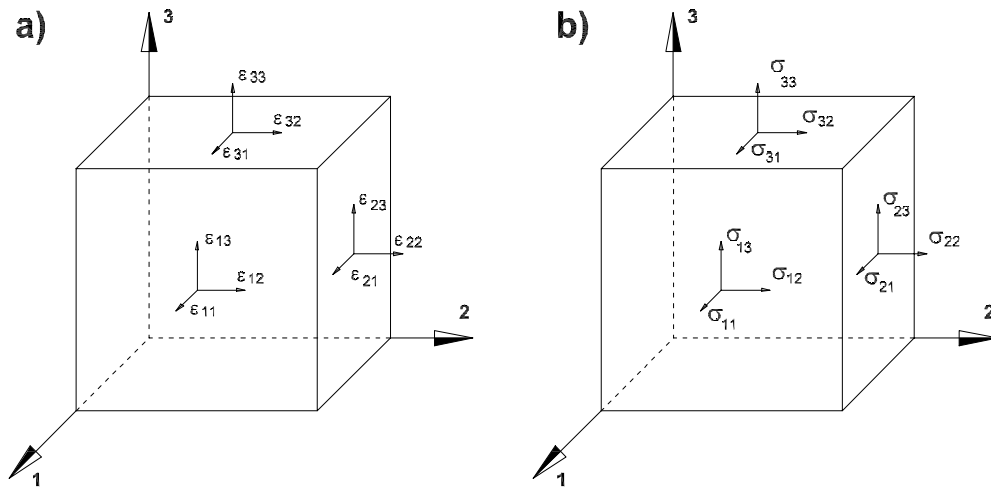


Figure 2-1: Components of strain (a) and stress (b) acting on an infinitesimal rectangular parallelepiped.

after the deformation. More precisely, For a linear elastic material, dilatation, which defines the increment of volume per unit of volume, can be expressed as:

$$\Delta = \epsilon_{11} + \epsilon_{22} + \epsilon_{33} = \frac{\partial u_1}{\partial x_1} + \frac{\partial u_2}{\partial x_2} + \frac{\partial u_3}{\partial x_3} \quad (2.3)$$

In general the motion of a point in a body is governed by a combination of distortion effects (2.2) and rigid-body rotation effects defined as:

$$\Omega_{ij} = \frac{1}{2} \left( \frac{\partial u_i}{\partial x_j} - \frac{\partial u_j}{\partial x_i} \right) \quad (2.4)$$

If the process of deformation does not create cracks or holes in the body the deformation is called compatible. Therefore, the body will remain continuous after the deformation. For linear strain these limitations generate six independent equations (compatibility equations) in the following form:

$$\frac{\partial^2 \epsilon_{jk}}{\partial x_i \partial x_j} + \frac{\partial^2 \epsilon_{il}}{\partial x_j \partial x_k} - \frac{\partial^2 \epsilon_{ik}}{\partial x_j \partial x_l} - \frac{\partial^2 \epsilon_{jl}}{\partial x_i \partial x_k} = 0 \quad (2.5)$$

all the parameters are defined before. Consider a body, which is in equilibrium under a system of external forces  $Q_i$ . Passing a fictitious plane through any point of this body, will divide it into two parts, where each of them will be in equilibrium under the applied forces and the effect of the separated part. This effect, called stress, is assumed to be continuous and distributed over the surface of intersection. Considering Newton's laws of motion the stresses ( $\sigma_{ij}$ ) at any point should satisfy the following equilibrium equations:

$$\frac{\partial \sigma_{ij}}{\partial x_j} + F_i = \rho a_i \quad (2.6)$$

$$\sigma_{i,j} = \sigma_{j,i} \quad (2.7)$$

where  $F_i$  is the body force,  $\rho$  is the mass density of the body and  $a_i$  is the component of the acceleration in the direction  $i$ . Although the stress components exist only in the deformed state of the body, for small deformations, it is assumed that there is no difference between the pre-deformation and post deformation areas and element directions. The stresses and strains are related through constitutive laws. For linear isotropic linearly materials this law is called the Generalized Hook's law and is given by:

$$\sigma_{i,j} = 2\mu \epsilon_{ij} + \lambda \delta_{ij} \Delta \quad (2.8)$$

where  $\Delta$  is the dilatation as defined in 2.3,  $\delta_{ij}$  is the Kronecer delta function.  $\mu$  and  $\lambda$  are Lamé's constants and are independent from each other. In engineering terminology the two independent constants that are commonly used are  $E$ , Young's modulus and  $\nu$ , Poisson's ratio. In geotechnical engineering it is very common to use the shear modulus of the soil ( $G$ ) and the Poisson's ratio ( $\nu$ ) as the two independent constants. The relation between various elastic constants are tabulated in . The parameter  $K$  is called Bulk modulus and is a measure of the change in volume per unit volume due a spherical stress.

Table 2.1: Relations between the various elastic constants

Constant	Basic Pair		
	$\lambda, \mu = G$	$E, \nu$	$K, \mu$
$\lambda$	$\lambda$	$\frac{\nu E}{(1+\nu)(1-2\nu)}$	$\frac{3K-2\mu}{3}$
$\mu = G$	$\mu = G$	$\frac{E}{2(1+\nu)}$	$\mu$
$K$	$\frac{3\lambda+2\mu}{3}$	$\frac{E}{3(1-2\nu)}$	$K$
$E$	$\frac{\mu(3\lambda+2\mu)}{\lambda+\mu}$	$E$	$\frac{9K\mu}{3K+\mu}$
$\nu$	$\frac{\lambda}{2(\lambda+\mu)}$	$\nu$	$\frac{3K-2\mu}{6K+2\mu}$

At each point, there are three equilibrium equations, six stress-strain relationships, and six strain-displacement relationships. Therefore, the total number of available equations is 15. Further, at each point there are six stress components, six strain components and 3 displacement components. Thus at each point 15 unknowns and 15 equations exist. Navier substituted the equations for strain (2.2) into the stress-strain relation (2.8) and that result into the stress equations of motion. The results are called Navier's equations and are vastly used in wave propagation problems. The implicit form of the Navier equations is:

$$\mu \nabla^2 \mathbf{u} + (\lambda + \mu) \nabla \Delta + \mathbf{F} = \rho \ddot{\mathbf{u}} \quad (2.9)$$

where  $\Delta$  is dilatation as defined in 2.3,  $\mathbf{F}$  is the vector of body forces, and the Laplacian operator is defined as:

$$\nabla = \frac{\partial}{\partial x_1} + \frac{\partial}{\partial x_2} + \frac{\partial}{\partial x_3} \quad (2.10)$$

Recalling the definition of rotation (2.4) the equation (2.9) can be rewritten as:

$$(\lambda + \mu) \nabla \Delta - 2\mu \nabla \times \boldsymbol{\Omega} + \mathbf{F} = \rho \ddot{\mathbf{u}} \quad (2.11)$$

The latter form displays the dialation and rotation in an explicit form and its results is valid in any curvilinear coordinate system.

In general, a problem of elasticity consists of finding a function that satisfy the Navier equations at any point within the body, and the boundary conditions. There is no need to check the compatibility since the strains are obtained from the displacements. Commonly these equations are solved by the aid of potential functions.

For linear materials subjected to small strains the principle of superposition is applicable. This principle states that if the developed stresses in a linear elastic body subjected to a set of external forces  $F_i$ , is  $\sigma_{ij}$ , and due to another set of external forces  $F'_i$  is  $\sigma'_{ij}$ , then the stresses developed in the body due to the combined effect of  $F_i + F'_i$  will be  $\sigma_{ij} + \sigma'_{ij}$ .

In many practical cases, the behavior of three dimensional medium is studied in a 2D plane. Two different plane states are defined in the theory of elasticity to estimate the behavior of three dimensional medium. These states are plane-strain and plane-stress. Generalized plane strain state requires that all the planes initially normal to  $Ox_3$  (2-1) remain normal to it and that all straight lines initially parallel to  $Ox_3$  remain parallel to it after deformation. These conditions are given by:

$$u_1 = u_1(x_1, x_2), \quad u_2 = u_2(x_1, x_2) \quad (2.12a)$$

$$u_3 = u_3(x_3) \quad (2.12b)$$

if  $u_3=0$  the body is in plain strain state; otherwise, it is in a state of generalized plain strain.

In the state of plane stress:

$$\sigma_{13} = \sigma_{23} = \sigma_{33} = 0 \quad (2.13a)$$

$$\sigma_{11} = \sigma_{11}(x_1, x_2), \quad \sigma_{22} = \sigma_{22}(x_1, x_2), \quad \sigma_{12} = \sigma_{12}(x_1, x_2) \quad (2.13b)$$



Beside the mentioned plain states, in some cases displacements may take place in planes through an axis and be the same in all such planes[14]. This case defines an axisymmetric condition and is best defined in cylindrical coordinates  $r$ ,  $\theta$  and  $z$ , by the equations:

$$u_\theta = 0 \quad (2.14a)$$

$$\frac{\partial u_r}{\partial \theta} = \frac{\partial u_z}{\partial \theta} = 0 \quad (2.14b)$$

### 2.2.2 Waves in unbounded media

In an unbounded media, boundary interactions are not possible. Although this is not a real case, it can be used to introduce the study of wave propagation. The equations of motion for the infinite medium hold for any stress-strain relationship. For a linear elastic medium, the solution of the Navier's equations in the absence of body forces must satisfy all the necessary conditions. By simple mathematical manipulations, the Navier equations yield the wave equations [10, 12]:

$$(\lambda + 2\mu) \nabla^2 \Delta = \rho \frac{\partial^2 \Delta}{\partial t^2} \quad \Longrightarrow \quad \nabla^2 \Delta = \frac{1}{C_p^2} \frac{\partial^2 \Delta}{\partial t^2} \quad (2.15a)$$

$$\mu \nabla^2 \left( \frac{\partial u_i}{\partial x_j} - \frac{\partial u_j}{\partial x_i} \right) = \rho \frac{\partial^2}{\partial t^2} \left( \frac{\partial u_i}{\partial x_j} - \frac{\partial u_j}{\partial x_i} \right) \quad \Longrightarrow \quad \nabla^2 \Omega = \frac{1}{C_s^2} \frac{\partial^2 \Omega}{\partial t^2} \quad (2.15b)$$

Equation 2.15a describes a dilatational wave travelling with a velocity  $C_p$  in the interior of an elastic body; whereas, equation 2.15b shows a rotational wave traveling with a speed  $C_s$ . These velocities are defined as:

$$C_p = \sqrt{\frac{\lambda + 2\mu}{\rho}} = \sqrt{\frac{E}{\rho} \frac{1 - \nu}{(1 + \nu)(1 - 2\nu)}} \quad (2.16a)$$

$$C_s = \sqrt{\frac{\mu}{\rho}} = \sqrt{\frac{G}{\rho}} \quad (2.16b)$$

Any wave propagating through an isotropic elastic medium must travel with one of the above velocities. The equations are uncoupled that means the two waves exist independent.

Volumetric waves, involving no rotation, propagate at  $C_p$ ; whereas, rotational waves, involving no volume changes, propagate at  $C_s$ . Dilational waves are also called irrotational or primary waves (p-waves), and rotational waves are named equi-voluminal, distortional, and secondary waves (s-waves). Considering  $0 \leq \nu < 0.5$ , it is concluded that always  $C_p > C_s$  and their ratio can be expressed as:

$$\kappa = \frac{C_p}{C_s} = \left( \frac{\lambda + 2\mu}{\mu} \right)^{\frac{1}{2}} = \left( \frac{2 - 2\nu}{1 - 2\nu} \right)^{\frac{1}{2}} \quad (2.17)$$

### 2.2.3 Waves in homogeneous semi-infinite media

It was shown that within an infinite elastic medium only two types of elastic waves can propagate. However, the situation is quite different in a bounded media such as in a half-space. When an elastic wave encounters a boundary, part of its energy is reflected back in the form of the incident wave. Further, mode conversion occurs i.e. the incident wave converts into other types of waves on reflection. In 1885, Lord Rayleigh [15] showed that due to the interaction between a surface and an incident elastic wave - no matter dilational or rotational - in a homogeneous semi-infinite medium, another type of wave is generated that its motion is concentrated in a shallow zone near the free surface. To describe the fore-mentioned behavior, consider a plane harmonic wave, i.e.  $\exp(i\omega t)$ , propagating in a half-space  $x_3 > 0$ , the  $x_1 - x_2$  plane ( $x_3 = 0$ ) is the free surface, and  $x_3$  directs downward, towards the interior of the body. For plain strain case,  $u_2 = \frac{\partial}{\partial x_2} = 0$  and Navier equations (2.9) can be solved with two potential functions,  $\Phi$  and  $\Psi$  defined as:

$$u_1 = \frac{\partial \Phi}{\partial x_1} + \frac{\partial \Psi}{\partial x_3} \quad (2.18a)$$

$$u_3 = \frac{\partial \Phi}{\partial x_3} - \frac{\partial \Psi}{\partial x_1} \quad (2.18b)$$

Substituting these equalities into the definitions of dialation (2.3) and rotation in  $x_1 - x_3$  plain (2.4) gives:

$$\Delta = \nabla^2 \Phi \quad (2.19a)$$

$$\Omega_{13} = \nabla^2 \Psi \quad (2.19b)$$

These equations show that  $\Phi$  and  $\Psi$  are associated with dialation and rotation respectively. Substitution of the expressions for  $u_1$  and  $u_3$  (2.18) into Navier equations (2.11) with no body force ( $\mathbf{F} = 0$ ) gives:

$$\nabla^2 \Phi = \frac{1}{C_p^2} \frac{\partial^2 \Phi}{\partial t^2} \quad (2.20a)$$

$$\nabla^2 \Psi = \frac{1}{C_s^2} \frac{\partial^2 \Psi}{\partial t^2} \quad (2.20b)$$

For the semi infinite media the boundary conditions are expressed as:

$$\sigma_{33} = 0 \quad \text{and} \quad \sigma_{21} = 0 \quad \text{at} \quad y = 0 \quad (2.21)$$

General solution for the case of the above equations are in the form:

$$\Phi = F(x_3) e^{i(\xi x_1 - \omega t)} \quad (2.22a)$$

$$\Psi = G(x_3) e^{i(\zeta x_1 - \omega t)} \quad (2.22b)$$

where  $F$  and  $G$  are general functions of  $x_3$ ,  $i = \sqrt{-1}$ ,  $\xi$  and  $\zeta$  are wave numbers in horizontal direction as shown in Fig. 2-2, and  $\omega$  represents circular frequency.

Substitution of 2.22 into 2.20 results in two different cases. Case 1 gives the solution for reflected waves, and case 2 leads to the surface wave solution. Each case will be studied separately.

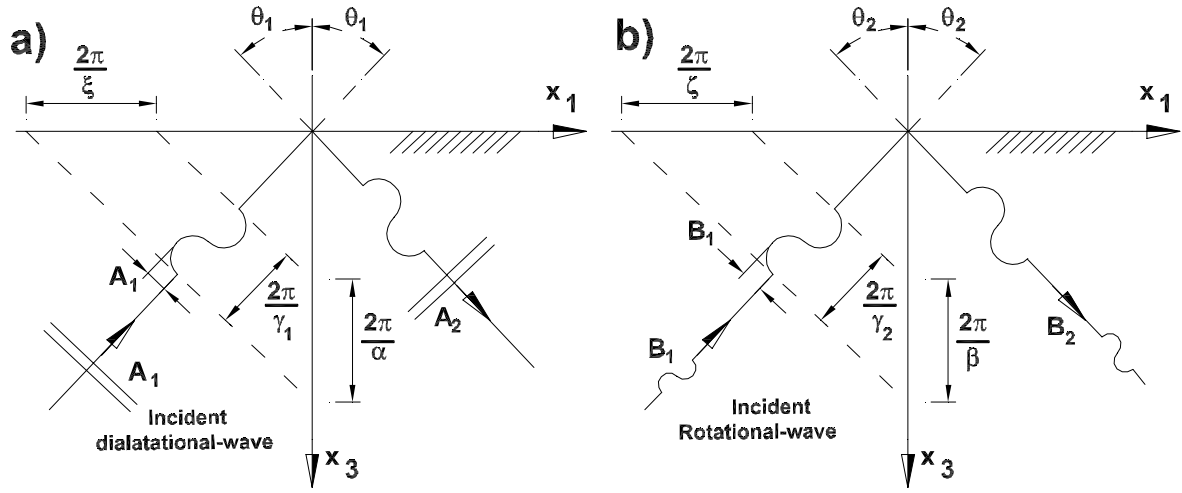


Figure 2-2: Incident and reflected wave system for dilatational (a) and rotational waves (b)

Case1:

$$\frac{d^2 F}{(dx_3)^2} + \alpha^2 F = 0 \quad (2.23a)$$

$$\frac{d^2 G}{(dx_3)^2} + \beta^2 G = 0 \quad (2.23b)$$

where

$$\alpha^2 = \frac{\omega^2}{C_p^2} - \xi^2 \quad (2.24a)$$

$$\beta^2 = \frac{\omega^2}{C_s^2} - \xi^2 \quad (2.24b)$$

From Fig. 2-2 it is observed that  $\alpha$  and  $\beta$  are the wave numbers in the vertical direction.

Consequently, the plain wave solution for dialation and rotation will be:

$$\Omega = A_I e^{i(\xi x_1 - \alpha x_3 - \omega t)} + A_R e^{i(\xi x_1 + \alpha x_3 - \omega t)} \quad (2.25a)$$

$$\Psi = B_I e^{i(\zeta x_1 - \beta x_3 - \omega t)} + B_R e^{i(\zeta x_1 + \beta x_3 - \omega t)} \quad (2.25b)$$

where all the parameters are explained before.  $A$  and  $B$  are the amplitudes of dialational and rotational waves respectively. The subscription  $I$  corresponds to the incident wave and  $R$  indicates the reflected wave. Thus, each of equations 2.25 shows an incident wave moving in  $+x_1$  and  $-x_3$  direction and a reflected wave moving in  $+x_1$  and  $+x_3$  direction (2-2). Introducing the obtained results for  $\Omega$  and  $\Psi$  into the boundary conditions (2.21) will give the ratios between the amplitudes of the incident and reflected waves. Achenbach [13] provides details of the corresponding amplitude ratios and partition of energy among each reflected wave.

**Case2:**

Another case can be considered in which:

$$\bar{\alpha}^2 = -\alpha^2 \quad (2.26a)$$

$$\bar{\beta}^2 = -\beta^2 \quad (2.26b)$$

which results in:

$$\frac{d^2 F}{(dx_3)^2} - \bar{\alpha}^2 F = 0 \quad (2.27a)$$

$$\frac{d^2 G}{(dx_3)^2} - \bar{\beta}^2 G = 0 \quad (2.27b)$$

The solution of 2.27 consists of two waves one with exponentially increasing and one with exponentially decreasing amplitude with depth. As the exponentially increasing part violates the principal of conservation of energy, it is disregarded, thus the solution for dialation and rotation will be in the following form:

$$\Omega = Ae^{-\bar{\alpha}^2 x_3} e^{i\xi(x_1 - C_R t)} \quad (2.28a)$$

$$\Psi = Be^{-\bar{\beta}^2 x_3} e^{i\xi(x_1 - C_R t)} \quad (2.28b)$$

where  $A$  and  $B$  are the amplitudes,  $C_R$  is the velocity of the generated surface wave, and the rest of the parameters are defined before. Substitution of the obtained results for the potential functions into the relations for displacements (2.18) results in the following forms of displacement functions:

$$u_1 = \left( i\xi A e^{-\bar{\alpha} x_3} - \bar{\beta} B e^{-\bar{\beta} x_3} \right) e^{i\xi(x - C_R t)} \quad (2.29a)$$

$$u_3 = - \left( \bar{\alpha} A e^{-\bar{\alpha} x_3} + i\xi B e^{-\bar{\beta} x_3} \right) e^{i\xi(x - C_R t)} \quad (2.29b)$$

and applying the boundary conditions (2.21) at the surface leads to the amplitude ratios:

$$\frac{A}{B} = \frac{2i\bar{\beta}\xi}{\bar{\beta}^2 + \xi^2} = \frac{\bar{\beta}^2 + \xi^2}{2i\bar{\alpha}\xi} \quad (2.30)$$

consequently the surface waves frequency equation will be in the following form:

$$\left( \bar{\beta}^2 + \xi^2 \right)^2 - 4\bar{\alpha}\bar{\beta}\xi = 0 \quad (2.31)$$

substituting the expressions for  $\bar{\alpha}$  and  $\bar{\beta}$  gives the following equation, from which the velocity of surface waves  $C_R$  is determined:

$$\left( 2 - \frac{C_R^2}{C_s^2} \right)^2 = 4 \left( 1 - \frac{C_R^2}{C_p^2} \right)^{\frac{1}{2}} \left( 1 - \frac{C_R^2}{C_s^2} \right)^{\frac{1}{2}} \quad (2.32)$$

For real media ( $0 < \nu < 0.5$ ), the above equation has only one real root that satisfies all the physical and mathematical requirements [16]. The corresponding wave is called Rayleigh wave that propagates with a velocity  $C_R$  and is confined to depths close to the surface. Detail review of major characteristics of Rayleigh waves will be provided later on in this chapter.

## 2.2.4 Dispersion curves, group and phase velocities

Relations, which give the apparent velocity,  $C_x$ , as a function of angular frequency  $\omega$  or horizontal wave-number  $k_x$ , are called dispersion relations or period equations [17].  $\omega$  is defined as  $\frac{2\pi}{T}$  where  $f$  is frequency and  $k_x$  is defined as  $\frac{2\pi}{\lambda}$  where  $\lambda$  is the wave length. In linear problems, dispersive waves usually are recognized by the existence of elementary solutions in the form of sinusoidal wave trains:

$$\phi(x, t) = Ae^{i(\omega t - k_x x)} \quad (2.33)$$

To satisfy the equilibrium equations,  $\omega$  and  $k_x$  should be related by an equation as:

$$G(\omega, k_x) = 0 \quad (2.34)$$

In each problem the function  $G$  is determined by applying boundary conditions and solving the corresponding equations. Commonly, solution of equation 2.34 leads to different values of  $k_x$  for a single value of  $\omega$ . These are called overtones or different modes. Physically, different modes indicate that a specific frequency can propagate with different velocities. The velocity with which a single frequency propagates in a media is called phase velocity ( $c$ ) and is defined as:

$$c = \frac{\omega}{k} \quad (2.35)$$

Further, in a wave that is composed of a narrow band of frequencies the packet of energy travels with an apparent velocity which is called group velocity and is defined as:

$$U = \frac{d\omega}{dk} = c + k \frac{dc}{dk} \quad (2.36)$$

Equation 2.36 states that group velocity is the limit of phase velocity ([18]). Moreover, the above equation shows the relation between the phase and group velocities. In a non-dispersive media the phase velocities are the same for all frequencies, thus  $\frac{dc}{dk} = 0$  and phase velocity is equal to group velocity. In a dispersive media and in the presence of wave with a wide band frequency, group velocity loses most of its applicability.

## 2.3 Seismic waves: characteristics and behavior

### 2.3.1 Body waves

As stated in previous sections, two types of mechanical waves - p- and s-waves - can propagate through the body of a media. The physical reason is that there are two fundamental ways that an elastic body can be strained. First, by volume change without change of shape, i.e. dilatation; second, by change of shape without change of volume,, i.e. distortion [19]. When a wave traverses a media it generates a field along its path. In mechanical waves a displacement or velocity field is generated. Therefore, each wave is characterized by two directions. One is the direction of wave propagation and the other is the direction in which the field that propagates changes [17].

P-waves generate successive compressions and elongations along their propagation path. Their propagation path is parallel to the displacement field that they cause in the media (2-3). These waves are associated with volume change, and are fastest waves that propagate through a media. As shown in (2.16a) their velocity is a function of the elastic modulus ( $E$ ), density ( $\rho$ ) and the Poisson ration of ( $\nu$ ) the media. In s-waves, the direction of propagation is perpendicular to the direction of particle motion (Fig. 2-3). They cause pure rotation in the media without any volume change. s-wave velocity is a function of shear modulus ( $G$ ), and density ( $\rho$ ). Thus, they can not propagate through fluids, i.e. air or water, because fluids do not have any shear resistance. Their velocity is about 60% of the p-wave velocity of the media. Table 2.2 provides some typical values of the p-wave velocity in different materials. Generally, there are two independent shear wave fields. SV and SH waves are vertically and horizontally polarized , i.e. their displacement field is along the  $x_3$  and  $x_2$  directions, respectively (Fig. 2-2).

Table 2.2: typical p-wave velocities in earth materials

Material	$C_p$ (km/s)	Material	$C_p$ (km/s)
Sand (dry)	0.2 – 1.0	Granite	5.5 – 6.0
Sand (Saturated)	1.5 – 2.0	Gabro	6.5 – 7.0
Clay	1.0 – 2.5	Air	0.3
Glacial till (Saturated)	1.5 – 2.5	Water	1.4 – 1.5
Sandstones	2.0 – 6.0	Steel	6.1
Limestones	2.0 – 6.0	Concrete	3.6



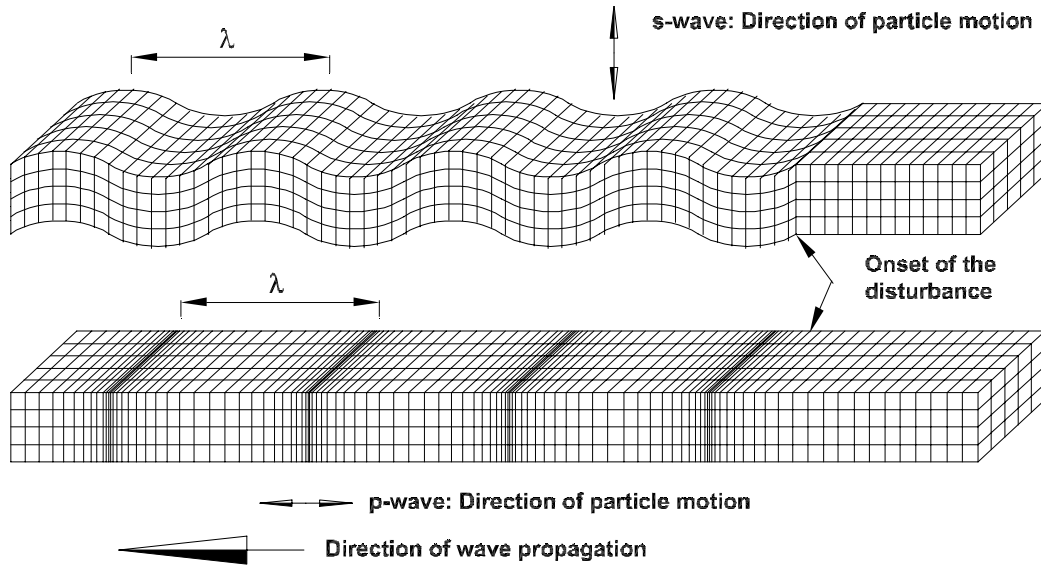


Figure 2-3: p-waves cause motion along the direction of propagation and s-waves cause motion perpendicular to the propagation path.

### 2.3.2 Surface waves

In a semi infinite media other types of waves can exist, beside body waves. These waves are generated due to the interaction of body waves and the surface and their energy is concentrated close to the surface. In 1885, Rayleigh [15] mathematically modeled the motion of plane waves in an elastic half space, and predicted the existence of surface waves. Later in 1911, Love [20] discovered another important surface wave, while investigating the mechanical wave propagation in a half space overlaid by a layer. Rayleigh and Love waves may be regarded as the result of interference of waves incident and reflected at the surface. As the surface waves spread in two dimensions, geometrical damping affect them less than body waves, which spread in three dimensions. Another important characteristic of surface waves is their dispersion. In a nonhomogeneous semi infinite medium, both Rayleigh and Love waves are dispersive, i.e. different frequencies travel with different velocities. Generally, the apparent velocities of different elastic waves in descending order is  $C_p > C_s > C_L > C_R$ ; whereas, the resulted amplitudes at the surface are in the reverse order. The following section explains the behavior of Love and Rayleigh waves in more detail.

## Love waves

Interaction of SH waves and free surface in a media that its velocity increases with depth, generates Love waves. Love waves can not develop in a homogeneous half space. Their deformation is parallel to the surface and decrease with depth exponentially (2-4). From a physical view point, the generation of Love waves are due to the entrapment of SH waves energy near the surface.

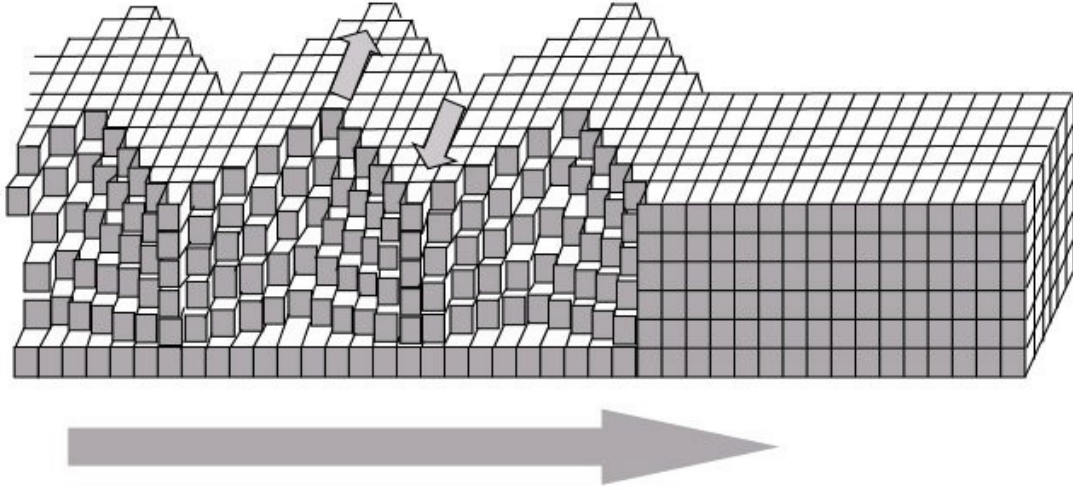


Figure 2-4: Surface deformation due to the propagation of Love waves (<http://www.geo.mtu.edu>)

Love waves are dispersive. In the case of a half space overlain by a layer with a thickness of  $h$ , the dispersion relation is in the form [17]:

$$\tan(\omega\eta) = \left( \frac{\mu_1 \sqrt{1 - \frac{C_x^2}{C_{s2}^2}}}{\mu_2} \right) \left( \frac{h}{C_x \eta} \right) \quad (2.37a)$$

$$\text{where } \eta = \frac{h}{C_x} \sqrt{\frac{C_x^2}{C_{s1}^2} - 1} \quad (2.37b)$$

where  $\mu_1$  and  $\mu_2$  are the shear modulus of the layer and half space respectively,  $C_x$  is Love wave velocity,  $C_{s1}$  is the shear wave velocity in the layer, and  $C_{s2}$  is shear wave velocity in the

half space. For energy to be trapped near the surface the calculated Love wave velocity should be bounded as:  $C_{s1} < C_x < C_{s2}$ . To show the application of equation 2.37 consider a half-space overlaid by a 40 m layer ( $h$ ). Shear wave velocity in the layer is  $C_{s1} = 390 \frac{m}{s}$  and in the half space is  $C_{s2} = 520 \frac{m}{s}$ . The unit density of the layer is  $\rho_1 = 2000 \frac{kg}{m^3}$  and of the half-space is  $\rho_2 = 3300 \frac{kg}{m^3}$ . Figure 2-6 shows the graphical solution of equations 2.37. Each set of graphs corresponds to a single frequency. In each graph the dashed line show the right side of equation 2.37a and the solid line show the left side of the same equation. Thus, the points at which the graphs cross each other represent a solution to the equation. For lower frequencies (Fig. 2-5a) the wave propagates with a single frequency or in just one mode. As the frequency increases the number of modes also increases. Thus, for a frequency of 19.1 Hz the wave propagates with three different velocities (Fig. 2-5c). The figures show that as the frequency of the vibration decreases the velocity of the fundamental mode of vibration (mode 1) gets closer to the velocity in the half space. For a single frequency with different modes, the higher modes propagate with a velocity close to the half-space velocity.

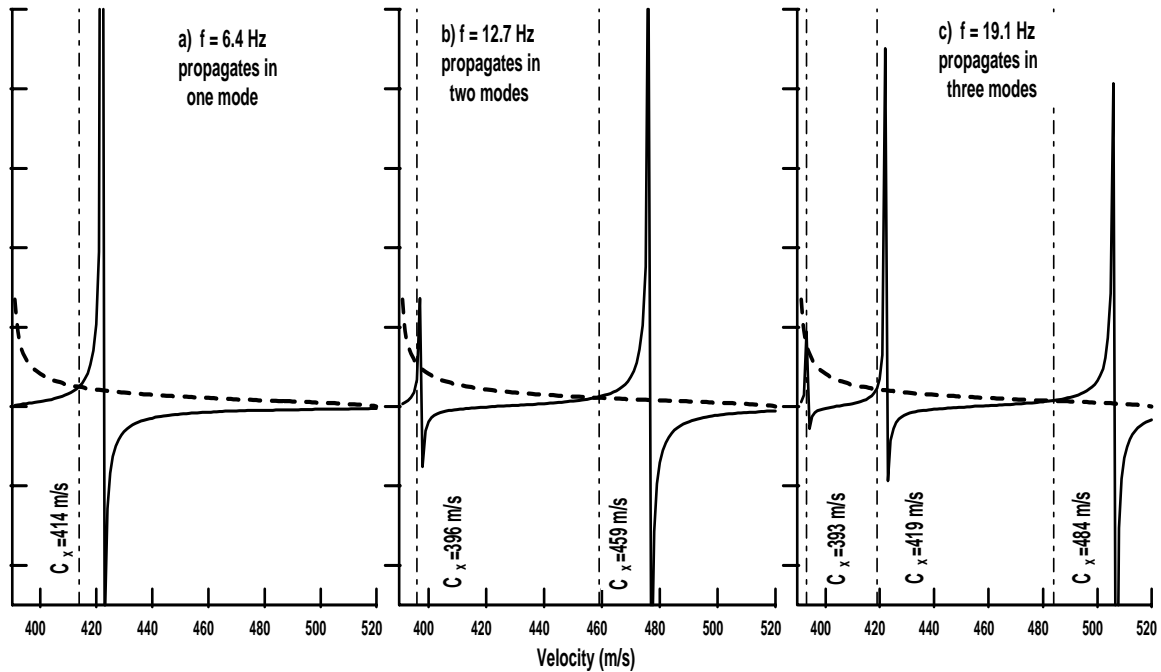


Figure 2-5: Graphical solution of the dispersion of Love waves in a layer over a halfspace.

Figure 2-6 depicts the deformation patterns corresponding to different modes and frequencies. The figures are generated based on the equations obtained from [17]. The patterns show that the deformations are confined to a relatively short distance below the surface. Comparing the results with the calculated velocities (Fig. 2-5) shows that as the velocity increases the deformations penetrate more into the half-space. Thus, the propagation characteristics of very low frequencies and/or higher modes of propagation are mostly affected by underlying layers and not the top ones. This behavior of surface waves is used in non-intrusive testing techniques to assess the condition of the underlying soil layers.

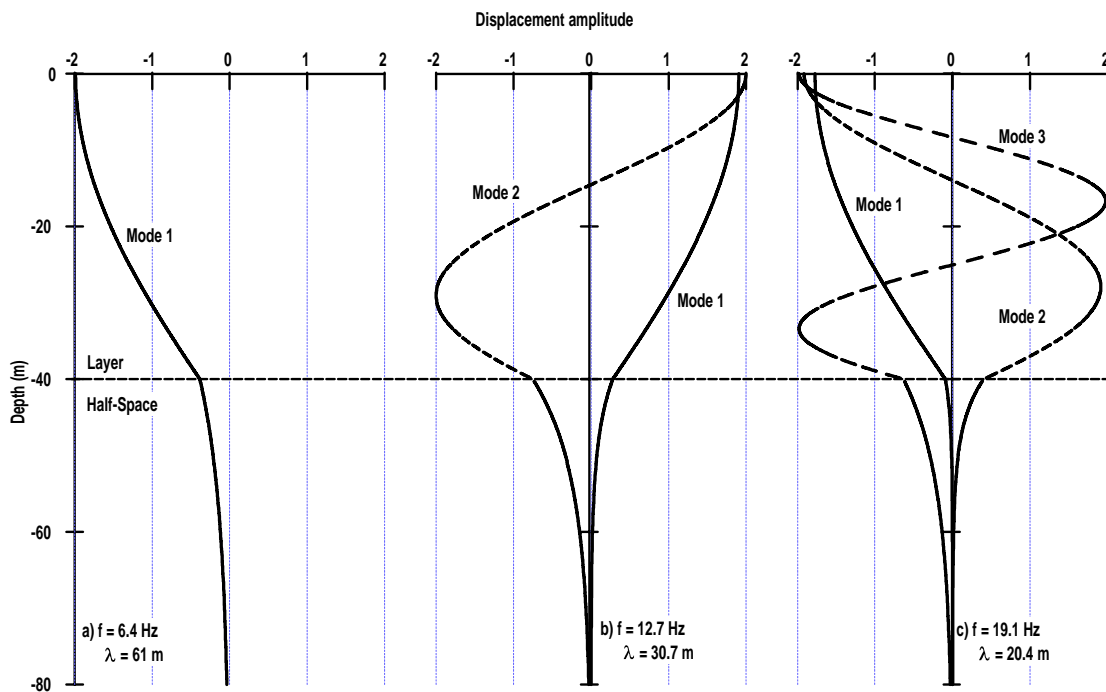


Figure 2-6: Displacements due to Love waves in a half space overlaid by a 40 m deep layer. Graph a shows the displacements due to low frequencies that only excites one mode. Graphs b and c show that higher frequency Love waves can propagate in more than one mode.

### Rayleigh waves

The second type of surface waves is called Rayleigh waves (Fig. 2-7). Their deformation is retrograde at the surface that changes into prograde at deeper levels of the media. These waves

are generated due to the interaction of p and SV waves with the free surface. They can exist in a homogeneous half-space as well as in a layered one. As shown in the previous sections, only p and SV waves are considered in the mathematical development of Rayleigh waves, because they completely satisfy boundary conditions and do not interact with the SH waves. Equation 2.32 is the dispersion equation for Rayleigh waves in a homogeneous half-space. It can be seen that in such a media, velocity is not a function of frequency; hence, Rayleigh wave is not dispersive in a homogeneous media. Though, similar to Love waves, in a layered medium Rayleigh waves are dispersive and can propagate in different modes.

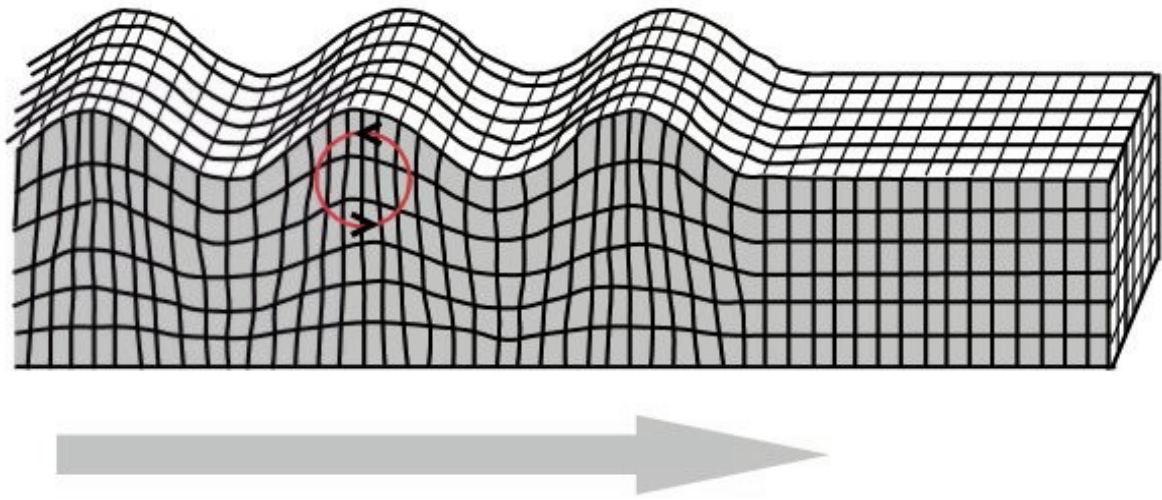


Figure 2-7: Surface deformation due to the propagation of Rayleigh waves (<http://www.geo.mtu.edu>)

To assure that energy is trapped near the surface, the mathematical solution should ensure that energy does not propagate away from the free surface. This condition is satisfied when Rayleigh wave velocity ( $C_R$ ) is smaller than the shear wave velocity ( $C_s$ ) in the media [17]. In a non-dispersive media, the following empirical relation gives good estimates of the Rayleigh wave velocity [16]:

$$C_R = \frac{0.87 + 1.12\nu}{1 + \nu} C_s \quad (2.38)$$

Rayleigh waves have displacement components both in parallel and perpendicular directions

to the free surface. Both components decay with depth as a function of  $e^{-k_x z}$  (equation 2.29) where  $z$  is the depth and  $k_x$  is the wave number in the direction parallel to the direction of wave propagation. In fact, the only meaningful wavelength is the one parallel to the free surface, because the harmonic wave solution applies only in this direction.

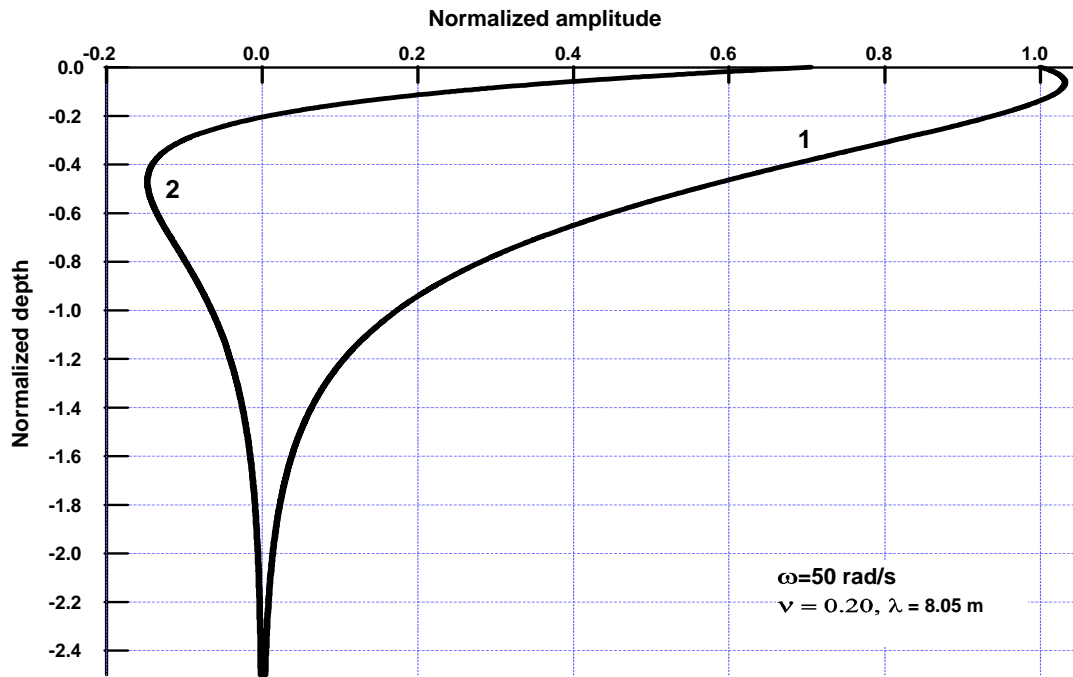


Figure 2-8: Variation of Rayleigh wave displacements with depth. Curves 1 and 2 show vertical and horizontal displacements respectively. The values of all displacements are normalized to the value of vertical displacement at the surface. Vertical axis shows depth normalized to the wavelength.

Figure 2-8 shows the pattern of the displacements due to Rayleigh wave excitations in a homogeneous medium. After a depth of about  $2\lambda$  the amplitudes are so small. Hence, it can be concluded that practically the maximum penetration depth of Rayleigh wave is  $2\lambda$ . At the surface, the amplitude of horizontal displacement (curve 2) is about 65% of the amplitude of vertical displacement. Horizontal displacement changes direction at a depth of about  $0.2\lambda$  and its maximum happens approximately at  $0.4\lambda$ . The maximum of vertical displacement occurs at a depth of about  $0.12\lambda$  and the curvature of the displacement pattern changes at a depth of

approximately  $0.4\lambda$ . From the figure it can be concluded that lower frequencies (longer periods) penetrate deeper into the medium. Thus the properties of deeper layers have mode effects on lower frequencies. As a rule of thumb Rayleigh waves are very sensitive to the mechanical properties at depths about  $0.4\lambda$  [19].

In time harmonic waves the flux of energy, which defines the rate at which energy is communicated per unit area, is proportional to material rigidity, and excitation frequency and amplitude squared [13]. Thus, the power of an excitation and its rate of change at each depth can be estimated by calculating the square of displacement amplitude at that depth. Summation of the values over depth results in cumulative energy flux, which is used to evaluate the penetration depth of Rayleigh waves. Figure 2-9 is based on the following integral equation:

$$P_z = \frac{1}{P_{tot}} \int_0^z u(z)^2 dz \quad (2.39)$$

$$\text{where } P_{tot} = \int_0^{z_{max}} u(z)^2 dz$$

In equation 2.39  $u(z)$  can be any displacement component as a function of depth ( $z$ ),  $P_{tot}$  is the total energy flux calculated between the surface and maximum depth of  $z_{max}$ . Figure 2-9 shows the cumulative energy flux calculated for horizontal (graph a) and vertical (graph b) components of displacements. Graph c corresponds to the values calculated for the total displacement, which is defined as  $\sqrt{u_x^2 + u_z^2}$ . The upper limit of the integral ( $z_{max}$ ) is chosen to be  $2.5\lambda$ . The figure shows that the curves are very steep up to a depth of about  $0.7\lambda$ , after that the slope decreases, and after a depth of about  $1.2\lambda$  the curves remain almost with no significant change. This behavior shows that the energy of Rayleigh wave is confined in a depth of about  $1.0\lambda$  to  $1.2\lambda$ . Thus, it can be concluded that the propagation of Rayleigh waves are almost irrespective of the properties of the layers located beyond a depth of  $1.0\lambda$ .

## 2.4 Damping and attenuation is seismic waves

A decrease in the amplitude of a wave in time, space or both, is called attenuation or damping. Generally, seismic waves attenuate due to six different processes: geometric or radiation damp-

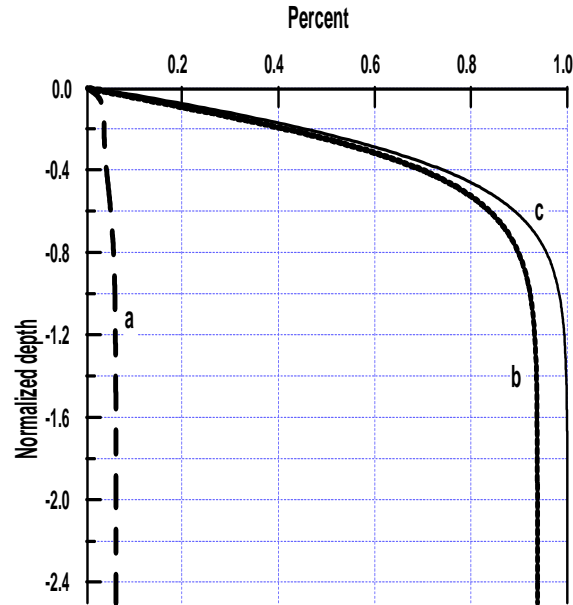


Figure 2-9: Variation of cumulative energy flux of Rayleigh wave with depth. Graph a corresponds to horizontal displacement and graph b corresponds to vertical displacement. Graph c shows the cumulative energy flux of total displacement.

ing, reflection and transmission at interfaces, scattering, multi-pathing and intrinsic damping. The first five processes are elastic in which energy is conserved. This means that the integral of energy over the whole wave field remains constant. Alternatively, in intrinsic damping elastic energy is not conserved and is converted into heat and other forms of energy. This process is due to anelasticity, which implies that the permanent deformation of the medium converts part of the kinetic energy of elastic wave motion into heat.

### 2.4.1 Geometrical damping

In spherical (i.e. p- and s- waves) or cylindrical (i.e. Rayleigh waves) waves, as the wave moves forward the size of the wave front increases. Thus, conservation of elastic energy requires that the density of energy at the surface of the wave front decreases. This phenomena is called geometrical damping. As Rayleigh wave has a cylindrical front in a half-space, the growing circumference of its front is a function of  $2\pi r$ , where  $r$  is the distance from source. Thus, the



energy per unit wave front decreases as a function of  $\frac{1}{r}$  to conserve energy, consequently the amplitude decreases as a function of  $\frac{1}{\sqrt{r}}$ . In body-waves (p- and s-waves) the front is spherical, and increases as a function of  $\pi r^2$ . Hence, the energy per unit wave front decreases as  $\frac{1}{r^2}$ , and the amplitude as  $\frac{1}{r}$ .

Mathematically the decay in the amplitude of the particle motion ( $A$ ) due to geometrical damping between two points at distances  $r_1$  and  $r_2$  from the source can be expressed as [18]:

$$\frac{A_2}{A_1} = \left(\frac{r_1}{r_2}\right)^\varsigma \quad (2.40)$$

where  $\varsigma$  is equal to 0 to plane waves, 0.5 for Rayleigh waves and 1 for body waves. In conclusion, geometric attenuation attenuates body waves more rapidly than Rayleigh waves.

#### 2.4.2 Reflection, transmission and scattering at interfaces

When a wave propagating through a medium encounters a discontinuity scattering of the wave might occur. Discontinuity is referred to any change in stiffness or geometry of the media, such as cavities, cracks, inclusions or free surfaces. Scattering could be in the form of reflection, refraction, diffraction, and mode conversion. The scattered and transmitted waves have the same angular frequency as the incident wave, otherwise continuity of the displacements at interfaces will not be satisfied. Conversely, the transmitted, refracted, reflected and incident waves might have different wavelengths and amplitudes [17]. In general, the relation between the amplitudes of the incident and transmitted waves can be stated in the form [18]:

$$\frac{A_2}{A_1} = T \quad (2.41)$$

where  $A_1$  and  $A_2$  are the amplitudes of the incident and transmitted waves respectively, and  $T$  is the transmission factor. For body waves encountering an interface, the difference between the properties across the interface determines the relative amount of the scattered and transmitted energy. Thus, the transmission coefficient ( $T$ ) depends on the product of density and velocity - acoustic impedance ( $\rho v$ ) - of each media. In cases that body waves encounter inclusions, such as cavities, the relative size of the cavity with respect to the wavelength of the incident wave also affects the value of the transmission factor. When the size of the inclusion is

much greater than the wavelength ( $d \gg \lambda$ ) scattering in the form of reflection, refraction and mode conversion occurs. On the other hand, if the size of the inclusion is much smaller than the wavelength of the incident wave ( $d \ll \lambda$ ), the wave travels through a medium with properties that reflects the combined properties of the media and inclusion. In this case energy scattering is a function of  $d^3\omega^4$ .

### 2.4.3 Intrinsic damping

Intrinsic damping is referred to the mechanisms which convert the mechanical energy into other types of energy such as heat. This conversion could be because of the developed nonlinear friction between the molecules and grains, viscoelastic behavior or non-elasticity of the material. In the earth, intrinsic damping is relatively small specially for low frequencies [19]. Intrinsic damping is commonly measured by a dimensionless parameter called quality factor as defined by:

$$\frac{1}{Q(\omega)} = \frac{\Delta W}{2\pi W} \quad (2.42)$$

Thus,  $Q$  - sometimes referred to as specific attenuation factor - represents the ratio between the total stored energy ( $W$ ) to the dissipated energy ( $\Delta W$ ) per volume per cycle of vibration. For high frequencies,  $Q$  can be regarded as nonelastic response of earth, and for low frequencies as viscosity [19]. The amplitude ( $A$ ) and frequency of vibration ( $\omega$ ) affect the value of  $Q$ . For small strains - in the order of  $10^{-5}$  or less -  $Q$  can be assumed to be independent of vibration amplitude. Laboratory experiments have shown that in solids, up to relatively high frequencies,  $Q$  is independent of frequency within the engineering accuracy. Thus, it is reasonable to assume that for a homogeneous sample,  $Q$  is independent of frequency at low frequencies. In the upper mantle of earth an average value of  $Q$  is 110 [21].  $Q$  is inversely proportional to attenuation of the wave, thus a large value of  $Q$  indicates a low loss medium and vice versa.

Another parameter that is used to assess the attenuation in a media is attenuation coefficient as:

$$\alpha = \frac{\omega}{2cQ} \quad (2.43)$$

where  $\omega$  is angular frequency,  $c$  is velocity and  $Q$  is quality factor.  $\alpha$  is measured in space and between two points. Thus, it represents the energy loss per wavelength of the excitation. As an example, the value of  $\alpha$  in granite is from 0.1 to 0.4  $km^{-1}$ . From 2.43 it is evident that if  $Q$  is independent of frequency,  $\alpha$  will be a function of first power of frequency. For the propagation of sinusoidal waves, intrinsic damping is modelled as an exponential decay, thus in lieu of any other type of damping the effect of intrinsic damping can be shown as:

$$\frac{A_2}{A_1} = e^{-\alpha(r_2-r_1)} \quad (2.44)$$

in which,  $A_1$  and  $A_2$  are the amplitudes at locations 1 and 2 respectively,  $r_1$  is the distance between location 1 and the source and  $r_2$  is the corresponding distance from location 2. similarly, the attenuation can be defined as the energy loss per cycle of vibration. This type of attenuation is called temporal attenuation coefficient and satisfies the following equality [18]:

$$\alpha_t T = \alpha \lambda \quad (2.45)$$

where  $T$  is the period of the excitation and  $\lambda$  is the wavelength.

Logarithmic decrement is also used to measure the attenuation in lossy media. The definition as stated in structural dynamics is the natural logarithm of the ratio between the successive amplitudes in a free vibrating system [22]. In mathematical form logarithmic decrement with respect to time can be stated as:

$$\Delta_t = \ln \left( \frac{u_n}{u_{n+1}} \right) \quad (2.46)$$

where  $u_n$  is the maximum amplitude at cycle  $n$  and  $u_{n+1}$  is the maximum amplitude in cycle  $n + 1$ . Likewise, equation 2.46 can be used to define logarithmic decrement in spatial domain ( $\Delta_x$ ). In the latter definition  $u_n$  will be maximum amplitude at location  $n$  and  $u_{n+1}$  the maximum amplitude at location  $n + 1$ . With the above definitions, the relation between the logarithmic decrement with respect to time and the attenuation factor will be [18]:

$$\alpha = \frac{\Delta_t}{\lambda} \quad (2.47)$$

Granular materials like soil, have very complex structure and no model can completely describe their behavior under all loading conditions. Kjartansson [23] reviews the theories related to the attenuation of waves in soil. For small strains two of the most commonly used mathematical models are Maxwell and Kelvin-Voigt models [21]. In both of these models a viscosity parameter ( $\eta$ ) is defined and the stress-strain relations are adjusted to take into account the effect of viscosity. The defined relations are:

$$\frac{d\epsilon}{dt} = \frac{1}{\mu} \frac{d\sigma}{dt} + \frac{\sigma}{\eta} \quad \text{Maxwell model} \quad (2.48a)$$

$$\sigma = \mu\epsilon + \eta \frac{d\epsilon}{dt} \quad \text{Kelvin-Voigt model} \quad (2.48b)$$

where  $\epsilon$  is strain component,  $\sigma$  is the corresponding component of stress, and  $\mu$  is an elastic constant in general that in this context it is the shear modulus  $G$ . Based on the above definitions the quality factors are:

$$Q = \frac{\omega\eta}{G} \quad \text{Based on Maxwell model} \quad (2.49a)$$

$$Q^{-1} = \frac{\omega\eta}{G} \quad \text{Based on Kelvin-Voigt model} \quad (2.49b)$$

The aforementioned models are considered to be constant  $Q$  models. Thus, it concludes that viscosity ( $\eta$ ) is a parameter that changes with frequency [24]. The corresponding attenuation factor in Maxwell model is frequency independent and in Kelvin-Voigt model is function of second power of frequency. Hardin [25] has shown that for steady-state vibration the logarithmic decrement with respect to time and space can be defined by:

$$\Delta_t = \frac{2\pi \left\{ 1 - \left[ 1 - \left( \frac{\omega\eta}{G} \right)^2 \right]^{\frac{1}{2}} \right\}}{\frac{\omega\eta}{G}} \quad (2.50a)$$

$$\Delta_x = 2\pi \left\{ \frac{\left[ 1 + \left( \frac{\omega\eta}{G} \right)^2 \right]^{\frac{1}{2}} - 1}{\left[ 1 + \left( \frac{\omega\eta}{G} \right)^2 \right]^{\frac{1}{2}} + 1} \right\}^{\frac{1}{2}} \quad (2.50b)$$

where all the parameters are defined previously. Combining the equalities 2.49 and 2.50, it will be clear that for Maxwell and Kelvin-Voigt models the values of logarithmic decrement are independent of frequency. Further, Hardin [25] shows that in sands subjected to small strains and confining pressures larger than 2 *psi* (13.7 *kPa*) the values of  $\Delta_x$  and  $\Delta_t$  are very close and can be used interchangeably.

#### 2.4.4 Total attenuation

Based on the previous discussions, the combined contributions of all types of dampings can be expressed in mathematical terms as [18]:

$$\frac{A_1}{A_2} = \left(\frac{r_2}{r_1}\right)^\varsigma e^{\alpha(r_2-r_1)}T^{-1} \quad (2.51)$$

For Rayleigh waves  $\varsigma = 0.5$ , thus calculation of the logarithmic decrement of total attenuation (equation 2.51) leads to:

$$\Delta_x = 0.5Ln\left(\frac{r_2}{r_1}\right) + \alpha(r_2 - r_1) - Ln(T) \quad (2.52)$$

This relation shows that in soils where attenuation coefficient ( $\alpha$ ) is small, the effect of intrinsic damping is conspicuous where  $r_2 \gg r_1$ . Further, in a homogeneous media where  $T = 1$  the only term that affects the amplitudes in short distances is the geometrical damping. Geometrical damping is the only parameter that has exact mathematical relation. Hence, to remove its effect each response can be multiplied by a calculated factor based on the ratio  $\frac{r_2}{r_1}$  and the wave type ( $\varsigma$ ). In this way, in a nonhomogeneous media, by removing the effect of geometrical damping and neglecting the effect of intrinsic damping for short distances the logarithmic decrement can be used to study the effect of inhomogeneities on the responses.

## 2.5 Forced vibration of an elastic semi infinite media

The analysis presented in previous sections corresponds to the steady-state vibration of an elastic half space. In many practical problems, the case of a forced vibration is more important. Although the steady-state vibrations case can be solved fairly easily, the solution of forced

vibrations involves complicated integrals that in many cases reduce to singular ones without a closed formed solution. Hence finding a general solution for all the practical cases is not possible.

The classical analysis in this area was performed by Lamb [26]. He considered a half space subjected to line and point loads on the surface and within the medium. Harmonic loadings were considered, and superposition technique was used to obtain results for pulse loadings. Ewing et al. [27] presented a thorough review of the analysis of this problem. Appendix A, contains the results of a few of these closed formed solutions.

In general, all the solutions confirm the existence of surface waves, which have larger components at the surface, in comparison with p- and s-waves. Table 2.3 shows that the geometrical damping is smaller for surface waves than for body waves because of the cylindrical nature of the propagation of surface waves.

Table 2.3: Amplitude distance relations in Lamb's problem (Bath 1984)

Force type	Medium	Rayleigh	p-	s-
Line	Infinite	$N/A$		$r^{-\frac{1}{2}}$
Line (normal or tangential)	Semi-infinite half-space	$r^0$		$r^{-\frac{1}{2}}*$
Point	Infinite	$N/A$		$r^{-1}$
Point	Semi-infinite half-space	$r^{-\frac{1}{2}}$		$r^{-1}*$
*- In the original table these values are stated differently and are modified here				

Cases 3 and 7 of Table A-2 (Appendix A) are of special importance in this study. These solutions are used to calibrate the developed numerical models. The surface displacements at the surface of a 3D semi-infinite elastic media are shown in Figure 2-10. The media is subjected to an axisymmetric loading (case 7 in Appendix A) and the presented displacements correspond to the effect of Rayleigh waves only. Details of the equations used to calculate the displacements in figure 2-10 are presented in Mathgram 2-1 (Appendix B). Farther from the source, the decreasing trend of the amplitudes is due to the effect of geometric damping, which is a function of  $r - \frac{1}{2}$  (Table 2.3). These solutions are only valid at large distances from the source. Details of the loading function for this case are presented in Chapter 6.

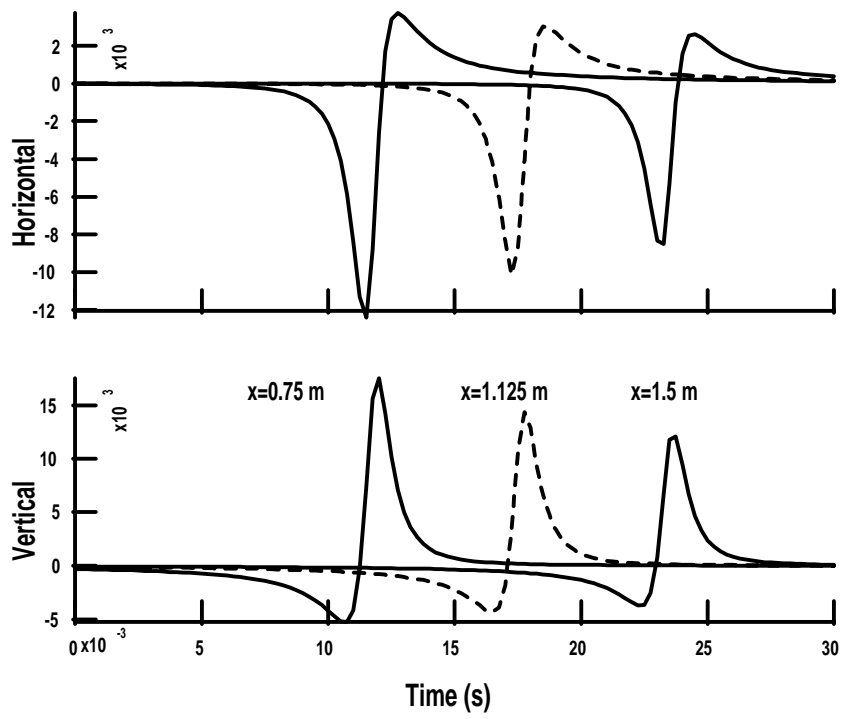


Figure 2-10: Lamb solution for forced vibration of a semi-infinite medium. Plot (a) shows the horizontal displacements and plot (b) shows the vertical displacements at distance  $x$  from source.

## Chapter 3

# Signal processing techniques

A large number of the physical quantities can be represented by a function that varies with one or more independent variables. The desired part of this function is called signal and the undesired part is called noise. Usually, a signal contains information about the behavior or nature of the phenomenon. For example, in geophysical techniques the displacement or velocity of the ground is measured and recorded as a function of time and/or position. It is shown that these recorded signals carry valuable information about the geological structure of the earth.

Signal processing deals with functions of time, frequency, space, and etc. without considering the physical concepts behind them. In this context, if the signal is decomposed into shifted and scaled impulses (or step functions) the study is performed in time domain. Likewise, if the signal is decomposed into sinusoids with different frequencies, the study is conducted in frequency domain [28].

### 3.1 Time domain analysis

In most of the engineering applications, signals are collected in time domain using a digital data acquisition system (DAQ). Digital data are the ones sampled at discrete time intervals, or they can be inferred as the intermittent observation of a continuous or discrete parameter. In mathematical term, a digitized signal is represented by a continuous function multiplied by a summation of delta functions repeated at a sampling interval  $\Delta t$  (Comb function). Figure 3-1 shows the effect of under-sampling or aliasing on the recorded signal. As it is seen the recorded



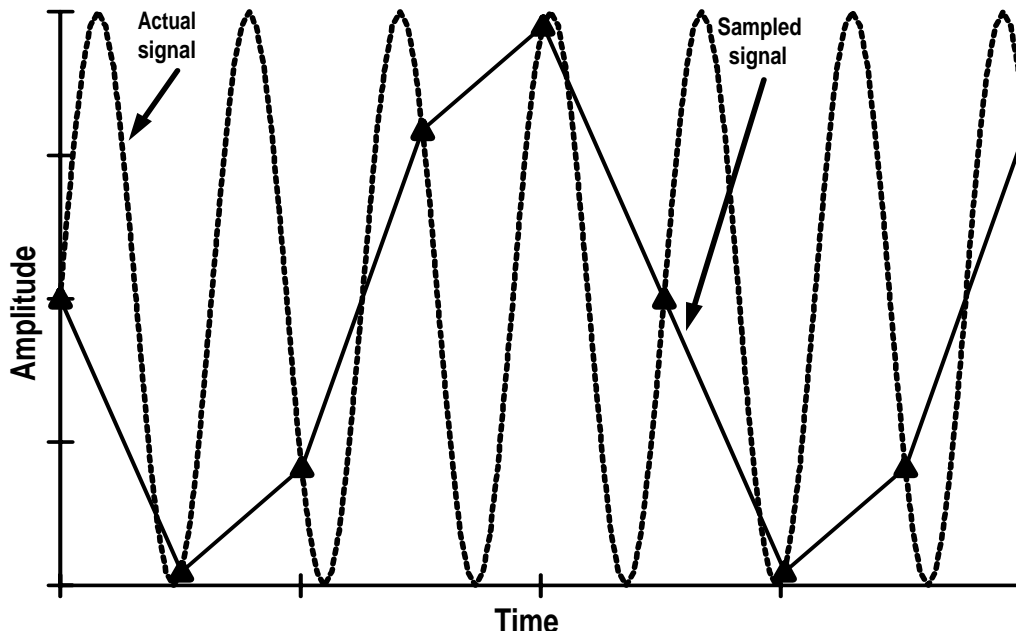


Figure 3-1: Effect of low sampling rate on the shape of the recorded signal.

digitized signal has a larger frequency than the actual one. To capture all the characteristics of the actual signal the sampling rate should be sufficiently small. Generally, to avoid aliasing in the recorded signal, the sampling rate ( $\Delta t$ ) or sampling frequency ( $f_s$ ) should satisfy the Nyquist criterion:

$$f_s = \frac{1}{2\Delta t} > f_{Nyquist} = \frac{2}{T} \quad (3.1)$$

where  $T$  is the largest period available in the signal. The sampling theorem states that in order to regenerate a continuous signal from discrete observations, the function should be sampled at least twice per period. In practice a minimum number of 10 sampling points per wavelength is recommended [28].

An important concept that plays a major role in the time and frequency domain analysis is the convolution integral as defined below:

$$x(t) * y(t) = \int_{-\infty}^{+\infty} x(\tau)y(t - \tau)d\tau$$

The convolution operator is cumulative, associative and distributive. Convolution, along with other tasks, such as windowing, stacking, and smoothing using moving averages have applications in smoothing the noisy signals, modulating amplitude and frequency, finding similarities between the signals, removing unwanted reflections and refractions, separating different events in a signal and etc. A discretized form of some of these applications will be covered later in this chapter. Cartwright [29] provides a more in-depth review of the subjects.

## 3.2 Frequency domain analysis

In mathematics, transformations are used to change the study domains. This domain change, enables us to perform some tasks in an easier manner, gain better insights into the behavior of some parameters, or define and measure new parameters. Fourier transforms are used to change the domain of the study from time to frequency. In a physical context, this transform can represent a change from time to frequency, or from distance to wave-number (spatial frequency). The basic assumption is that any time series can be decomposed into a sum or integral of harmonic waves with different frequencies. When different harmonics behave differently, Fourier analysis makes it possible to study the behavior of each individual harmonic. The general definition of Fourier transform is:

$$f(t) = \frac{1}{2\pi} \int_{-\infty}^{+\infty} F(\omega) e^{i\omega t} d\omega \quad \text{Fourier transform} \quad (3.2a)$$

$$F(\omega) = \int_{-\infty}^{+\infty} f(t) e^{-i\omega t} dt \quad \text{Inverse Fourier transform} \quad (3.2b)$$

in which  $\omega$  is angular frequency, and  $F(\omega)$  is the Fourier transform of the time signal  $f(t)$ . For real valued  $f(t)$  functions, the Fourier transform will be a complex number in the following form:

$$F(\omega) = |F(\omega)| e^{i\phi(\omega)} \quad (3.3a)$$

where

$$|F(\omega)| = \sqrt{\text{Re}[F(\omega)]^2 + \text{Im}[F(\omega)]^2} \quad \text{Amplitude spectrum} \quad (3.3b)$$

$$\phi(\omega) = \tan^{-1} \left( \frac{\text{Im}[F(\omega)]}{\text{Re}[F(\omega)]} \right) \quad \text{Phase spectrum} \quad (3.3c)$$

Equation 3.3 shows another advantage of using Fourier transforms. To completely describe a cosine function in time domain a large number of points are required (i.e. 10 points per wave-length), but representation of the same function in frequency domain requires just two complex numbers [17]. Thus, the frequency domain description of a function is simpler.

The evaluation of Fourier integrals for discretized signals is performed by using discrete form of Fourier transforms (DFT) or Fourier sums:

$$X_u = \sum_{i=0}^{N-1} x_i e^{-j(u\frac{2\pi}{N}i)} \quad (3.4a)$$

$$x_i = \frac{1}{N} \sum_{u=0}^{N-1} X_u e^{j(u\frac{2\pi}{N}i)} \quad (3.4b)$$

where  $j = \sqrt{-1}$ ,  $x_i$  is the amplitude of the recorded signal at time  $i$ ,  $N$  is the total number of records, and  $X_u$  is the Fourier amplitude of the signal at frequency  $f_u$ . The analysis equation (3.4a) is used to transform the signals from time into frequency domain, and to perform the inverse transformation the synthesis equation (3.4b) is used. In practice fast Fourier transform (FFT), which is an efficient numerical procedure, is used to evaluate DFT sums [30]. The main assumption in FFT is periodicity of the signals. In other words, any recorded signal has a period of repetition equal to its recording duration. In some cases, this assumption might cause some discrepancies in the evaluated frequency contents. In the FFT algorithm, the number of available points in time should be a power of two.

### 3.2.1 Properties of Fourier transform

The properties of Fourier transforms, presented here, are extensively used in signal processing. These properties are recalled here without any proof. Hsu [31] and Kreyszig [32] provide more coverage of the theoretical background of these properties. In all the following explanation  $f(t)$  and  $g(t)$  are general time functions,  $F(\omega)$  and  $G(\omega)$  are the corresponding Fourier transforms,  $a$  and  $b$  are constants, and  $F$  and  $F^{-1}$  are the Fourier and inverse Fourier operators respectively..

- Linearity:  $F [af(t) + bg(t)] \implies aF(\omega) + bG(\omega)$
- Shift in time:  $F [f(t - t_0)] \implies e^{-i\omega t_0} F(\omega)$
- Shift in frequency:  $F^{-1} [F(\omega - \omega_0)] \implies e^{i\omega_0 t} f(t)$
- Scaling in time and frequency:  $F [f(at)] \implies \frac{1}{|a|} F\left(\frac{\omega}{a}\right)$
- Derivative:  $F\left(\frac{df(t)}{dt}\right) = i\omega F(\omega)$
- Convolution:  $f(t) * g(t) = F(\omega) G(\omega)$ . Convolution in time is equivalent to multiplication in frequency and vice versa.
- Parseval's theorem:  $\int_{-\infty}^{+\infty} |f(t)|^2 dt = \frac{1}{2\pi} \int_{-\infty}^{+\infty} |F(\omega)|^2 d\omega$ . This theorem relates the energy contents in time and frequency domains.
- Fourier transform of a signal + reflection:  $F [g(t) + ag(t - t_0)] \implies G(\omega) (1 - ae^{-i\omega t_0})$ . Figure 3-2 explains the interpretation of this equality. In the bottom plots a signal in time domain and its Fourier transform are depicted. In the top plots the same signal is shown in time domain and a late reflection is added to it. As it is seen, the effect of reflection in frequency domain is seen as successive peaks and valleys, though the general trend of the Fourier responses is not changed.

### 3.3 System: definition and characteristics

Any mathematical model that transforms an input signal (excitation) into an output signal (response) is called a system [31]. A system is called linear if it satisfies the following conditions:

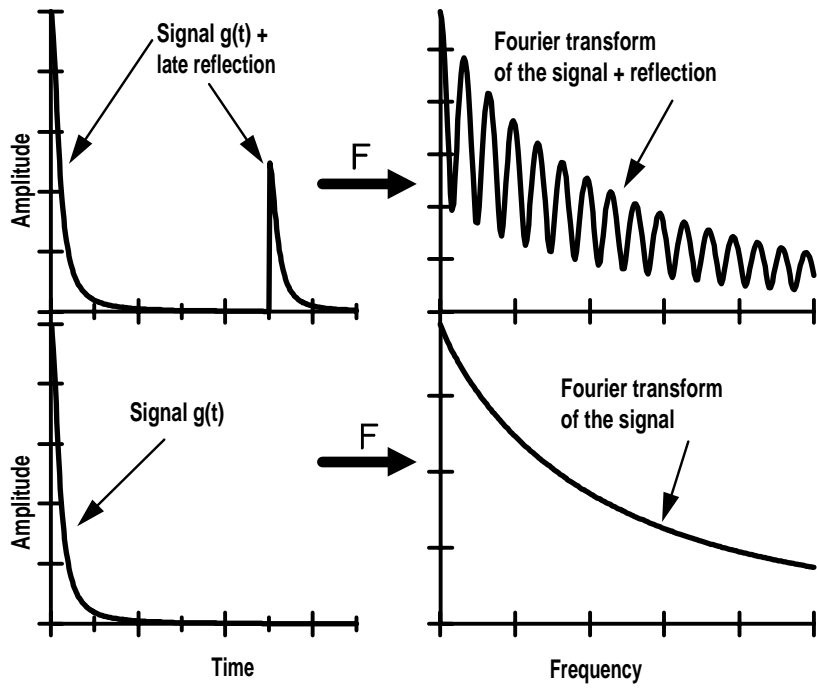


Figure 3-2: Effect of reflection on the frequency response of a signal.

$$\begin{aligned} \text{If } Tx_1 &= y_1 \wedge Tx_2 = y_2 \text{ then} & (3.5) \\ T(x_1 + x_2) &= y_1 + y_2 \text{ and } T(\alpha x_1) = \alpha y_1 \end{aligned}$$

Where  $T$  is the system operator. Equation 3.5 states that in a linear system the superposition principle is valid. If a time shift in the input causes the same time shift in output, the system is called time-invariant. In other words, in a time invariant system the response to a specific input does not change with time. Almost all the civil engineering systems are inherently time-variant, though for short perturbations they can be considered time invariant [28]. In general, when the duration of the input signal is much smaller than the characteristic period of the system, the system can be considered time-invariant. Another characteristic of a system is its stability. If a bounded input results in a bounded output the system is called stable.

Any linear time-invariant system (LTI) can be characterized by its response to an impulse function -i.e.  $\delta_i = 1$  if  $i = 0$  and  $\delta_i = 0$  otherwise. To rephrase, if the impulse output of an LTI system ( $h(t)$ ) is known, its output to any other excitation can be predicted. The output of an LTI system is defined as:

$$y(t) = x(t) * h(t) \quad \text{response in time domain} \quad (3.6a)$$

$$Y(\omega) = X(\omega) H(\omega) \quad \text{response in frequency domain} \quad (3.6b)$$

where  $x(t)$  and  $y(t)$  are the input and output of the system in time domain,  $X(\omega)$  and  $Y(\omega)$  are the Fourier response of the input and output respectively, and  $h(t)$  and  $H(\omega)$  are the impulse response of the system in time and frequency domains respectively. Equation 3.6 clearly shows the advantage of investigating the behavior of a system in frequency domain, where instead of calculation of a convolution integral in time to obtain the output, the same response can be obtained by a simple multiplication in frequency domain. Hsu [31] shows that in an LTI system the amplitude and phase spectra ( $|Y(\omega)|$  and  $\phi_Y(\omega)$ ) of the output are related to the corresponding values of the input and impulse response as:

$$|Y(\omega)| = |X(\omega)| |H(\omega)| \quad (3.7a)$$

$$\phi_Y(\omega) = \phi_X(\omega) + \phi_H(\omega) \quad (3.7b)$$

The function  $|H(\omega)|$  is called the gain of the system. It can be easily shown that if a system is to transmit the input without any change in the shape of the signal, i.e. just a change in the amplitudes and shift in time, the gain and phase spectra of the system should be:

$$|H(\omega)| = \text{const.} \quad (3.8a)$$

$$\phi_H(\omega) = -j\omega t_0 \quad (3.8b)$$

The concept introduced in equation 3.8 is called distortionless transmission, and is used in

the design of data acquisition systems and receivers to assure that the collected data are not distorted. In practice, all the systems have a bandwidth in which distortionless transmission is possible and beyond that the responses are distorted.

Generally, two types of problems can be defined with respect to the systems. Forward problems are the ones in which the input and the desired range of outputs are known in advance. The objective of the analysis is to design the system parameters such that the responses fall in the acceptable range. In civil engineering, this can be seen in the design of structures under estimated loadings to satisfy the serviceability and strength requirements. The other type of problem is called inverse problems, where the output and the input are available, or can be measured, and the system parameters and characteristics are of interest. An important application of this problem is in the non-intrusive evaluation of structures or soil. In non-intrusive assessments, the structure is excited by a source and the responses are recorded. Processing of the recorded signals along with the source information reveal the structure properties.

### 3.4 Processing of discrete signals

As mentioned before, almost all of the signals that are collected and processed are digitized. Digitization is equivalent to multiplying a continuous function in time with a comb function, or convolving it with a comb function in frequency domain. This task affects the amplitudes of the impulse response of the system, thus the recorded amplitudes are a function of the sampling frequency. It is well understood that as far as the Nyquist criterion is satisfied the frequency content, the rate of energy loss, and the output for an input are irrespective of sampling rate [28].

The length of a recorded signal determines its resolution in frequency. For a recorded signal with sampling rate  $\Delta t$ , and  $N$  number of recorded points the uncertainty principle states that higher resolution in frequency ( $\Delta f$ ) can be achieved, only in the expense of resolution in time. In other words:

$$\Delta f \times \Delta t = \frac{1}{N} \quad (3.9)$$

This principle infers that a longer signal in time will give a better resolution in frequency;

however, in practice the effect of noise on longer signals are more notable than on short ones. As a solution to this problem, zeros are added to the tail of a signal (zero-padding) to increase its fundamental period ( $N\Delta t$ ). Zero-padding is also used to obtain the required number of points for FFT algorithm. Further, zero-padding helps to solve the problems associated with the periodicity assumption in FFT. Zero-padding results in a denser sampling-frequency; although, it just performs a smooth interpolation within the range of actual resolution [17].

In a forward problem the input to the system (i.e.  $x_i$  in time or  $X_u$  in frequency) and the impulse response of the system (i.e.  $h_i$  in time and  $H_u$  in frequency) are known. Then, convolution operation is used to determine the output of the system (i.e.  $y_i$  in time or  $Y_u$  in frequency). Convolution integral in its discrete form is demonstrated as:

$$y_i = \sum_{k=0}^{N-1} x_k h_{i-k} \quad (3.10)$$

To obtain the time lag, or determine the similarities between two signals cross-correlation can be used. Cross-correlation is the convolution between the first signal and the time reverse of the second one. Similarly, in frequency domain cross-correlation is represented by multiplication of the Fourier response of the first signal and the complex conjugate of the second signal. Figure 3-3a shows two signals in time domain. The first signal is a sinusoid and the second is the same sinusoid modulated with a higher frequency and shifted in time. The calculated cross-correlation function for the two signals is also depicted in the same figure. As can be seen, maximum of the cross-correlation happens exactly at the beginning of the second signal. This behavior of cross-correlation function is used to evaluate the time delay between different signals. In figure 3-3b, the Fourier amplitudes of the two signals along with the Fourier amplitudes of the cross-correlation function (cross-spectral density) are depicted. It is observed that the notable amount of energy of the cross-spectral density is concentrated in the region that the two signals have common frequencies. Thus, cross-spectral density functions are used to evaluate the similarities between different signals.

Cross-correlation of a signal with itself is called auto-correlation. Auto-correlation enhances the information about the amplitude spectrum of a signal without taking into account phase spectrum information [17]. The Fourier response of the auto-correlation function of a signal is:



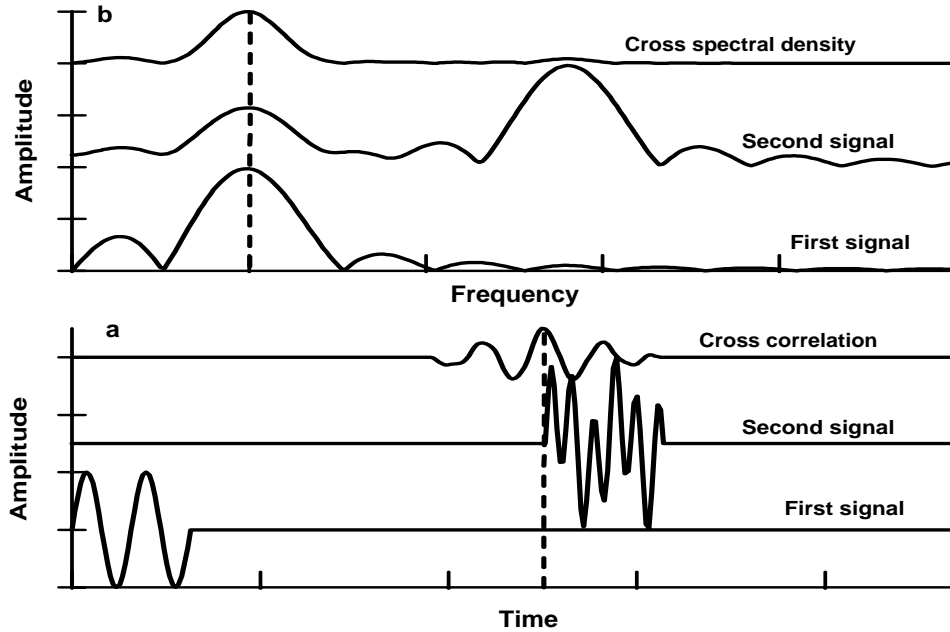


Figure 3-3: Cross correlation of two signals. Time delay between the two signals is shown as a peak in the cross correlation function (dashed line).

$$AC_u^{(x)} = |X_u|^2 = \left[ \text{Re}(X_u)^2 + \text{Im}(X_u)^2 \right] \quad (3.11)$$

Thus, functions with similar amplitude spectra and different phase spectra show similar auto-correlations. Further, as the energy of the signal is related to the square of its amplitude, the auto-correlation function is used as an indicator of the variation of energy with frequency. The plot of auto-correlation function of the signal versus frequency is called auto-spectral density, or power-spectral density.

Due to the memory limitations of the DAQ systems any recorded signal is limited or truncated in time. Energy leakage is a problem that is associated with the sharp truncation of signals. Figure 3-4a depicts two sinusoids with same frequency and different recording times. The frequency content of the signals (Fig. 3-4b) shows that due to truncation the energy is leaked to different frequencies, and thus the frequency content of the two signals are different. Very sharp cuts results in the leakage of energy to high frequencies. Further, truncation of signals at the middle of their cycles leads to DC components - energy at 0 frequency or static

component. Leakage happens because of the periodicity assumption in the FFT algorithm and can be mitigated by using smooth truncation windows.

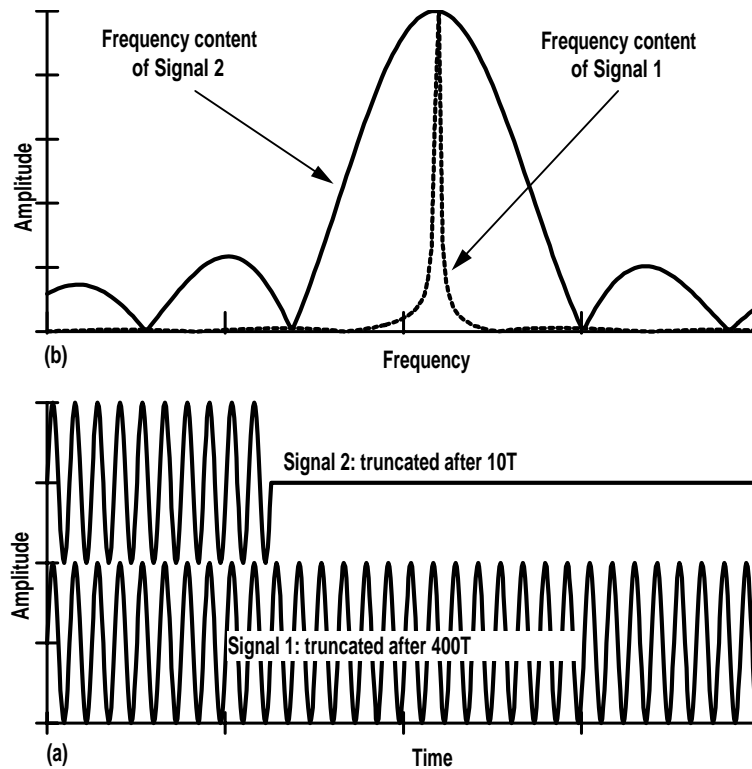


Figure 3-4: Energy leakage due to truncation of signals. Signal 1 has a record length equal to 400 times its period ( $T$ ), and the recording length of signal 2 is 10 times its period.

Windowing is the task of multiplication of a signal by a predefined function in time or frequency. Windowing is used to mitigate energy leakage, reduce the noise, eliminate unwanted parts or enhance specific parts of a signal. Some of the most popular windowing functions are as follows [28]:

$$w_i = \begin{cases} 0.5 + 0.5 \cos \left[ \frac{2\pi}{E} (i - M) \right] & \text{if } |i - M| \leq \frac{E}{2} \\ 0 & \text{otherwise} \end{cases} \quad \text{Hanning} \quad (3.12a)$$

$$w_i = \begin{cases} 0.54 + 0.46 \cos \left[ \frac{2\pi}{E} (i - M) \right] & \text{if } |i - M| \leq \frac{E}{2} \\ 0 & \text{otherwise} \end{cases} \quad \text{Hamming} \quad (3.12b)$$

$$w_i = \begin{cases} 1 & \text{if } |i - M| \leq \frac{E}{2} \\ 0 & \text{otherwise} \end{cases} \quad \text{Rectangular} \quad (3.12c)$$

in the above relations  $E$  is the total length of the signal, and  $M$  is the center of the window. Generally, windowing will reduce the energy of the windowed signal.

Filtering is a special type of windowing in frequency domain. Filtering is used to change or eliminate the amplitudes of certain range of frequencies in a signal. Three types of filters are used in signal processing. Low-pass filters are used to eliminate frequencies beyond a certain range; whereas, high-pass filters are used to eliminate frequencies lower than a certain range. Band-pass filters are designed to enhance the energy of certain frequency range. The amplitude spectrum of ideal filters are as follows:

$$H(\omega) = \begin{cases} 1 & \text{if } |\omega| < \omega_1 \\ 0 & \text{otherwise} \end{cases} \quad \text{low-pass} \quad (3.13a)$$

$$H(\omega) = \begin{cases} 0 & \text{if } |\omega| < \omega_1 \\ 1 & \text{otherwise} \end{cases} \quad \text{High-pass} \quad (3.13b)$$

$$H(\omega) = \begin{cases} 1 & \text{if } \omega_1 < |\omega| < \omega_2 \\ 0 & \text{otherwise} \end{cases} \quad \text{Band-pass} \quad (3.13c)$$

where  $\omega_1$  and  $\omega_2$  are limiting frequencies. In ideal filter to allow for distortionless transmission the phase spectrum should be  $\phi(\omega) = -\omega t_0$ .

Very often, bandwidth is used to quantify the range of frequencies in a signal that carries most of the energy or power. The Half-Power bandwidth is defined as the difference between the positive frequencies at which the amplitude spectrum drops to a value equal to  $\frac{|H(\omega)|_{\max}}{\sqrt{2}}$

[31]. Figure 3-5 explains the concept of half-power bandwidth.

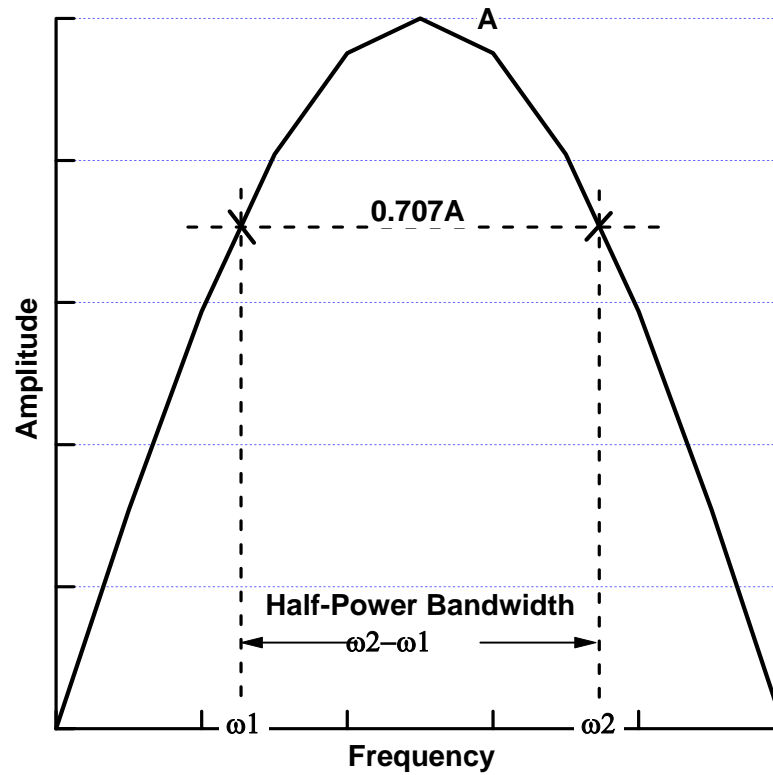


Figure 3-5: Definition of Half-Power Bandwidth. A is the maximum amplitude of the spectrum.

## 3.5 Signal analysis in frequency-wavenumber domain

### 3.5.1 Two dimensional (2D) signals: characteristics and representation

In geophysical field, signals are collected in real time and at different spacial locations. Thus, they have two independent dimensions, time and space. In many applications, i.e. determining wave velocity, assessing soil properties, and etc., it is required to analyze these signals in two dimensions. In graphical form, 2D signals can be represented in wiggle, contour or image, isometric, and perspective plots [33]. In this study all the data are either shown in wiggle plots or contour forms.

In figure 3-6a, wiggle plot is used to depict a set of data. In this form of representation

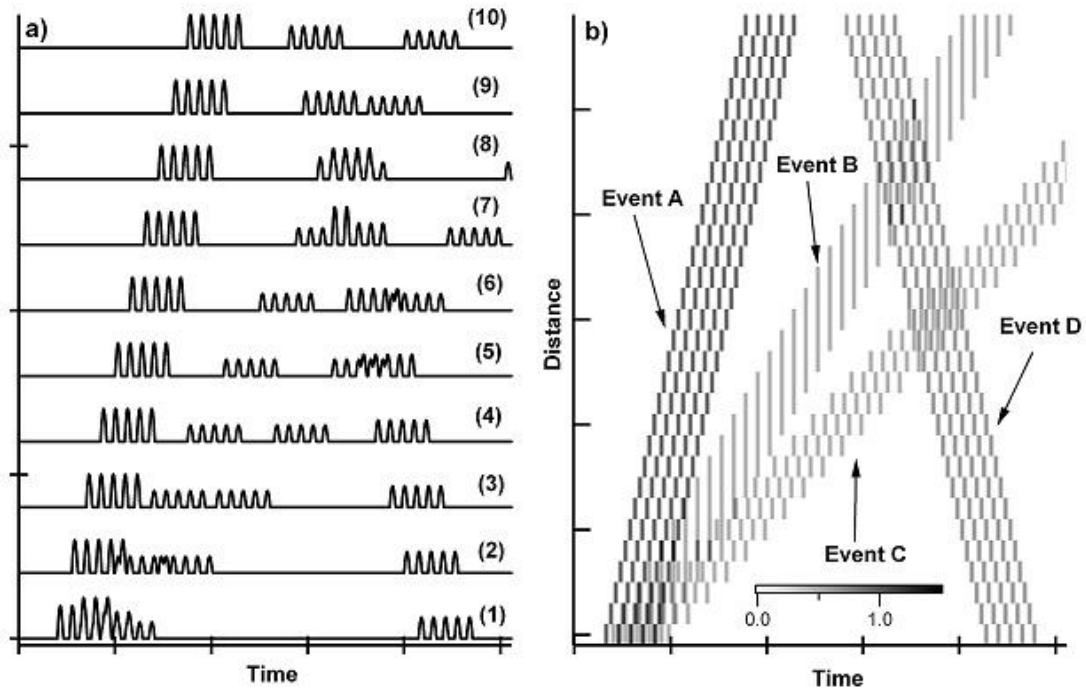


Figure 3-6: Representation of signals in wiggle and contour plots. Figure a shows the wiggle plot of a set of signals. In figure b the same data are shown in contour form.

the signals are all plotted on the same axes, with an offset. The offset is used to delineate the distance between the recording points. In this plot, the group velocity of the wave can be determined by connecting the peaks or valleys of the wave trains with a line; the slope of the line is a measure of the wave velocity. A more informative form of presentation of 2D data is the contour plot. In figure 3-6b the same set of data is plotted in contour form. The horizontal axis is time and the vertical axis is the actual distance. Different values of the amplitude are shown by different colors, and a color scale clarifies the contour levels. In this plot 4 different events are distinguishable. Events A,B and C are traveling in the same direction with three different velocities; whereas, event D is traveling in the opposite direction. The tangent of the line passing parallel to each event is equal to the group velocity of that event.

### 3.5.2 2D Fourier transform - FK transform

FK transform is referred to the 2D Fourier transform applied to a 2D signal with dimensions of time and distance. In the continuous form the FK transform is represented as:

$$S(\omega, k) = \int_{-\infty}^{+\infty} \int_{-\infty}^{+\infty} s(x, t) e^{-i\omega t} e^{-ikx} dt dx \quad (3.14)$$

where  $s(x, t)$  is the set of data in time-distance, and  $S(\omega, k)$  is the same data in FK domain. Angular frequency is represented by  $\omega = \frac{2\pi}{f}$  and  $k = \frac{2\pi}{\lambda}$  is the wavenumber or spacial frequency. In almost all applications the amplitude spectrum of the FK transform is of interest. That is because, the phase spectrum is very difficult to interpret. More specifically, the problem is with the phase unwrapping [33]. From the definition of FK transform (equation 3.14) it is clear that 2D Fourier transform is similar to applying the 1D Fourier transform in one dimension and then in the next dimension. Thus, most of the characteristics of 1D Fourier transform as defined in latter sections, such as linearity, shifting properties, convolution, and etc., are applicable to the FK transform with minor changes [34].

To investigate the behavior of FK transforms, a series of artificial signals are generated in time-distance domain and the corresponding FK transforms are calculated. The contours in figure 3-7a show half of a sinusoidal wave propagating from left to right. The corresponding amplitude spectrum of the FK transform is depicted in plot a1. It is observed that a line in time-distance domain transforms into a similar line with the same slope in FK domain. In both domains, the slope of the line determines the velocity of the wave. Plot b depicts the same half-sinusoid repeated five times in time. The corresponding FK transform (plot b1) shows one line with different notches. A half-sinusoid with a late reflection is represented in plot c. In FK domain (plot c1), the main event is transformed into a line in the first quadrant, and the reflection into a line in the second quadrant. Always, waves propagating in different directions transform into lines in different quadrants. Thus, FK transform is a very useful tool to separate events with different velocities and/or different directions. Each event is transformed into a separate line that passes through the origin, with a slope corresponding to the group velocity of that event. The amplitude spectrum of FK transform of dispersive events do not pass through the origin, and are curved rather than a straight line.

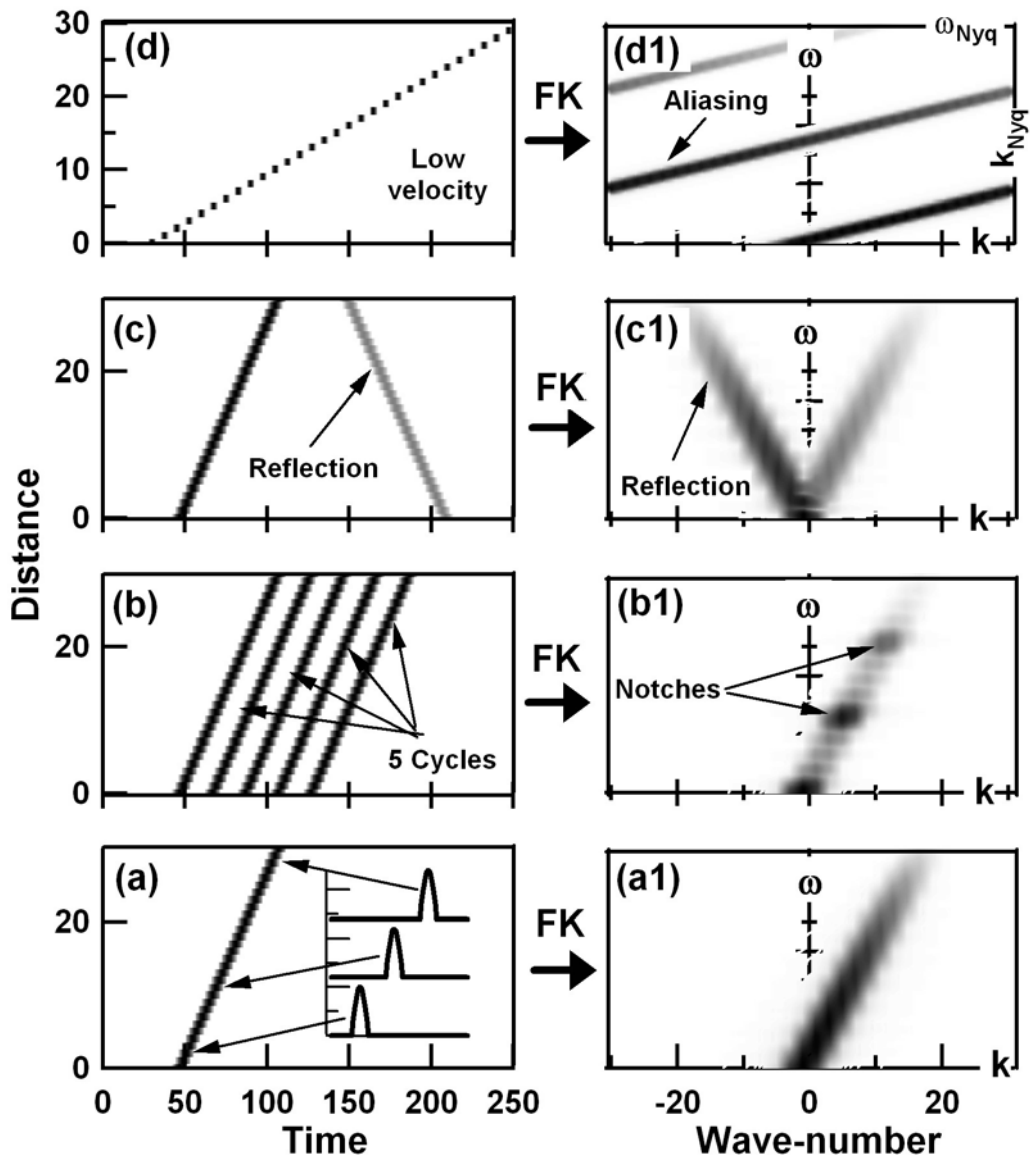


Figure 3-7: Signals generated in time-distance domain and the corresponding spectrum in FK domain. Plot a shows half cycle of a sinusoid propagating from left to right. Plot b shows the same half-sinusoid repeated 5 times. Plot c shows the same Half-sinusoid along with a late reflection propagating from in the opposite direction. Plot d shows the half-sinusoid propagating with a smaller velocity. Plots a1 to d1 show the corresponding FK transforms.

Figure 3-7d shows the same half-sinusoid propagating with a smaller velocity. Consequently, the slope of its FK transform is smaller. The lower velocity results in a split in the FK amplitude spectrum, and in fact, the three events seen in plot d1, are the continuation of a single event that passes through the origin. The split happens due to under-sampling of the signals, and thus plot d1 shows an aliased signal in FK domain. In 2D Fourier analysis, aliasing could occur in spatial, temporal or both domains. The sampling theorem, as stated before, is valid in both domains, and the Nyquist frequency ( $f_{Nyq}$ ) and wave-number ( $k_{Nyq}$ ), and resolution of the discrete 2D signal are defined as:

$$f_{Nyq} = \frac{1}{2\Delta t} \text{ and } k_{Nyq} = \frac{1}{2\Delta x} \quad (3.15a)$$

$$\Delta f = \frac{1}{T_{\max}} \text{ and } \Delta k = \frac{1}{X_{\max}} \quad (3.15b)$$

where  $\Delta t$  and  $\Delta x$  are sampling rates in temporal and spatial domains,  $T_{\max}$  is the largest available period, and  $X_{\max}$  is the largest available distance. In general, in under-sampled signals if the velocity of an event is less than  $\frac{\omega_{Nyq}}{k_{Nyq}}$ , it will be aliased in wave-number domain, and if the velocity is larger than  $\frac{\omega_{Nyq}}{k_{Nyq}}$  aliasing occurs in frequency domain. Aliasing in temporal domain could be prevented by using anti-aliasing filters, but spatial aliasing is troublesome and special techniques should be used to mitigate its effect [33].

### 3.5.3 Calculation technique

Mathgram 3-1 (Appendix B) shows the procedure of calculating FK transform for a set of synthetic data. A  $1024 \times 30$  data matrix (*Data1*) is generated, where the rows and columns show recording points in time and space, respectively. The signal consists of 5 cycles of a sinusoid ( $\omega = 100 \frac{rad}{sec}$ ) that is predecimated and tailed with zeros. Wavelength of the signal is assumed to be  $\lambda = 1.0 \text{ m}$ . The temporal and spacial sampling rates ( $\Delta t$  and  $\Delta x$ ) are chosen to have 10 sampling points per period, and per wavelength; therefore, the discrete signals are not aliased. A similar matrix is regenerated (*Data2*) and is used as the reference. To alleviate the effect of energy leakage and smearing the signals are multiplied by a Hanning window, both in time and space (matrices *wData1* and *wData2*). To simplify the final data representation



optical transform is applied to the *wData1*. Optical transform in time-space domain is defined as [35]:

$$B_{i,j} = (-1)^{i+j} A_{i,j} \quad (3.16)$$

where  $A$  and  $B$  are the original and the transformed matrix respectively, and  $i$  and  $j$  are rows and columns. This multiplication in temporal-spacial domain is equivalent to a convolution in FK domain, and redistributes the FK information as shown in figure 3-7. In plot a the 2D Fourier transform is applied to the original data. It can be seen that the dispersion information is scattered around the corners of the plot. Plot b shows the FK transform of the same data, but the data is multiplied by optical transformation (equation 3.16) in time, and the 2D Fourier transformation of the obtained data is calculated. It is observed that all the dispersion data are transferred to the center of the plot, and the center of the matrix is the origin. After all (Plot c), the data are flipped around zero frequency axis to ensure that the direct arrivals fall to the right of the frequency axis.

To enhance amplitude spectrum, the obtained Fourier amplitudes are scaled based on the following equation [36]:

$$D_{i,j} = c \log [\alpha + |F_{i,j}|] \quad (3.17)$$

in which,  $c$  and  $\alpha$  are constants that are selected for each case, and  $|F_{i,j}|$  is the magnitude of the 2D Fourier spectra. The mentioned procedure is called data reduction procedure and is widely used to analyze dispersion data [37]. In Mathgram 3-1, the final values are divided by the maximum of the matrix for normalization. Further, two plots are provided at the end of Mathgram. In one, the data reduction procedure is followed to generate the amplitude spectra, and for comparison in the other plot, the calculated values without any additional transformation are depicted.

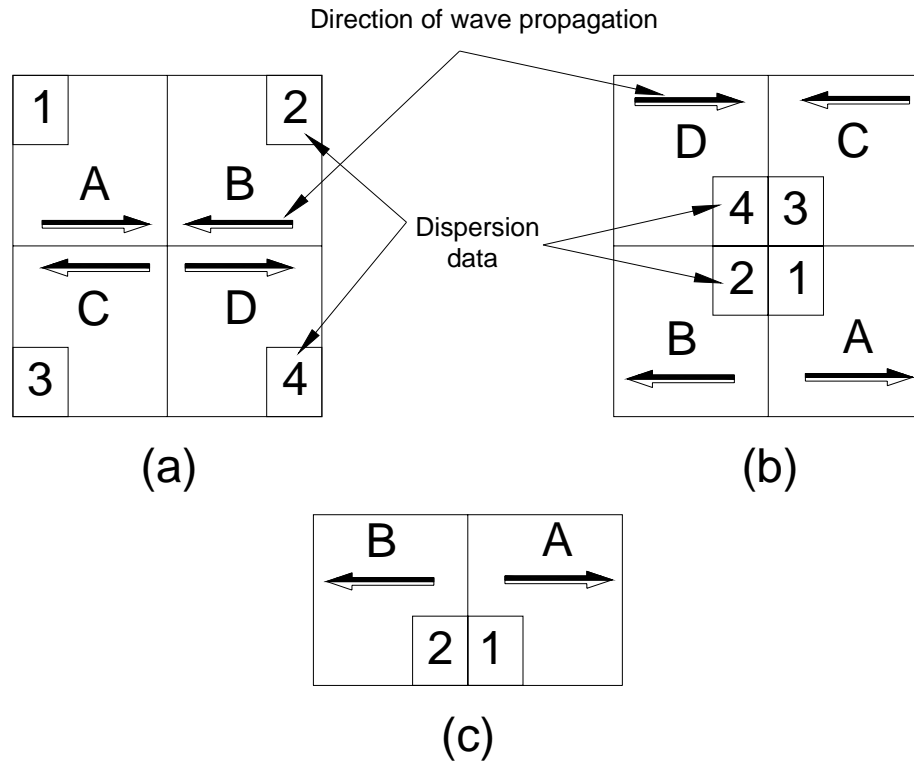


Figure 3-8: Schematic of the effect of data reduction procedure on the FK data. Plot a shows FK data obtained by applying 2D Fourier transform to a set of data. In plot b the data are multiplied by optical transform prior to the application of 2D Fourier transform. Plot c is the output in which data are flipped, and the repetitive data are eliminated.

## Chapter 4

# Geophysical exploration techniques

### 4.1 Introduction

In general, the objective of geophysics is to utilize physical laws to investigate the interior of the earth. This investigation could cover the whole or a substantial part of the planet (pure geophysics), or just the earth's crust and near-surface (applied geophysics). In recent years, a new discipline in geophysical exploration has developed to meet the requirements in environmental studies [38]. Thus, environmental geophysics deals with the investigation of physicochemical phenomena in the near surface.

The objective of applied geophysics is to achieve a practical or an economic goal. Applied geophysics is usually restricted to depths shallower than 300 m [38], and its objectives can be classified (and not limited to) as follows [39, 1]:

- determine the thickness of the crust (i.e. in hydrocarbon investigation)
- investigate engineering sites (i.e. to determine soil mechanical properties, or predict site amplification during earthquakes)
- explore groundwater, mines and other resources
- locate mine-shafts and buried cavities
- detect archeological inheritance
- find buried utilities (i.e. pipes, cables, water mains, etc.)

The benefit of applied geophysics over other near-surface investigation methods (i.e. digging boreholes) is that it provides information for a larger zone (rather than discrete locations) with relatively low cost. Further, it assesses the in-situ condition without any disturbance (non-intrusive method). Geophysical techniques do not provide a unique solution to the problem in most cases. This ambiguity stems from the fact that these methods try to solve an inverse problem, that is indeterminate. In these techniques the input and output are known and the system properties, which are the earth's properties, should be determined. Geophysical methods are often used in combination, or along with other investigation methods to increase the accuracy of the interpretations.

Table 4.1, lists the major geophysical methods that are currently in use [1]. The second column of the table demonstrates the physical properties that the method is based on. Various geophysical methods are sensitive to different properties of the geomaterials. These physical properties determine the applicability range of the technique. For example, to locate a near surface water resource the gravity method, which works based on the gravity contrast, is not a good option. Because, there is not a big difference between the density of surrounding saturated soil or rock, and the water basin. In this case, a seismic reflection or refraction method will work better, because of the strong impedance contrast between the shear moduli of the water basin and surrounding soil. Moreover, geophysical techniques can be classified as passive and active ones. Passive methods are the ones that are sensitive to the natural fields associated with earth, i.e. gravity or magnetic methods. In active methods a disturbance is generated artificially in the ground and the responses are recorded, i.e. seismic or EM techniques. The main applications of each method are marked in the rest of the columns of Table 4.1. The information is based on reported or successful case histories, and should be used just as a general framework.

The objective of any geophysical survey is to extract subsurface information; however, the success of a survey is sensitive to the site conditions. For each project, the main objective (or objectives), and proper strategies should be specified in advance. In lieu of financial or logistic constraints, it is recommended to try different geophysical methods at the same time to determine the most appropriate technique and verify the results [1]. Darracott and McCann [40] claim that in almost all the unsuccessful or less successful case histories, either the planning was inadequate, or the technical specifications were not correctly chosen, or the personnel involved

Table 4.1: Geophysical methods, the physical property that they are based on, and their main applications [1]

Geophysical method	Physical property	Applications *									
		1	2	3	4	5	6	7	8	9	10
Gravity	Density	<b>P</b>	<b>P</b>	s	s	s	s	-	-	s	-
Magnetic	Susceptibility	<b>P</b>	<b>P</b>	<b>P</b>	s	-	m	-	<b>P</b>	<b>P</b>	-
Seismic refraction	Elastic moduli; Density	<b>P</b>	<b>P</b>	m	<b>P</b>	s	s	-	-	-	-
Seismic reflection	Elastic moduli; Density	<b>P</b>	<b>P</b>	m	s	s	m	-	-	-	-
Resistivity	Resistivity	m	m	<b>P</b>	<b>P</b>	<b>P</b>	<b>P</b>	<b>P</b>	s	<b>P</b>	m
Spontaneous potential	Potential differences	-	-	<b>P</b>	m	<b>P</b>	m	m	m	-	-
Induced polarization	Resistivity; Capacitance	m	m	<b>P</b>	m	s	m	m	m	m	m
Electromagnetic (EM)	Conductance; Inductance	s	<b>P</b>	<b>P</b>	<b>P</b>	<b>P</b>	<b>P</b>	<b>P</b>	<b>P</b>	<b>P</b>	m
EM-VLF	Conductance; Inductance	m	m	<b>P</b>	m	s	s	s	m	m	-
EM- ground penetrating radar	Permittivity; Conductivity	-	-	m	<b>P</b>	<b>P</b>		s	<b>P</b>	<b>P</b>	<b>P</b>
Magneto-telluric	Resistivity	s	<b>P</b>	<b>P</b>	m	m	-	-	-	m	-
<b>P</b> = primary method; s = secondary method; m = may be used but not necessarily the best approach, or has not been developed for this application											
<b>*-Applications</b>											
1	Hydrocarbon exploration (coal, gas, oil)										
2	Regional geological studies (over areas of 100s of km <sup>2</sup> )										
3	Exploration/development of mineral deposits										
4	Engineering site investigations										
5	Hydrogeological investigations										
6	Detection of subsurface cavities										
7	Mapping of Leachate and contaminant plumes										
8	Location and definition of buried metallic objects										
9	Archeogeophysics										
10	Forensic geophysics										

were not enough experienced. The outcome of a geophysical survey is a function of the size, shape and the physical properties of the target. In geophysical terminology, any object with a significant contrast in physical properties with the surrounding medium is called a target. In a geophysical survey, the variation of the physical properties of the target, relative to the background value is measured. Consequently, the boundaries and limits of the target are determined.

To show the results of a geophysical survey, the common methods are profiling and mapping. In profiling, a two dimensional cross section of the earth is chosen, and the variation of the objective parameter is measured along the line at the surface. The results are depicted in a graph in which the horizontal axis is distance along the surface, and vertical axis is depth. To obtain satisfactory results, the best orientation of a profile is at right angles to the strike of a target [1]. The width of the profile should be larger than the expected width of the target, otherwise it will not be possible to determine the background values. As an example, the results of resistivity techniques are usually presented in this format. In mapping, a set of parallel lines or a grid across the ground surface are chosen, and the measurements are conducted. The measured values are contoured between the points and a two dimensional map is prepared. This technique is vastly used to depict the results of gravity surveys. Station is the term used to refer to the points at which the measurements are made, and the distance between successive measurements is known as station-interval. The larger the station interval is, the more high-frequency data is lost (spatial aliasing). Contouring the data could also cause spatial aliasing. As a general rule of thumb, any geophysical anomaly found in the profiles or maps are larger than the feature causing it. Thus, the interpretation of profiles and maps need some expertise.

Signals collected in the field are contaminated with noise, which could be:

- Coherent noise: this type of noise happens systematically, i.e. the ones produced by power lines. In most cases it is relatively easy to distinguish and eliminate them using filters.
- Incoherent noise: this noise occurs randomly, such as traffic noise, water waves breaking at the shore, or the ones produced by wind. If the duration of the recorded signal is long enough, it is expected that this noise can be cancelled by averaging.

In general, each type of geophysical survey is sensitive to a specific noise type and range.

Table 4.2 lists the common geophysical techniques and the main sources of noise that affect their results [1]. The techniques discussed in the previous chapter can be utilized to mitigate the effect of noise on the contaminated signals.

Table 4.2: Sources of noise that affect different geophysical methods [1]

<b>Geophysical method</b>	<b>Sources of noise that affect the results</b>
Seismic	Engine/Ship noise; Sea state; Breaking wave; Wind; Root vibration; Heavy rain; Vehicles
EM	Vehicles; Fences (metal and electric); Power lines; Electric and magnetic storms
Electrical	Fences (metal and electric); Power lines; Electric and magnetic storms
Magnetic	Fences (metal and electric); Power lines; Electric and magnetic storms

The primary geophysical techniques that are used to detect underground cavities are resistivity, electromagnetic (EM) and EM ground penetrating radar (Table 4.1). As the main focus of this dissertation is on the application of geophysical methods to cavity detection, the mentioned techniques will be reviewed briefly in the following sections. The final section of this chapter explains the basics and details of a seismic technique named multi channel analysis of surface waves (MASW) test. This technique uses the dispersion of Rayleigh waves to assess in-situ soil properties. The direct application of the results of this study is in MASW test to detect underground cavities. Thus, to provide necessary background for the subsequent chapters, an in-depth overview of the theoretical aspects, field procedures, numerical simulations, and case histories of MASW test is presented.

## 4.2 Resistivity method

A group of geophysical techniques that use direct-currents (DC) or very low frequency alternative-currents (AC) to investigate the electrical properties of subsurface are categorized under electrical methods. The most common electrical methods are resistivity, induced-polarization, and self-potential methods [41]. The purpose of this section is to introduce the basics of resistivity method, and its applications in the detection of lateral subsurface inhomogeneities.

In resistivity method, electrodes are deployed at the surface to transmit artificially-generated

currents into the ground. The resulting potential differences at the ground are measured. Theoretically, the patterns of potential differences in a homogeneous medium are known, thus the deviations of the recorded potential differences from the theories yield to information about the existent inhomogeneities. generally, Resistivity ( $\rho$ ) of a block of a material with cross section ( $\delta A$ ) and length ( $\delta L$ ) and resistance ( $\delta R$ ) is defined as:

$$\rho = \frac{\delta R \delta A}{\delta L} \quad (4.1)$$

The SI unit of resistivity is  $\Omega m$ , and the resistivity of geological materials shows one of the largest ranges of all physical properties, from  $1.6 \times 10^{-6} \Omega m$  for native silver to  $10^{16} \Omega m$  for pure sulphur [1].

Table 4.3: Resistivity values and ranges for common geological materials [1].

<b>Material</b>	<b>Nominal resistivity (<math>\Omega m</math>)</b>
Granite	$3 \times 10^2$ to $3 \times 10^6$
Granite (Weathered)	$3 \times 10$ to $5 \times 10^2$
Clay	1 to 100
Alluvium and Sand	10 to $8 \times 10^2$
Soil (40% clay)	8
Soil (20% clay)	33

For a general electrode configuration in a resistivity survey over a homogeneous half-space (figure 4-1), combining Ohm's law ( $V = RI$  where  $V$  is potential,  $R$  is resistance, and  $I$  is current) and equation 4.1 leads to equalities in the following form:

$$\rho_a = \frac{2\pi}{\left(\frac{1}{r_A} - \frac{1}{r_B}\right) \left(\frac{1}{R_A} - \frac{1}{R_B}\right)} \frac{\Delta V}{I} = K \frac{\Delta V}{I} \quad (4.2)$$

where  $\rho_a$  is apparent resistivity,  $\Delta V$  is the potential difference between the potential electrodes,  $I$  is the induced current,  $K$  is geometric factor, and the rest of the parameters are as defined in figure 4-1. For a homogeneous ground,  $K$  is independent of the location of electrodes, but in layered media, or in the presence of any type of inhomogeneities geometric factor changes with the choice of electrode configuration. Various electrode configurations along with the corresponding relation for geometric factor has been developed [42, 43]. The penetration depth of the current increases as the separation between the current electrodes increases. Thus, in



the planning for resistivity survey, the current electrode separation should be chosen in a way that the ground be energized to the required depth. The rule of thumb is the separation should be at least equal to the depth of interest.

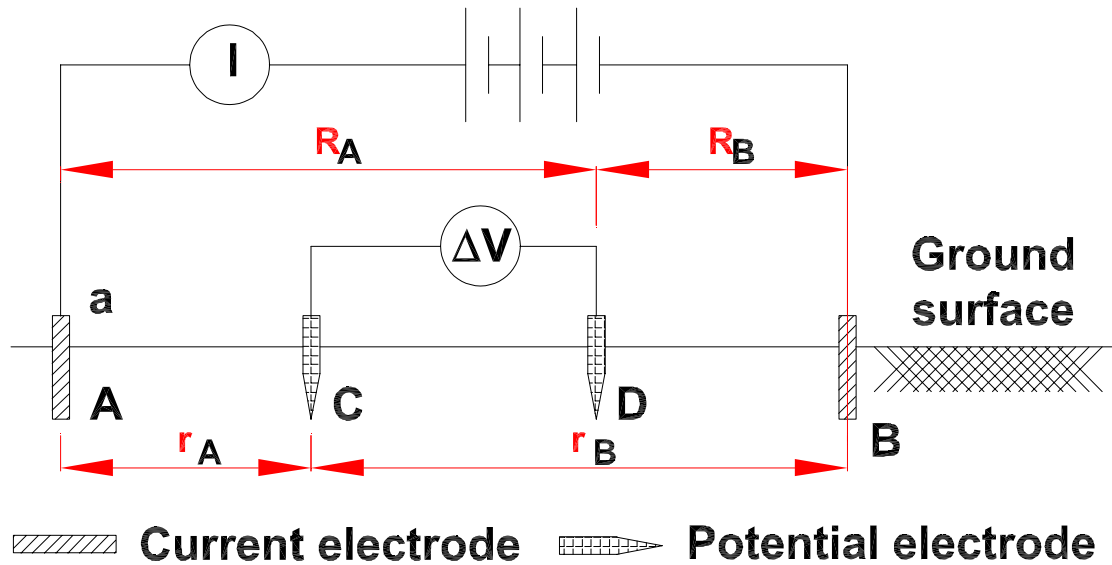


Figure 4-1: General electrode configuration in a resistivity survey.

Resistivity is conducted in two different forms:

- Vertical electrical sounding (VES): This form is used for studying horizontal interfaces beneath the surface. The common practice is to keep the relative distance between the current and potential electrodes constant. To increase the penetration depth, the whole configuration is expanded about a fixed central point. Measurements are started at shortest electrode separation, and progressively increased to larger spacings. The values of  $I$  and  $\Delta V$  are measured, and using appropriate geometric factors the apparent resistivities are calculated. The results are plotted on a graph with the x-axis showing the electrode separation (or its logarithm), and y-axis showing the apparent resistivities. Finally, data inversion is performed.
- Constant separation traversing (CST): To assess the lateral variation of resistivity in an area, CST method is used. The spacings between the electrodes are kept constant in

this method, and the whole configuration is moved along the surface of a profile. At each location, the apparent resistivities are measured. A plot of the variation of apparent resistivities with respect to the distance along the surface is prepared. Any significant variation in the plot shows the location of an anomaly with a salient change in resistivity.

The resistivity instruments are designed to measure the ratio  $\frac{\Delta V}{I}$  (equation 4.2). The equipment are able to measure very low level of resistivities. Although, the corresponding theories are developed based on the assumption that DC current is used, what is used in practice is low frequency AC currents ( $f \approx 10 - 100Hz$ ). The reason is to avoid problems like electrolytic polarization and telluric currents. Thus a frequency of about  $100 Hz$  is used for penetrations in the order of  $10 m$ . For penetrations of up to  $100 m$  frequencies less than  $10Hz$  are used, and for deeper penetrations DC currents are utilized. To receive the data either spike electrodes or antennas are used [41].

Among the geophysical methods, the interpretation of resistivity data is one of the most difficult ones. Also, it is less developed for CST technique than for the VES. Because of this difficulties, the final results are ambiguous. Figure 4-2 shows a typical apparent resistivity curve, expected for a layer overlain a half-space. When the separation is small the measured apparent resistivity is close to the one of the top layer, and as distance increases the apparent resistivity gets closer to the half space one. Theoretically, for a small electrode spread the penetration depth is small, thus the potential is mostly affected by the properties of top layer. As the spread increases the potential is affected by both layers, and finally for enough large spreads the potential is almost affected only by the half space. For more complex geological structures the curves, and therefore the interpretation, becomes more complicated. In practice, different resistivity structures can result in similar curves, which is a source of ambiguity of the interpretations. Noticeable resistivity boundaries may not necessarily coincide with the lithological boundaries [1].

Initially, interpretations of VES field measurements were made by comparing them with master graphs. More sophisticated interpretation techniques superseded the curve matching method [44, 45]. In recent methods, the parameters of theoretical relations are adjusted in to match field data curves with theoretical ones. The results are depicted in the form of pseudosections (Fig. 4-3). With the aid of inversion techniques, the apparent resistivity data

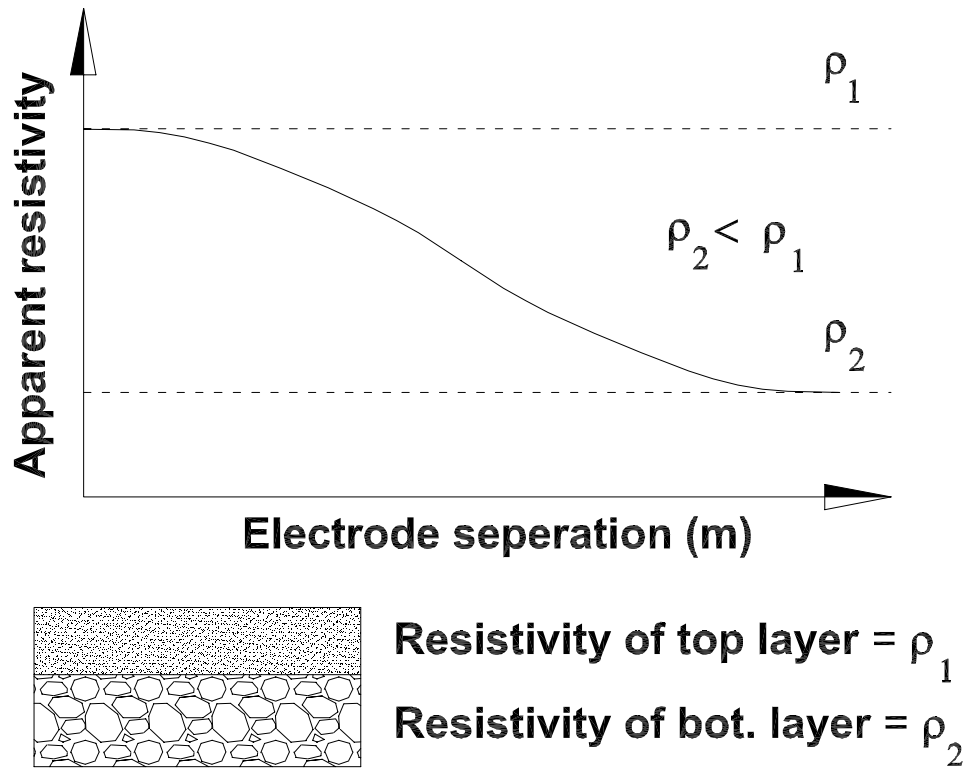


Figure 4-2: The variation of apparent resistivity curve with electrode separation over a halfspace overlaid by a layer [41].

are converted into geoelectric profiles. In more recent methods, data are collected along parallel spreads and 3D resistivity models are constructed. A key assumption in most of the available inversion theories is that the layers are horizontal and isotropic. In practice, this assumption is violated in the presence of dipping layers, or in cases that the resistivity in the horizontal and vertical directions are different. In the upper layers, the thicknesses and measured resistivities are accurate to between 1% to 10%, and the accuracy decreases for deeper layers [1].

To detect lateral resistivity inhomogeneities the CST technique is utilized. CST is based on the fact that a vertical discontinuity distorts the direction of current flow, as a result the distribution of the potential in its vicinity will be affected. CST survey is usually conducted on grid lines that cover a surface area. Then, the results of CST lines are contoured onto a map, and the extents of a 3D anomaly are determined. In order to detect 3D objects the top of the

object should be close to surface and the traverses should be made directly over or near the edges of the object [41].

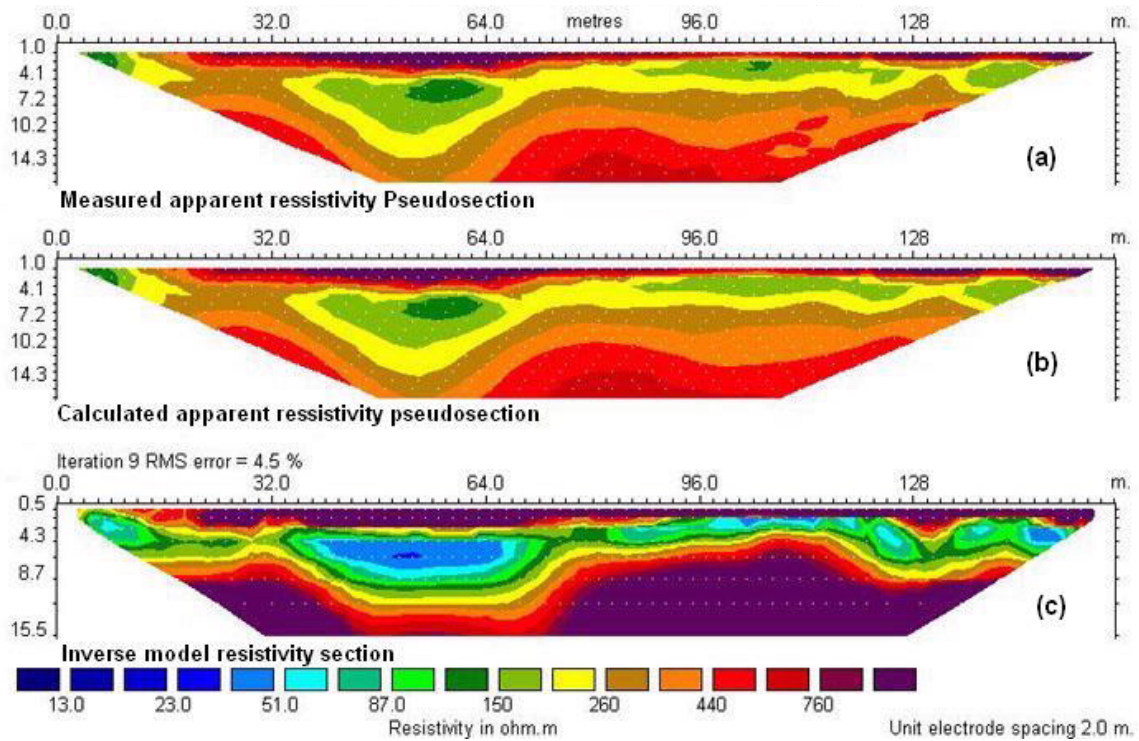


Figure 4-3: Pseudosections to interpret the resistivity data. In each graph horizontal axis is the distance along the surface and the vertical axis is the depth. Plot (a) shows the raw data obtained from the field. Plot (b) shows the calculated resistivities for a theoretical model. Plot (c) shows the inverted geological information, resulted from plots (a) and (b) [46].

The main limitations of resistivity methods are [41, 47, 1]:

- The interpretations could be ambiguous and subjective, specially for complex geological structures
- The resistivity of top layers can mask the resistivity of underlain layers
- The maximum electrical power limits the depth of penetration.
- Out-of-line electrode arrays can result in erroneous apparent resistivities

- The internal resistance of the potential measuring circuit should be higher than the ground resistance between the electrodes
- The data are sensitive to small anomalies that are insignificant to the main target. For instance, the presence of pipes, and sand lenses affect the quality of the data
- In the presence of buried pipes, or conductors that run parallel to the survey line, current leakage happens

The most widely application of resistivity method is in hydrogeological investigations, it has been also used to locate and monitor ground water pollution extents [48], and to determine the bedrock depth for foundation purposes [49]. Successful application of CST method to detect embedded anomalies are also reported:

- Reynolds reports the detection of a cavern in a small village east of Devon, UK [1].
- Prentice and McDowell proposed the application of CST to detect the locations of near surface bedrock (that needed blasting) along the material through which a trunk sewer was planned to be constructed [50].
- Osterkamp and Jurick report the detection of permafrost zones in Fairbanks, Alaska [51].
- Reynolds and Taylor report the application of resistivity method to detect the location and determine the embedment depth of two abandoned concrete foundations, in about one meter below the surface [47].

## **4.3 MASW method**

### **4.3.1 Development of the technique and related theories**

Multi channel analysis of surface waves (MASW) is a seismic technique to assess subsurface soil condition. MASW is a nondestructive testing method, e.g. it causes no damage to the structure that it is applied to. It is performed from the surface and does not need any borehole or access pit. Moreover, the test setup and procedure are simple and has the potential to be fully automated [52]. MASW uses the dispersive characteristic of Raleigh wave to evaluate

the low strain (in the order of 0.001% or less) elastic properties of different layers. Dispersion could happen due to changes in geometry, i.e. layered system, or due to intrinsic damping of the material. It is understood that when a semi-infinite media is excited at the surface with a vertical load, about two thirds of the energy is carried parallel to the surface in the form of Rayleigh waves. [53, 54]. Further, the effect of geometrical damping on the Rayleigh waves is less than on body waves. These characteristics make Rayleigh waves very favorable for nondestructive testing, because they can be generated with relatively small energy, and recorded at longer distances.

In the last decade of 21st century, MASW evolved from the combination of SASW (spectral analysis of surface waves) theories and experiences, and the advances in the data acquisition equipment. Table 4.4 provides a bibliographic history of this evolution. The main difference between SASW and MASW is that the former is performed with two receivers; whereas, the latter uses several receivers (the use of 12 to 48 receivers are reported [55]). In compare with SASW test, in MASW:

- The choice of optimum frequency range for phase velocity calculation is easier and more accurate.
- Noise detection and filtering is easier with data obtained from several receivers [56].
- The errors are averaged and attenuated.
- The ability to separate different modes is improved.
- The capacity of recognition and separation of different events, such as reflections and refractions.

The main objective of MASW is to determine the shear modulus or shear wave velocity profile of the soil and pavement at low strains . The results of MASW is used to:

- design vibrating machine foundations
- be used as a reference level to evaluate dynamic soil performance or seismic site response assessment

Table 4.4: Historical development of MASW test

Year	Development
1938	Records show that for the first time, German society of soil mechanics used surface waves for soil assessment [57].
1946 to 1953	Several researchers used surface waves to generate soil profiles and assess pavement conditions in Sweden & Holland [58]. Surface wave results were compared to plate bearing test results [59].
1958	Jones proposed an analytical procedure to compute the moduli of different layers in a pavement system using the steady-state Rayleigh wave method [60].
1958 to 1984	The steady-state Rayleigh wave technique was applied broadly to determine elastic properties of soil in-situ, and appraise pavement condition [61, 42, 62, 63] <b>Ballard1964</b> , . Solution techniques for the propagation of waves in stratified media are developed [64, 65]. Data are published that compares surface wave test results with other methods, such as resonant column test [66, 67]. Attempts have been made to facilitate field procedure [68]. More than two receivers are utilized to record surface waves to locate subsurface cavities and assessing soil condition [69, 70, 71]. Inversion techniques are developed to obtain soil profile from dispersion curves [72]. f-k transforms are used to separate higher modes of propagation [73].
1984	The works of Nazarian and Stokoe II had profound impact on the advancement of the theory and interpretation techniques of SASW test. Also, they developed the first computer algorithm (INVERT) to determine stiffness profile from dispersion data [74, 75].
1985 to 1995	Passive sources are used for subsoil characterization [76, 77]. The effect of higher modes of Rayleigh waves on the inversion results are studied [78]. Various inversion techniques are developed and applied to real sites [79, 80, 81, 76, 82] <b>Addo1992</b> , . SASW technique is applied to different cases such as hard to sample soils [83], and is compared with other geophysical techniques [84].
1995 to 2005	The advances of electronic equipment resulted in the development of MASW test [56]. Inversion techniques are developed to consider several modes of propagation in the MASW analysis [85, 86, 87]. Numerical and experimental studies are performed to consider the effect of inverse dispersion (soft layers overlain by stiff layers) on the MASW test results [88]. Wavelet transforms are used to generate dispersion curves from synthetic and experimental data [89, 90]. Attenuation characteristics of soils are inverted from MASW test results [91, 92]. The effect of lateral inhomogeneities on the propagation of Rayleigh waves, and the application of MASW test to locate underground cavities are studied using a combination of numerical and experimental models [93, 94, 95, 96, 97, 98, 99] .

- evaluate liquefaction potential during earthquake shaking
- identify soft layers
- assess hard to sample deposits, in-situ
- analysis of pavement systems
- evaluate damping properties of soil

Current practice of MASW test consists of conducting field test, determining experimental dispersion curve, and constructing the stiffness profile. The key point in a MASW field test is to generate primary Rayleigh waves and measure the corresponding responses. In the field, a broad band frequency source excites the ground surface, and several receivers - deployed in a line at a distance from source - record its responses [4-4]. The receivers could be geophones to measure the velocity or accelerometers, though geophones are more common. A vertical low frequency geophone (4.5  $Hz$ ) is a common receiver for MASW testing. For investigating depths up to 50  $m$  common receiver spacing ( $\Delta$ ) are: 0.5, 1, 2, 4, 8, 16, 32 and 64  $m$ . For pavement investigations, the suitable receiver spacing is between 0.075  $m$  to 2  $m$ . Receiver spacing determines the minimum reliable wavelength ( $\lambda_{\min}$ ) that can be extracted from MASW data. Park et al. [56] suggests that  $\lambda_{\min} = 2\Delta$  to avoid spatial aliasing; whereas, Socco [55] suggests that  $\lambda_{\min} = \Delta$ . The receivers should [100]:

- have significant output over the frequency range of interest
- match with each other, thus the differences in phase can solely be associated with responses
- couple well with soil
- have same coupling for each receiver

The source could be a transient load, steady state vibrator, random noise (active), or ambient noise (passive). The source type (its frequency content), and its location influence the energy partition between different Modes of propagation [55]. Common sources in MASW testing are [100]:



- for close receiver spacings: hand held hammer
- for receiver spacings between 2 to 8 *m*: sledge hammer or large drop weights (between 20 to 70 kg in weight)
- for receiver spacings larger than 8 *m*: dropped weights from 70 to 900 *kg*, bulldozers or very large weights used for dynamic compaction
- For very deep surveys: passive sources such as micro-tremor or ambient noise [77].

Finally, the recording device should have several channels (a minimum of 12 is recommended [56]), have a minimum dynamic range of 100 *dB*, and have an anti aliasing filter. Three parameters are of large importance in a swept frequency record: minimum frequency ( $f_{\min}$ ), maximum frequency ( $f_{\max}$ ), and the length of the record or time window ( $T$ ). In the presence of rapid changes in the near-surface properties, longer recording time ( $T$ ) is required. Further, the time window should be long enough to record responses on all the receivers. For each receiver set up 3 to 5 tests are conducted and their average values are used as the test result. Also, it is a common practice to run the test from both sides of a receiver set up (forward and reverse testing), and compare the results.

Two types of geometries are frequently used in the field 4-5. In common receiver midpoint (CRMP) geometry, an imaginary midpoint is considered for the receiver array, and the array is scaled up around that center line. In common source geometry, the location of the source is kept constant, and the array length and offset is scaled up to cover larger areas. Studies on the effect of array geometry for SASW shows that in a laterally homogeneous media both CS and CRMP methods lead to similar results. Though, in the presence of lateral inhomogeneities CRMP gives less scatter than obtained from CS geometry **Hiltunen1989**. So far, no comprehensive research on the effect of the choice of geometry on MASW is published. For both geometries it is recommended to apply the source to both sides of the array (reverse profiling) and compare the results **Nazarian1993**.

The choice of total array length, offset value ( $D$ ), and receiver spacings ( $\Delta$ ) have significant effect on the results. Array length has a direct relation with wave-number resolution ( $\Delta k$ ) that plays a role in the separation between different modes. On the other hand, short arrays are less sensitive to lateral variations, produce better signal to noise ratios, and are less sensitive to high

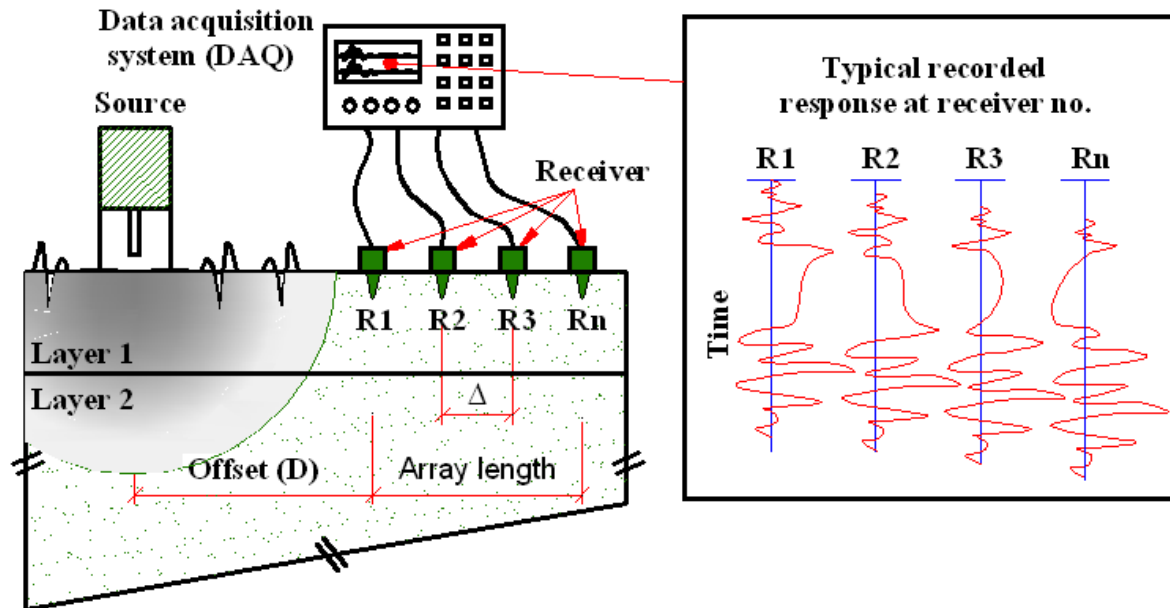


Figure 4-4: Schematic of the field layout of MASW test. Receivers acquire the surface responses due to the excitation in time domain. The DAQ system could perform real time analysis or save the data for future.

frequency attenuation (far field effect). For investigation depths of 20 to 30 *m*, typical array length is 50 to 100 *m*. The offset value should be large enough to allow for large wavelengths to be fully developed (near field effect). A rule of thumb is to set the offset value at least equal to the required investigation depth. It is recommended to run the test with different offset values [55]. According to Hiltunen and Woods [52], the factors that affect the offset value are:

- stiffness of the material to be tested
- desired depth of investigation
- working frequency range
- attenuation properties of the medium
- sensitivity of the instruments

It is understood that the maximum reliable wavelength that can be extracted from a set of data is related to the offset value, but ambiguous criteria are stated to describe this nature. Al-

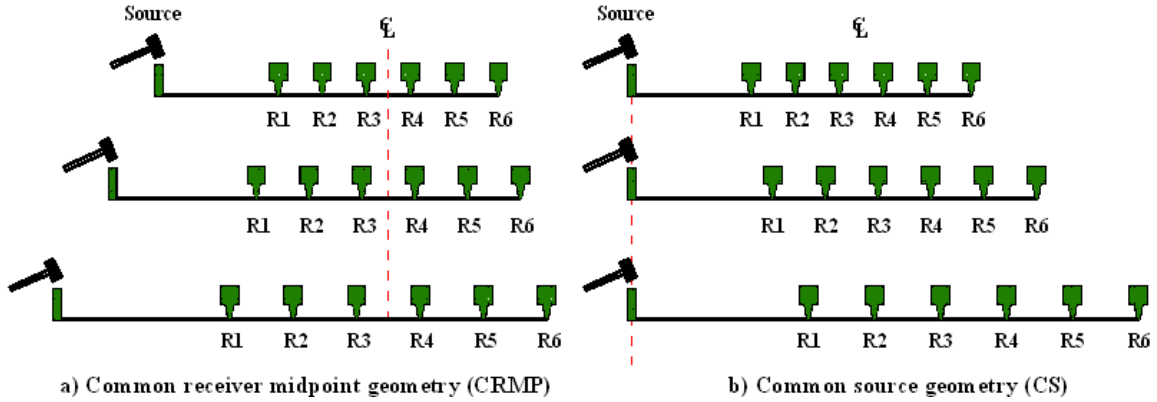


Figure 4-5: Schematics of different geometries of MASW test. Plot a shows the CRMP geometry, in which the imaginary middle point of the receivers array is kept constant. Plot b depicts the CS method, where the source location is constant and the array scale is increased.

Hunaidi [101] suggestion is to disregard wavelengths that do not satisfy the inequality  $0.5D < \lambda_{R_{\max}} < 3D$ . Hiltunen and Woods [102] limits the upper bound to  $2D$ , where  $D$  is the offset value. This criteria guarantee that high frequencies ( $0.5D < \lambda_{R_{\max}}$ ) that might be affected by noise (far field effect), and low frequencies ( $\lambda_{R_{\max}} < 3D$ ), which are not fully developed (near field effect) are eliminated from the data. Based on their theoretical works, Sanchez-Salinerio et al. suggest a completely contradictory criteria  $\lambda_{R_{\max}} < 0.5D$  [103]. Alternatively Park et al. restate that in a MASW test, plain wave assumption can be assumed only when  $\lambda_{R_{\max}} < 3D$  [56]. Al-Hunaidi propose that Hitunen and Woods criterion is insufficient to ensure the presence of only one mode of propagation, but the criterion suggested by Sanchez-Salinerio et al. is more likely to be valid. In brief, because of the different practical conditions, it is improbable to come up with a generally applicable criterion with this respect.

To determine an experimental dispersion curve, the frequency content of the time response at each station is calculated. For each frequency, the phase difference between the receivers are calculated and the time delay ( $t(f)$ ) for each frequency is estimated using:

$$t(f) = \frac{\phi(f)}{2\pi f} \quad (4.3)$$

where  $\phi(f)$  is the phase difference in radian, and  $f$  is frequency in Hz. In SASW test where only

two receivers are used, calculation of phase difference between the receivers is fairly straightforward [74, 104]. Whereas, in MASW for each frequency the phase difference between various receivers might be different, hence more rigorous techniques should be utilized for  $\phi(f)$  evaluation (see for example [97]). Another problem with phase difference calculation is phase unwrapping. When the phases are calculated as stated in the previous chapter, the results are stated as an angle in the range  $\pm\frac{\pi}{2}$  (wrapped phase). Thus, to obtain the correct phase for each frequency an appropriate number of cycles should be added to the phase, in other words the phase should be unwrapped (figure 4-6). The problem arises when due to the existence of noise, or higher modes of propagation the phase has a jump and is spurious. In these cases the phase unwrapping procedure could be erroneous and needs special attention. Shalito [105] reviews phase unwrapping techniques and associated difficulties and problems. Afterward, spurious cycles in one receiver geometry and spacing might not be spurious in other geometries [101].

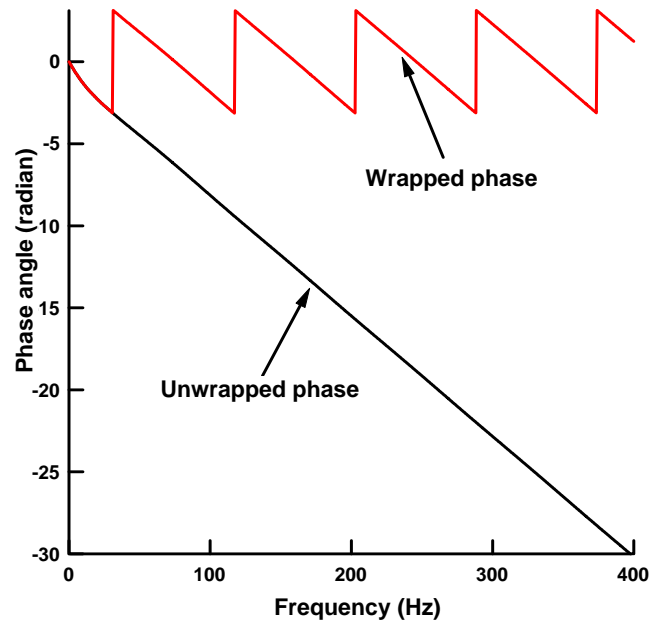


Figure 4-6: Calculated wrapped and unwrapped phases for a set of data.

Time delays are used to calculate the phase velocity ( $V_R$ ) for each frequency:

$$V_R = \frac{\Delta x}{t(f)} \quad (4.4)$$

where  $\Delta x$  is the receiver spacing (for non uniform receiver spacing  $t(f)$  and  $\Delta x$  should correspond to each other). Finally the wavelength ( $\lambda_R$ ) is calculated as:

$$\lambda_R = \frac{V_R}{f} \quad (4.5)$$

a plot of the obtained values of  $V_R$  verses  $\lambda_R$  is referred to as experimental dispersion curve.

The next step in a MASW test is to construct the shear modulus profile from the dispersion curve. In the early methods, it is assumed that most of the energy of Rayleigh wave is concentrated in a depth equal to its wavelength. As a result, the velocity that each frequency propagates with ( $V_R$ ), can be assumed to represent the properties of the material that lies about half or one third of the wavelength ( $\frac{\lambda}{2}$  or  $\frac{\lambda}{3}$ ) deep, thus the wavelength is associated to depth. By assuming values for Poisson ratio and density, Rayleigh wave velocity ( $V_R$ ) is associated to shear wave velocity ( $V_s$ ), and the latter to the shear modulus of the soil [106, 101].

More advanced techniques are developed based on the theoretical solutions for the propagation of plain waves in a horizontally layered media and the corresponding theoretical dispersion curves [65, 64, 107]. In these techniques system parameters (Poisson ratio  $\nu$ , shear wave velocity  $V_s$ , density  $\rho$ , depth  $h$ , and number of layers) for a horizontally layered system are assumed. The stiffness matrices for each layer are constructed and assembled into a global stiffness matrix. By setting the determinant of the global stiffness matrix equal to zero, a relation between the wavelength and Rayleigh wave velocity is obtained. The general form of the obtained relation is [55]:

$$F(k, f) = 0 \text{ or } F_R[v(z), G(z), \rho(z), k, f] = 0 \quad (4.6)$$

Generally, the above function is a multi-valued function of wavelength, that it has more than one solution for each wavelength. Thus theoretical dispersion curves are obtained for the assumed system. Then, a comparison is made between the theoretical and experimental dispersion curves. The assumed parameters are changed until a good match between the two curves are obtained. As a result, the assumed parameter values in the last iteration will be a representative of the soil profile. This iterative technique is called inversion. It is shown that the choice of Poisson ratio ( $\nu$ ) and density of layers ( $\rho$ ) have small effect on the results, thus they are

usually assumed based on local material types, and kept constant throughout the procedure [82]. Two approaches are available for the inversion algorithms. In the velocity-inversion approach, the layer thicknesses are assumed and the only variables are the shear-wave velocities. The other approach is complete-inversion, in which both the layer thicknesses and shear-wave velocities are assumed unknowns, and are changed during the iteration. The advantage of the first approach is that more layers can be assumed; whereas, complete-inversion leads to smoother changes in the shear-wave velocities of the layers [82].

As stated in table 4.4, various inversion techniques are developed and are in use. The basis of all of these techniques are the same; however, their difference are in the optimization techniques and parameters that they consider to match the two curves, their sensitivity to noise, their stability, robustness, and their capacity to differentiate between different events [55]. The common assumptions in almost all of the inversion techniques are:

- The predominant wave propagation mode is the first mode Rayleigh mode
- The problem is in the state of plain strain
- The media is laterally homogeneous and extend to infinity with respect to the source-receiver configuration
- The layers are horizontally stratified.

For naturally deposited systems (stiffness increases with depth), the mentioned theories give real valued stiffness matrices and the procedure is the same as noted. In systems where stiff layers overlay softer ones, the matrices could be complex valued. More simplifying techniques should be considered in these cases. Generally, the errors in the estimation of shear wave velocities of top layers will distribute to the bottom layers and cause a wrong answer. More often, this distribution of error happens in models with stiffer layers on top. An equally important issue in the interpretation of data is to distinguish the higher modes of propagation. If these modes are not recognized in the theoretical models, larger shear wave velocities are estimated for the layers, thus the elastic properties will be over estimated. For deep layers the acquired data in the field, and the theoretical interpretation techniques loose their resolution. A rule of thumb is that the thickness of each layer should be at least equal to one fifth of its depth to

be differentiable [100]. Finally, it should be noted that the obtained values from MASW test are global values (average values) and might not exactly match with the local values obtained from bore holes or other in-situ testing techniques.

The successful application of MASW faces with several challenges and difficulties, such as:

- There is no standard interpretation method.
- It is limited to certain frequencies, and the results might not be continuous.
- Spurious cycles might be present in the phases that causes difficulties in the phase unwrapping procedure.
- In a vertically inhomogeneous media, Rayleigh wave propagation is a multi mode phenomena. Thus, modal superposition occurs. Difficulties in distinguishing between different Rayleigh modes impose ambiguity and complication in data interpretation. Further, the experimental dispersion curve might not coincide with any branch of the modal curve.
- Uncertainties are present in the current criteria for the choice of receiver-to-source and receiver-to-receiver spacings. This leads to erratic decisions about the reliable frequency and wavelength ranges.
- Acquisition method, and lack of resolution or sensitivity to a certain target limit the reliable investigation depth.
- Lateral inhomogeneities are not accounted for in the theories associated with MASW.

## Chapter 5

# Numerical modeling of Rayleigh wave propagation

### 5.1 Introduction

A number of different numerical schemes of varying complexity have been used to solve elastic wave propagation problems. Alterman et. al. [108] and Bertholf [109] provided a brief review of most of these methods. More involved methods, which are capable of following the motion through regions of plastic, shock, or brittle behavior have been devised by researchers such as Petschek [110]. The finite element (F.E.) method has also been used extensively in this field [3]. Little attention has also been paid to the methods such as wave scattering method [111] and the perturbation method (1970), though they are potentially valuable [2]. The usefulness of any of the above schemes depends greatly on the characteristics of the problem to solve. The best method is the one that gives reasonable answers in the shortest time.

The finite differences (F.D.) technique, is based on replacing the difference equations and the boundary conditions by simple finite difference approximations in such a way that an explicit recursive set of equations is formed. In this method, every derivative in the governing equations is replaced directly by an algebraic expression in terms of the field variables at discrete points in space and time; these variables are not defined within the elements [4]. The final result is a time marching procedure that can be used to solve for the displacements at each grid point as



a function of time given the motion at the first two steps [2].

Both of the finite differences and finite element methods produce a set of algebraic equations to solve. Even though these equations are derived in different ways, in specific cases the resulting equations are identical for the two methods. It is pointless, then, to argue about the relative advantages of either of them because the resulting equations are the same [4].

Among the advantages of F.D. method are its ease to be programmed, its capability of solving many different problems with only minor alterations to the scheme and its ability to solve problems with transient loading. Also a very convenient feature is that displacements as a function of time at a given site or pictures of the total wave field at a given time can be obtained with equal ease [2]. This technique also has some limitations. For example it is most useful in the near field region of sources, where the sources are real. Thus it would be impractical to use the F.D. method to evaluate the surface displacements of a short period body wave incident upon an irregular interface [2].

## 5.2 Principles of finite differences method

The F.D. technique is based on replacing differential operators by difference approximations. A number of ways are available to find the governing differences schemes from which a few will be presented and discussed here. This section is summarized mostly from Boore [2], Itasca [4] and Strikwerda [112].

In the standard finite differences method, the continuous spatial-time domain ( $x, y, z$  and  $t$ ) is divided into rectangular blocks. The displacement field is then specified by a discrete set of nodal points represented by the corner intersection of the blocks. For constant  $x$ ,  $z$  and  $t$  spacing  $\Delta x$ ,  $\Delta z$  and  $\Delta t$ , any node is uniquely determined with reference to an arbitrary coordinate origin by the indices  $m$ ,  $n$ , and  $p$ . Hence  $u_{m,n}^p = u(m\Delta x, n\Delta z, p\Delta t)$ , where subscripts refer to spatial location and superscripts to time. Also in the presence of two media, the subscripts 1 and 2 will be used to denote the respective medium.

### 5.2.1 Derivative approximations

The standard approximations for the first and second derivatives and the corresponding error functions can be derived using Taylor expansions [113], [114]. The derived schemes are called centered or single sided based on their symmetry about the expansion point. A single sided scheme is called forward scheme if it evaluates the function at larger values of  $m$ ,  $n$  or  $p$ , otherwise it is called a backward scheme. Typical expansions of the most common schemes are:

$$\left(\frac{\partial u}{\partial x}\right)_m \simeq \frac{u_{m+1} - u_{m-1}}{2\Delta x} \quad (5.1a)$$

$$\left(\frac{\partial u}{\partial x}\right)_m \simeq \frac{u_{m+1} - u_m}{\Delta x} \quad (5.1b)$$

$$\left(\frac{\partial^2 u}{\partial x^2}\right)_m \simeq \frac{u_{m+1} - 2u_m + u_{m-1}}{\Delta x^2} \quad (5.1c)$$

Equations 5.1a and 5.1c are centered schemes, because they are symmetric around a center point, whereas equation 5.1b is an example of a single sided-forward scheme. Generally, the single sided schemes are less accurate than a centered scheme. With a few changes all of these expressions can be applied to derivatives with respect to  $z$  and  $t$ . Formulations for non-constant  $\Delta x$ ,  $\Delta z$  and  $\Delta t$  can also be found in Lick [113] and Boore [2].

Finally an explicit F.D. scheme is any scheme that can be stated in the form:

$$u_{m,n}^p = a \text{ finite sum of } u_{m,n}^{p^0} \text{ with } p^0 \leq p \quad (5.2)$$

### 5.2.2 Difference form of equation of motion for homogeneous medium

For a homogeneous medium, the general equation of motion (Chapter 2) is presented in this section in difference form for the case of zero dilatation ( $\Delta = 0$ ) is presented. The simplified differential equation is:

$$\rho \frac{\partial^2 u}{\partial x^2} = \mu \nabla^2 u \quad (5.3)$$

Where  $\nabla^2$  is the Laplacian operator,  $\rho$  is density,  $\mu$  is the shear modulus and  $u$  is the displacement. Replacing the derivatives by difference approximations (equations 5.1 a & c) and

rearranging gives:

$$u_{m,n}^{p+1} = 2u_{m,n}^p - u_{m,n}^{p-1} + C_s^2 \Delta t^2 \left( \frac{u_{m+1,n}^p - 2u_{m,n}^p + u_{m-1,n}^p}{\Delta x^2} + \frac{u_{m,n+1}^p - 2u_{m,n}^p + u_{m,n-1}^p}{\Delta z^2} \right) \quad (5.4)$$

where  $C_s$  is the shear wave velocity.

Equation 5.4 is a recursive, explicit equation in the displacement at new time level  $p + 1$ . Using a forward time marching process it is easy to compute displacement at any time, given the initial displacements at two consecutive time points.

### 5.2.3 Difference form of equation of motion for non-homogeneous medium

Equation 5.3 for a non-homogeneous medium is written as:

$$\rho \frac{\partial^2 u}{\partial x^2} = \frac{\partial}{\partial x} \left( \mu \frac{\partial u}{\partial x} \right) + \frac{\partial}{\partial z} \left( \mu \frac{\partial u}{\partial z} \right) \quad (5.5)$$

where  $\mu(x, z)$  is the rigidity of the material and  $\rho(x, z)$  is the density.

To solve this equation, the derivative with respect to time can be replaced by standard difference equations. Similar difference schemes are developed For the spatial derivatives:

$$\frac{\partial}{\partial x} \left( \mu \frac{\partial u}{\partial x} \right)_m = \frac{\mu_{m+\frac{1}{2}} u_{m+1} - \left( \mu_{m+\frac{1}{2}} + \mu_{m-\frac{1}{2}} \right) u_m + \mu_{m-\frac{1}{2}} u_{m-1}}{\Delta x^2} \quad (5.6)$$

Tikhonov and Samarskii [115] developed a method which is more dependent on the variation of  $\mu(x, z)$ . The following equation states their final conclusion:

$$\frac{\partial}{\partial x} \left( \mu \frac{\partial u}{\partial x} \right)_m = \frac{A_{m+1} u_{m+1} - (A_m + A_{m+1}) u_m + A_m u_{m-1}}{\Delta x^2} \quad (5.7a)$$

$$\text{where } A_l = \Delta x \left[ \int_{x_{l-1}}^{x_l} \frac{dx}{\mu} \right]^{-1} \quad (5.7b)$$

Equations 5.6 and 5.7 determine the equivalent values of rigidity at node points in the computational zone. These formulas hold for any arbitrary rigidity i.e. when the rigidity has a step change in value.

## 5.2.4 Boundary and initial conditions

The condition that the dependent variable should satisfy around the boundary curve is termed boundary condition. It is also usual for the variable distribution through out the medium to be known at some particular instant, which is usually taken as zero time. This variable distribution is called initial condition [114].

Two types of boundary conditions are common in F.D. models: physical boundaries and artificial boundaries.

### Physical boundaries

This type of boundary condition arises when an abrupt change in rigidity occurs at some interface in the body. These conditions are expressed as the continuity of stress and displacement. Also it is common to call them as displacement and velocity boundary conditions. In the mathematical form they are expressed as:

$$u_+ = u_- \quad (5.7c)$$

$$\left(\mu \frac{\partial u}{\partial n}\right)_+ = \left(\mu \frac{\partial u}{\partial n}\right)_- \quad (5.7d)$$

where  $u$  is the displacement and  $\partial / \partial n$  is the derivative normal to the interface. Equation 5.7c satisfies the continuity of displacements and equation 5.7d satisfies the continuity of velocity at the interface.

Most published applications of the finite difference method to elastic wave propagation involve plane rather than curved interfaces [116], [2]. These approximations are difficult to generalize to complicated boundaries. In 1970s several methods based on the heterogeneous wave equation (equation 5.5) have been developed which can be utilized for either curved or plane boundaries with the same ease [2]. As stated in the previous sections one method is the heterogeneous media approach that utilizes equation 5.7 to approximate the equivalent stiffness of the node.

The other approach is called explicit continuous stress method that was developed by Boore [2]. This method is based on expanding the Laplacian at the interface points in terms of an

irregular mesh with short legs. The difference form of the Laplacian in this case is:

$$\left(\frac{\partial^2 u}{\partial x^2}\right)_m \simeq 2 \left[ \frac{u_{m+1}}{\Delta x_2 (\Delta x_1 + \Delta x_2)} - \frac{u_m}{\Delta x_1 \Delta x_2} + \frac{u_{m-1}}{\Delta x_1 (\Delta x_1 + \Delta x_2)} \right] \quad (5.8)$$

where  $u$  is displacement and  $\Delta x_1$  and  $\Delta x_2$  are the  $x$  distance between grid points  $m - 1, m$  and  $m, m - 1$  respectively.

A fictitious computation star is defined which involves displacements at actual grid points and at curved points, defined by interface grid line intersections (Figure 2 1). Knowing the displacements at times  $p$  and  $p-1$ , all the displacements for time  $p+1$  can be generated except for point D which the following procedure is used to calculate it:

- normal to the boundary curve is constructed at D
- displacement at the normal-gridline intersection C is determined by linear interpolation between grid points A and B (and similarly for C').
- approximation to equation 5.7d is given by:

$$\mu_1 \frac{u_D^{p+1} - u_C^{p+1}}{DC} = \mu_2 \frac{u_C^{p+1} - u_D^{p+1}}{DC'} \quad (5.9)$$

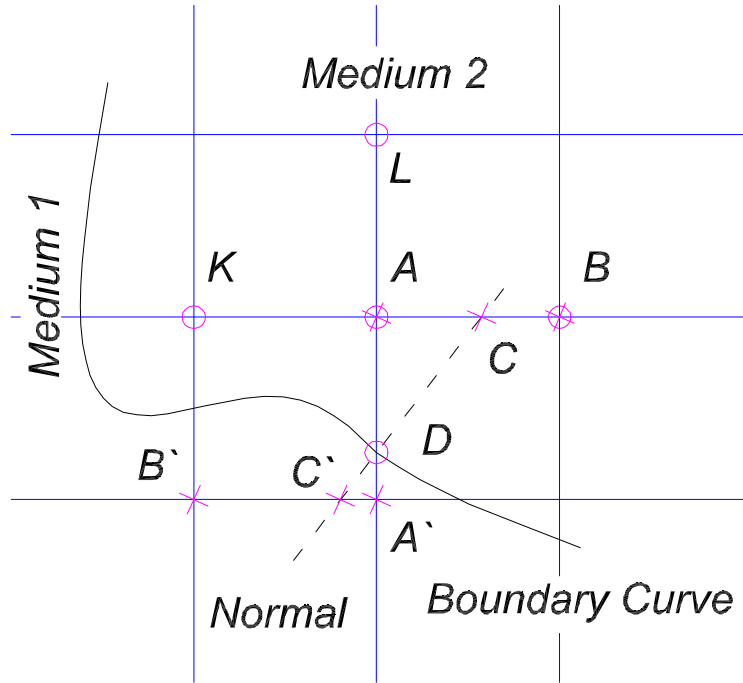
In which  $u$  is the displacement,  $\mu_1$  and  $\mu_2$  are the rigidities of medium 1 and medium 2 respectively and  $DC$  and  $DC'$  are as defined in Figure 5-1.

Equation 5.9 is used to determine the new curve point displacement  $u_D^{p+1}$ .

### Artificial boundaries

The wave propagation in an unbounded medium in any direction cannot be modeled directly, because of the limitations of finite computer storage. Hence artificial boundaries should be introduced. This places some definite constraints on the length of time for which the computed solution can be considered free of contamination. The manner in which these boundaries are treated is highly dependant on the problem and a general comment on all the models might not be always applicable.

The simplest model is the one used for a symmetric structure. In this model half of the region can be modeled provided that the condition  $\partial u / \partial x = 0$  is satisfied all along the line of



- ✕ Grid points involved in computing displacement at D
- Computational star grid points

Figure 5-1: A portion of the spatial grid near a curved boundary (after [2])

symmetry. Also the model can be prepared large enough that the compressional waves reflected from the boundaries and the imaginary obstacles (in an axisymmetric model) do not reach the recording points.

Lysmer and Kuhlemeyer [3] proposed a general method through which an infinite system can be by a finite system with a special viscous boundary condition. The physical interpretation of the method can be explained using Figure 5-2 which, shows a typical example of an infinite system.

An imaginary convex boundary is considered that encloses all sources of disturbance and irregular geometrical features. Propagation of the energy occur only from interior to the exterior region and all the energy arriving at the boundary will pass to the exterior region. The effect

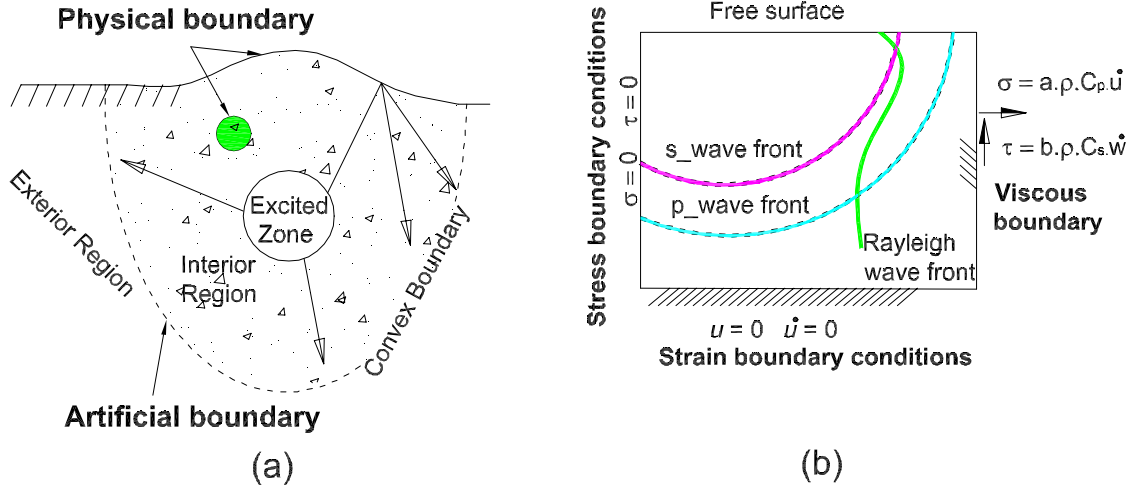


Figure 5-2: a) Typical infinite system b) Typical equivalent bounded model (after [3])

of the exterior region on the interior region is thus similar to that of an energy- absorbing boundary. This observation leads directly to the idea of determining the dynamic response of the interior region from a finite model consisting of the interior region subjected to a boundary condition, which ensures that all energy arriving at the boundary is absorbed. Analytically this can be expressed by the following boundary condition:

$$\sigma = a\rho C_p \dot{w} \quad (5.10a)$$

$$\tau = b\rho C_s \dot{u} \quad (5.10b)$$

Where  $\sigma$  and  $\tau$  are the normal and tangential stresses respectively;  $\dot{w}$  and  $\dot{u}$  are the normal and tangential velocities;  $\rho$  is the mass density;  $C_p$  and  $C_s$  are the p-wave and shear-wave velocities respectively and  $b$  and  $a$  are constants.

The introduced boundary condition corresponds to a situation in which the boundary is supported on infinitesimal dash pots oriented normal and tangential to the boundary. Numerical investigation of the absorbing boundary method shows that for a given choice of  $a$  and  $b$  the ratio between the reflected and absorbed energy depends on the incident angle  $\theta$  and Poisson

ratio  $\nu$ . It has been shown that the absorption cannot be perfect over the whole range of incident angles by any choice of  $b$  and  $a$ . Nearly perfect absorption is obtained for the range  $\theta > 30^\circ$  for  $a = b = 1$ , while some reflections happen at smaller incident angles. For a choice of  $a = b = 1$  and  $\nu = 0.25$  they showed in that their method is 98.5% effective in absorbing p-waves and 95% effective in absorbing s-waves. By using  $b$  and  $a$  varying with depth along the boundary, this method is almost perfect in absorbing Rayleigh waves. Finally it should be mentioned that this method is not frequency dependent and it can be applied to transient waves as well as harmonic excitations.

The above methods are only approximate except for the symmetric condition. The difference between the computed solution and the actual solution that would exist in the absence of boundaries, acts as secondary sources and produce spurious reflections, which contaminate the solutions at surface. At free surface, contamination usually is present only in later parts of time records. This is because of the fact that the secondary sources are generated when the incident waves have a chance to reach the artificial boundary and reflect back toward the free surface. In case of existence of several waves with different velocities, there is a chance for low velocity waves to be contaminated by the reflections of high velocity waves. In general, contamination is unavoidable and the more easily it is recognized the less chance there is of interpreting it as real motion.

As a general comment it can be stated that in practice the artificial boundaries should be placed as far from the region of heterogeneity as it is feasible. Numerical experiments, using different distances to the sides and bottom are essential to define the space-time region that is free of contamination.

### **Consistency, Stability and Convergence**

The most basic property that a scheme must have in order to be useful is that its solutions approximate the solution of the corresponding partial differential equation and that the approximation improves as the grid spacing ( $\Delta x$ ,  $\Delta z$  and  $\Delta t$ ) tend to zero. This property is called convergence of a scheme.

In general, direct attempt to prove that a given scheme is convergent is not easy. However in practice this problem has been replaced by investigating the consistency and stability of the



scheme. Lax proved mathematically [112] that a consistent finite difference scheme for a partial differential equation is convergent if and only if it is stable. In this way in a finite difference model it is necessary to assure that it is stable and convergent.

The truncation error of a difference equation measures how closely the exact solution of the differential equation satisfies the corresponding difference equation. In a finite difference approximation, a measure of truncation error is given by inserting the solution to the corresponding differential equation into the difference approximation. In general the truncation error is a function of a power of grid spacing and is expected to vanish in the limit  $\Delta x, \Delta z$  and  $\Delta t \rightarrow 0$ . In the mathematical form it can be stated as:

$$ERROR = O(\Delta x^\alpha, \Delta z^\alpha, \Delta t^\alpha) \longrightarrow 0 \quad \text{as} \quad \Delta x, \Delta z, \Delta t \longrightarrow 0 \quad \text{provided } 0 \leq t \leq T \quad (5.11)$$

in which  $\alpha$  is called the degree of accuracy of the difference scheme.

If the condition of equation 5.11 is satisfied the difference equation is said to be consistent with the partial differential equation. In practice to assure the consistency of the partial differential equation  $Pu = f$ , with a finite difference scheme  $P_{k,h}u = f$  it is sufficient to find a smooth function  $\phi(t, x, z)$  that satisfies the following condition [114]:

$$P\phi - P_{k,h}\phi \longrightarrow 0 \quad \text{as} \quad k, h \longrightarrow 0 \quad (5.12)$$

Stability of a difference approximation is the requirement that there should be a limit to the extent to which any component of the initial function can be amplified in the numerical procedure. During World War II, von Neumann [114] developed a way to investigate the stability of a scheme. This method is based on the Fourier series method and uses a time harmonic plane wave for the wave field, as follows:

$$u_i(x, z, t) = u_i(0, 0, 0) e^{i(k_x x + k_z z)} e^{-i\omega t} \quad (5.13)$$

in which,  $k_x$  and  $k_z$  are the wave numbers in  $x$  and  $z$  directions respectively,  $\omega$  is the excitation frequency and  $u_i(0, 0, 0)$  is the initial condition. In the matrix form the propagation of the wave

field in a homogeneous medium unbounded can be described as [117]:

$$U(t + \Delta t) = AU(t) \quad (5.14)$$

Where  $U(t)$  denotes the generalized wave field which contains all wave field parameters that are necessary to calculate the next time step. To ensure that the errors at some time step do not become magnified with time, it is necessary for the eigenvalues of  $A$  to be less than one. Mitchel [115] showed that for a general three level scheme with 2 spatial dimensions the above condition is satisfied when the following condition is fulfilled:

$$\beta \frac{\Delta t}{\Delta x} \leq \frac{1}{\sqrt{2}} \quad (5.15)$$

where  $\beta$  is the equivalent wave velocities in the node points in the computational star surrounding any arbitrary point at  $m\Delta x, n\Delta z$ . For a non-uniform grid  $\beta$  would be a non-constant function over  $(x, z)$ . In practice no instability occurs when the highest uniform media velocity replaces  $\beta$ .

Stephen [118] used a less restrictive condition for stability of his proposed finite difference scheme as follows:

$$\frac{\Delta t}{\Delta x} \leq \frac{1}{\sqrt{C_p^2 + C_s^2}} \quad (5.16)$$

where  $C_p$  and  $C_s$  are the p- and s- wave velocities respectively. Also Saenger et al. (2000) used the following stability condition for a standard staggered grid :

$$\frac{\Delta t}{\Delta x} \leq \frac{1}{C_p^2 \sqrt{2} \sum_{k=1}^n |c_k|} \quad (5.17)$$

where  $c_k$  denotes the difference coefficients. This equation gives a more restrictive condition than the one in equation 5.15.

Finally the following criterion was used by Otter et al. [119] to be used with dynamic relaxation scheme , This equation is stated for  $m$  spatial coordinates:

$$\frac{\Delta t}{\Delta x} \leq \frac{1}{C_p} \left\{ \left( \frac{1}{x_1} \right)^2 + \dots + \left( \frac{1}{x_n} \right)^2 \right\}^{-\frac{1}{2}} \quad (5.18)$$

It should be reminded that von Neumann criteria has been developed for homogeneous, elastic media with no damping. Stability limits and error analysis of finite difference schemes, which include anisotropy and attenuation has never been performed [117]. Also application of most of the developed conditions is restricted to the special schemes and grids that they are associated with. So in general, they are sufficient and necessary for some of the schemes though not necessary always [114]. In practice the above methods give useful results even when their application is not fully justified.

Instability is seen to be rapid growth of high frequency modes in the solution of the finite difference solution. This means that using initial data that contains larger amplitudes for higher frequencies causes a sooner evidence of instability. Instability is a local phenomenon, which propagates to other regions and usually starts at points of discontinuity [112].

### **Nyquist frequency**

The minimum reliable frequency that can be extracted from a finite difference scheme is called Nyquist frequency and is defined as:

$$f_{\max} \leq f_{Nyq} = \frac{1}{2\Delta t} \quad (5.19)$$

where  $\Delta t$  is the time increment of finite difference scheme.

### **Numerical dispersion**

The term dispersion is associated with the phenomena of waves of different frequencies traveling with different speeds. This causes the shape of the wave not to be preserved as the wave moves away from the source. Despite of the stability condition, where the model is stable if the stability condition is satisfied, numerical dispersion can only be reduced to some degree [117].

To control the numerical dispersion the following parameters are introduced [120]:

$$\gamma = \sqrt{2}C_p \frac{\Delta t}{\Delta x} \quad (5.20a)$$

$$H = \frac{\Delta x}{\lambda} \quad (5.20b)$$

Equation 5.20a controls the numerical dispersion, which its maximum is defined with the stability criteria ( $\gamma_{max}$ ), and equation 5.20b controls the number of nodes per wavelength of the plane wave. Then the non-dimensional velocities (the ratio between the numerical phase velocity to the true phase velocity) are defined as follows:

$$q_p = \frac{\sqrt{2}}{\pi\gamma H} \sin^{-1} \left[ \frac{\gamma}{\sqrt{2}} \sqrt{\sin^2(\pi H \cos(\theta)) + \sin^2(\pi H \sin(\theta))} \right] \quad (5.21a)$$

$$q_s = \frac{C_p}{C_s} \frac{\sqrt{2}}{\pi\gamma H} \sin^{-1} \left[ \frac{C_p}{C_s} \frac{\gamma}{\sqrt{2}} \sqrt{\sin^2(\pi H \cos(\theta)) + \sin^2(\pi H \sin(\theta))} \right] \quad (5.21b)$$

where equations 5.21a and 5.21b define the nondimensional p- and s-wave velocities, respectively. In above  $\theta$  is the angle that the wave makes with horizontal axis, and the rest of the parameters are defined previously.

Equation 5.21a implies that the dispersion of p-wave velocity does not depend on the Poisson ratio though the dispersion of s-wave velocity depends on the Poisson ratio through the ratio of  $C_p$  to  $C_s$ . Also maximum dispersion occurs when the incident angle is equal to  $0^\circ$  or  $90^\circ$ . Figure 5-3 shows the plot of non-dimensional p- and s-wave phase velocities for a case where  $C_p = 114.9 \frac{m}{s}$ ,  $\nu = 0.2$ ,  $\gamma = 2.031$ , and  $\theta = \frac{\pi}{20} rad$ .

As it can be seen increasing the number of grid points per wavelength decreases the dispersion of the numerical approach. Virieux [120] suggested to use at least 10 nodes per wavelength though other researchers proposed more restrictive conditions, i.e. Lysmer and Kuhlemeyer [3] suggested 12 nodes per wavelength and Holberg [121] proposed 20 grid points per wavelength. Figure 5-3 shows that for 10 nodes per wavelength ( $H = 0.1$ ) the computed phase velocity would be about 98% of the actual velocity. To reduce the numerical dispersion for a given scheme the following procedures can be followed [117]:

- large wavelengths with respect to the grid spacing (minimizing H)

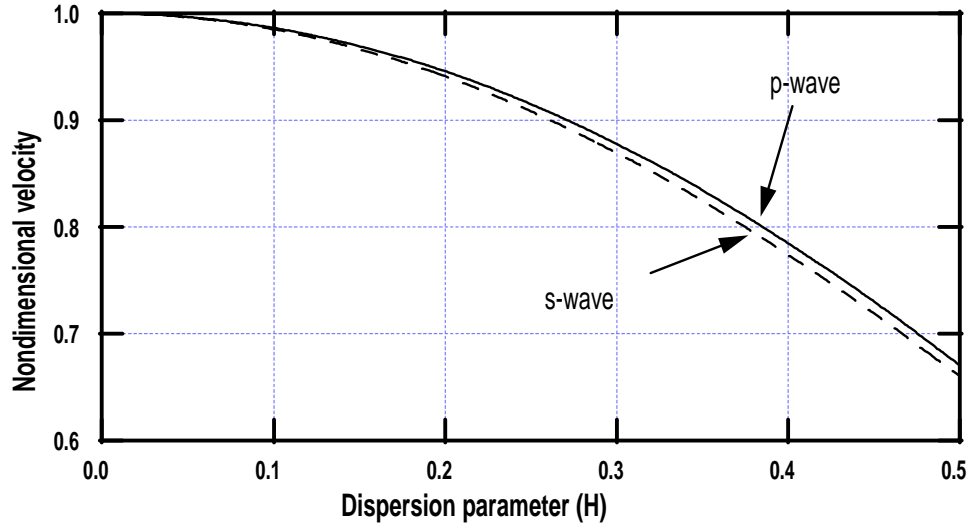


Figure 5-3: Dispersion curve for non dimensional s-wave phase velocity.

- a small dispersion parameter  $\gamma$  with respect to  $\gamma_{max}$ .

In a mathematical form the above conditions can be stated as:

$$\Delta x \leq \Omega \lambda_{\min} \quad \text{where} \quad \lambda_{\min} = \frac{C_P}{f_{\max}} \quad (5.22)$$

Where  $\Omega$  is a positive factor and  $f_{max}$  is defined in equation 5.19. In practice 10 to 15 nodes per wavelength ( $\Omega = 0.1$  to  $0.067$ ) gives reasonable results. Combining equations 5.19 and 5.22 gives the following lower restricting boundary:

$$\frac{1}{2\Omega C_P} \leq \frac{\Delta t}{\Delta x} \quad (5.23)$$

Another approach that clearly defines the numerical dispersion phenomenon is based on 2D Fourier analysis method [122]. In this method displacement time histories are assembled in a matrix and a 2D Fourier transform is applied to the array. Thus, the data are converted into frequency-wave number (f-k) domain. The trends of the peaks in the f-k plots show the dispersive characteristics of the finite difference mesh. This method will be utilized later in this study to improve the mesh behavior.

### 5.2.5 Description of finite differences program FLAC

As Itasca 2000 defines, FLAC is an explicit finite differences program that performs a Lagrangian analysis. The purpose of this section is to introduce the basic features of the program that are relevant to this study. This section presents a summary from Itasca [4] and other references mentioned throughout the text.

#### Governing equations

The general governing equations are the equilibrium,  $\Sigma F = m.\ddot{a}$ , and constitutive laws,  $\sigma = f(\epsilon)$ , (Chapter 1). Rearranging the mentioned equations and stating them in terms of velocities, a set of first order differential equations is obtained, which is used in FLAC. As the strains are calculated from displacements the compatibility condition is implicitly satisfied through the cycle.

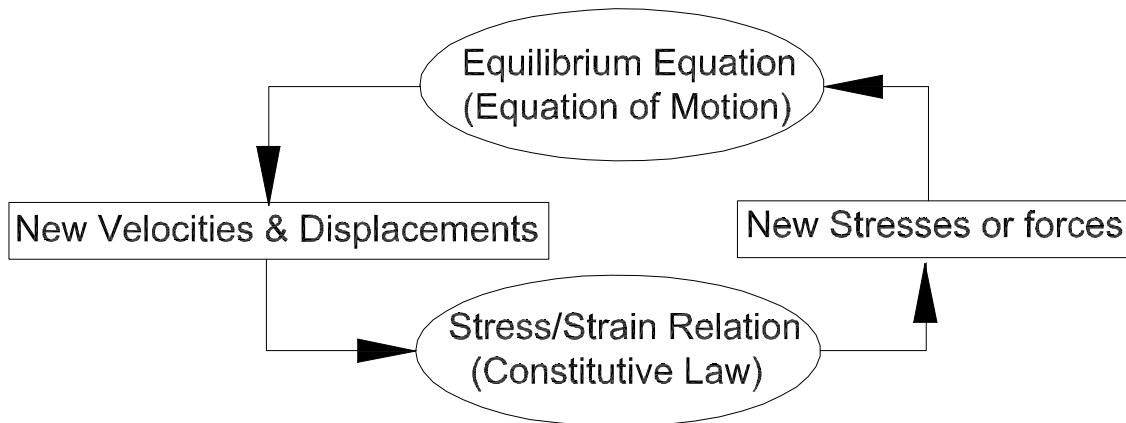


Figure 5-4: Basic explicit calculation cycle

Figure 5-4 shows the basic calculation cycle utilized in FLAC. The detailed formulations can be found in Itasca [4] and Otter et al. [119]. A staggered grid in time is utilized, the stresses are calculated at times  $n\Delta t$  and the corresponding velocities at times  $(n + \frac{1}{2})\Delta t$ . The iteration can be started from any compatible set of initial stresses and either stress or displacement boundary conditions can be applied to the physical boundaries.

### Finite differences equations

The finite difference scheme used in FLAC follows the approach of Wilkins [123], because this method can model non-straight boundaries. The user divides the medium into quadrilateral elements. Then internally, FLAC divides each element into two overlaid sets of constant-strain triangular elements (Figure 5-5).

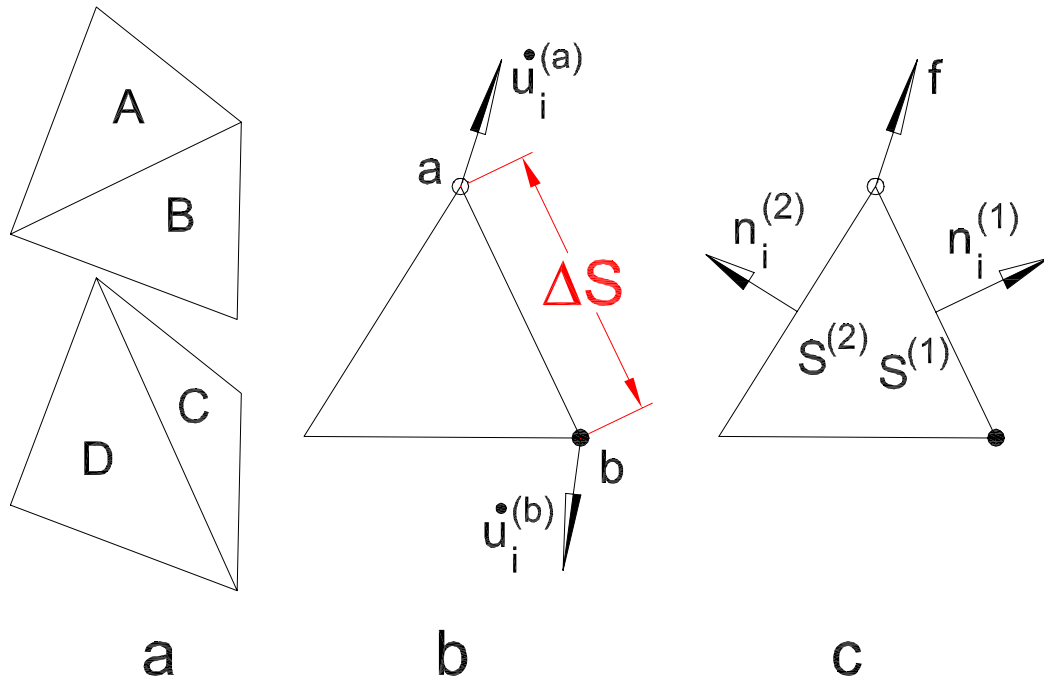


Figure 5-5: a) Overlaid quadrilateral elements used in FLAC b) Typical triangular element with velocity vectors c) Nodal force vector (after Itasca 2000 [4] with modifications)

The four triangular sub-elements are termed A, B, C and D. The force exerted at each node is the average of the forces exerted by the overlaid quadrilaterals. At this stage FLAC imposes a limitation on the shape of the elements, if the area of one triangle becomes much smaller than the area of its companion, then the corresponding quadrilateral is not used. If both overlaid sets of triangles are badly distorted, then an error message will appear.

The difference equations used in FLAC, are based on the generalized form of Gauss' divergence theorem [124]. The utilized finite difference formulation for a triangular sub-element

is:

$$\left\langle \frac{\partial f}{\partial x_i} \right\rangle = \frac{1}{A} \sum_S \langle f \rangle n_i \Delta s \quad (5.24)$$

where  $\left\langle \frac{\partial f}{\partial x_i} \right\rangle$  is the average derivative over the perimeter of the triangle,  $\Delta s$  is the length of a side of the triangle, and summation occurs over the three sides of the triangle.  $A$  is the area of the triangle,  $\langle f \rangle$  is taken to be average (in this study force) over the side and  $n_i$  is the normal vector to the side (Figure 5-5c).

### Stability

The built in scheme in FLAC is not unconditionally stable. A time step must be small enough so that the speed of the calculation front is greater than the speed of the faster existent wave. Thus, a critical time step is defined as:

$$\Delta t_{crit} = \min \left( \frac{A}{C_P \Delta x_{max}} \right) \quad (5.25)$$

where  $\Delta x_{max}$  is the maximum zone dimension, which is usually a diagonal distance and  $A$  is the area of the triangle. The  $\min()$  function is taken over all zones. For a right angle triangle with two equal sides ( $\Delta s = \Delta x$ ) the area would be equal to  $\frac{1}{2} \Delta x^2$  and the maximum dimension would be equal to  $\Delta x \sqrt{2}$ . Hence the following stability condition is obtained for a factor of safety  $F.S. = 2$ :

$$\frac{\Delta t}{\Delta x} \leq \frac{1}{4C_P \sqrt{2}} \quad (5.26)$$

This equation requires smaller time increments than the ones introduced in previous sections. however numerical dispersion should still be considered. Also this equation is set for a homogeneous medium with no damping, hence it should be used cautiously.



## Chapter 6

# Behavior of Rayleigh waves in the presence of lateral and vertical inhomogeneities

### 6.1 Introduction

#### 6.1.1 Background

The study of the behavior of Rayleigh waves in an elastic medium with different boundary conditions has gained attention in the past century. This attention is partly because of the use of Rayleigh waves in nondestructive testing of soils and other materials. One specific application is the use of MASW test for the detection of underground cavities or anomalies and the estimation of their embedment depths and size. Another application is in the quality assessment of materials (i.e. concrete, pavement, wood, etc.) by means of nondestructive methods. In this case, the objective is to locate cracks or fractures within an element and estimate their size. Further, with extension and modification of the aforementioned problem, it is possible to explain the behavior of underground structures and utilities (i.e. tunnels, water mains ...) while subjected to earthquake/explosion loadings or vibrations due to machineries located at the ground surface.

The Lamb solution [26] relates the surface response of a homogeneous half-space to an

arbitrary transient dynamic surface load. The solution is frequency independent, and shows that geometrical damping is smaller for Rayleigh waves than for body waves. The propagation of Rayleigh waves in layered media, where individual layers are homogeneous, is well understood [12]. Thomson [65] and Haskell [125] describe the behavior of a horizontally layered medium to dynamic loading by computing a stiffness matrix for the medium. As the derivation of analytical solutions for the scattering of Rayleigh waves around heterogeneities is complicated and cumbersome, researchers often perform experimental tests or develop numerical models to study this problem [85, 126]. Watkins et al. [69] and Rechten and Stewart [70] conducted seismic field tests on sites with known embedded anomalies; they report disturbances in the recorded time domain signals near the void. The numerical studies of Al-Hunaidi [101] reveal that either plane or axisymmetric numerical models are justified for the simulation of wave propagation, and that there is good agreement between field and numerical data in both cases. Gucunski and Woods [127] show that for regular soil stratification (i.e., shear stiffness increases with depth), the source-to-near receiver spacing has a strong effect on the dispersion curve. In 1996, Gucunski et al. [94] developed finite element models to investigate the effect of lateral inhomogeneities on the dispersion curves from the recorded signals at the surface. They reported reflections from the void (in time domain) and fluctuations in the dispersion curves for long wavelengths. They tried to develop a simple mathematical model to predict the dispersion curves. Leparoux et al. [128] applied the SASW test to locate two cavities: one embedded at 3.0 m below the ground surface with a masonry lining, and the other one embedded at about 8.0 m beneath the surface, without any lining. They developed finite differences models to explain the field data, and they concluded that energy partitioning occurs as the Rayleigh wave encounters a void. Part of the energy is reflected back, part of it travels around the void, and part of it continues along its direct path. Thus, the reflections in time domain responses can be used to locate a void. Further, they indicated that there is a relation between the cavity depth and the frequencies that are affected. Deep cavities affect low frequencies and shallow cavities affect high frequencies. This effect is shown through a comparison of dispersion curves. Other researchers have also tried to associate the surface response of a medium to the location and size of a void. Field tests, experiments on prototypes, and numerical studies by Phillips et al. [129, 130, 97] show high energy concentrations in the Fourier spectra of

the surface responses over different voids. Results from various numerical models with lateral inhomogeneities [131, 94, 126] show that the presence of an anomaly causes rippled time signals. The ripples are more conspicuous in the area between the source and anomaly, because the obstacle reflects part of the energy of the incident wave. In general, field results and numerical studies show good agreement. Phillips et al. conducted laboratory and field tests and studied the results in the frequency domain. They detected regions with energy concentrations, in the power spectral values obtained from responses recorded in the proximity of a void. Hence, they proposed the use of power spectral density functions (PSD method) to detect voids. Shokouhi and Gucunski [96] reported a similar phenomenon based on wavelet analysis of the responses. They concluded that energy concentration and reflection peaks occur in front of the cavity. They observed reflections from near and far boundaries of the cavity. Accordingly, a method for evaluation of the width of the cavity was proposed, which is based on calculation of the time difference between the reflections from near and far boundaries of the void. Lastly, they observed that by increasing the depth of the void the observed responses at the surface are mitigated. Hevin et al. [132] applied similar techniques to determine the depth of a surface crack in a concrete element.

Despite of all the efforts, neither of the above researches was able to explain the physical behavior of the cavity and medium that causes the observed behavior. Further, a clear relationship between the surface responses and void geometry is not devised, and studies with various layers are rare. In almost all of the numerical studies the three dimensional nature of the problem is ignored for simplicity.

### **6.1.2 Statement of the problem**

Relatively limited experimental and theoretical information is available that address the propagation of mechanical waves in an inhomogeneous semi-infinite half space. Some solutions are available to account for the effect of vertical inhomogeneities (i.e. layering) on the Rayleigh wave fronts. Though, theoretical approaches to this problem have not led to a general solution. Further, the combined effect of lateral and vertical inhomogeneities on the propagation of Rayleigh waves is not studied in detail, yet.

The studies referenced in the previous section are based on qualitative changes of the surface

responses, without a physical interpretation of the observations. Thus, their applications are limited to the studied cases or similar ones and are not versatile. Both field and numerical studies confirm the occurrence of energy concentration (in different domains) in the vicinity of the void. Though, some researchers reported that it happens over the void [129], and others observed it in front of the cavity [96]. Moreover, its physical reason is not explained. The relation between the size and embedment depth of a cavity and the surface responses is still under investigation, and the evaluation of the embedment depth of a void is not possible. Limited information is also available that discuss the combined effect of void and horizontal layering on the surface responses. In previous studies, the limitations and errors of the methods are not clarified. Moreover, the detection of underground cavities is a three dimensional problem, and the effect of third dimension has been neglected in most of the conducted numerical studies .

This chapter explains the results of a series of studies that have been conducted to investigate the effect of lateral and vertical inhomogeneities (i.e. voids or a combination of void and layers) on the propagation of Rayleigh wave fronts in an elastic medium. The main objective is to derive physical relations between the responses at the surface of a medium and the characteristics of a cavity. The relation between the location, size, and embedment depth of a cavity and the surface responses is of a major concern. Further, the effect of the third dimension on the investigations is considered. This work will provide a basis for the successful application of MASW technique to detect underground cavities and evaluate their extents.

## 6.2 Numerical experimental methodology

The numerical modelling activity in this research consist of five stages (table 6.1), where this chapter explains the results of stage number S00. At this stage, two dimensional (2D) axisymmetric finite differences models are constructed to simulate the propagation of Rayleigh waves in an elastic half space in the presence of anomalies. The models simulate the MASW test method in the presence of lateral inhomogeneities. The models are calibrated against the Lamb ([26]) solution (Chapter 5). Rectangular voids with different sizes, width to height ratios, and embedment depths are incorporated into the medium. Figure 6-1 shows the model numbers and the geometry of the voids. Each model is numbered as  $SXX\_YY$ , where  $XX$  represents a model type, and  $YY$  represents the study number. Table 6.1 shows the description of model types used in this study. In each model type, voids with different sizes and embedment depth are inserted. Same model types with different void sizes are distinguished by their study number ( $YY$ ). Thus, model number  $S00\_05$  corresponds to model type  $S00$  (2D elastic half-space) and study number 05 (void at a depth of  $0.08\ m$ , height of  $0.08\ m$  and width of  $0.64\ m$ ). The model  $S00\_01$  corresponds to the half-space without any void. The responses of this model have been used as a reference for comparison of the results. All the values of the responses obtained from different studies of types  $S00$ ,  $S01$ , and  $S02$  are normalized to the corresponding maximum value of the study  $S00\_01$ . In this way, a common scale is used for all the results.

Table 6.1: Model types used in this study

<b>Model Type</b>	<b>Description</b>
$S00$	2D- elastic half-space
$S01$	2D- a layer underlain by a very stiff half space
$S02$	2D- a stiff layer underlain by a soft half-space
$S03$	3D- elastic half-space
$S04$	3D- a layer underlain by a very stiff half space

The responses along the surface, around the void, along several vertical, horizontal and circular lines inside the models are studied. The recorded responses are analyzed in time-space, frequency-space, and wavenumber-frequency domains. Snapshots of displacement fields of the surface, around the void, and inside the medium at different times (2DSpace-time domain) are also studied. The study in the 2D space-time domain allows for the correlation of the surface

responses with the deformations of the void and inside the medium. Thus, it leads to a better understanding of the governing physical phenomena.

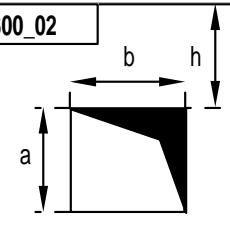
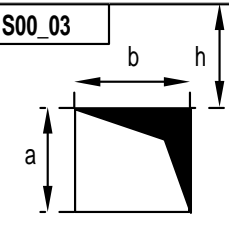
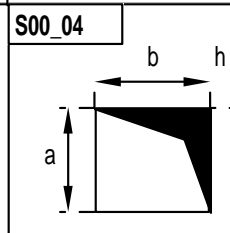
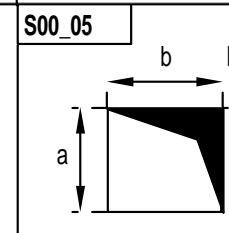
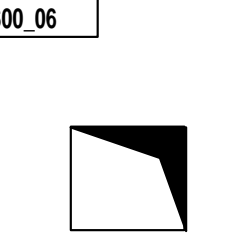
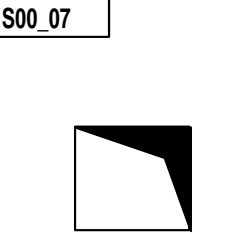
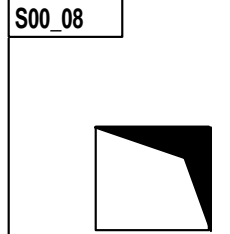
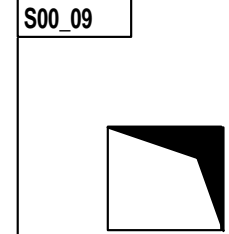
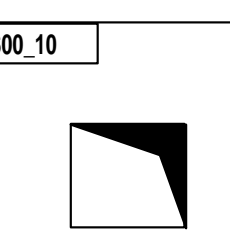
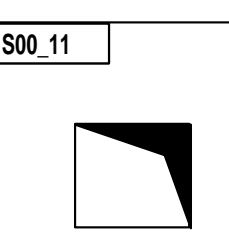
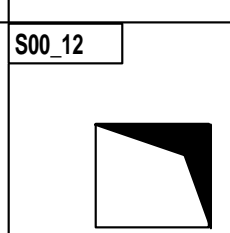
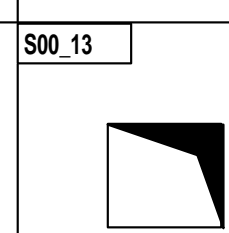
		Width (m)			
		b = 0.08 m	b = 0.16 m	b = 0.32 m	b = 0.64 m
Embedment depth (m)	h = 0.08 m	<div style="border: 1px solid black; padding: 2px; display: inline-block;">S00_02</div> 	<div style="border: 1px solid black; padding: 2px; display: inline-block;">S00_03</div> 	<div style="border: 1px solid black; padding: 2px; display: inline-block;">S00_04</div> 	<div style="border: 1px solid black; padding: 2px; display: inline-block;">S00_05</div> 
	h = 0.16 m	<div style="border: 1px solid black; padding: 2px; display: inline-block;">S00_06</div> 	<div style="border: 1px solid black; padding: 2px; display: inline-block;">S00_07</div> 	<div style="border: 1px solid black; padding: 2px; display: inline-block;">S00_08</div> 	<div style="border: 1px solid black; padding: 2px; display: inline-block;">S00_09</div> 
	h = 0.32 m	<div style="border: 1px solid black; padding: 2px; display: inline-block;">S00_10</div> 	<div style="border: 1px solid black; padding: 2px; display: inline-block;">S00_11</div> 	<div style="border: 1px solid black; padding: 2px; display: inline-block;">S00_12</div> 	<div style="border: 1px solid black; padding: 2px; display: inline-block;">S00_13</div> 

Figure 6-1: Model numbers and main characteristics of each model. Study numbers are stated in the small box at the top left corner of each cell. In each cell the size and embedment depth of the void, corresponding to that model, number is shown.

### 6.2.1 Model description

All the numerical models used in model type S00, are developed from the basic model represented in figure 6-2. The basic model consists of a uniform grid surrounded by a nonuniform grid, to reduce the computation time. The left boundary is fixed in horizontal direction (X-direction), thus represents an axis of symmetry. The bottom and right boundaries are free, and

quieted boundary conditions are applied to them to mitigate the effect of reflections. To prevent the free body motion of the model in vertical direction (Z-direction) the vertical displacement of the bottom-left corner of the model is fixed in Z-direction. For more details of the model see Chapter 5. The size of the model is 20.0 m in both the X- and Z- directions. The uniform grid size is 8.0m in X-direction (1000 grid spaces), and 2.12m in the Z-direction (266 grid spaces). Hence, the grid size in both X- and Z- directions for the uniform grid is  $\Delta s = 0.008m$ .

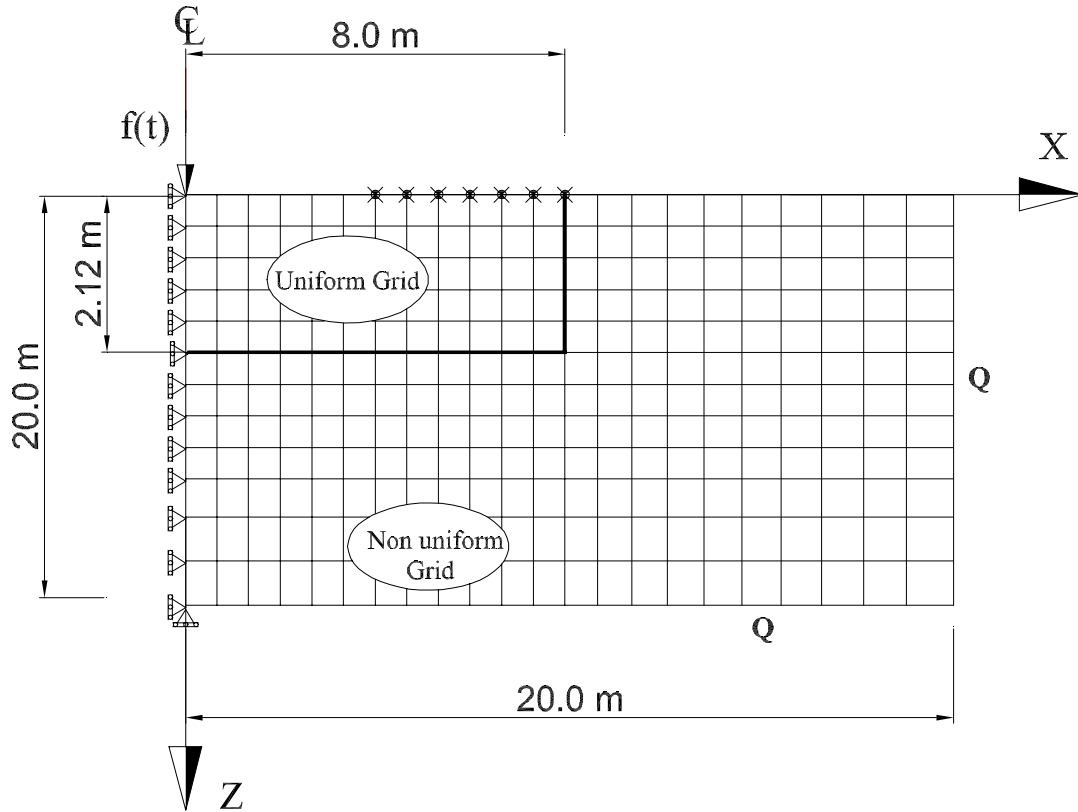


Figure 6-2: Geometry and dimensions of the basic finite differences model used in this chapter. Axis Z is the axis of symmetry.

The focus of this study is on R-waves; therefore, in each model the surface is excited by a vertical Lamb source (Chapter 5) to transfer most of its energy to the medium in the form of Rayleigh wave [54]. The Lamb source (Chapter 5) with the following parameters is chosen for the input source:

$$\psi = 0.00075; F_b = 1000; \text{Time Shift} = 0.036s \quad (6.1)$$

Figure 6-3 is a graphical representation of the used Lamb source in time and frequency domains. This source has energy in a wide frequency range; though, about 50% and 97.5% of its energy is concentrated in the frequency ranges below 150 Hz and 800 Hz, respectively.

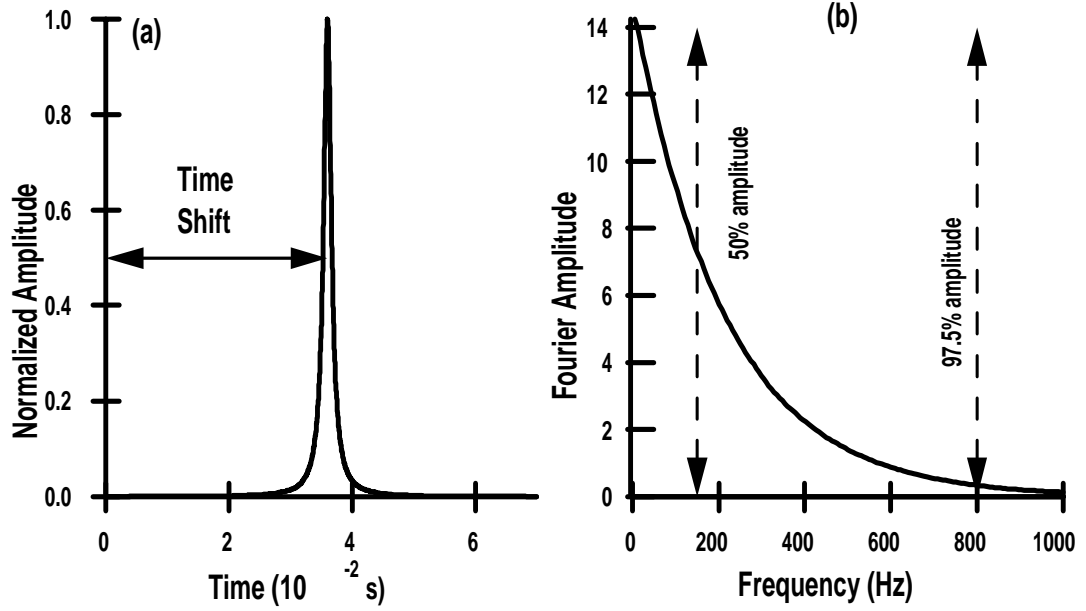


Figure 6-3: Representation of used Lamb source in time (a) and frequency (b) domains.

Material type I as introduced in table 6.2 is used in this phase. The P-wave ( $C_P$ ), S-wave ( $C_s$ ), and Rayleigh wave ( $C_R$ ) velocities are 114.87, 70.34, and 64.08  $\frac{m}{s}$  respectively. Following the procedures explained in Chapter 5, the dynamic time step ( $\Delta t$ ) and the maximum dynamic time ( $t_{\max}$ ) are selected as  $1 \times 10^{-5} s$  and 0.185 s, respectively.

To simulate lateral inhomogeneities, rectangular voids are introduced into the model. Figure 6-4 shows the general geometry of the voids and their location relative to the source. The voids are always centered at 5.592m from the source, thus the center of the void is not coincident with the center of the receivers line at the surface, which is located at 5.992m from the source. The width ( $b$ ), height ( $a$ ), and embedment depth ( $h$ ) of the void change in each study. The



width to height ratios ( $\frac{b}{a}$  ratio) are varied from 0.125 to 8 and the embedment depth to height ratios ( $\frac{h}{a}$  ratio) are varied from 0.125 to 4 (Figure 6-1).

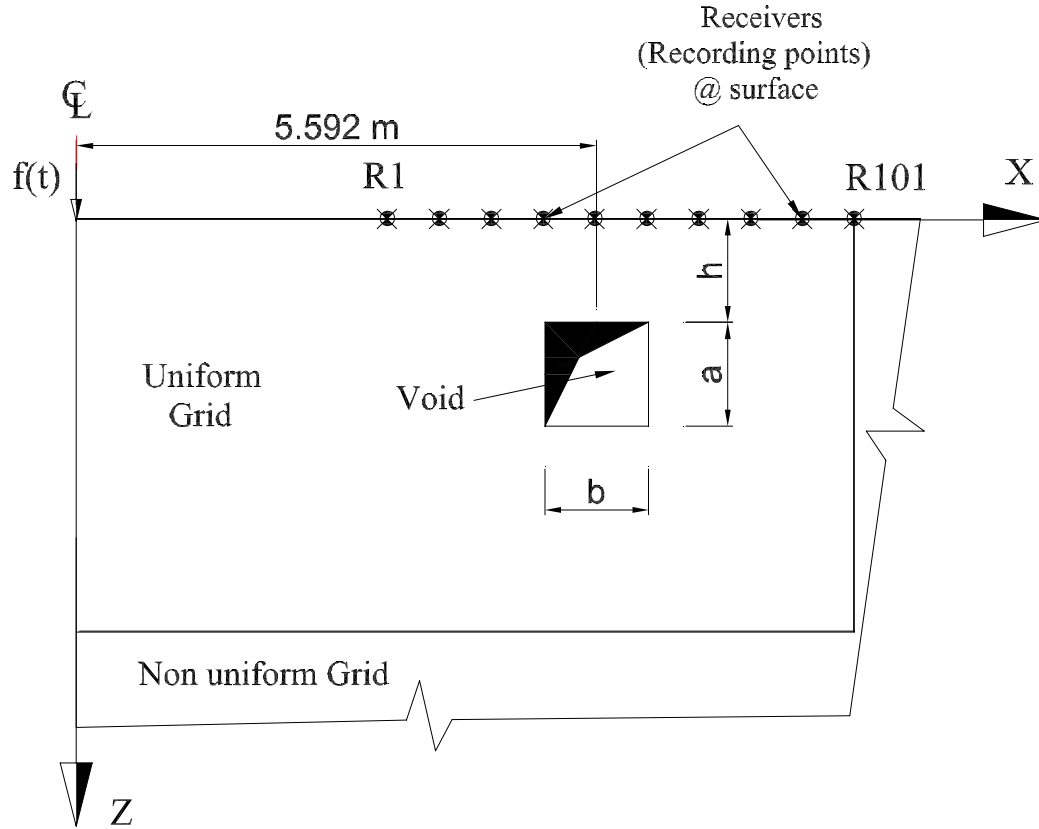


Figure 6-4: General geometry of a model with void. The width ( $b$ ), height ( $a$ ), and embedment depth ( $h$ ) of the void are variables.

### 6.2.2 Recording points and analysis parameters

To record the surface responses, 101 recording points (R1 to R101) along the surface are chosen (Figure 6-5a). R1 is 3.992  $m$  away from the source (offset value or  $D_x$ ) and the distance between R101 and the source is 7.992  $m$ , thus the array length is  $L_x = 4.00 m$ . The receivers are located far from the source to reduce the near field effect. The responses are recorded every other 5 grid points. Therefore, the distance between the receivers is  $\Delta x = 0.04m$ . Both the horizontal and vertical displacements ( $\delta x$  and  $\delta z$ ) are recorded and analyzed.

To enhance the study Rayleigh waves in the presence of a void, the responses inside the medium are recorded and analyzed in conjunction with the surface responses (figure 6-5) In the vertical direction five lines (V1 to V5), with 50 recording points are chosen (Fig 6-5a). The horizontal distance between V1, V2, V3, V4, and V5 and the source are 3.992 m, 4.792 m, 5.592 m, 6.392 m, and 7.192 m, respectively. The first recording point on each vertical line is located at the surface and the last recording point is located at a depth of  $-2.0$  m, the vertical distance between the consecutive receivers is 0.04 m. In the horizontal direction four lines (H1 to H4) are chosen at the depths of  $-0.04$  m,  $-0.08$  m,  $-0.16$  m, and  $-0.20$  m, respectively (Fig 6-5a). Similar to the surface, the responses are recorded at 101 points along each horizontal line. The first receiver is located 3.992 m and the last receiver is located 7.992 m away from the left boundary of the model. The distance between the recording points is 0.04 m.

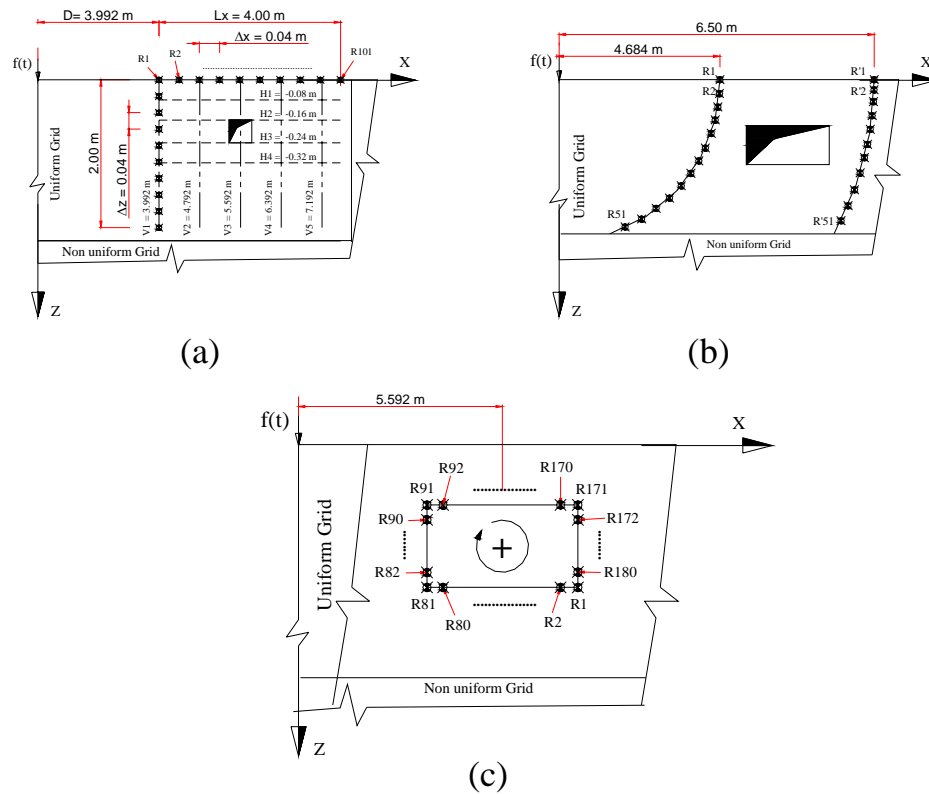


Figure 6-5: Location of recording points a) along the surface of the model, vertical lines, and horizontal lines inside the medium b) along arcs, and d) around the void

Figure 6-5b shows the recording points chosen along two arcs that start at the surface and ends at a depth of  $-2.00\text{ m}$ . The radius of the first arc is  $4.684\text{ m}$  and the second arc has a radius of  $6.50\text{ m}$ . Both arcs are located at the same horizontal distance from the middle of the void. 51 points are chosen around the arc to record the responses. Finally, the responses around the void are measured at 180 points. The numbering sequence of the points around the void is shown in figure 6-5c, they increase in the clockwise direction. On each side of the void the distance between the recording points is  $0.008\text{ m}$ .

Preliminary investigations with different medium physical properties showed that the measured trends are independent of the medium properties. Therefore, all the studies in model type *S00* are performed with the material properties presented in table 6.2. The properties are similar to the ones of the sand material that is used in the sand box test (Chapter 9).

Table 6.2: Material properties used in model type *S00*

	<b>Material Type I</b>
<b>Density</b> ( $\text{kg/m}^3$ )	<b>1600</b>
<b>Poisson ratio</b> ( $\nu$ )	<b>0.2</b>
<b>Modulus of Elasticity</b> $E$ (MPa)	<b>19.0</b>
<b>Shear modulus</b> $G$ (MPa)	<b>7.92</b>
<b>P-wave velocity</b> $C_p$ (m/s)	<b>114.87</b>
<b>Shear wave velocity</b> $C_s$ (m/s)	<b>70.34</b>
<b>Rayleigh wave velocity</b> $C_R$ (m/s)	<b>64.08</b>

The dynamic time increment for all the models is  $\Delta t = 1 \times 10^{-5}\text{ s}$ , which satisfies the stability and accuracy conditions. The responses are saved every ten time steps; hence:

$$\delta t = \text{Sampling time} = 1 \times 10^{-4}\text{ s} \quad \text{and} \quad \delta f = \text{Sampling frequency} = \frac{1}{\delta t} = 10\text{ kHz} \quad (6.2)$$

Thus, the Nyquist frequency is  $5\text{ kHz}$  ( $f_{Nyq} = 1/(2\delta t)$ ). The following sections present the numerical results along with the discussions. Mathgram 6-1 (Appendix B) shows the details of the calculations to assure the stability of the models. Mathgram 6-2 (Appendix B) explains the procedures followed for the calculations in time, frequency, and FK domains. Samples of the developed FLAC files are presented in Appendix C.

### 6.2.3 Normalization and characteristic wavelength

To generalize the results, all the responses are normalized to the maximum or minimum of the corresponding value from the model without void (model *S00\_01*). The concept of characteristic wavelength is also introduced as a benchmark for the measurement of time and distance. The characteristic wavelength should reflect the energy input to the medium, and the filtering effect of the medium. As explained in Chapter 5, the frequency spectrum of the applied source is altered by the medium. Figure 6-6 shows the cumulative energy content of the source, and the responses at a distance 3.992 *m* from the source (first receiver study *S00\_01*). It shows that lower frequencies (larger wavelengths) are filtered out by the medium. Therefore, a characteristic wavelength is defined as the wavelength corresponding to a 50% cumulative energy of the responses. The defined characteristic wavelength is a function of the source input energy, medium elastic properties, and the offset distance (the distance between first receiver and the source). Thus, characteristic wavelength ( $\lambda_{ch}$ ) for the defined configuration in model type *S00* is:

$$\lambda_{ch} = 0.36 \text{ m} \quad (6.3)$$

A characteristic time is defined as the time that it takes for the Rayleigh wave to travel a length equal to the characteristic wavelength. Hence, characteristic time ( $t_{ch}$ ) for material type I is:

$$t_{ch} = \frac{\lambda_{ch}}{C_R} = \frac{0.36 \text{ m}}{64.08 \frac{\text{m}}{\text{s}}} = 5.618 \times 10^{-3} \text{ s} \quad (6.4)$$

Therefore, in model type *S00*, the grid spacing ( $\Delta x = 0.008 \text{ m}$ ) is  $0.022\lambda_{ch}$ , the offset distance ( $D = 3.992 \text{ m}$ ) is  $11.1\lambda_{ch}$ , and dynamic time increment is  $1.8 \times 10^{-3}t_{ch}$ . In the following, the terms normalized depth, distance, and length are associated to the corresponding values divided by  $\lambda_{ch}$ . Similarly, normalized time is referred to the time divided by  $t_{ch}$ .

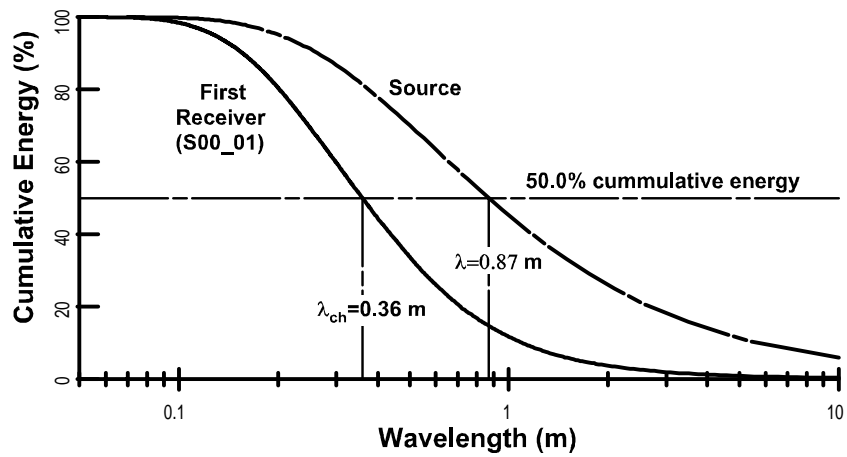


Figure 6-6: Variation of the cumulative energy of the applied source, and the first receiver responses with wavelength. The wavelengths are calculated based on the R-wave velocity of material type I ( $C_R = 64.08 \frac{m}{s}$ ).

## 6.3 Time responses

### 6.3.1 Surface responses

Figure 6-7 shows the time responses recorded at the surface of model S00\_01 (Homogeneous medium with no void). Figures 6-7a and c show the traces of horizontal (x) and vertical (z) responses recorded at different distances, respectively. The fluctuations at the end of the traces are associated to the reflections by the transition between the uniform to nonuniform grid. Same time responses are depicted in figures 6-7b and d in a contour format. The depicted values are normalized to the minimum of responses, thus the minimum value in each contour plot is equal to  $-1$ . In these contour plots the horizontal axis shows the time in seconds and the vertical axis shows the distance from source in metres. Thus, the slope of each event represent the parameter  $\frac{\Delta d}{\Delta t}$ , which is the apparent velocity of the event. In this case the measured apparent velocities of the first event and the following event are  $113.8 \frac{m}{s}$ , and  $64.23 \frac{m}{s}$ , respectively. These values are in good agreement with the theoretical p- and Rayleigh-wave velocities, associated to the medium (table 6.2). Body-waves attenuate faster with distance than R-waves (geometric damping); thus, as the result of the selected testing configuration, the amplitudes of the recorded p-waves are much smaller than the amplitudes of R-waves. For example, the ratio of maximum amplitude of the R-wave to the maximum amplitude of p-wave at the first receiver (in figure 6-7b) is 27. As the particle motion of p-wave is perpendicular to the direction of propagation, at surface the p-waves can be traced better in the horizontal responses (figures 6-7a and b). In the responses in z direction, only the Poisson ratio effect is visible. As s-wave and R-wave velocities are close ( $\frac{C_R}{C_s} = 0.91$ ), the large amplitude Rayleigh wave overshadows the arrival of s-waves in recorded responses.

Fig. 6-8a and b show typical contour plots of the horizontal and vertical normalized surface responses in the presence of a void. Dashed lines show projection of the void boundaries to the surface. For these typical results, the width of the void (b) is  $0.64 m \simeq 1.8\lambda_{ch}$  (model S00\_05), and the void's width to height ratio is equal to 8. The normalized amplitude values show that in the presence of a void the values change significantly. In this case the minimum values are more than doubled, though the changes in the maximum values are not conspicuous. Different events are marked on the figures by capital letters. Event 'A' shows the incident Rayleigh wave.

After the interaction between the incident Rayleigh wave and the near boundary of the void, part of the energy is reflected back. A considerable amount of the reflected energy is in the form of Rayleigh waves (event 'D1'); whereas, the rest is in the form of p-wave (event 'G1'). Event 'B' represents part of the incident energy that is transmitted into the region with void. This energy splits into three parts. One part travels faster than the other two, and its velocity is close to the p-wave velocity of the medium (this part is more conspicuous in figure 6-8a). Another part continues to travel with the Rayleigh wave velocity, and another part travels at a smaller velocity. When event 'B' encounters the void's far boundary, the p-wave part passes without any significant interaction, and it can be traced almost completely after the void. The Rayleigh wave transmits part of its energy beyond the void region (event 'C'), though interaction happens and part of it is transformed into p-wave (event 'G2') and part of it is reflected back from the far boundary. The slower part of event 'B' reflects back almost completely, and is trapped between the void boundaries (event 'E'). The measured velocity of event 'E' varies between 49.1 to 31.1  $\frac{m}{s}$  which is about 75% to 50% of the Rayleigh wave velocity of the medium. Thus, the velocity of the trapped energy decreases after each interaction with the boundaries. The measured velocities of event E corresponds to the velocities of anti-symmetric Lamb waves traveling on a slab of equal thickness as the top of the void. The propagation of Lamb waves on the top of the void is also suggested by results in the frequency domain; which are discussed in following sections. This trapped energy bounces back and forth between the void boundaries, until it attenuates completely. Part of this attenuation is due to geometrical damping and part of it is due to late interactions with the boundaries that cause energy transfer beyond the void region (events 'D2' and 'F'). Both events 'D2' and 'F' are in the form of Rayleigh waves. In figures 6-8a and b, event 'H' corresponds to the incident p-wave, which traverse the medium almost without any significant interaction with the void. Experiments with different void sizes and embedment depths confirm these observed trends. Experiments with different void sizes and embedment depths confirm the observed trends. For brevity, the results of the other models are presented in Appendix CD-Chapter6.

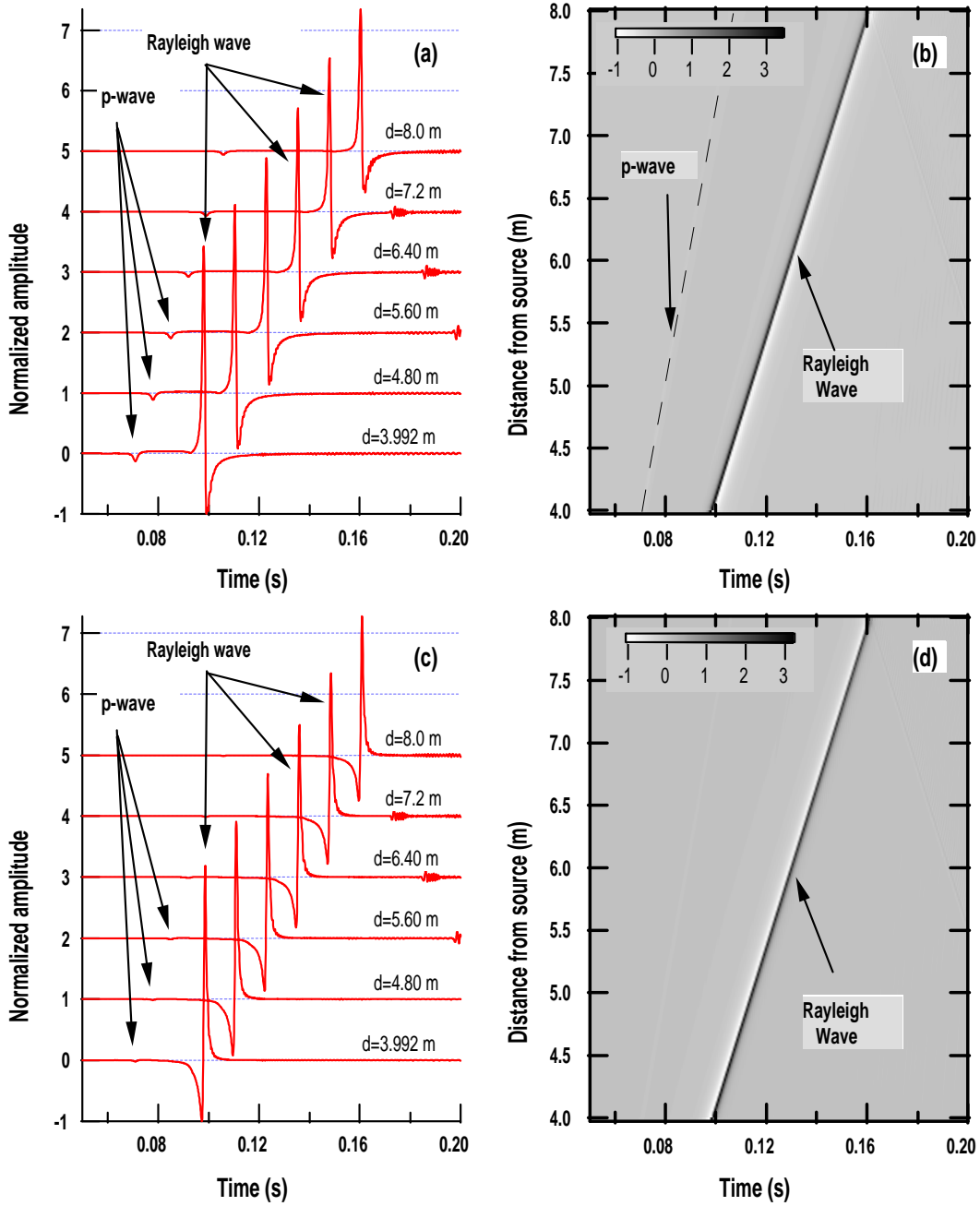


Figure 6-7: Time responses at the surface of model S00-01. Figures (a) and (c) show time traces of normalized vertical and horizontal responses. Figures (b) and (d) show the corresponding the contours of normalized horizontal and vertical time responses at the surface.



The normalized group velocities at the surface are depicted in Figure 6-9. The velocities are normalized to the Rayleigh wave velocity of the medium ( $C_R$ ). The group velocities are calculated as:

$$V_z = \frac{d_z}{\Delta t_z} \quad (6.5)$$

where  $d_z$  is the distance between receiver number  $z$  and the first receiver, and  $\Delta t_z$  is the time difference between the maximum response at receiver number  $z$  and the maximum response at the first receiver. Theoretically, the measured velocities should be equal to the Rayleigh wave velocity, i.e. a normalized value equal to 1. The values are in good agreement with the theory. Smooth curves are used to eliminate numerical errors. The changes in the graph can be associated to near-field effect. Up to the near boundary of the void (dashed line) there is a good agreement between the results for the void and no void cases. Over the void (between the dashed lines), a drop in the group velocity is observed, with the maximum difference close to the far boundary of the void. After the void, the group velocity increases again, though even after a distance of about two times the width of the void it is not still regained its original value.

### 6.3.2 Responses inside the medium

If the surface of a homogeneous half-space is excited by a point load, Rayleigh waves are generated. These waves propagate as a cylindrical front, with their base at the surface and centered at the location of point load. If they are recorded along vertical lines inside the medium the observed responses should show one event at a specific time. On the other hand, body waves propagate as a spherical front. If they are recorded along a vertical line inside the medium, they arrive to the top of the line sooner than to the bottom of it, i.e. their records inside the medium should look like a curved event. Figure 6-10 (a, b, and c) shows the responses (in  $z$  direction) inside the model S00\_01 (homogeneous medium) along vertical lines V2, V3, and V4. All the responses are normalized to the maximum of the response recorded along line V1, from model S00\_01. In each plot, the arrival of Rayleigh waves is observed as a strong event in time, with its maximum at the surface. The curved lines in each plot show the arrival of incident s-waves. Because of the chosen time frame, the arrival of p-waves is not seen. Figure

6-10 (e, f, and g) shows the normalized time responses recorded in a medium with void (model S00\_08). Before the void, along the line V2 (plot 'e'), the incident wave arrivals are seen along with late reflections in the form of Rayleigh waves. Along lines V3, and V4 (plots 'f' and 'g'), the Rayleigh wave arrival are also clearly seen at the surface. The arrival of the incident Rayleigh wave is delayed, and is more spread in time than in the corresponding cases without void. Other visible events are the curved lines below the void, based on their arrival times, these lines are associated to the generated body waves, specially p-waves. In a homogeneous medium the amplitudes should decrease with distance due to geometric damping (in plots 'a', 'b', and 'c' the maximum amplitudes are less than one). Though, the void cause the maximum amplitudes increase and the minimum ones decrease over and after the void (plots 'f' and 'g', respectively).

Similar trends are observed in the responses along arcs inside the medium (Figure 6-11). Plots 'a' and 'b' correspond to the homogeneous medium (S00\_01), and plots 'c' and 'd' correspond to the responses in the presence of a void (model S00\_09). In each plot, events **A**, and **B** show the theoretical arrival time of the s- and Rayleigh waves, respectively. Due to the interaction of Rayleigh waves with void, reflections from both the near and far boundaries of the void occur. In plot 'c', events **C** and **D** correspond to reflections from near and far boundaries of the void. The amplitudes of these reflections are small in comparison with the amplitudes of the incident Rayleigh wave. Theoretically, the time difference between the two events is related to the width of the void. Theoretical arrival times of the reflections from near and far boundaries of the void to arc R1 are computed as:

$$\text{Near boundary: } t_{near} = \frac{2 \times 5.272 - 4.684}{64.08} + 0.036 = 0.127s = 22.6t_{ch} \quad (6.6a)$$

$$\text{Far boundary: } t_{far} = \frac{2 \times 5.912 - 4.684}{64.08} + 0.036 = 0.147s = 26.2t_{ch} \quad (6.6b)$$

where 5.272 *m* and 5.912 *m* are distances from source to the near and far boundaries of the void, respectively. The value 0.036*s* is the time for the maximum amplitude of the source, 64.08 is the Rayleigh wave velocity of the medium, and  $t_{near}$  and  $t_{far}$  are the arrival time of the Rayleigh wave to the nearest and farthest boundaries of the void to the source, respectively.

The direct measurement of the time of event '**C**' shows a good agreement with  $t_{near}$  (plot 'c'). Though, the measured time for event **D** is  $0.149s = 26.5t_{ch}$ , which is about 1.5% larger than  $t_{far}$ . This difference is produced by the lower velocity of the reflected wave, while traversing the void. Therefore, if the time difference between the two reflections is used for the calculation of the void width, some errors are involved, which will increase with the increase of the width of the void. Further, various experiments show that as the width of the void decreases, it is more difficult to separate the two events. Plot 'd' (after the void) shows that the arrival of Rayleigh wave is delayed (event **B1**) with respect to the theoretical arrival time (event **B**). This observation confirms that existence of a void affects the R-wave velocity in the void region. Event **E** which is curved toward the direction of propagation of the wave, is an indication of generated body waves.

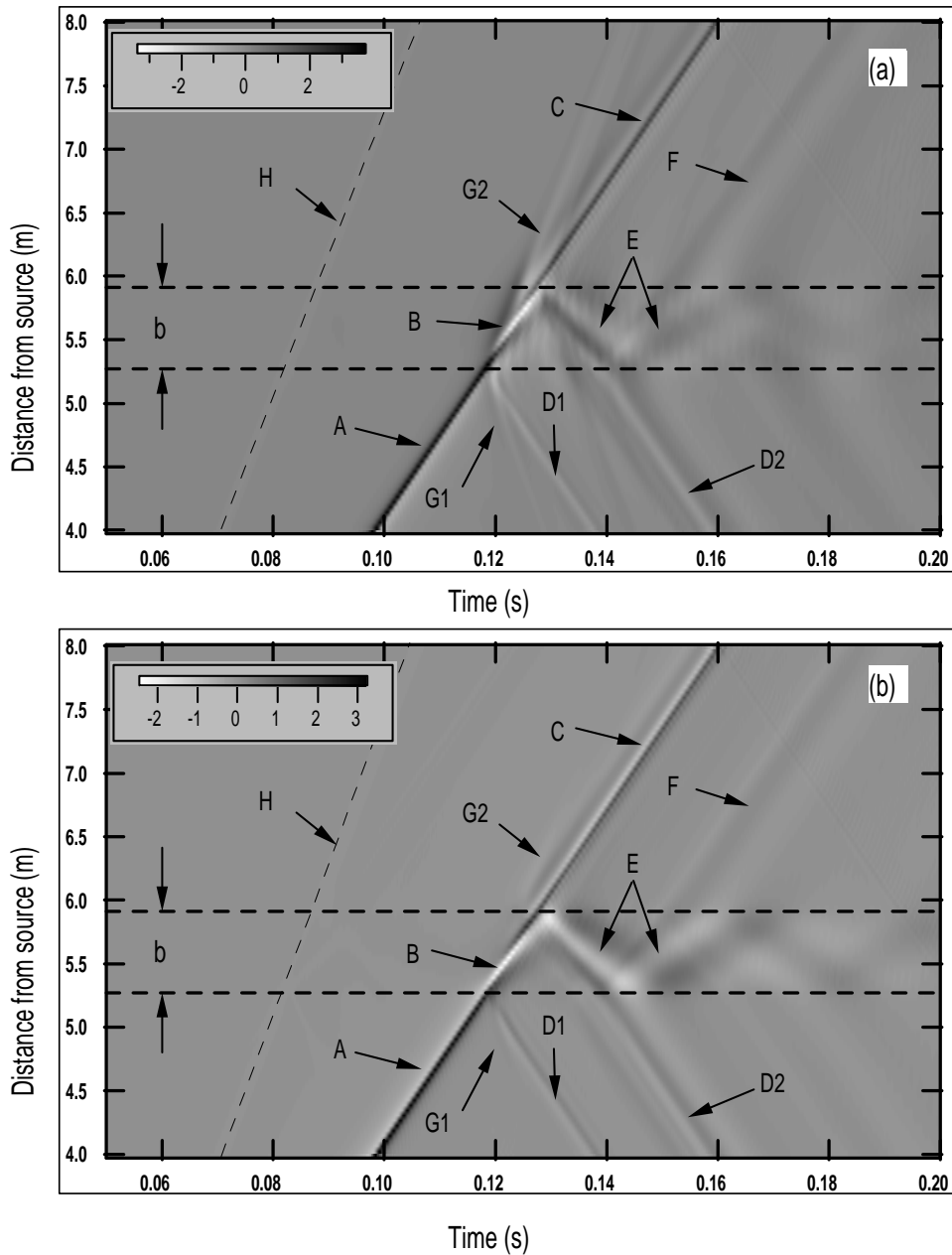


Figure 6-8: Time responses along the surface of model S00\_05. Figure (a) shows the horizontal (x) responses and figure (b) shows the vertical (z) responses. All the responses are normalized to the corresponding responses of model S00\_01. The dashed lines show the projection of the void boundaries to the surface. Different events are marked with capital letters.

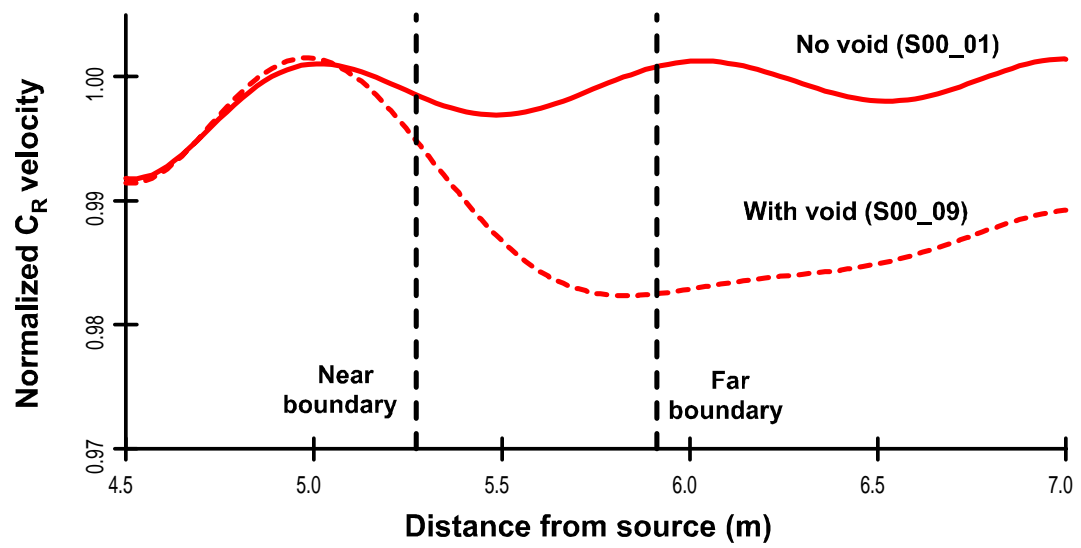


Figure 6-9: Group velocities measured at the surface of the models. Dashed lines show the boundaries of the void.

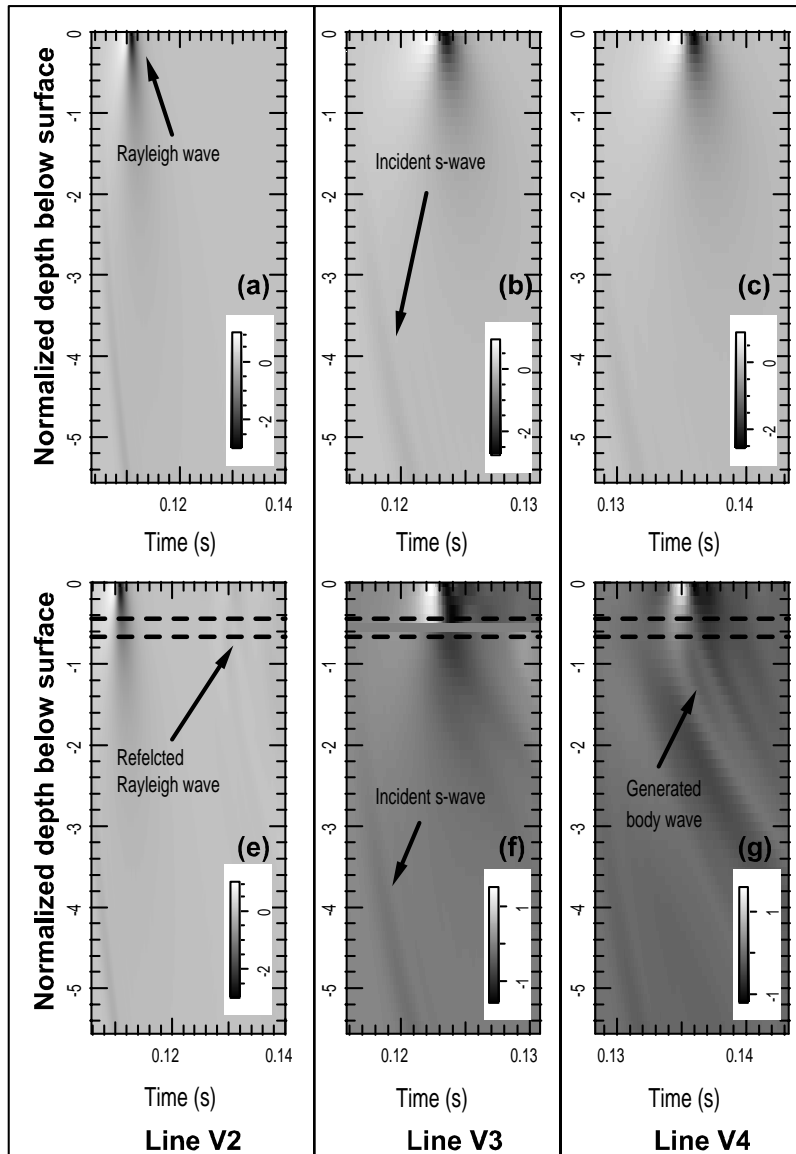


Figure 6-10: Normalized time responses (in z direction) along vertical lines inside the medium. Plots (a), (b), and (c) correspond to the responses of model with no void (S00\_01). Plots (e), (f), and (g) correspond to the responses of a model with void (S00\_08). The horizontal dashed lines show the top and bottom boundaries of the void. Line V3 passes through the void, and lines V2 and V4 are located before, and after the void respectively.

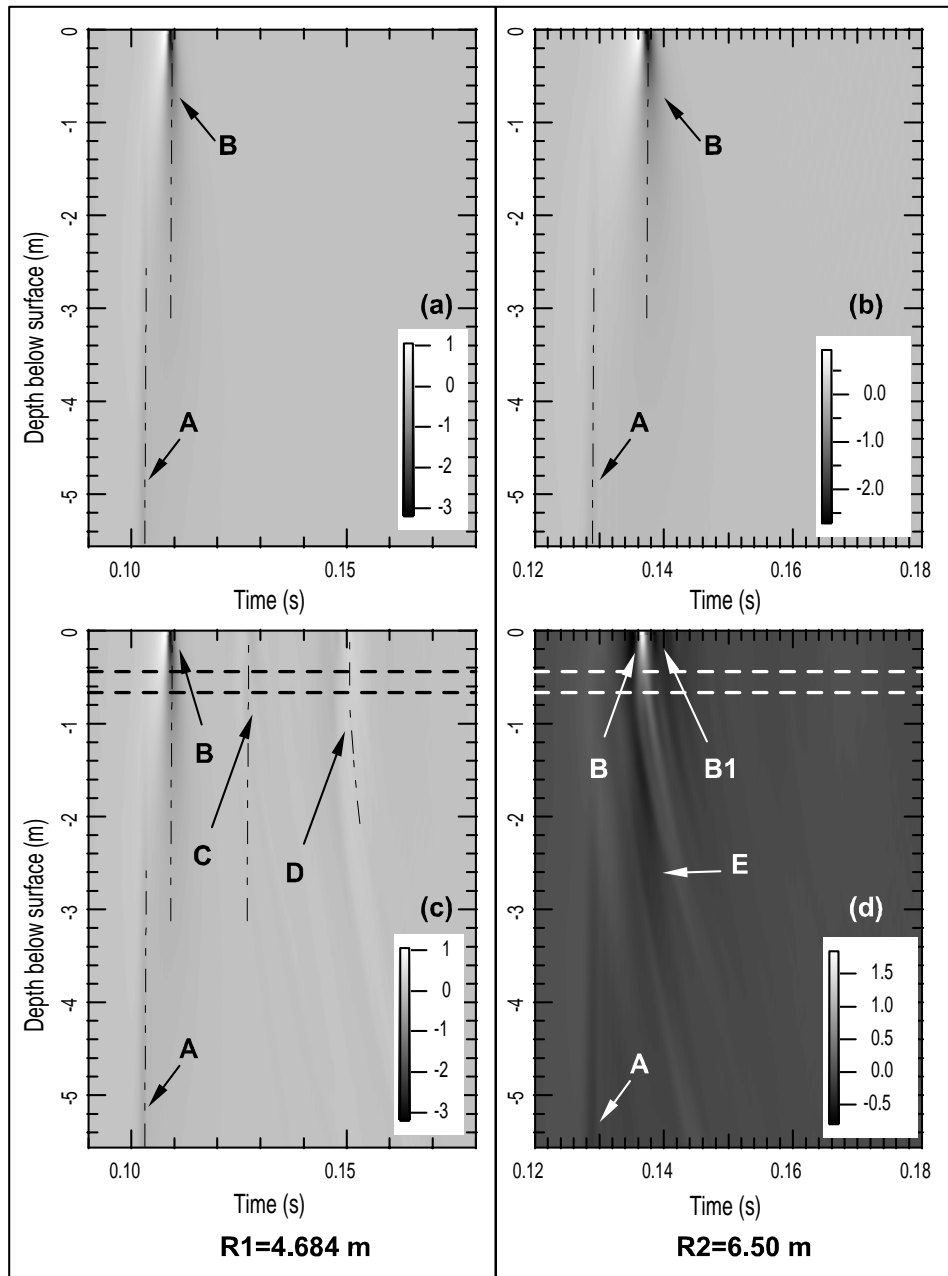


Figure 6-11: Normalized time responses ( $z$  direction) along arcs inside the medium. Plots (a) and (b) correspond to model S00\_01, and plots (c) and (d) correspond to the void case (S00\_09). The responses are normalized to the maximum of the records along arc R1 (plot a). Dashed lines show the top and bottom boundaries of the void. Different events are named with capital letters. Same events in different plots are named with the same letter. The void is centered at  $R=5.592$  m.

## 6.4 Frequency responses

### 6.4.1 Surface responses

Figure 6-12 shows the frequency content of the recorded surface responses in studies S00\_01 and S00\_13. All the frequency amplitudes are normalized to the maximum of the amplitudes in S00\_01. Plots 'a' and 'b' show typical traces recorded at different locations (different  $d$ ) along the surface. In a homogeneous media (plot 'a') the traces are smooth and their shape does not change with distance, though their amplitude decreases as they go farther from the source. The peak energy occurs at a frequency of about  $100 \text{ Hz}$ , i.e. a wavelength of  $0.6408 \text{ m} = 1.78\lambda_{ch}$  ( $\lambda = \frac{C_R}{f}$ ). If this is compared to the frequency content of the source (6-3), it can be concluded that the medium filters some low frequencies. In the presence of void -plot 'b'- the spectra are distorted. Different shapes of the frequency spectra indicate that the medium is dispersive. Further, the change in the amplitudes is not uniform with distance. Contour plots of the same data are depicted in plots 'c' and 'd'. A comparison of these contour plots show that in the presence of the void ripples occur in the responses before the void. According to Fourier theory, these ripples show the presence of reflections in the recorded data ([133]). The ripples are curved and are closer to each other at larger frequencies. The distance between the consecutive ripples is a function of the time delay between the main signal and its reflection - i.e. the larger the delay the closer will be the ripples to each other. Thus, the ripples in plot 'd' point out that different frequencies are reflected back from the void with different delay times. In the region over the void, energy concentrations are observed and two main energy concentrations are conspicuous. The first one corresponds to a frequency of  $27 \text{ Hz}$  ( $\lambda = 2.67\text{m} = 7.42\lambda_{ch}$ ) and the second one to a frequency of  $174 \text{ Hz}$  ( $\lambda = 0.37\text{m} = \lambda_{ch}$ ). The latter value is close to the embedment depth of the void, though the former value could not be associated to any meaningful parameter. However, if the velocity of a Lamb wave propagating at the top of the void is used ( $V_L = 34.0 \frac{\text{m}}{\text{s}}$ ), this frequency ( $f = 27 \text{ Hz}$ ) exactly represents the period of the trapped energy at the top of the void (event 'E', 6-8). Similar trends are observed in other models (see Appendix CD-Chapter6). In the region right after the void, a significant attenuation is observed. Measured amplitudes ('c', and 'd') show that in the region over the void higher amplitudes are recorded. This confirms that in the presence of void, not only energy



concentration occurs, but also amplification or attenuation happens in certain frequency ranges.

#### 6.4.2 Responses along vertical lines inside the medium

To evaluate the penetration depth of the energy the data from line V1 of study S00\_01 are used to calculate the cumulative energy at different depths. the cumulative energy is calculated as:

$$CE_d = \frac{\sum_{above} A^2}{\sum_{depth} A^2} \quad (6.7)$$

where  $CE_d$  is the cumulative energy above the depth  $d$ ,  $\sum_{depth} A^2$  is the square of the spectrum area summed over the total length of line V1, and  $\sum_{above} A^2$  is the square of the spectrum area over the length above depth  $d$ . Figure 6-13 shows the cumulative energy verses normalized depth. About 50% and 95% of the energy is concentrated at a depth less than depths of  $0.26\lambda_{ch} \simeq 0.1m$  and  $2.5\lambda_{ch} \simeq 0.9m$ , respectively. Therefore, most of the energy of the propagating wave is concentrated in regions close to the surface. The decrease of energy with depth explains the smaller interaction of the voids with the incident wave at larger depths.

Figure 6-14 shows the frequency spectra of the responses along vertical lines inside the medium. Plots 'a' to 'e' corresponds to medium without void (S00\_01). The difference in the amplitudes in these plots are small, and the trends of the plots are almost the same. As expected, these plots show that the penetration depth of each frequency decreases with the increase in frequency. To express this fact quantitatively, the total energy of each frequency ( $f_j$ ) along line V1 is calculated ( $Etot_j$ ). Similarly, the total energy of each frequency along line V1, up to selected arbitrary depths are calculated ( $Etot_{_d_j}$ ). The ratio of the latter value to the former value is always smaller than one, and gives an estimation of the penetration depth of each frequency. Thus. it is found that about 90% of the energy of each frequency is confined to a depth that is equal to about 1.5 times the wavelength of that frequency ( $1.5\lambda_j$ ). Consequently, it is expected that each frequency ( $f_j$ ) to interact with inhomogeneities that are embedded within  $1.5\lambda_j$  below surface.

Figure 6-14( 'f' and 'j') corresponds to study S00\_06 ( $a = b = h = 0.16 m = 0.44\lambda_{ch}$ ). The top and bottom boundaries of the void are marked on figures by solid lines. The ripples in

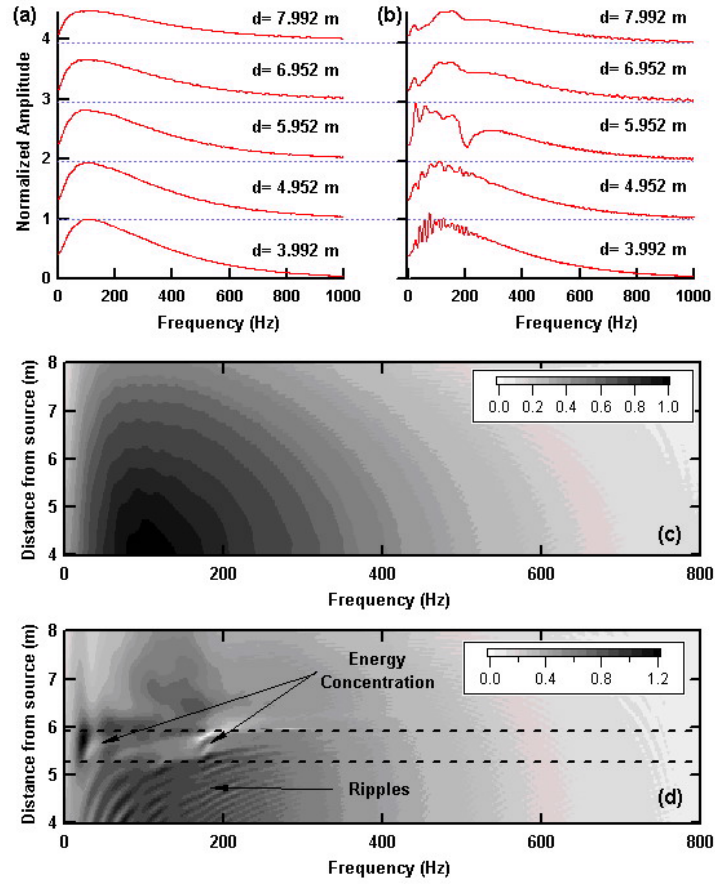


Figure 6-12: Frequency spectra at the surface of the medium. Plots (a) and (c) correspond to study S00\_01, and plots (b) and (d) correspond to study S00\_13 ( $a = 0.08 \text{ m}$ ,  $b = 0.64 \text{ m}$ ,  $h = 0.32 \text{ m}$ ). The parameter  $d$  in plots (a) and (b) represents the distance of the recording point from the source. The dashed lines in plot (d) show the projected boundaries of the void to the surface. In the contour plots the horizontal axis is frequency and vertical axis shows the distance from source.

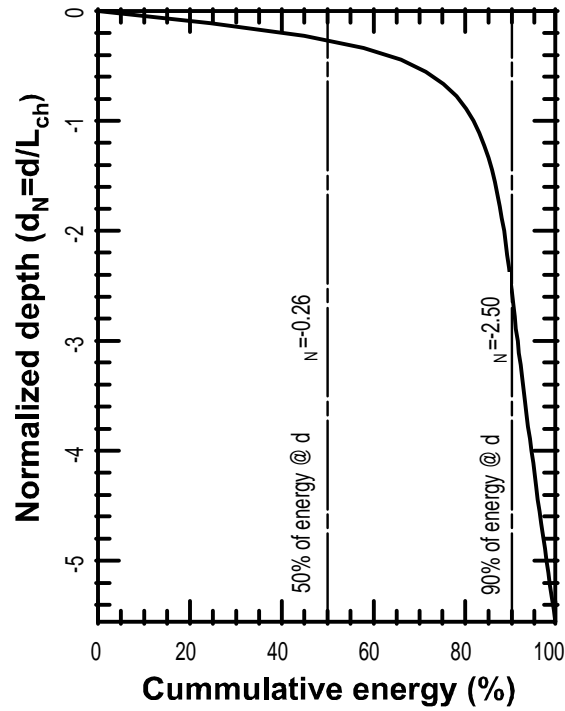


Figure 6-13: Cumulative energy versus normalized depth, along lone V1 (S00\_01). The depth is normalized to the characteristic length ( $L_{ch}$ ).

the responses before the void (plots 'f' and 'g') are an indication of waves reflected back from the near boundary of the void. The ripples in plot 'f' are closer to each other than in plot 'g', because line V2 is closer to the void than line V1, and the delay time of reflections is shorter for line V2 than V1. Plots 'a', 'b', 'f', and 'g' show that in the presence of a void larger amplitudes are recorded - up to 60% larger in this case. Plot 'c' corresponds to the middle of the void; therefore, zero energy is recorded at the depths between the top and bottom boundaries of the void. A region with high energy concentration is present in this plot. The central frequency of this region is about  $100 \text{ Hz}$  ( $\lambda = 0.64m = 1.78\lambda_{ch}$ ), which is close to the central frequency of the incoming wave (figure 6-12). The frequency spectra recorded after the void (plots 'i' and 'j') show that the presence of a void decreases the bandwidth and the amplitude of the recorded energy. This means that the void filters the energy of some frequencies and attenuate the energy of other frequencies. Further, the energy recorded below the void is considerably

larger than in the other plots.

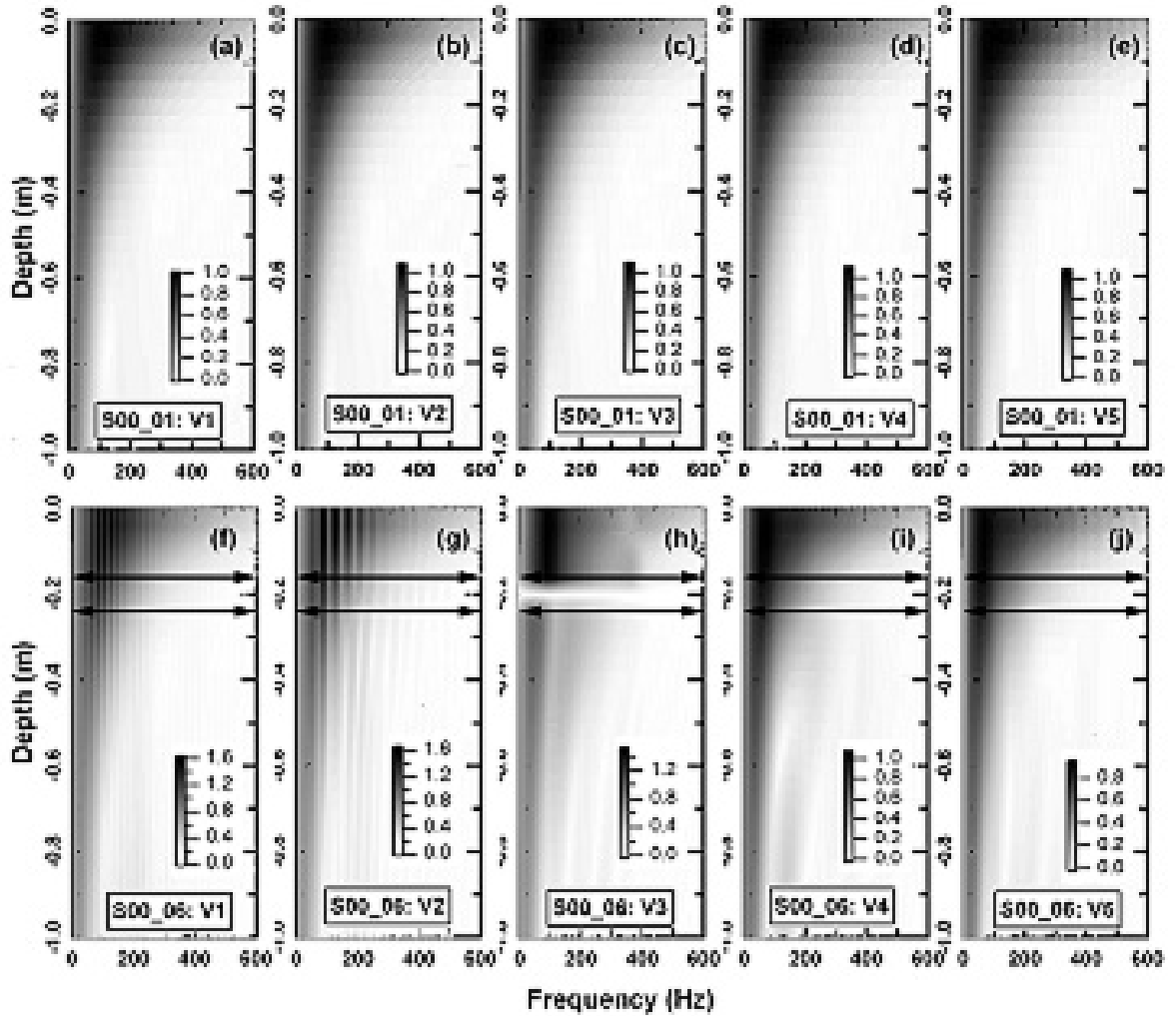


Figure 6-14: Frequency spectra of the responses along vertical lines inside the medium. Plots (a) to (e) correspond to model S00\_01 (half space without void), and plots (f) to (j) correspond to model S00\_06. The values are normalized to the corresponding values in S00\_01. In each plot the horizontal axis is frequency in Hz, and the vertical axis is normalized depth below surface. The solid arrows show the location of the top and bottom boundaries of the void.

## 6.5 2D Fourier transforms

A powerful technique to study the seismic responses is the two dimensional Fourier transforms. In the 2D Fourier transforms, data from the time-distance domain (t-d domain) is mapped to frequency-wavenumber domain (f-k domain). A simple way to calculate the 2D Fourier transform is to compute the standard transform of the time-domain data first, and then of the space-domain data ([133]). Mathgram 6-2 provided in Appendix B shows the procedure followed in this work to obtain the 2D Fourier transforms.

In the following examples, the sampling rates in frequency and wavenumber are  $\delta f = 0.61$  Hz and  $\delta k = 0.0977 \frac{1}{m}$ , and the Nyquist frequencies are  $f_{Nyq} = 5.0$  kHz and  $k_{Nyq} = 12.5 \frac{1}{m}$ , respectively. As explained in Chapter 3, the ratio between  $\omega$  and  $k$ , defines a velocity. In these cases the defined velocity is:

$$V_{\text{lim}} = \frac{\omega_{Nyq}}{k_{Nyq}} = \frac{f_{Nyq} \times 2\pi}{k_{Nyq}} = \frac{5000 \times 2\pi}{12.5} \simeq 2500 \frac{m}{s}$$

The velocity  $V_{\text{lim}}$  gives a measure to distinguish between the events aliased in frequency and the ones aliased in wavenumber domain. Therefore, the events with a velocity less than  $2500 \frac{m}{s}$  will get aliased in wavenumber domain sooner than in frequency domain; whereas, the events with a velocity larger than  $2500 \frac{m}{s}$  will get aliased in frequency domain sooner than in wavenumber domain.

Figure 6-15 depicts the normalized 2D Fourier responses for models S00\_01, and S00\_12. Plots 'a' and 'b' show the 2D Fourier transforms of horizontal and vertical components of the homogeneous medium (model S00\_01). The values are normalized to the maximum of each plot. Chapter 3 showed that in the 2D Fourier plots events with different propagation directions will show up in different quadrants. Thus, events **A** and **B** are propagating in the same direction. The event **A** corresponds to the incident Rayleigh wave ( $C_R = 64.08 \frac{m}{s}$ ) and event **B** corresponds to the incident p-wave ( $C_p = 114.0 \frac{m}{s}$ ). The linearity of event A shows that there is no numerical dispersion for the frequency-wavenumber range depicted in these figures [122]. As the horizontal components of p-waves at the surface are larger than their vertical components (vertical component is solely due to the Poisson effect), event **B** is more conspicuous in plot 'a' than in plot 'b'. In both plots, the effect of noise is observed. This noise is associated

to reflections from physical boundaries and the ones imposed by discretization of the medium. Plots 'c' and 'd' correspond to a void case ( $a = h = 0.32 \text{ m} = 0.89\lambda_{ch}, b = 0.08\text{m} = 0.22\lambda_{ch}$ ). In each plot, four events are observed. Events **A**, and **B** are the same as explained before. Events **C**, and **D** are located in the second quadrant, which shows waves traveling in a direction opposite to events **A**, and **B**. Event **C** travels with a velocity close to Rayleigh wave velocity of the medium ( $V_C = 63.8\frac{m}{s}$ ), thus it can be associated to the Rayleigh wave reflected from the void. The amplitude of the reflected wave (event **C**) is smaller than the amplitude of incident wave (event **A**), which shows that only part of the incident Rayleigh wave is reflected. The velocity of event **D** ( $V_D = 113.5\frac{m}{s}$ ) is close to the p-wave velocity of the medium . A qualitative comparison of the amplitudes of events **D** and **B** shows that they are almost in the same order of magnitude, thus event **D** can not be only associated with the reflection of incident p-wave (event **B**). Event **D** can also be associated with the p-waves generated due to the interaction of incident Rayleigh wave (event **A**) with the void. This interpretation is consistent with the observations in time domain, as explained in previous sections.

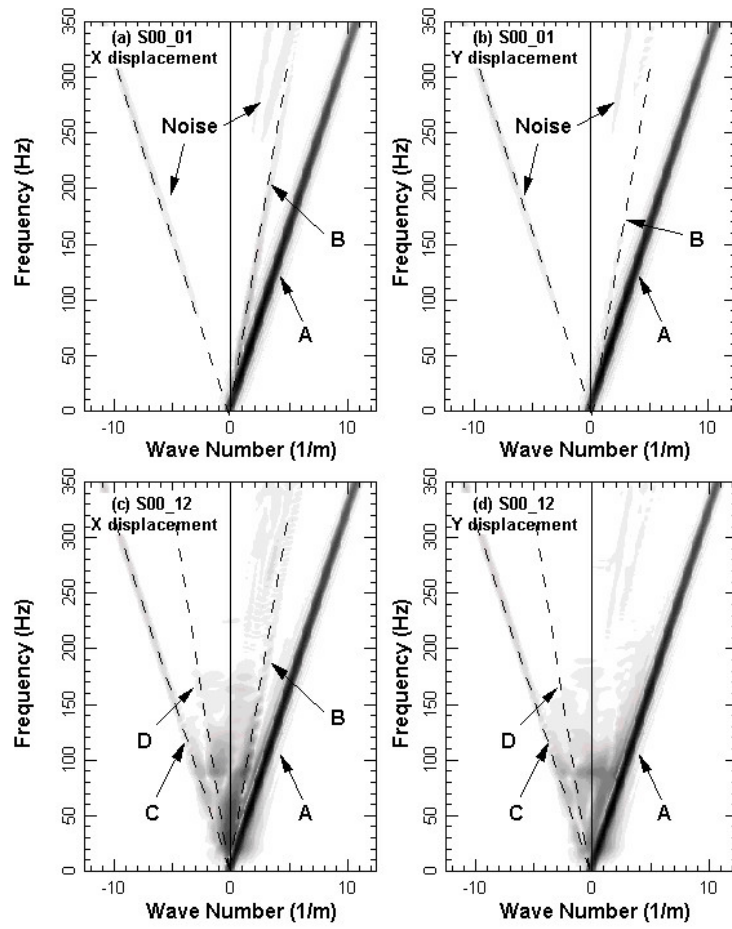


Figure 6-15: 2D Fourier amplitudes of surface responses. Homogeneous medium (plots a, and b), and medium with void (plots c, and d).



## 6.6 Discussions

The observations presented in the previous sections, along with the ones in Appendix CD-Chapter6, show that a void interacts with the incident Rayleigh waves, and p-waves to a minor extent. To comprehend the nature of this interaction, the displacements around the void are recorded in time domain, and the corresponding frequency contents are evaluated. As a basis for comparison, the responses around an imaginary boundary, similar to the void boundary, inside a homogeneous medium (model S00\_01) are also recorded.

Figure 6-16 shows the contour plots of the displacements in time domain around the imaginary boundary in model S00\_01 (plots 'a', and 'c'), and around the void in model S00\_09 (plots 'b', and 'd'). The height of the void is  $a = 0.08 m = 0.22\lambda_{ch}$ , the width of the void is  $b = 0.64 m = 1.78\lambda_{ch}$ , its embedment depth is  $h = 0.16m = 0.44\lambda_{ch}$ , and its width to height ratio is  $R = 8$ . This high value of R is selected to study the effect of void rather than the effect of the depth of the top and bottom boundaries.

Again, the responses are normalized to the maximum of the corresponding displacements in model S00\_01, thus the maximum of responses in plots 'a', and 'c' are equal to 1. The boundaries of the void (bottom, near, top, and far) are marked with dashed lines. Plots 'a' and 'b', and in plots 'c' and 'd' show that, in general, the displacement in the presence of void are larger than the corresponding responses in homogeneous model. In these plots, event **A** shows the arrival of p-waves to the void. The amplitude of the p-wave is small with respect to the amplitudes of Rayleigh wave, the p-wave does not cause significant interactions with the void, thus its effect is not clearly seen in either of the plots 'b' or 'd'. Events **B** (**B-bot**, **B-near** and **B-top**) show the arrival of Rayleigh wave to the void. The Rayleigh wave front is cylindrical, thus its arrival to the near and far boundaries of the void is observed as a single event in time (vertical line event **B-near**). Correspondingly, its arrival to the top and bottom boundaries of the void is observed as an inclined line (events **B-bot** and **B-top**). Events **B-bot** and **B-top** show that the incident Rayleigh wave energy causes the top boundary of the void to vibrate. This vibration is seen as event **E** in both plots 'b' and 'd'. This vibration lasts for a relatively long time ( $t = 10.2t_{ch}$ ) with respect to the duration of the main event ( $t = 0.87t_{ch}$ ). Due to the interaction of Rayleigh wave with the near boundary of the void, part of the energy is transformed into p-waves waves (event **C**). The incident Rayleigh wave show minor dispersion

(spread in time), which is better observed when comparing events **B-bot** in plots 'a' and 'b'. The void causes some frequencies to travel with lower velocities. Events **D1** and **D2** show the reflection of the incident wave from the far boundary. The trace of the reflections can be seen at later times, indicating that some of the incident energy is trapped in the void region and bounces back and forth between the boundaries until it is attenuated. Also, the induced displacements at the top side of the void are larger and last longer than at the bottom boundary. The effect of almost all of these events can be seen at the surface as explained in previous sections of this chapter.

Figure 6-17 shows contour plots of the frequency spectra of the z displacements around the void boundaries (models S00\_01, and S00\_09). In plot 'a' (no void case) the variation of the contours are smooth and more energy is spread along the top side of the region. The variation of spectra is similar to the ones observed at the surface (figure 6-12). Whereas, in plot 'b', void case, a region with high energy concentration is observed almost at the middle of the top boundary (event **A**) and along the left boundary, though the amplitudes at the top are larger. This concentrated energy is associated to the effect of the trapped energy, which was observed in the time domain plots (figure 6-16). The effect of reflection is seen on both top and bottom boundaries as ripples. High frequencies are less present at the bottom than at the top boundary; because, the penetration depth of higher frequencies is smaller than the penetration depth of lower frequencies (plot 'a'). Also, part of this attenuation can be associated to the filtering effect of the void (plot 'b'). Event **B** in plot 'b', shows another energy concentration along the top boundary. The main frequency of this event is equal to  $350 \text{ Hz}$ , with a wavelength equal to  $0.18 \text{ m}$  ( $0.5\lambda_{ch}$ ). This wavelength is very close to the embedment depth of the void ( $0.16 \text{ m}$ ). Thus, not only the shape of the void, but also the embedment depth of the void, affects the wave propagation.

To better understand the vibration of the void, the deformation of the void is depicted in time domain in figures 6-18 to 6-21. Each figure consists of four snapshots that show the surface responses along with the deformation of the void at the same time. For comparison, in each plot the undeformed shape of the void is also shown with dotted lines. The plots 'a' to 'p' are in timed sequence. Before the arrival of the main event (plot a) the void is in its initial undeformed shape. Upon the arrival of the wave, the void starts to deform, with a pattern similar to the

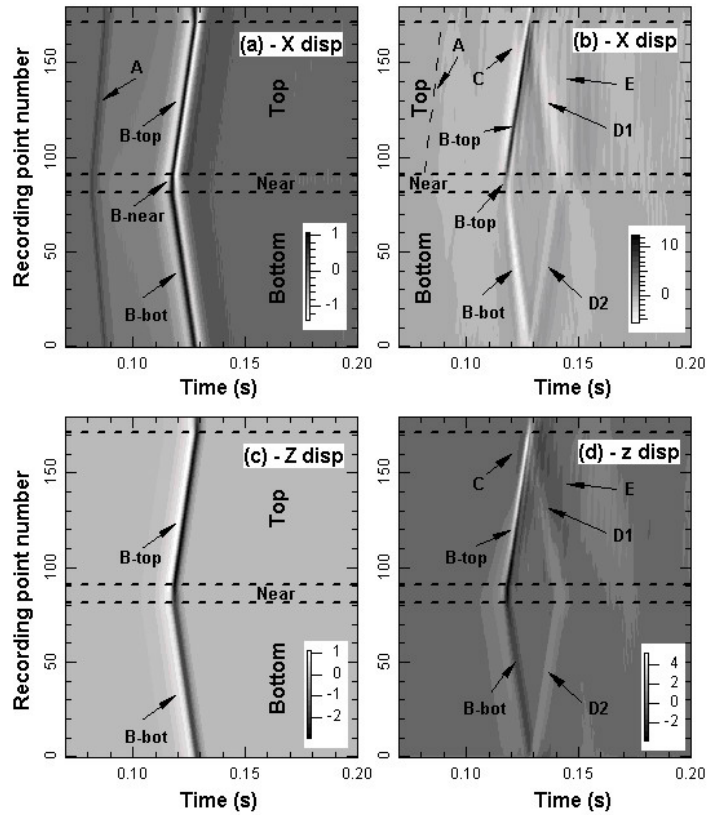


Figure 6-16: Time responses recorded around and imaginary boundary (S00\_01) and a void (S00\_09). Dashed lines show the limits of the boundaries of the void. The void numbering sequence is shown in figure 6-5c. Plots a, and c correspond horizontal (x) and vertical (z) displacements in model S00\_01, respectively. Plots b, and d correspond to the horizontal (x) and vertical (z) displacements in model S00\_09, respectively. For comparison, the responses are normalised to the corresponding responses in model S00\_01.

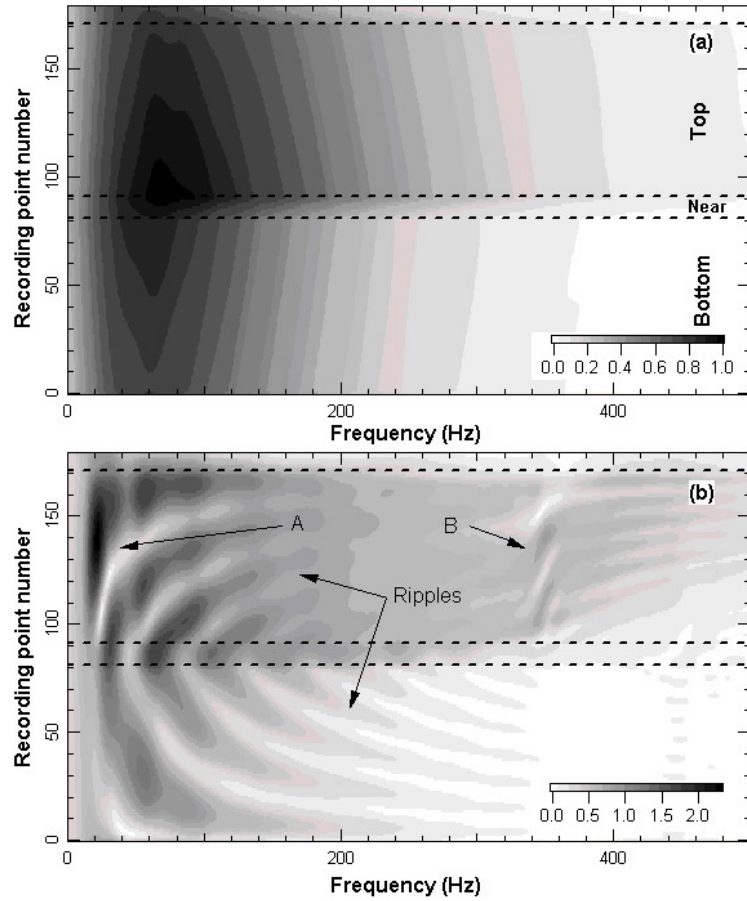


Figure 6-17: Frequency responses around the void. Dashed lines show the void boundaries. The numbering of recording points is shown in figure 6-5c. Plots a, and b correspond to vertical ( $z$ ) displacements in models S00\_01 and S00\_09, respectively. For comparison, the responses in both plots are normalized to the maximum of S00\_01.

general pattern of the incident wave (plots 'b', 'c', and 'd'). The void starts to interact with the wave, and part of the incident energy reflects back and part of it is transmitted (plots 'd', and 'e'). The void causes some frequencies slow down, while the others travel with the same velocity (dispersion). This dispersion results in a distortion in the surface responses (plots 'e' to 'g'). When the incident energy hits the far boundary of the void again part of the energy reflects back and part of it travels beyond the void boundary (plots 'g' and 'h'). At this time, almost all of the void is vibrating, although the incident energy has passed (plots 'i' and 'j'). Vibration of the void, for a relatively long time after arrival of the incident wave, proves that the void traps part of the energy. This trapped energy bounces back and forth between the void boundaries until it is damped. Each time that this trapped energy hits the void boundaries, part of it is transferred beyond the void region (plots 'j' to 'p'). Therefore, late reflections are observed in the surface responses.

## 6.7 Summary of the conclusions

This chapter investigated the interaction between a void and Rayleigh wave in a homogeneous half-space. A commercial finite differences package FLAC was used to simulate the propagation of Rayleigh wave. The numerical models were calibrated against theoretical solutions to assure the quality of the obtained data. The surface responses of the medium were studied in combination with the responses along vertical and horizontal lines, and arches inside the medium, and around the void.

The concept of characteristic wavelength was introduced to generalize the results. The introduced characteristic wavelength is a function of the frequency content of the source, as well as the medium properties. The characteristic wavelength is used to describe the limits of the observations.

The responses in time, frequency, and f-k domains showed that the void interacts with the incident Rayleigh wave. The extents of this interaction depends on the void size, and embedment depth, as well as the frequency content of the incident energy. The void starts to vibrate in response to the Rayleigh wave excitation, which causes energy partitioning. Part of the energy is reflected toward the source in the form of Rayleigh waves. The interaction of the

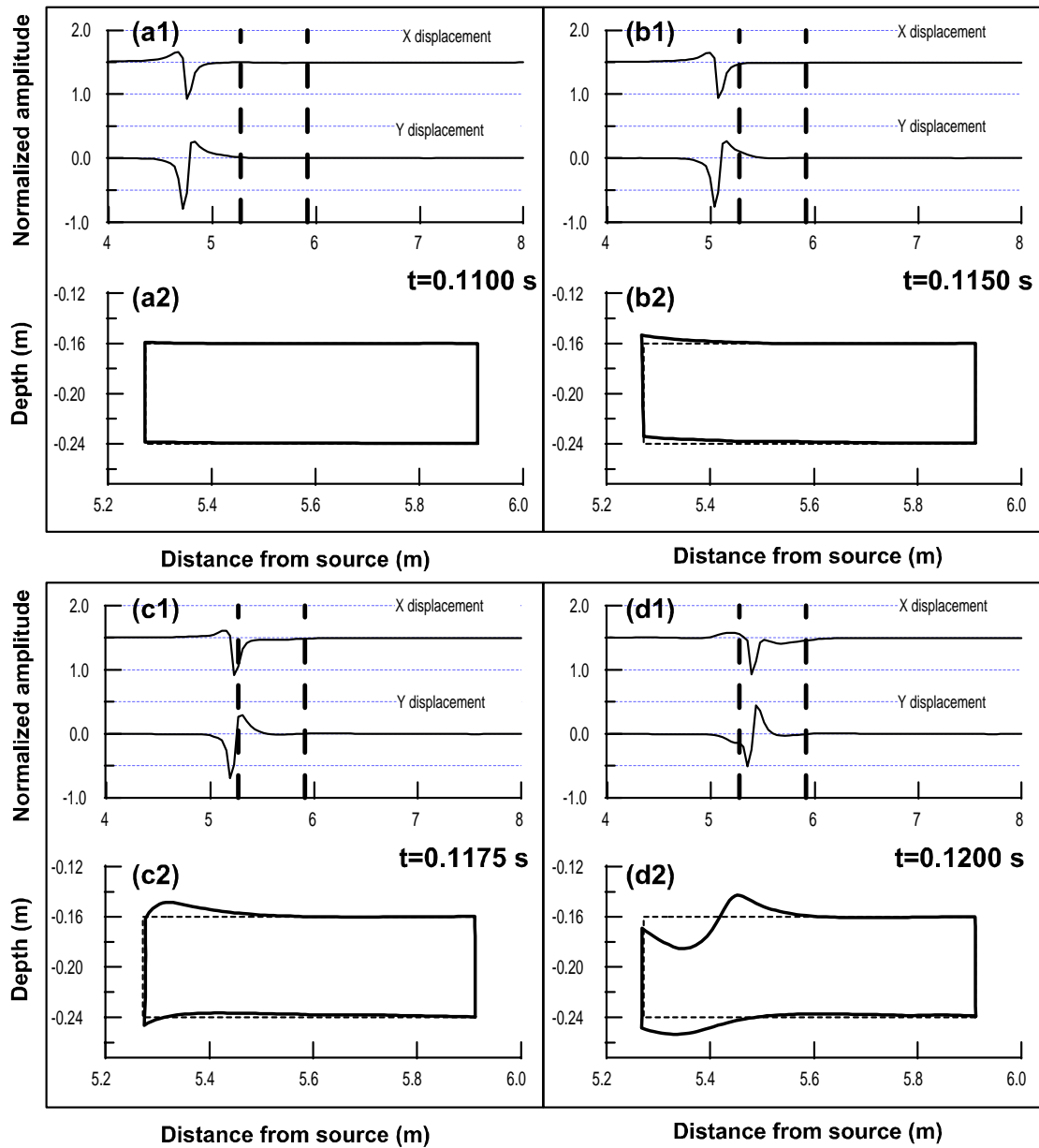


Figure 6-18: Surface displacements and void deformations at times  $t = 0.11s$  to  $t = 0.12s$ . In the figures a1 to d1 correspond to the surface responses in which the horizontal axis is distance from source and vertical axis shows the normalized amplitudes. The vertical dashed lines show the projected boundaries of the void. Plots a2 to d2 shows the corresponding deformed shape of the void, where the horizontal axis is the distance from source and vertical axis is the depth below surface. The associated time is shown in each figure.

incident energy with the near and far boundaries of the void causes the conversion of part of the energy into body waves. The body waves are mostly in the form of p-wave and propagate inside the medium. Another part of the energy is trapped in the void region. The velocity of this part of energy decreases as it bounces back and forth between the void boundaries. The studies showed that this energy is in the form of antisymmetric Lamb wave that is produced in the upper part of the void. The effect of the trapped energy is seen as energy concentration in the vicinity of the void, in frequency domain. The dispersive effect of the void is also observed.

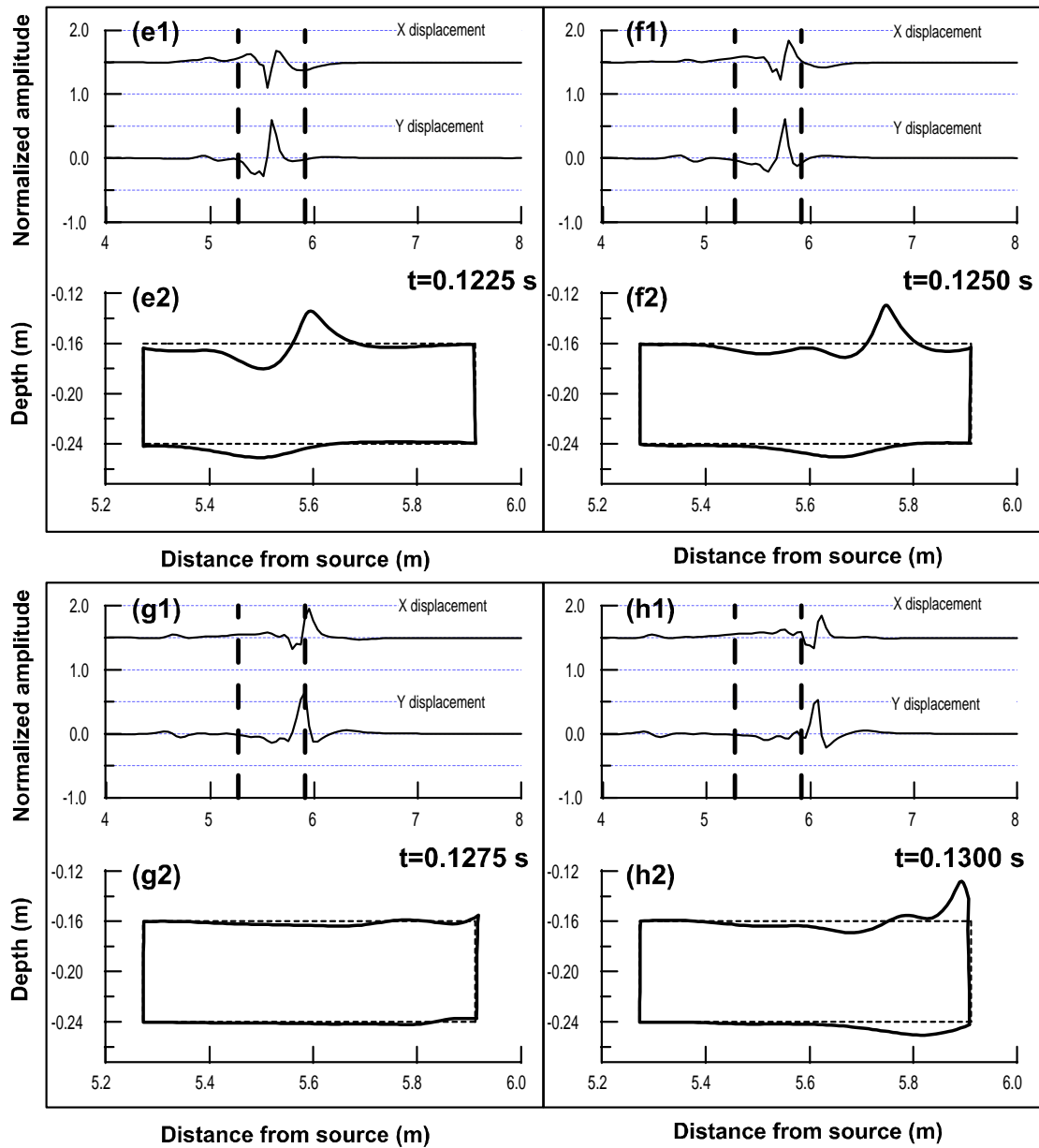


Figure 6-19: Surface displacements and void deformations at times  $t = 0.1225s$  to  $t = 0.13s$ . In the figures e1 to h1 correspond to the surface responses in which the horizontal axis is distance from source and vertical axis shows the normalized amplitudes. The vertical dashed lines show the projected boundaries of the void. Plots e2 to h2 shows the corresponding deformed shape of the void, where the horizontal axis is the distance from source and vertical axis is the depth below surface. The associated time is shown in each figure.



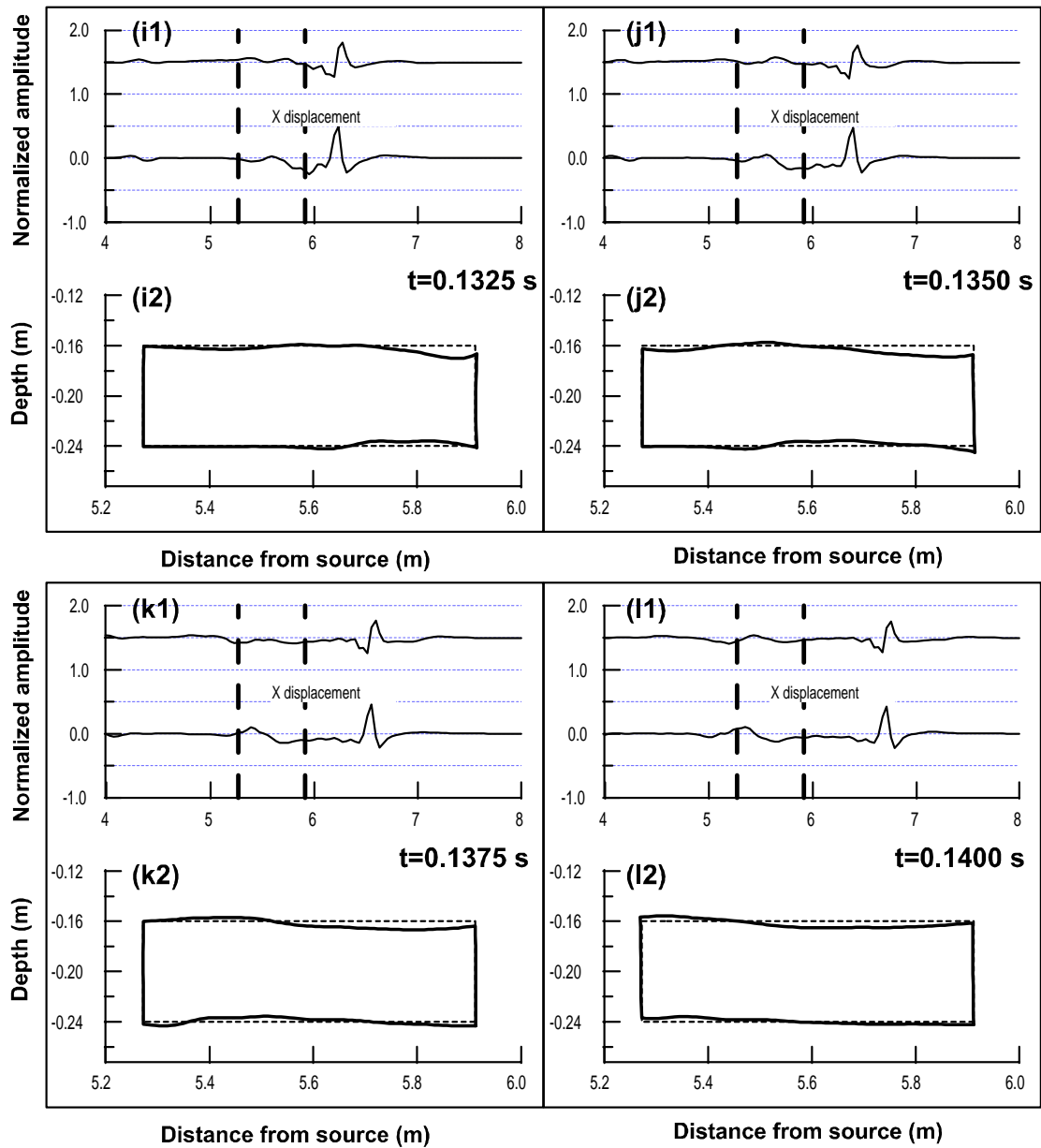


Figure 6-20: Surface displacements and void deformations at times  $t = 0.1325s$  to  $t = 0.14s$ . In the figures i1 to l1 correspond to the surface responses in which the horizontal axis is distance from source and vertical axis shows the normalized amplitudes. The vertical dashed lines show the projected boundaries of the void. Plots i2 to l2 shows the corresponding deformed shape of the void, where the horizontal axis is the distance from source and vertical axis is the depth below surface. The associated time is shown in each figure.

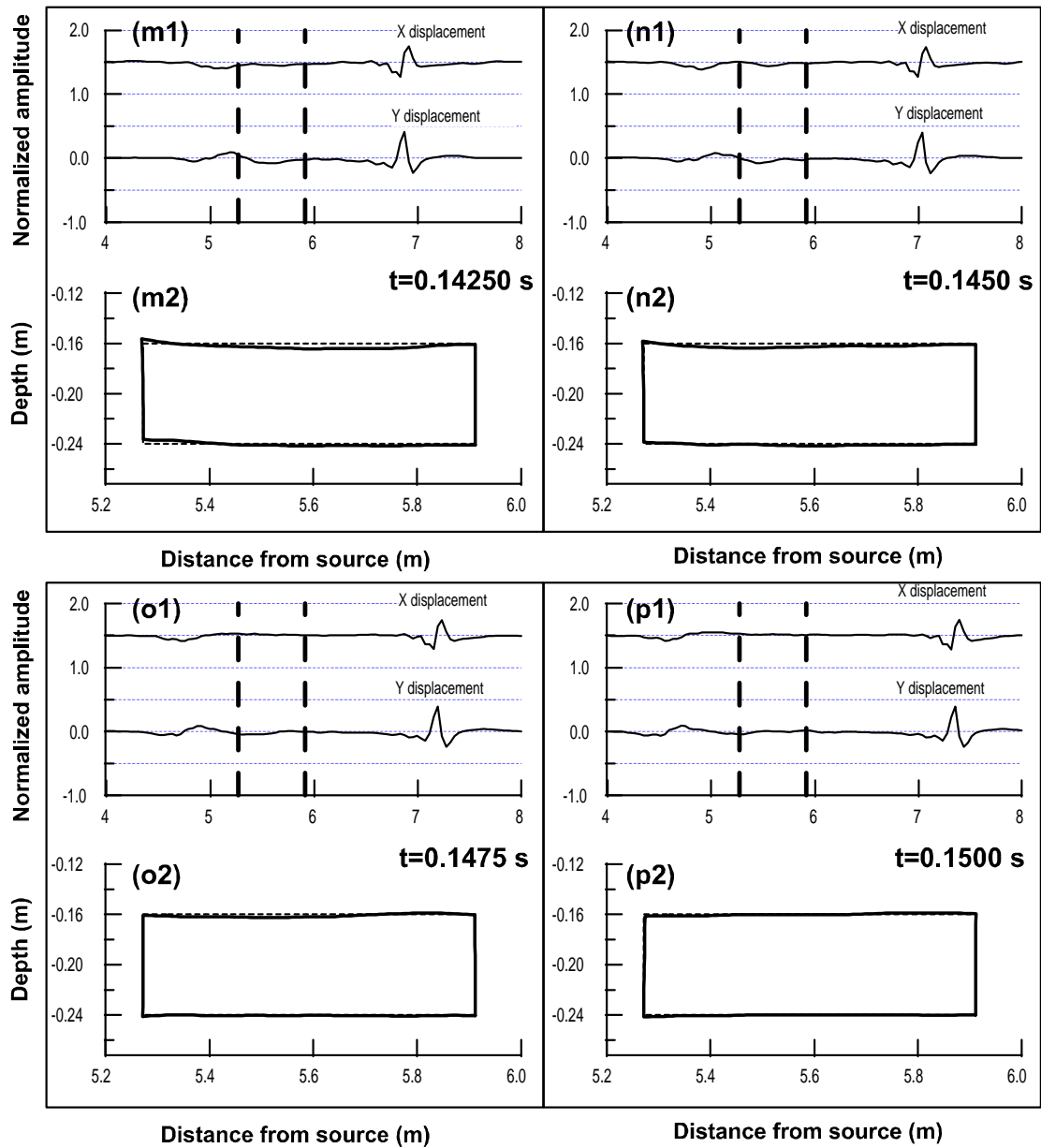


Figure 6-21: Surface displacements and void deformations at times  $t = 0.1425s$  to  $t = 0.15s$ . In the figures m1 to p1 correspond to the surface responses in which the horizontal axis is distance from source and vertical axis shows the normalized amplitudes. The vertical dashed lines show the projected boundaries of the void. Plots m2 to p2 shows the corresponding deformed shape of the void, where the horizontal axis is the distance from source and vertical axis is the depth below surface. The associated time is shown in each figure.

## Chapter 7

# Effect of cavity properties on surface responses

### 7.1 Introduction

In Chapter 6, it was shown that cavities interact with propagating Rayleigh waves. This interaction causes distortions in surface responses in time and frequency domains. It was proved that in the presence of a void the medium is dispersive- i.e. different frequencies traverse the medium with different velocities. Although, the provided studies and discussions are generally valid for any void, the extent of the interaction depends on the geometrical and mechanical properties of the void and the medium. The objective of the studies presented in this chapter is to show that how various medium and void properties affect the surface responses of a medium in the presence of a void. To be able to find the correlations between the properties and observed responses, different properties are considered separately. This chapter is organized as follows:

- Section 7.2 discusses the effect of width of the void on the surface responses(case 1)
- Section 7.3 explains the effect of depth of the void on surface responses (case 2)
- Section 7.4 presents the methodology used to investigate the surface responses in the presence of a void in a layered system. Further, the concept of characteristic wavelength is extended for the layered systems.

- Section 7.5 investigates the effect of medium with two layers - Natural Layering: Soft layer overlying bedrock (case 3)
- Section 7.6 considers the effect of medium with two layers - Inverse Layering: Stiff layer overlying soft layer (case 4)
- Section 7.7 discusses the effect of lateral dimension of the void - 3D effect of the cavity (case 5)

The numbering system for the models developed for void in half-space (cases 1 and 2) are as introduced in chapter 6. For the rest of the cases the numbering system will be introduced in the corresponding sections. In this chapter sample plots are provided to show the trends. A complete set of colored plots corresponding to each study number is provided in Appendix CD-Chapter7.

## 7.2 Effect of width of the void (case 1)

Figure 7-1 shows contour plots of the vertical displacements recorded at the surface of four different models. In each plot the vertical axis shows the distance from source in meters, and horizontal axis shows the time in seconds. In all the models the depth to the top of the void is  $0.16\text{ m}$  ( $0.44\lambda_{ch}$ ), and the height of the void is  $0.08\text{ m}$  ( $0.22\lambda_{ch}$ ). The width of the void is  $0.08\text{ m}$  ( $0.22\lambda_{ch}$ ),  $0.16\text{ m}$  ( $0.44\lambda_{ch}$ ),  $0.32\text{ m}$  ( $0.88\lambda_{ch}$ ), and  $0.64\text{ m}$  ( $1.78\lambda_{ch}$ ) in plots 'a', 'b', 'c', and 'd', respectively. All the responses are normalized to the maximum of vertical responses recorded at the surface of study number S00\_01 (half-space with no void). It is seen in all the plots that when the Rayleigh wave encounters the void, it interacts with the near boundary of the void. Due to this interaction part of the energy is reflected back and part of it is transformed into p-waves (events 'A' and 'B'). The amplitude of these first reflections are almost the same in all the plots. Thus it is concluded that the width of the void does not have any effect on the first interaction of the void and the incident wave. As the width of the void increases from plot 'a' to plot 'd', the width of event 'A' increases. This is due to the interaction of void with the far boundary. In case that the width of the void is small, the time difference between the reflections from near and far boundaries are relatively small. Therefore, the latter is seen as

a continuation of the former. When the width of the void increases two separate events are observed, each related to a reflection from a boundary - i.e. events 'A' and 'C' in plot 'd'.

The interaction of the incident wave with the far boundary becomes stronger as the width of the void increases. This fact results in generated p-waves (event 'D'), and reflected waves (event 'E') at the location of far boundary, which can be seen in plot 'd'. This effect gets weaker in other plots. It is seen that events 'F' and 'C' become wider in time as the width of the void increases. Widening of these events indicate that the void emanates energy or vibrates for a longer time, when the width of the void increases. Therefore, wider voids trap more energy. Comparing the amplitudes of the surface responses shows that in the presence of wider voids the maximum amplitude of the responses also increase. The latter can be associated to the larger amount of energy trapped in the void region.

To demonstrate the effect of the width of the void on frequency responses, the frequency content of the eight different models are depicted in figures 7-2 and 7-3. All the models have the same properties as the ones shown above for time domain responses, except that the models in figure 7-3 have a larger embedment depth of  $0.32 \text{ m}$  ( $0.88\lambda_{ch}$ ). Again, the vertical axis is the distance from source in meter, and horizontal axis is frequency in Hz. All the contours are normalized with respect to the maximum frequency amplitude of model S00\_01 (half-space with no void). Event 'A' in all the plots shows the ripples before the void, which corresponds to the effect of reflections in time domain - as explained in the previous chapters. In figure 7-2 the relative amplitude of the ripples decreases with the increase in void width up to plot 'c', and increases in plot 'd'. Conversely, the relative amplitude of event 'B', which is the energy amplification over the void, increases from plot 'a' to 'c' and decreases in plot 'd'. This observation indicates that the vibration of the void in plot 'c' is stronger than in the rest of the cases. In figure 7-3 the relative amplitude of the ripples and the energy concentration, respectively decrease and increase from plot 'a' to plot 'd'. The latter indicates that in this case void vibration is stronger in plot 'd'. Strong void vibrations indicate that more energy is trapped in the void region, thus the responses over the void overshadow other events. The above observations show that the combination of void width and its embedment depth determines the amount of the energy that is trapped by the void. In both figures, event 'B' gets narrower in frequency, and shifts toward lower frequencies as the width of the void increases. The

interpretation is that the void tends to vibrate with its natural frequencies. As the void size increases its natural frequencies shift toward lower frequencies. Meanwhile, as shown in the previous chapter, most of the energy of the incident wave is concentrated in lower frequencies. Therefore, larger voids interact more with the incident wave and trap more energy. In general, when the incident wave carries enough energy in the frequency ranges that resonate with the void, strong interactions occur, which is seen as regions with energy concentration over the void. In this case the width of the region with energy concentration will be very close to the width of the void.

Another event that is observed in some of the cases (plots 'b' to 'd' in figure 7-2 and plots 'c' and 'd' in figure 7-3) is event 'E'. This event is concentrated around frequency 350 *Hz* in figure 7-2, and around frequency 175 *Hz* in figure 7-3. The corresponding wavelengths are  $\lambda = \frac{64.08}{350} = 0.18m$  ( $0.5\lambda_{ch}$ ) and  $\lambda = \frac{64.08}{175} = 0.37m$  ( $1.0\lambda_{ch}$ ). The latter values are very close to the embedment of the voids which are 0.16 *m* ( $0.44\lambda_{ch}$ ) and 0.32 *m* ( $0.88\lambda_{ch}$ ), respectively. This observation shows that a relatively strong interaction occurs between the void and the incident wave in the frequencies corresponding to the embedment depth of the void. In general, it is concluded that events 'B' and 'C' define a bandwidth in which most of the interactions occur. For voids, that their width is larger than their embedment depth, the lower limit of this bandwidth is determined by the void width, and the upper limit of the bandwidth is influenced by the embedment depth of the void. This observation will be taken further in the next section of this chapter.

For the wide void (Fig. 7-13), energy concentration happens over the void; which have spectral amplitudes larger than the amplitudes of the ripples before the void. In this case, the width of the energy concentration region is close to the width of the void. The low frequency associated with the energy concentrations ( $f = 25$  *Hz*, Fig. 7-13c and d) corresponds to a large wavelength  $\lambda = 2.56$  *m* for a Rayleigh wave. The pulse introduced into the medium has low energy at this wavelength (less than 2%). Thus, it is unlikely that an R-wave is responsible for the spectral amplifications over the void. However, a Lamb wave with velocity  $C_L = 31 \frac{m}{s}$  has a wavelength  $\lambda = 1.24$  *m*, which is close to two times the width of the void. This wavelength is required to produce amplifications on a slab fixed at both ends ( $\lambda = 2w/i$ , where *i* is an integer  $i=1, 2, 3, \dots$  [12]). Therefore, the frequency domain data confirms the observations on

time domain results about the propagation of Lamb waves over the void.

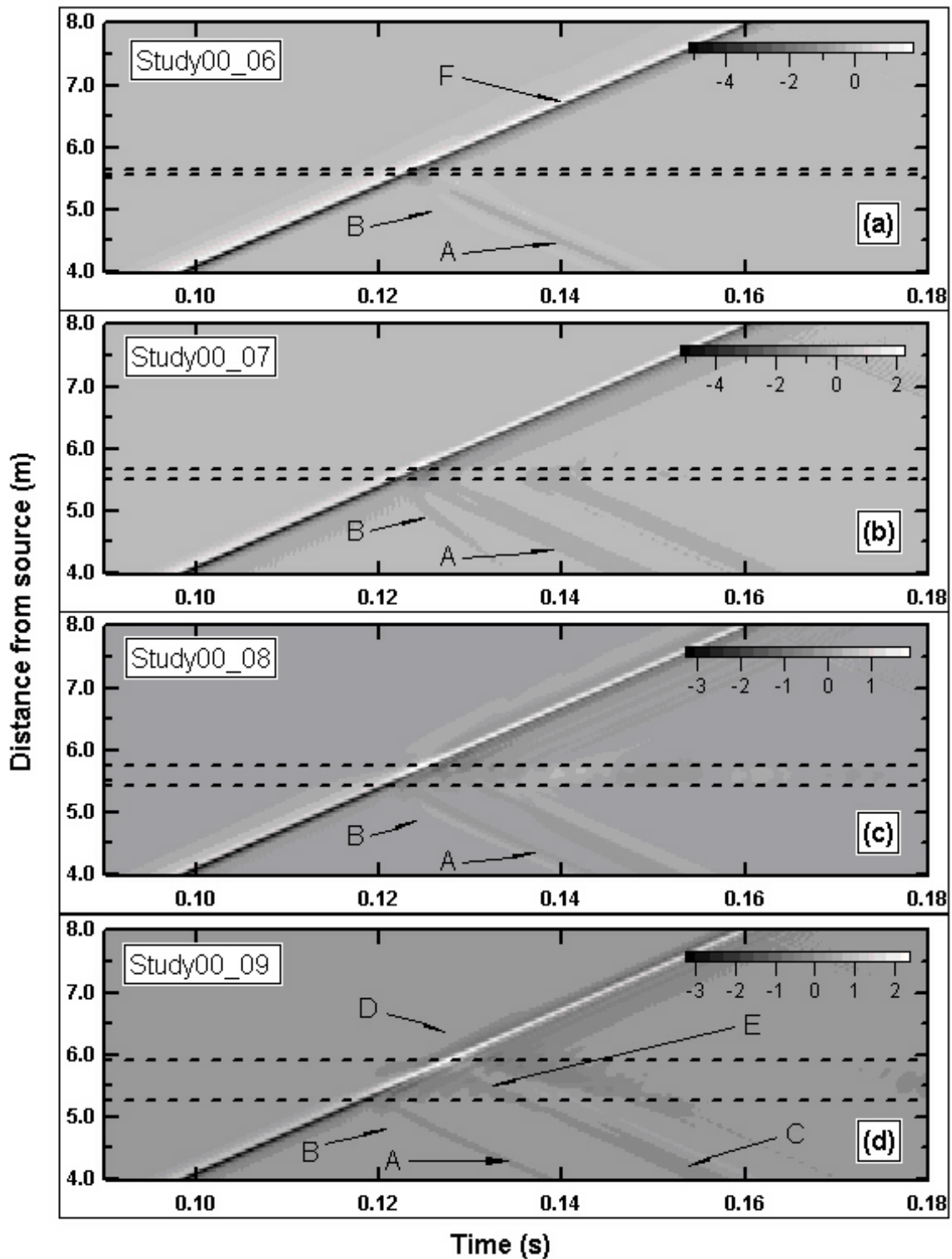


Figure 7-1: Effect of the void width on the surface responses. Plots 'a' to 'd' show the contour plots of the vertical responses recorded at the surface of models. The corresponding model number is shown on each plot. All the responses are normalized to the maximum vertical displacement recorded at the surface of study S00\_01 (model with no void). Dashed lines show the boundaries of the void projected to the surface.



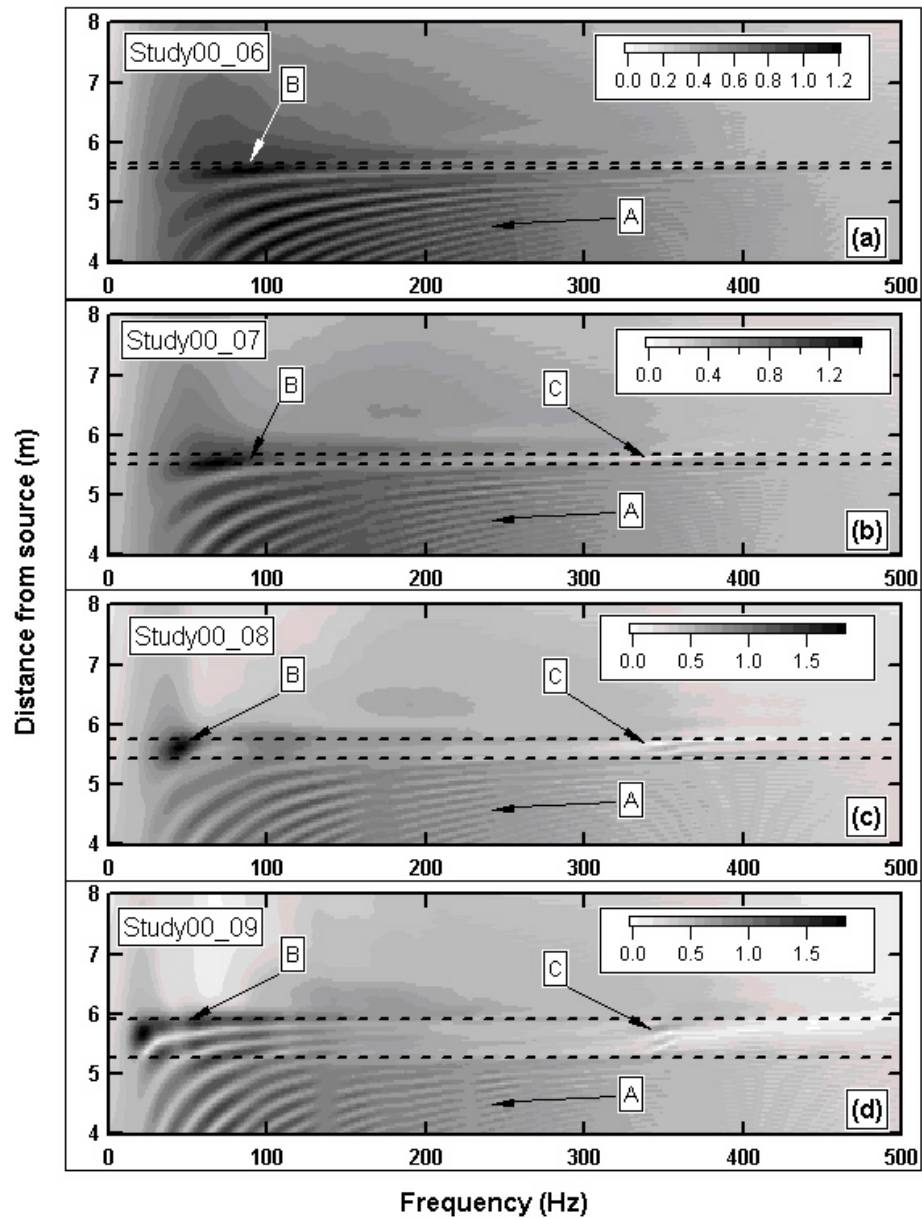


Figure 7-2: Effect of the width of the void on the frequency content of surface responses. Plots 'a' to 'd' show the contour plots of the frequency content of the vertical responses recorded at the surface of models. The corresponding model numbers is shown on each plot. All the responses are normalized to the maximum of the frequency content of the vertical displacements recorded at the surface of study S00\_01 (model with no void). Dashed lines show the boundaries of the void projected to the surface.

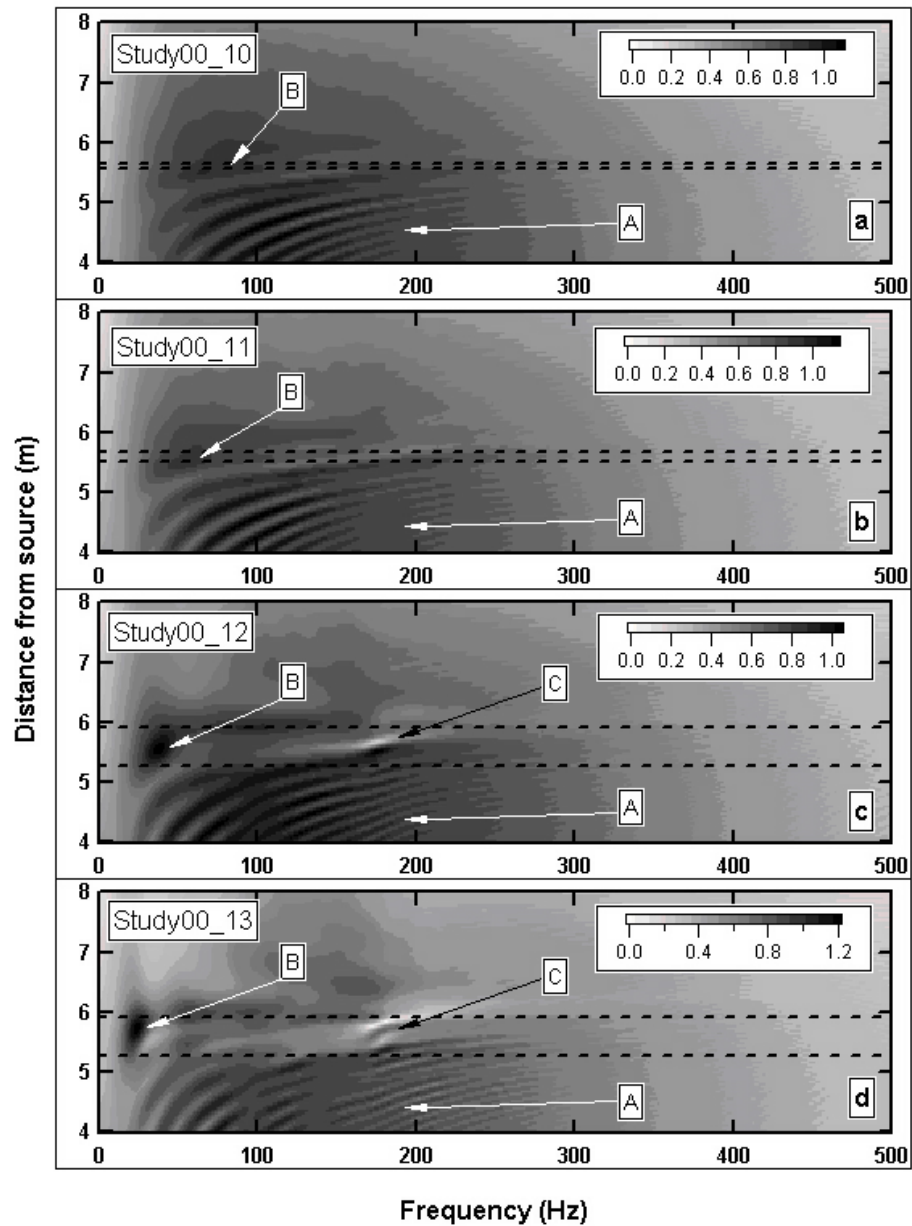


Figure 7-3: Effect of the width of the void on the frequency content of surface responses. Plots 'a' to 'd' show the contour plots of the frequency content of the vertical responses recorded at the surface of models. The corresponding model numbers is shown on each plot. All the responses are normalized to the maximum of the frequency content of the vertical displacements recorded at the surface of study S00\_01 (model with no void). Dashed lines show the boundaries of the void projected to the surface.

### 7.3 Effect of depth of the void (case 2)

An important parameter that influences the effect of the void on surface responses is the embedment depth of the void. Figures 7-4 and 7-5 show how a change in depth affects the recorded responses in time domain. The void height is  $0.08\text{ m}$  ( $0.22\lambda_{ch}$ ) and its width is  $0.32\text{ m}$  ( $0.88\lambda_{ch}$ ), which are kept constant for all the plots. The depth of the void varies from  $0.08\text{ m}$  ( $0.22\lambda_{ch}$ ), to  $0.64\text{ m}$  ( $0.1.78\lambda_{ch}$ ) as described in table 7.1.

Table 7.1: Embedment depth of the void in different studies

Model	S00_04	S00_08	S00_12	S00_14	S00_15	S00_16
<b>Embedment depth</b>	$0.08m$ ( $0.22\lambda_{ch}$ )	$0.16m$ ( $0.44\lambda_{ch}$ )	$0.32m$ ( $0.88\lambda_{ch}$ )	$0.48m$ ( $1.33\lambda_{ch}$ )	$0.56m$ ( $1.50\lambda_{ch}$ )	$0.64m$ ( $1.78\lambda_{ch}$ )

The trends are similar in all the plots. Reflections from near and far boundaries, trapped waves, and generated body waves are observed in all the plots. However, by increasing the depth, magnitude of the responses decreases, and the mentioned effects are not as conspicuous for deeper voids as they are for shallower ones. As mentioned in the previous chapters, the penetration depth of Rayleigh wave depends on its wavelength or frequency, i.e. more energy is confined in the top layers. Therefore, stronger interactions occur between the void and the wave, when the void is closer to the surface.

Figures 7-6 and 7-7 show the frequency content of the above studied cases. Similar trends are observed in all the plots, and as mentioned above the amplitudes drop significantly with the increase in depth. It is observed that event 'C' shifts toward lower frequencies. As previously mentioned the wavelength of the central frequency of event 'C' is directly related to the embedment depth of the void. The reason that event 'C' is not visible in plot 'a' is that in this case the frequency that its wavelength corresponds to the embedment depth of the void ( $f = \frac{64.08\frac{m}{s}}{0.08m} = 801\text{ Hz}$ ) carries a small amount of energy. Thus, its effects are overshadowed by the lower frequencies that carry more energy. From the plots it is concluded that events 'B' and 'C' define a frequency bandwidth in which major interactions between the void and the incident wave occur. As the void's embedment depth increases the amplitude of the reflections and the trapped energy gets closer to each other. Therefore, for deep voids it is not possible

to distinguish between the two effects. In conclusion the physical behavior of the void remains the same as the void's embedment depth increases. But, the combination of void size and embedment depth, and the frequency content of the source determine how conspicuous is the effect of the void on the surface responses. For the studied combination of void size and source frequency content, the effect of the void is not observable after a depth of about  $1.50\lambda_{ch}$ .

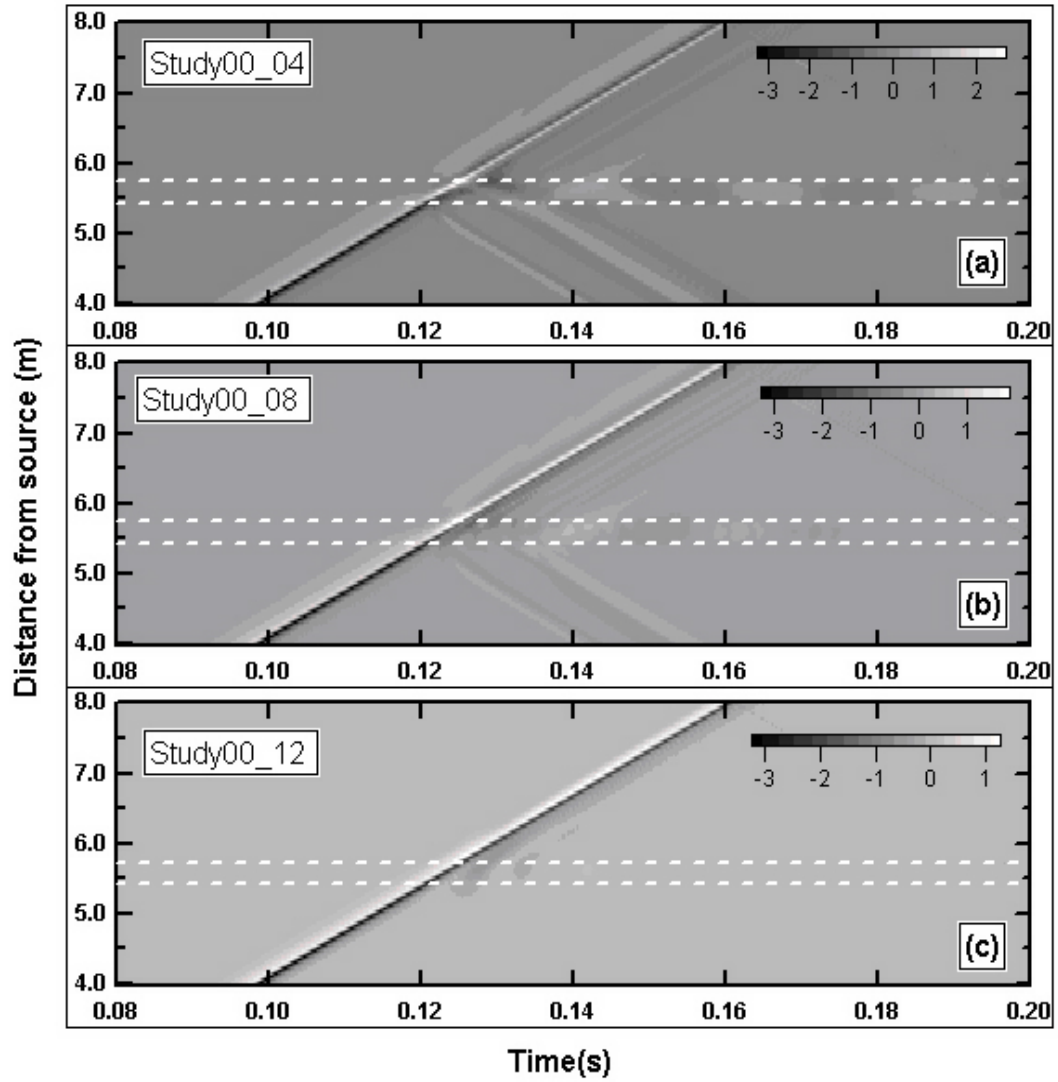


Figure 7-4: Effect of the void depth on the time responses at the medium surface. Plots 'a' to 'c' show the contour plots of the vertical responses recorded at the surface of models. The corresponding model number is shown on each plot. All the responses are normalized to the maximum of the vertical displacements recorded at the surface of study S00\_01 (model with no void). Dashed lines show the boundaries of the void projected to the surface.

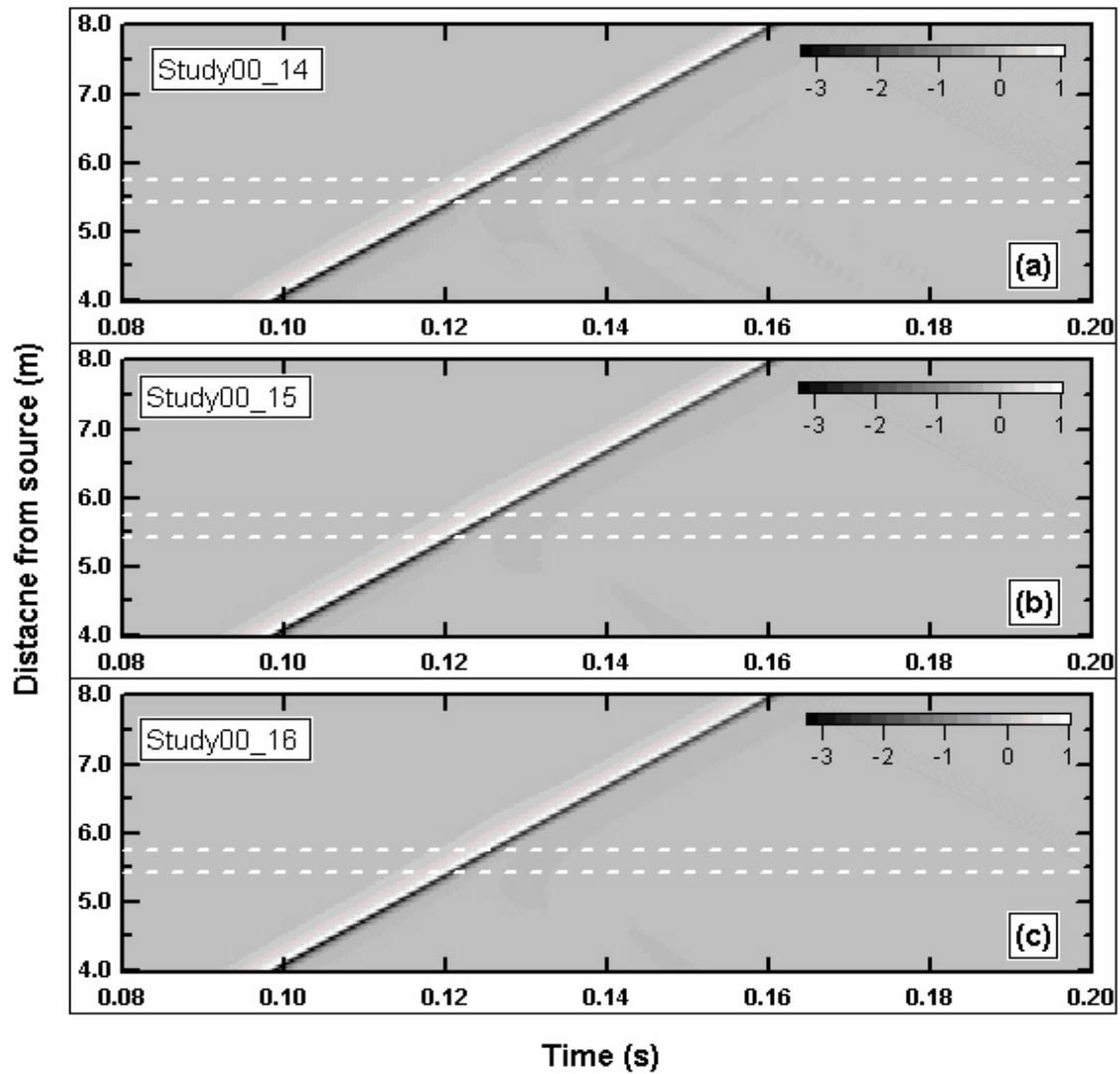


Figure 7-5: Effect of the void depth on the time responses at the medium surface. Plots 'a' to 'c' show the contour plots of the vertical responses recorded at the surface of models. The corresponding model number is shown on each plot. All the responses are normalized to the maximum of the vertical displacements recorded at the surface of study S00\_01 (model with no void). Dashed lines show the boundaries of the void projected to the surface.

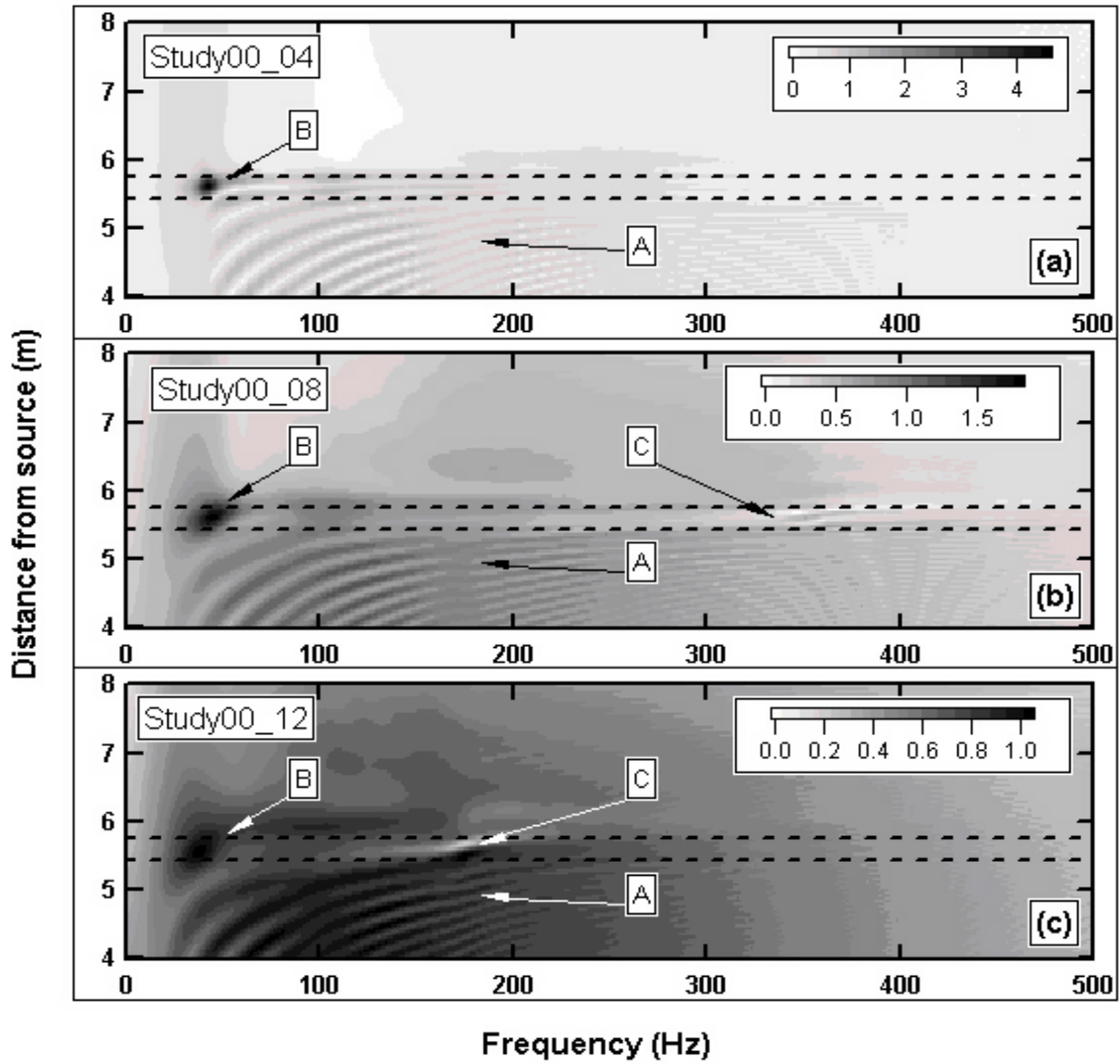


Figure 7-6: Effect of the void depth on the frequency content of the vertical displacements at the medium surface. The corresponding model number is shown on each plot. All the responses are normalized to the maximum frequency magnitude of the vertical displacements recorded at the surface of study S00\_01 (model with no void). Dashed lines show the boundaries of the void projected to the surface.

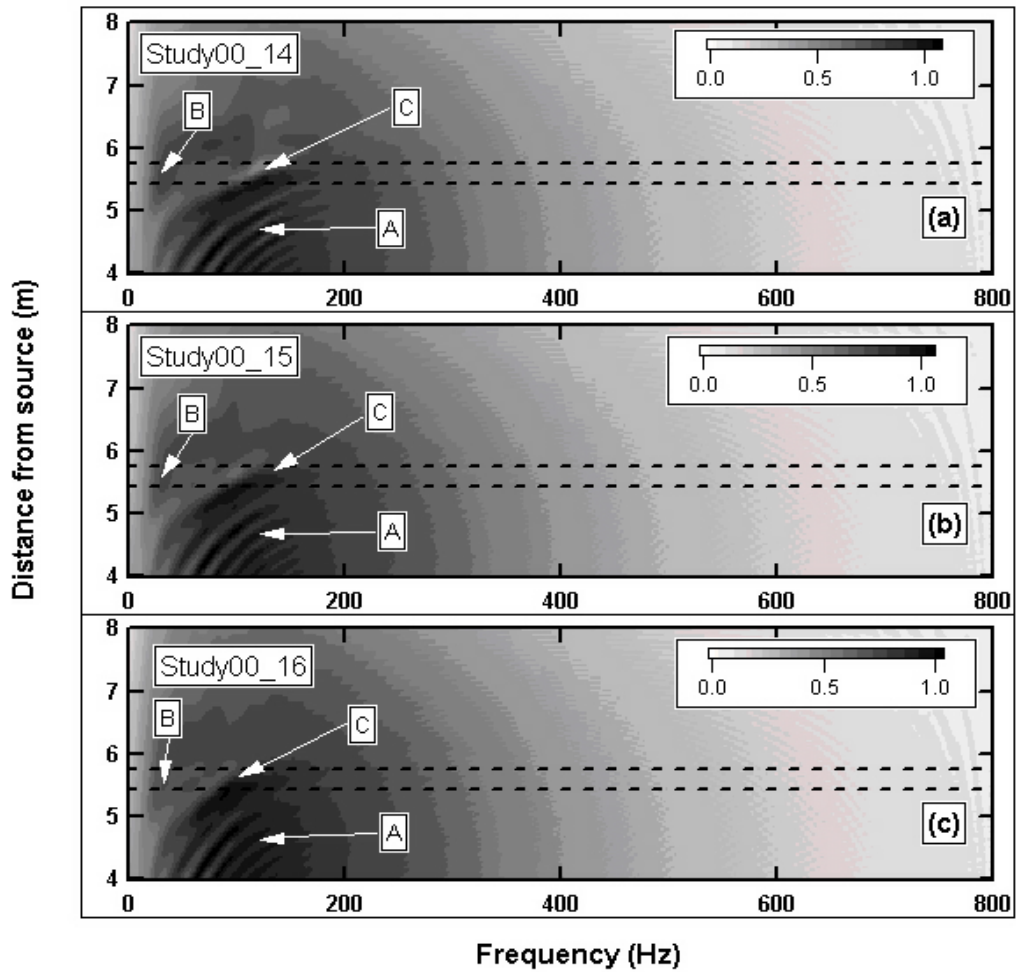


Figure 7-7: Effect of the void depth on the frequency content of the vertical displacements at the medium surface. The corresponding model number is shown on each plot. All the responses are normalized to the maximum frequency magnitude of the vertical displacements recorded at the surface of study S00\_01 (model with no void). Dashed lines show the boundaries of the void projected to the surface.



## 7.4 Effect of medium with two layers - Natural layering: Soft layer overlying bedrock (case 3)

This section explains the results obtained from model type S01 with the study numbers shown in figure 7-8. This model type consists of 2D axisymmetric finite differences models that simulate the propagation of Rayleigh waves in an elastic medium overlying a very stiff layer, representing bedrock. Material type I (as introduced in Chapter 6) is used for the elastic medium, and bedrock is simulated by fixing vertical displacements of the bottom boundary of the model. As no displacement is allowed at the bottom boundary its impedance is equal to infinity. Thus, no energy transfer occurs across this boundary and all the energy bounces back into the elastic medium. The minimum thickness assigned to the elastic layer is 0.232 *m* in models S01\_02 and S01\_03, which is doubled successively to a maximum of 1.856 *m* in models S01\_08 and S01\_09. For each thickness of the elastic layer two models are constructed, one without void and one with a void, i.e. the thickness of elastic layer is similar in models S01\_02 and S01\_03. Thus, model type S01 simulates the MASW test method in the presence of lateral and vertical inhomogeneities. The the void's width, height and embedment depth are 1.00 *m*, 0.112 *m*, and 0.12 *m*, respectively that are kept constant in all the studies. Model characteristics (grid size, dynamic time, time step, number and location of recording points) are the same as the ones used in model type S00. For further reference, all the source flac files are presented in Appendix CD-Chapter7.

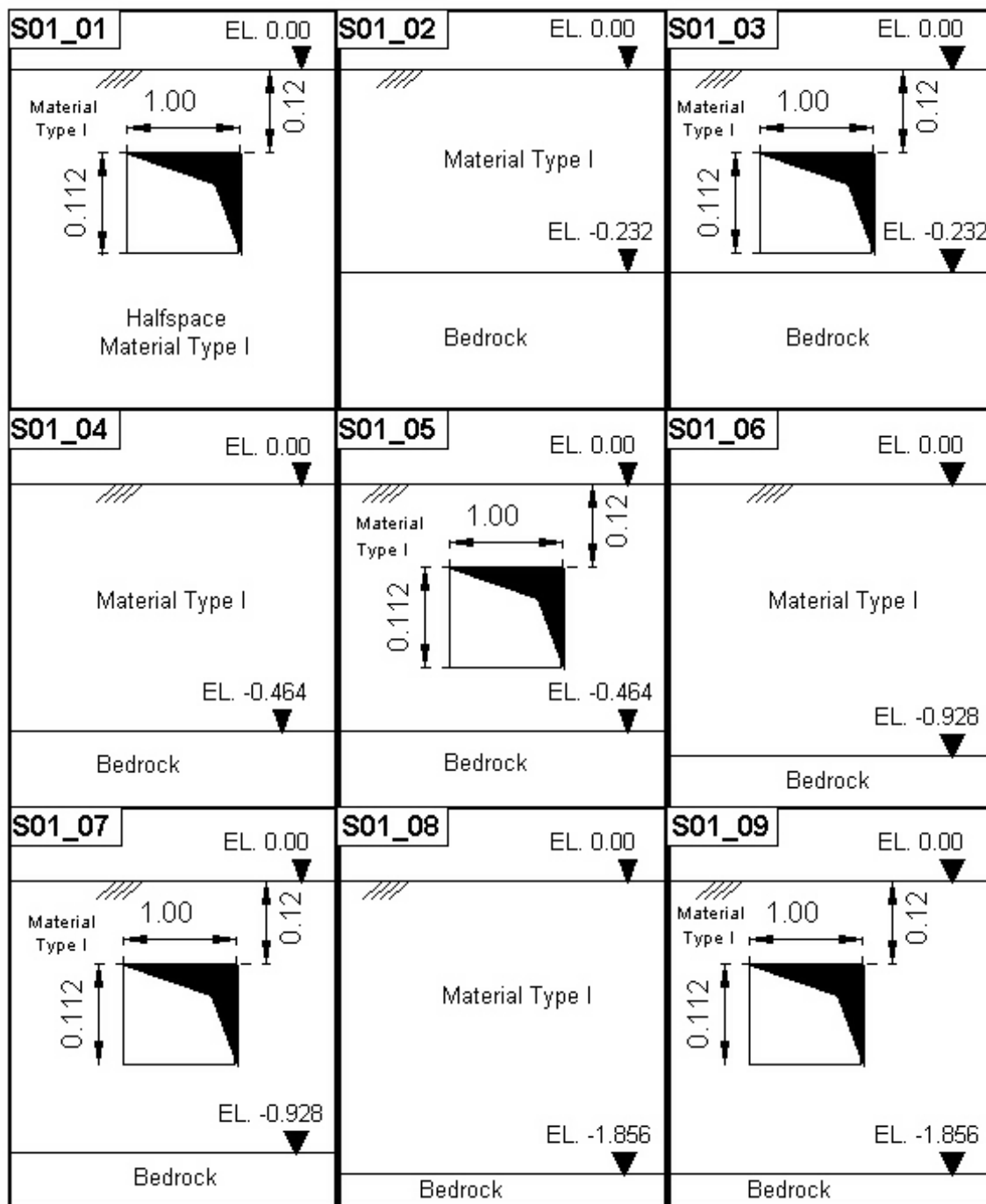


Figure 7-8: The numbering system for model type S01 along with the characteristics of each model. Study numbers are stated in the small box at the top left corner of each cell. The void size is 1.00 m (width) by 0.112 m (height) and is embedded at a depth of 0.12 m below surface.

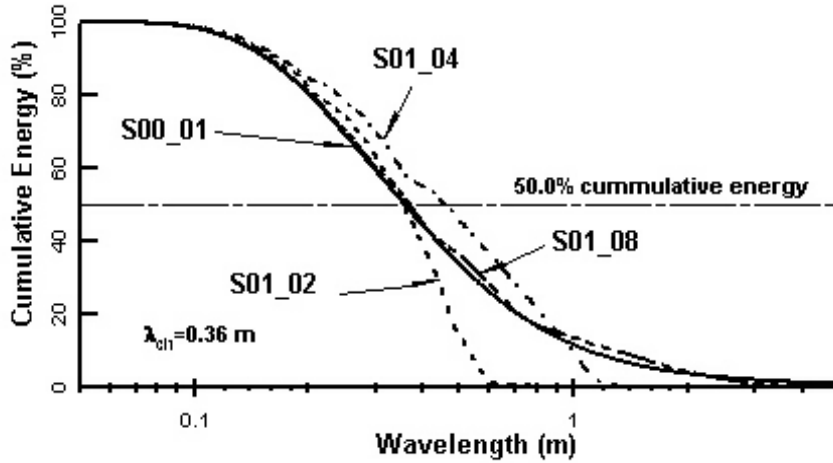


Figure 7-9: The cumulative energy versus wavelength for models with a soft layer overlying a stiff layer (model S01\_XX). The effect of filtration of low frequencies in models with shallow elastic layer is observed in the plots.

The concept of characteristic wavelength, as defined in chapter 6, is utilized to normalize the distances and void dimensions. Figure 7-9 shows the cumulative energy content of the responses at the location of first receiver (3.992 m from source) obtained from four different models of type S01. For comparison, the results obtained from model S0\_01 (homogeneous half space with no void) is included. The plots show that lower frequencies (larger wavelengths) are absent in the models with shallower elastic layers, i.e. model S01\_02 has less energy in longer wavelengths than model S01\_08. Thus, higher frequencies are filtered in models with shallow depth of elastic layer. The wavelengths corresponding to 50% of cumulative energy are shown in table 7.2.

Table 7.2: Model types used in this study

Model Type	S00_01	S01_02	S01_04	S01_06	S01_08
Wavelength (m)	0.36	0.36		0.48	0.38

The corresponding wavelengths differ with the value of the characteristic wavelength, defined based on model S00\_01 ( $\lambda_{ch} = 0.36$ ), but the measured values are close to  $\lambda_{ch}$ . Thus, for consistency the same characteristic wavelength is used in this this section.

Responses of model S00\_01 are used as a reference for the models without void. Model

S01\_01 represents a half-space containing a void with the above mentioned size. The responses of this model are similar to the ones studied in detail in Chapter 6, and it is reproduced herein as a reference for the models containing a void. All the response values, obtained from different study numbers of model type S01, are normalized to the corresponding maximum value of study S00\_01. In this section, all the presented responses correspond to the vertical displacements recorded at the surface of the models. Sample figures are presented in this section, and a complete set of colored figures is provided in Appendix CD-Chapter7.

#### 7.4.1 Time responses

Figure 7-10 shows contour plots of the time responses along the surface of models without void. Plot 'a' corresponds to the half-space without void (Study00\_01). In the chosen time frame only event **A**, which corresponds to the arrival of Rayleigh wave is visible. Plots 'b', 'c' and 'd' show the responses recorded along the surface of models S01\_02, S01\_04, and S01\_08, where bedrock (fixed boundary) is located at  $0.232\text{ m}$  ( $0.64\lambda_{ch}$ ),  $0.464\text{ m}$  ( $1.29\lambda_{ch}$ ), and  $1.856\text{ m}$  ( $5.15\lambda_{ch}$ ) below surface, respectively. In all the plots, event **A** shows the arrival of main Rayleigh wave. A series of events are represented by **B** that occur before the arrival of main Rayleigh wave. The common characteristic of the waves constituting event **B** is that their velocity is larger than the Rayleigh wave velocity of the medium, and are associated to higher modes of s-wave and p-waves. Another series of events occur after event **A** that are represented by event **C**. The velocity of these waves gradually increases from Rayleigh wave velocity to velocities larger than the s-wave velocity of the medium. These events can be associated to higher modes of Rayleigh waves and Lamb waves. Both events **B** and **C** are generated due to the interaction of the input energy with the fixed boundary. As the fixed boundary is moved farther from the surface (from plot 'b' to 'd') the interactions are less; therefore, the number of waves that constitute events 'B' and 'C' decrease. Due to destructive interference of the generated waves, the maximum amplitude of surface responses in plots 'b' and 'c' are smaller, than the ones in plot 'a'. It is known that energy does not radiate below the fixed boundary. Hence, conservation of energy implies that the duration of surface vibrations be larger when the fixed boundary is close to the surface. In general, the source gives significant excitation of fundamental Rayleigh wave mode. Weaker high modes of Rayleigh waves are also excited due to

the interaction of input energy with the reflecting bottom boundary. Two dimensional Fourier transforms are utilized to further study the nature of these events that will be discussed later in this section. Extensive theoretical studies have been published that address the behavior of seismic waves in layered systems [134].

The plots in figure 7-11 depicts the trends of the surface responses of a soft layer overlying bedrock, in the presence of a void. The void is located in the soft layer. Plot 'a' shows the responses of a half-space in the presence of the void that is reproduced here for comparison. Plots 'b', 'c' and 'd' show the responses recorded along the surface of models S01\_03, S01\_05, and S01\_09, where bedrock (fixed boundary) is located at  $0.232\text{ m}$  ( $0.64\lambda_{ch}$ ),  $0.464\text{ m}$  ( $1.29\lambda_{ch}$ ), and  $1.856\text{ m}$  ( $5.15\lambda_{ch}$ ) below surface, respectively. These plots are comparable to the corresponding plots in figure 7-10, where voids were not included in the medium. The general trends that were discussed for the cases with no void are observed in these plots. Further, the concepts of reflected energy from void boundaries and trapped energy in the void region (that were discussed in Chapter 6) are also visible in these cases. When the fixed boundary is very close to the surface, as in plot 'b', the behavior of the surface responses are more similar to the ones obtained from model S01\_01 (figure 7-10 plot 'b'), rather to the responses in model S01\_01 (figure 7-11 plot 'a'). This behavior reveals that in this case the dominant vibration is the vibration of the whole medium even in the vicinity of the void region. As the fixed boundary moves farther than the surface the interaction between the void and the incident energy becomes more conspicuous.

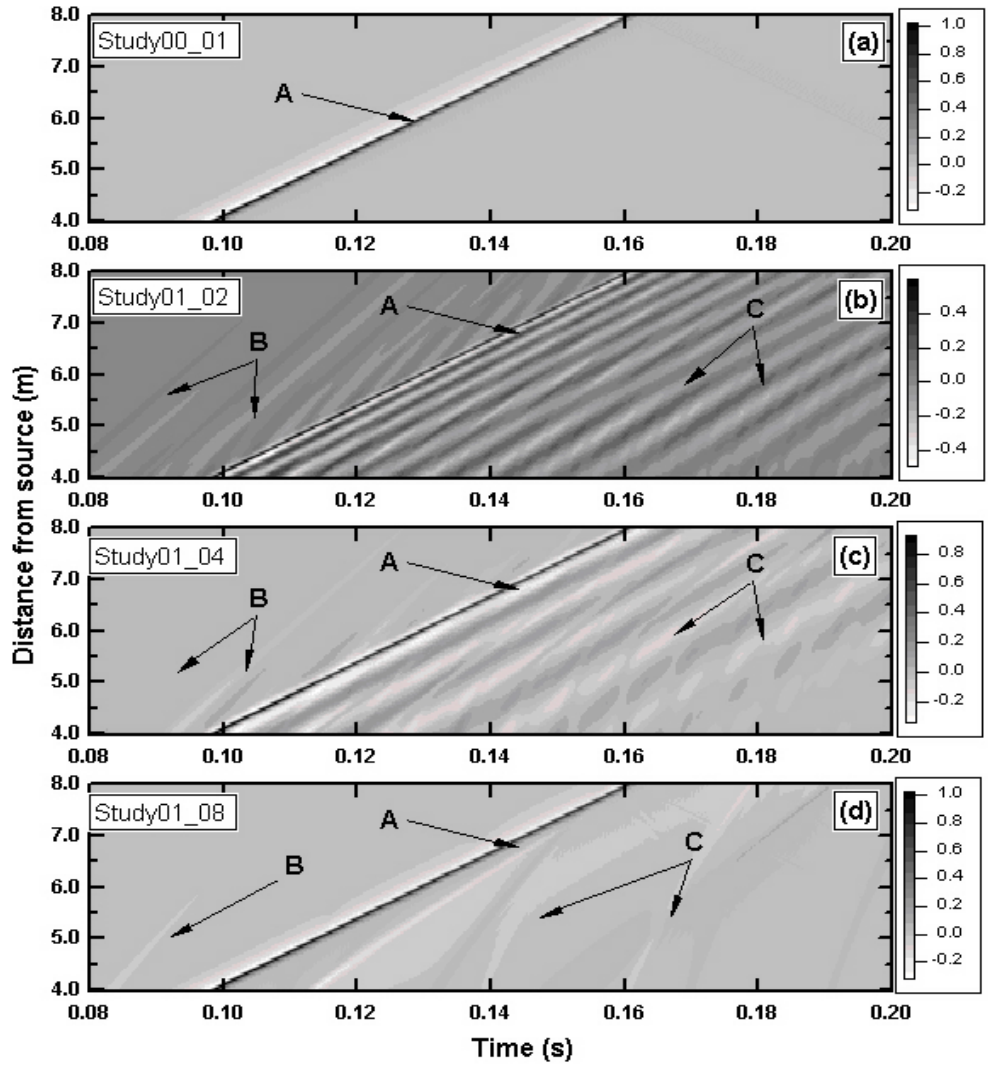


Figure 7-10: Contour plots of the vertical displacements recorded at the surface of model type S01. The presented plots correspond to models without void. The study numbers are shown on each plot. In each plot the horizontal axis shows time in second and vertical axis shows distance from source in meter.

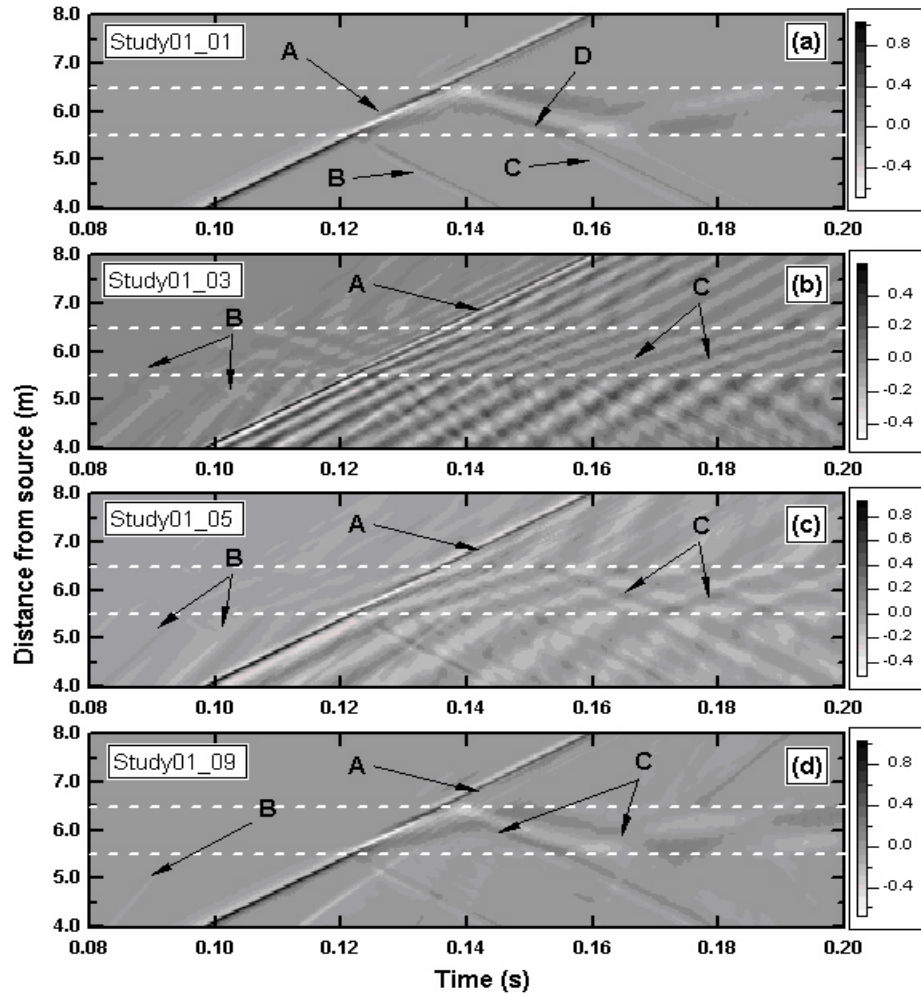


Figure 7-11: Contour plots of the vertical displacements at the surface of model type S01. The presented plots correspond to models with void. The study numbers are shown on each plot. In each plot the horizontal axis shows time in second and vertical axis shows distance from source in meter. Dashed lines show the projection of the vertical boundaries of the void to the surface.

### 7.4.2 Frequency responses

Figure 7-12 shows the behavior of the layered medium with no void in frequency domain. Plot 'a' shows the spectrum of a half-space, and plots 'b', 'c' and 'd' correspond to layered models. In such systems lower frequencies are filtered by the medium. Table 7.3 shows the frequencies below which are filtered from the spectrum of each model.

Table 7.3: Frequencies below which are filtered from models

<b>Model Type</b>	<b>S01_02</b>	<b>S01_04</b>	<b>S01_06</b>	<b>S01_08</b>
Frequency ( $Hz$ )	100	50	29	16
Wavelength $\lambda$ ( $m$ )	0.64	1.28	2.21	4.0
Layer depth $d$ ( $m$ )	0.232	0.464	0.928	1.856
$\lambda/d$	2.76	2.75	2.60	2.16

Same table shows the corresponding wavelengths and depth of the top layer of each model. The ratio between the wavelength and the layer depth shows that in each model wavelengths larger than about 2.5 times the layer depth are filtered out. In the presented spectrum the effect of reflections from bottom boundary are observed as ripples. The amplitudes (which are normalized with respect to corresponding values in model S00\_01) in the layered systems are larger with respect to the ones in a half-space. As the depth of fixed boundary increases the spectrum gets closer to half space spectrum.

Figure 7-13 shows the spectrum in the presence of a void. Plot 'a' corresponds to a half-space with void. The depth to the fixed boundary increases from plot 'b' to 'd'. In plot 'b' reflections with large amplitudes in compare with plot 'a', are observed before the void, but amplification over the void is not seen. Thus, energy entrapment is not occurring in this case. In plot 'c' reflections before the void is observed and minor energy entrapment over the void can be traced. In plot 'd' the amplitudes of the trapped energy is much larger than the amplitudes of reflected waves. Even, the amplitudes in plot 'd' are larger than the ones in plot 'c'. In all the above models the dimensions of the void are the same, and the only difference is the depth to the fixed boundary, which has a filtering effect on the input frequency. It is concluded that a very stiff underlying layer acts as a filter, which can eliminate the frequencies that interact with the void. Thus the presence of an anomaly (such as a layer) that interacts with the same frequencies that the void interacts with, can overshadow the effect of the void on surface responses. This



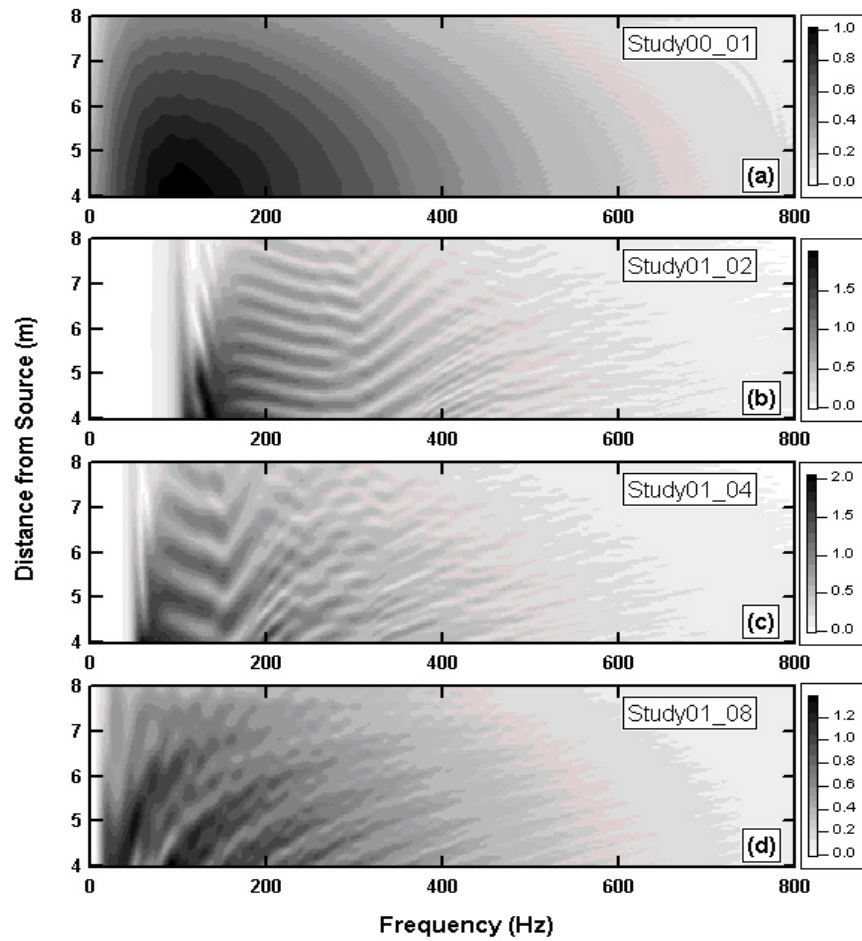


Figure 7-12: Contour plots of the spectrum of layered models. The values are normalized to the corresponding values in model S00\_01 (Homogeneous medium with no void).

experience clearly proves that the vertical and horizontal sides of the void interact with different wavelengths (frequencies). The relative amplitudes of the reflections from the boundaries with respect to the amplitudes of the trapped energy, depends on the amount of the energy that is carried in the corresponding frequency ranges.

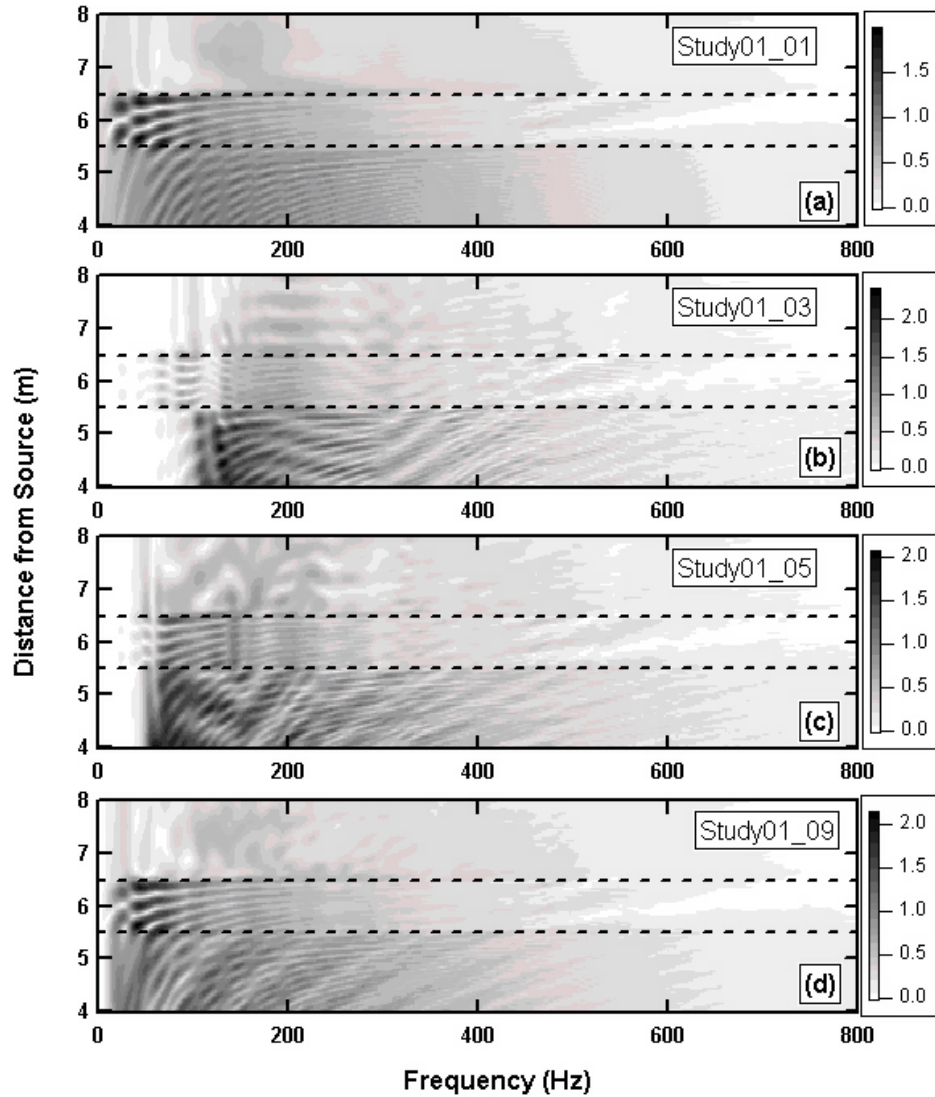


Figure 7-13: Contour plots of the spectrum of layered models with void. The values are normalized to the corresponding values in model S00\_01 (Homogeneous medium with no void). The dashed lines show the projected boundaries of the void. The depth to the fixed boundary is 0.232 m, 0.464 m and 1.856 m, in plots 'b', 'c', and 'd', respectively.

### 7.4.3 2D Fourier spectrum

Figure 7-14 shows the 2D Fourier responses of Type S01 models without void. In plot 'a', which corresponds to the homogeneous half-space the fundamental Rayleigh wave mode is observed as an inclined line that passes through the origin. The effect of reflected wave from quiet boundaries are also observed. In plots 'b' to 'd' the energy is split between the fundamental and higher modes of Rayleigh wave. These higher modes are observed as lines that do not pass through the origin. The higher modes are excited due to the presence of fixed boundary, and are eliminated as the boundary gets farther than the surface. In plot 'd' beside the fundamental Rayleigh wave, strong p-wave and s-waves are observed which are associated to the multiple interaction of incident wave with the fixed and free boundaries.

Figure 7-15 shows the 2D Fourier spectrum in the presence of void. Branches in the negative wavenumber axis indicate that the energy is reflected. As observed, not only the fundamental Rayleigh wave mode but also the higher modes interact with the void. These interactions are observed a V shaped events in plots 'b' to 'd'. These figures prove that even in the presence of higher modes of vibration, which introduce difficulties in the interpretation of the data, the 2D Fourier transform is a promising tool for the detection of cavities from the surface responses.

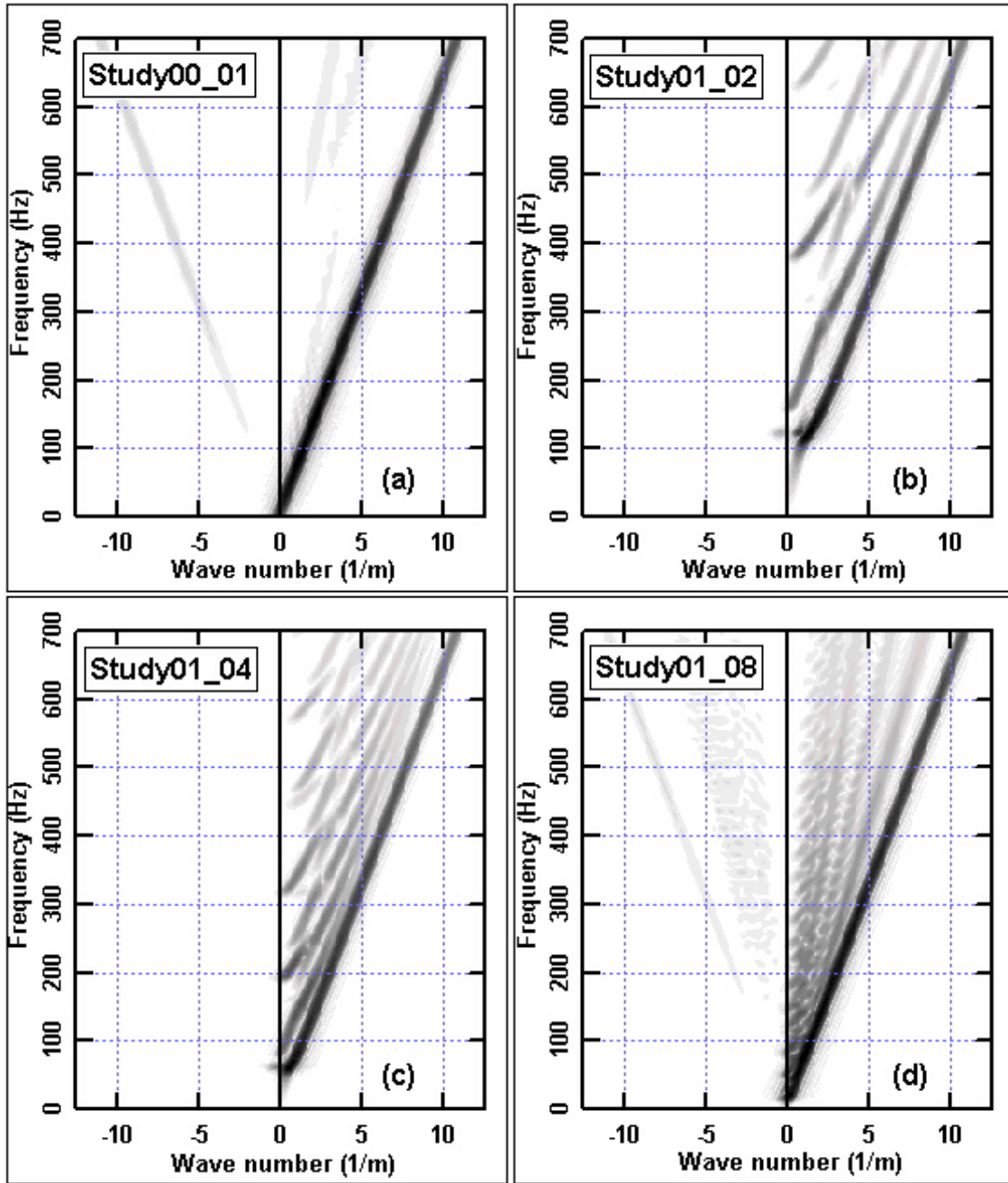


Figure 7-14: 2D Fourier responses of layered models (Type S01) with no void. Plot (a) correspond to the halfspace with no void. The effect of higher Rayleigh modes are observed as branches that do not pass through the origin.

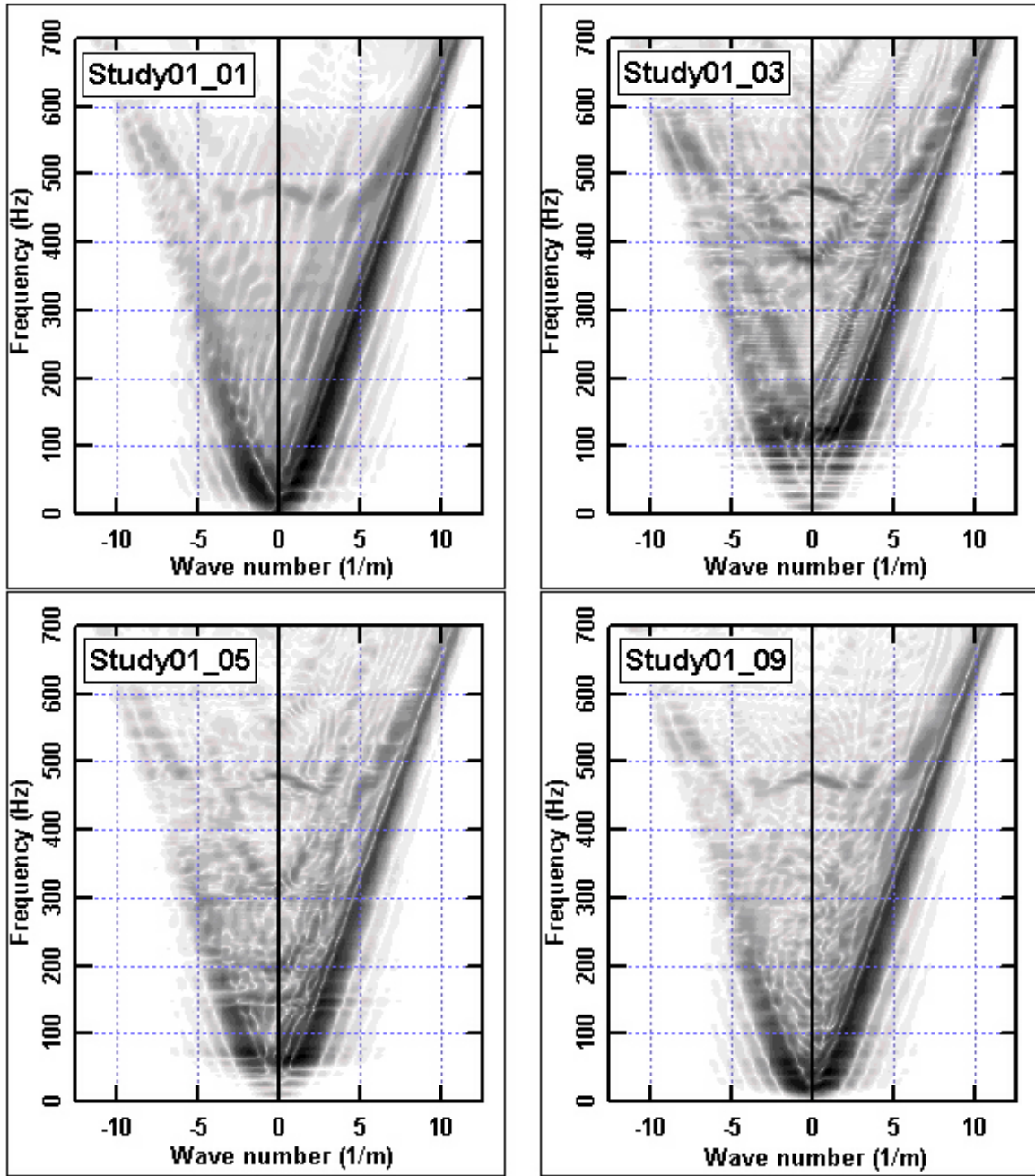


Figure 7-15: 2D Fourier responses of layered models (Type S01) with void. Plot (a) correspond to the halfspace with void. The effect of void is observed as reflections of fundamental and higher modes of Rayleigh waves.

## 7.5 Effect of medium with two layers - Inverse layering: Stiff layer overlying soft layer (case 4)

The results of model type S02 are explained in this section, and the corresponding study numbers are depicted in figures 7-16 and 7-17. This model type consists of 2D axisymmetric models that simulate the propagation of Rayleigh waves in a stiff layer overlying a soft layer. In all the models material Type I is used for the underlying medium. In models S02\_01 to S02\_08 the top layer consists of material Type II and in models S02\_11 to S02\_14 the top layer is comprised of material Type III. The material properties are presented in the corresponding figures. The depth of the top layer is varied between 0.504 *m* to 2.016 *m*. The stiffness of the materials can be compared by using the concept of acoustic impedance [17]. The acoustic impedance (*z*) is defined as the product of unit mass of the material ( $\rho$ ) and wave velocity in the material (*v*) and has the unit of  $ML^{-2}T^{-1}$  (*M*, *L*, and *T* represent mass, length and time, respectively):

$$z = \rho v \quad (7.1)$$

In layered systems, the acoustic impedance is used to determine the amount of energy that is transmitted between the layers and the amount of energy that is reflected from the boundaries between the layers. The reflection and transmission coefficients are defined as:

$$R_{1 \rightarrow 2} = \frac{z_1 - z_2}{z_1 + z_2} = \frac{\rho_1 v_1 - \rho_2 v_2}{\rho_1 v_1 + \rho_2 v_2} \quad (7.2a)$$

$$T_{1 \rightarrow 2} = \frac{2z_1}{z_1 + z_2} = \frac{2\rho_1 v_1}{\rho_1 v_1 + \rho_2 v_2} \quad (7.2b)$$

where *R* is the reflection coefficient, *T* is the transmission coefficient, and the symbol 1 → 2 means that the wave travels from material 1 to material 2. The Reflection coefficient represents the ratio between the amplitudes of reflected wave and the incident wave. The transmission coefficient shows the ratio between the amplitudes of the transmitted wave into the second medium and the incident wave. Based on the above definitions the values of the acoustic impedance for materials Type I, II, and II are 183'792  $\frac{kg}{m^2s}$ , 236'646  $\frac{kg}{m^2s}$ , and 368'179  $\frac{kg}{m^2s}$ ,

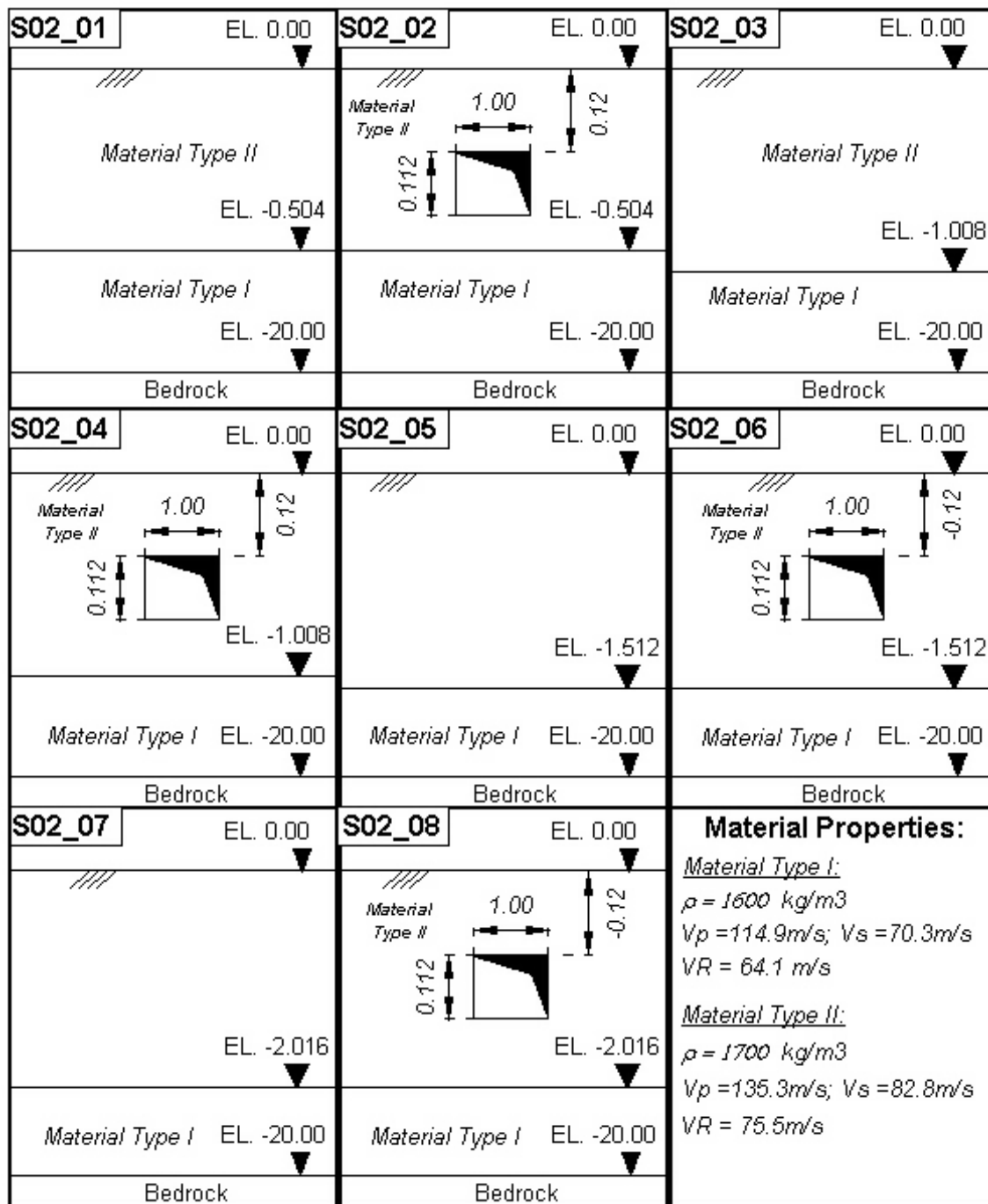


Figure 7-16: The numbering system for model type S02 along with the characteristics of each model. Study numbers are stated in the small box at the top left corner of each cell. The top layer consists of material Type II with the properties presented in the paper.

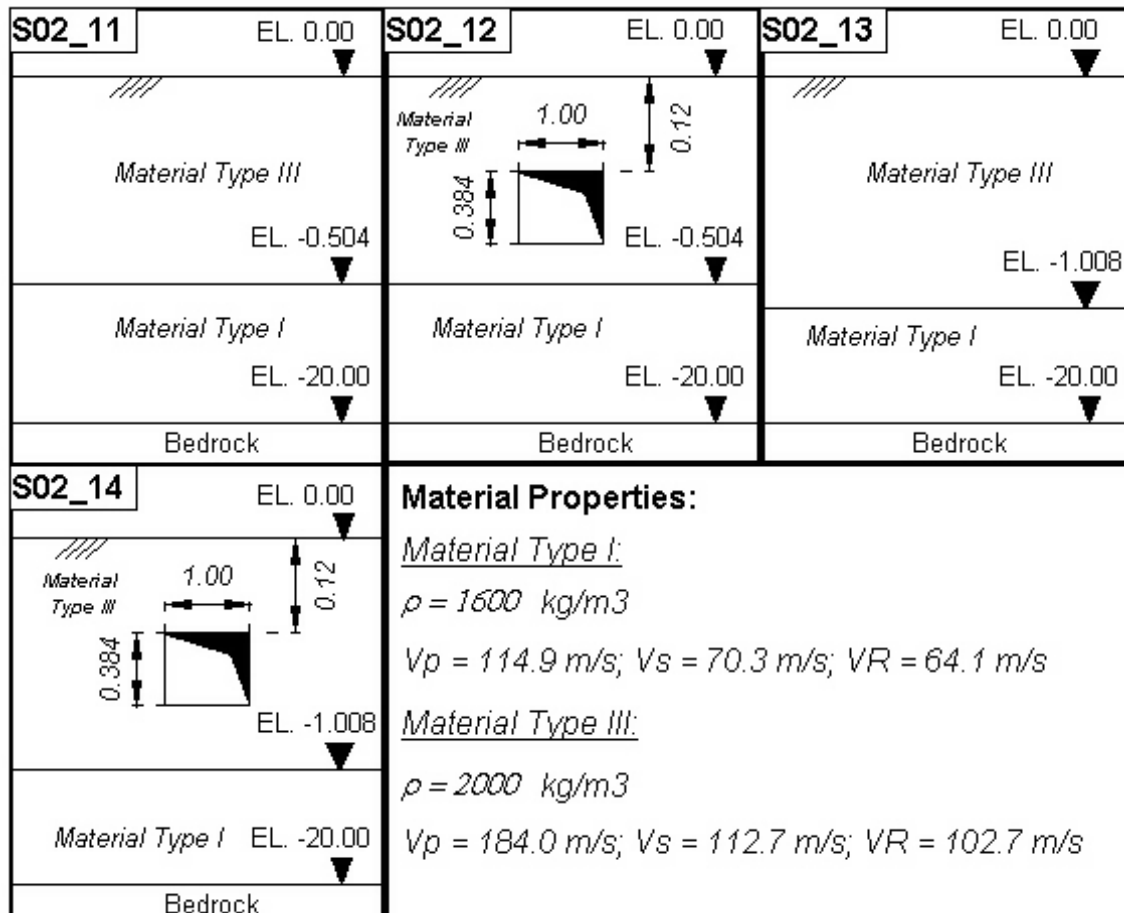


Figure 7-17: The numbering system for model type S02 along with the characteristics of each model. Study numbers are stated in the small box at the top left corner of each cell. In these cases the top layer consists of material Type III with the presented material properties.



respectively. The values of the reflection and transmission coefficients for the studied cases are presented in the following table.

Table 7.4: Reflection and transmission ratios between the materials used in model type S02

<b>Medium</b>	<b>II <math>\rightarrow</math> I</b>	<b>III <math>\rightarrow</math> I</b>
<b>R</b>	0.125	0.33
<b>T</b>	1.125	1.33
<b>Impedance ratio</b>	1.29	2

The positive values of the reflection and transmission coefficients show that the incident, and the reflected/transmitted waves have the same polarity. The reflection coefficients smaller than one show that only a fraction of the incident energy is reflected back to the top layer and part of it is radiated into the bottom layer.

Figure 7-18 shows the cumulative energy verses wavelength for model type S02. In plots 'a' and 'b' the impedance ration between the top and bottom layers are about 1.3, and 2.0, respectively. For reference, the graph for study S00\_01 (homogeneous half-space) is included in plot 'a'. In general, the plots indicate that in compare to study S00\_01 smaller wavelengths (larger frequencies) are filtered out by the medium. The filtering effect is not very susceptible to the depth of the stiff layer when the impedance ratio between the two layers is small. Thus in plot 'a', a characteristic wavelength of  $\lambda_{ch} = 0.53 \text{ m}$  can be defined for all the models with sufficient accuracy. In the presence of significant difference between the impedance ratio of the top and bottom layers, the range of the filtered wavelengths changes considerably with the depth of the stiff layer. In plot 'b' the horizontal segments of the graphs show the range of the filtered wavelengths. The measured characteristic wavelengths for models S02\_11, and S02\_13 are  $\lambda_{ch} = 2.45 \text{ m}$  and  $\lambda_{ch} = 0.63 \text{ m}$ , respectively.

Figure 7-19 shows the representative time responses of the systems with inverse layering. Plots 'a' and 'd' show the corresponding contour plots for the half-space. Plots 'a', 'b' and 'c' correspond to cases without void, and plots 'd', 'e', and 'f' correspond to models with void. Interactions similar to the ones observed in cases S00 and S01 are observed herein. Reflections from near and far boundaries and trapped waves bouncing back and forth between the void boundaries are observed in the plots. By increasing the depth of the top stiff layer the interaction trends get closer to the ones for half space. The interesting observation is that in plot 'e' the

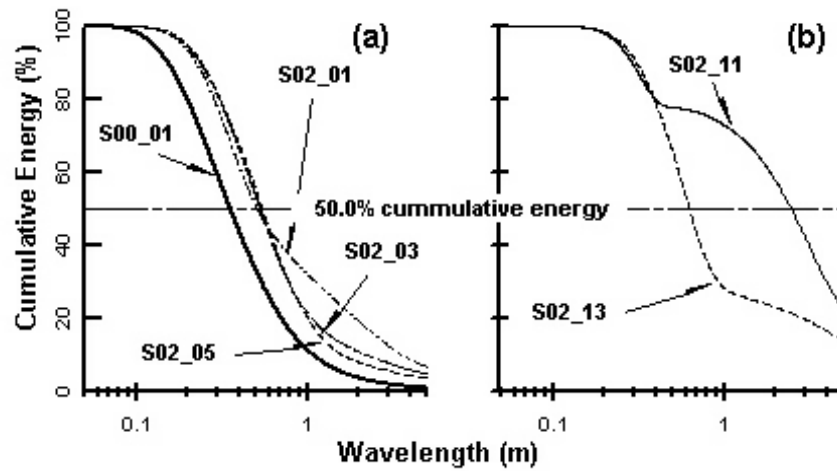


Figure 7-18: The cumulative energy versus wavelength for models with a stiff layer overlying a soft layer (model S02\_XX). The effect of filtration of low frequencies in models with shallow elastic layer is observed in the plots.

interaction of trapped energy with the void boundaries are stronger than in plot 'f'. The size of the void is the same in both cases, and the only difference is the depth of the stiff layer that is doubled in S02\_14 with respect to S02\_12. The physical reason for this behavior is explained by investigating the corresponding spectrum.

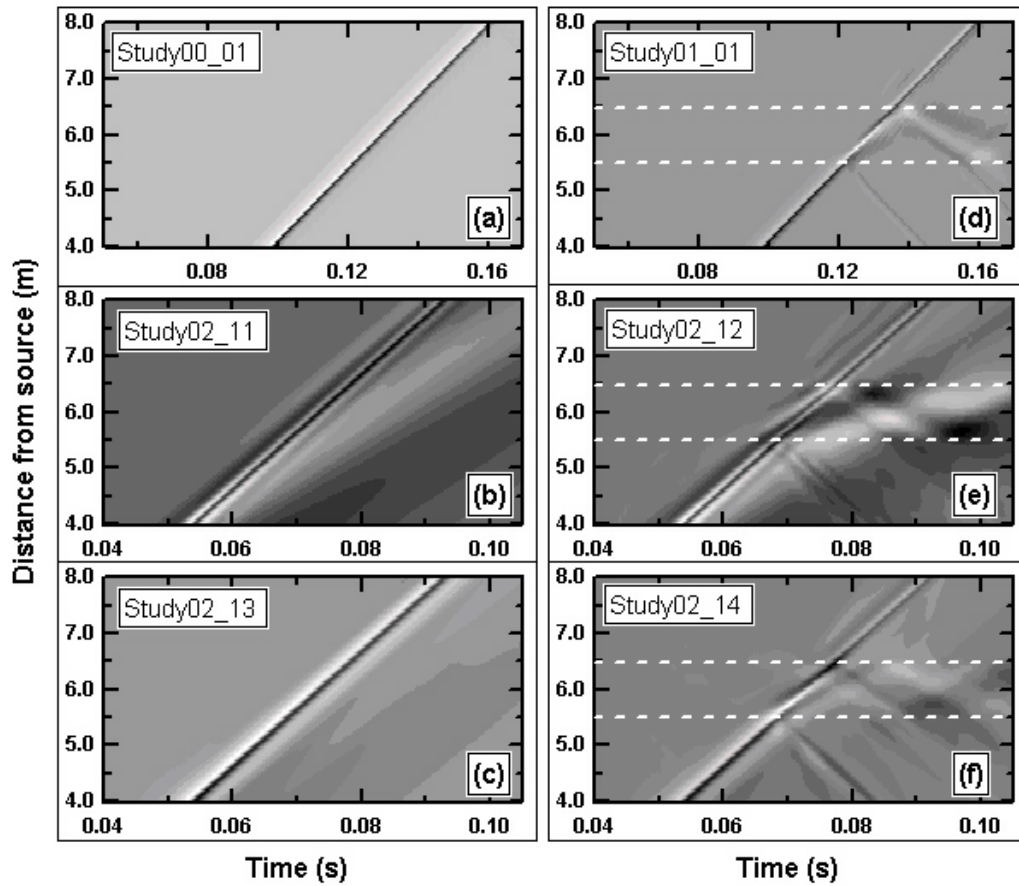


Figure 7-19: Contour plots of the vertical displacements at the surface of model type S02. Plots (a), (b), and (c) correspond to models without void. The study numbers are shown on each plot. In each plot the horizontal axis shows time in second and vertical axis shows distance from source in meter. The dashed lines show the projected boundaries of the void.

Figure 7-20 shows the spectrum of the responses from model type S02. Plots 'a' and 'd' correspond to the half-space and are presented for reference. All the responses are normalized to the maximum of the spectrum of model S00\_01 (half-space with no void). As the top layer in S02 is stiffer than the material assigned to S00, the measured amplitudes in model S02 are smaller than the ones in S00. The filtering effect of layered system is seen in plots 'b' and 'c'. The filtered frequencies are centered around  $f = 200 \text{ Hz}$  ( $\lambda = 0.51m$ ) and  $f = 100 \text{ Hz}$  ( $\lambda = 1.03m$ ), in plots 'b' and 'c', respectively. The wavelengths are calculated based on Rayleigh wave velocity of top layer  $C_R = 102.7 \frac{m}{s}$ . The latter wavelengths are very close to the depth of the top layer. Thus, the inverse layered system filters frequencies with wavelengths in the range of the depth of the top layer. Plots 'd', 'e', and 'f' shows the spectrum in the presence of void. In plot 'd' (half-space) energy concentration is observed in the frequency range of  $50 \text{ Hz}$  to  $100 \text{ Hz}$ . As observed in plots 'b' and 'c', these frequency ranges are filtered in the inverse layered systems. Thus, strong energy concentrations as observed in plot 'd' are not seen in plots 'e' and 'f'. The frequency range that is filtered by model S02\_13 is closer to the frequency range that interact with the void ( $f = 100 \text{ Hz}$ ), than the ones in model S02\_11. Therefore, the energy concentration over the void region is more conspicuous in plot 'e' than in plot 'f'. This observation explains the reason that in the time contours (7-19) stronger interaction between the void and the wave were observed in plots 'e' than in plot 'f'. Generally, it is concluded that inverse layered systems filter some frequencies. The range of the filtered frequencies is a function of the depth of the layer. When a void is present in the top layer, it interacts with the available wavelengths and frequencies. If the medium filters the wavelengths that interact with the void, then the effect of the void in surface responses might not be observable.

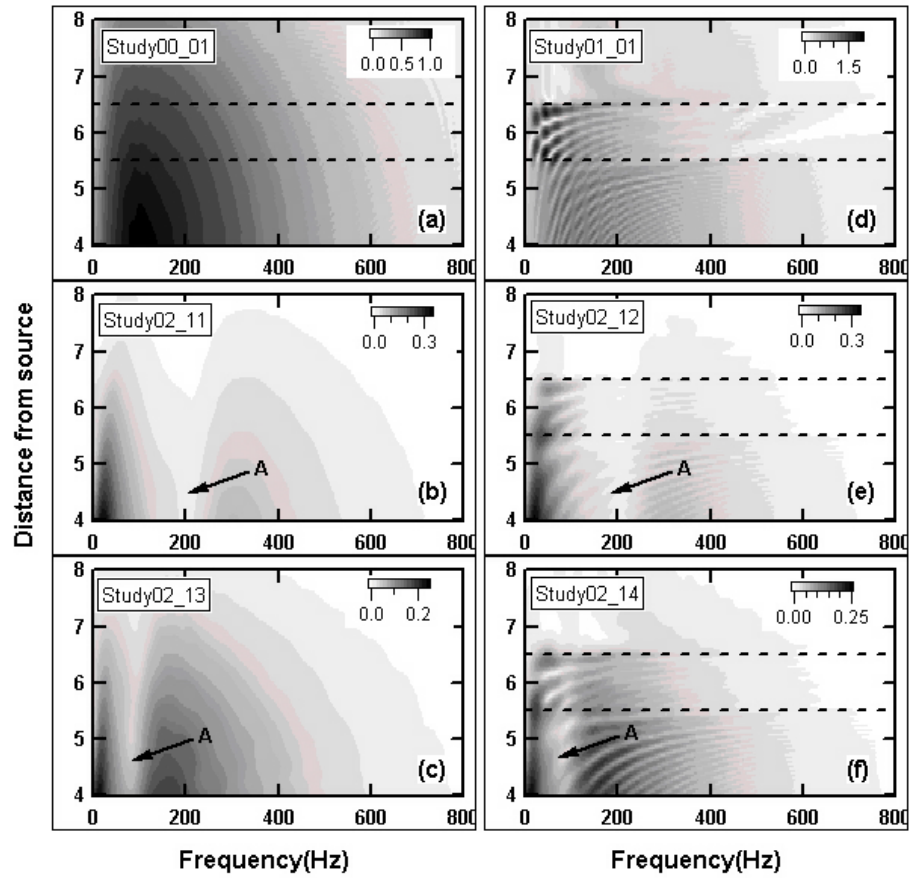


Figure 7-20: Spectrum of the vertical displacements at the surface of model type S02. Plots (a), (b), and (c) correspond to models without void. The study numbers are shown on each plot. In each plot the horizontal axis shows time in second and vertical axis shows distance from source in meter. The dashed lines show the projected boundaries of the void.

## 7.6 Effect of lateral dimension of the void - 3D effect of the cavity (case 5)

The problem of propagation of Rayleigh waves in the presence of lateral inhomogeneities is a three dimensional problem, in nature. Chapter 6 discussed the available literature on the numerical studies of this problem. So far, almost all of the conducted studies used two dimensional simulations to investigate the problem. Because of the hardware and software limitations, simplifying assumptions were made and the effect of out of plain dimension of the void is neglected. By introducing high speed computers with large memory and hard drive capacities the hardware limitations are solved to some extent. In parallel, new softwares are developed that could handle dynamic finite element or finite differences problems in three dimensions. Among the commercially available softwares ABAQUS (<http://www.hks.com>), ADINA (<http://www.adina.com>) and FLAC3D (<http://www.itascacg.com/flac3d.html>) provide powerful tools for three dimensional modeling of dynamic problems.

So far, all the discussions that have been presented in this research were based on axisymmetric models (as explained in the Chapter 6 and the previous sections of this chapter). The available 2D studies either assume that the problem is axisymmetric or plain strain. Inherent in these assumptions is that the out of plain dimension of the void is much larger than its in-plain dimensions. These assumptions might not be valid in all the circumstances. For example cavities developed in karstic regions usually have limited extents in all directions. In this study FLAC3D (Version 2.1) is utilized to simulate the effect of out of plain dimension of cavity on surface responses. The following sections explain the results obtained from various developed models.

### 7.6.1 Model description

Figures 7-21 and 7-22 describes the geometry of the 3D models that are developed in this work. Study S03\_00 shows the basic model that is used for calibration. It comprises of a cube with dimensions 8.02 *m*, 5.0 *m*, and 5.0 *m*, in *x*, *y*, and *z* directions, respectively. The latter dimensions are chosen based on the memory limitations of the available computers (2.0 *MB* of RAM). The cube consists of 2 regions. **Region 1** comprises of uniform grids in *x*- and

nonuniform grids in  $y$ - and  $z$ - directions. The size of the uniform grid is  $\Delta s_x = 0.035\text{ m}$ , with 172 grid zones (total length of the region is 6.02 m). In this region, the nonuniform grids comprise of a basic grid size of  $\Delta s_y = \Delta s_z = 0.035\text{ m}$ . The grids expand at a rate 1.01 times the previous grid size in the  $y$ - and  $z$ - directions, with a total of 68 grid zones in each direction. In **Region 2**, the grid geometry in  $y$ - and  $z$ - directions are the same as in **Region1**. In  $x$ - direction the grids expand at a rate 1.032 times the previous grid size, with the basic grid size of  $\Delta s_x = 0.035\text{ m}$ . The dimensions of **Region 2** are 2.0 m, 5.0 m and 5.0 m, in  $x$ -,  $y$ -, and  $z$ - directions, respectively.

Material Type I (Chapter 6, table 6.1) is used for all the models. The boundary conditions assigned to each boundary plain are shown in table ???. Symmetry boundary conditions are defined along plains corresponding to  $x = 0$  and  $y = 0$ . To mitigate the effect of reflected waves quiet boundaries are defined along plains corresponding to  $y = -5.0\text{ m}$  and  $x = 8.02\text{ m}$ . Experiments with different types of boundary conditions show that reasonable results are obtained by fixing the bottom boundary of the model ( $z = -5.0\text{ m}$ ) in  $z$  direction. Thus, the homogeneous model (S03\_00) does not represent a half-space. Simulating a dynamic 3D half-space, needs models with larger sizes, that consequently requires more sophisticated hardware that were not available for this study. Experience with different models showed that the applied quiet boundaries do not provide sufficient damping to eliminate reflections from boundaries. Therefore to mitigate the effect of reflections, 2% of Rayleigh damping at a center frequency of 100 Hz is applied to the whole model.

Table 7.5: Boundary conditions assigned to different boundary plains in model type S03

Plain	Free			Fixed			Quiet		
	Direction			Direction			Direction		
	$x$	$y$	$z$	$x$	$y$	$z$	$x$	$y$	$z$
$x - z @ y = 0\text{ m}$	*		*		*				
$x - z @ y = -5.0\text{ m}$							*	*	*
$x - y @ z = 0\text{ m}$	*	*	*						
$x - y @ x = -5\text{ m}$	*	*				*			
$y - z @ x = 0\text{ m}$		*	*	*					
$y - z @ x = 8.02\text{ m}$							*	*	*

The dynamic time increment for all the models is  $\Delta t = 5 \times 10^{-5}\text{ s}$ , which satisfies the stability and accuracy conditions. The responses are saved at every time steps; hence:

$$\delta t = \text{Sampling time} = 5 \times 10^{-5} s \quad \text{and} \quad \delta f = \text{Sampling frequency} = \frac{1}{\delta t} = 20 \text{kHz} \quad (7.3)$$



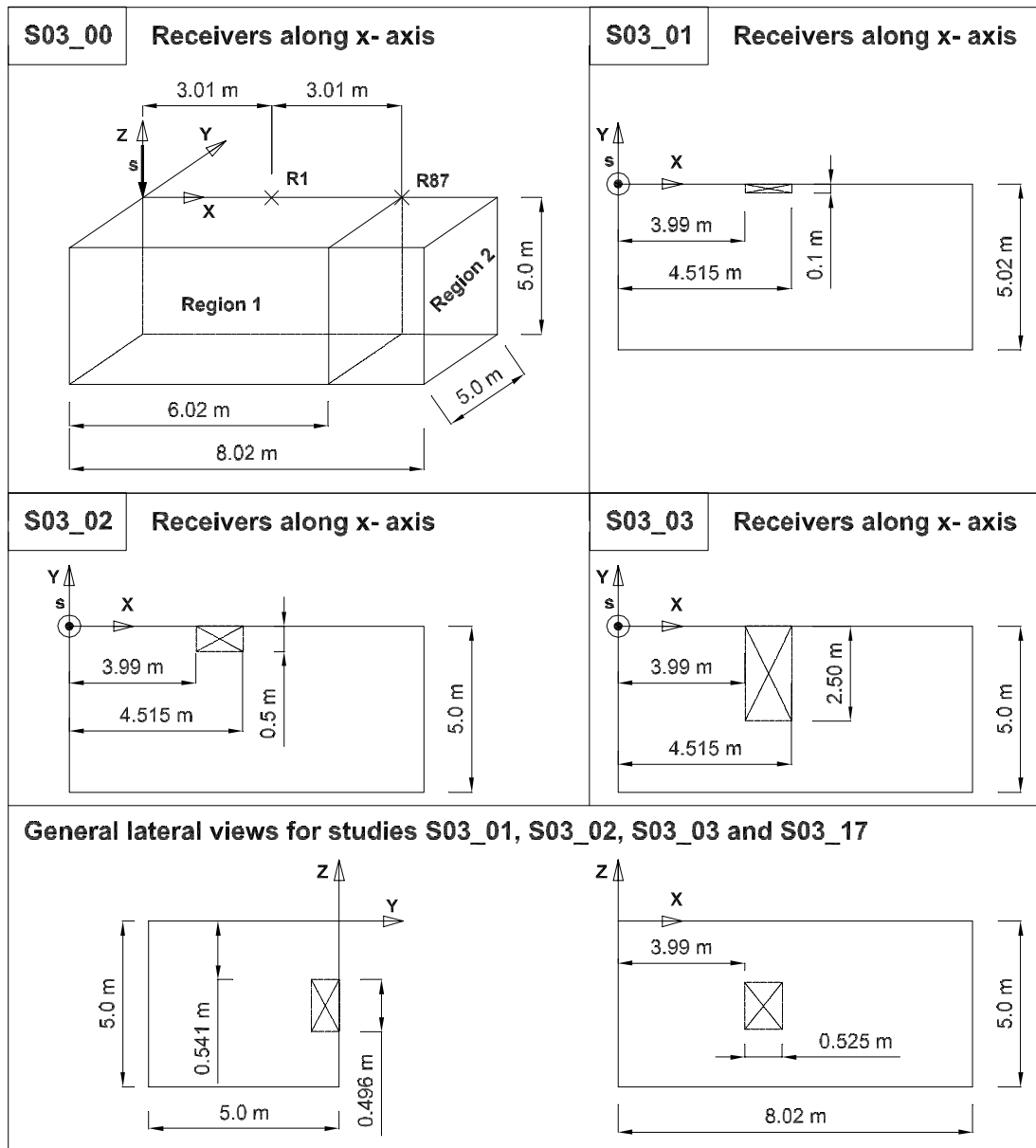


Figure 7-21: Description of 3D models developed in this study (Study S03). The basic model is S03\_00, which consists of two regions. Region 1 consists of uniform grids in x- direction and nonuniform grids in y- and z- directions. Region 2 has non uniform grids in all the three dimensions. The geometry of the voids considered in each study is presented in the associated figure. at the bottom of the figure views of the models in y-z and x-z plains are shown.

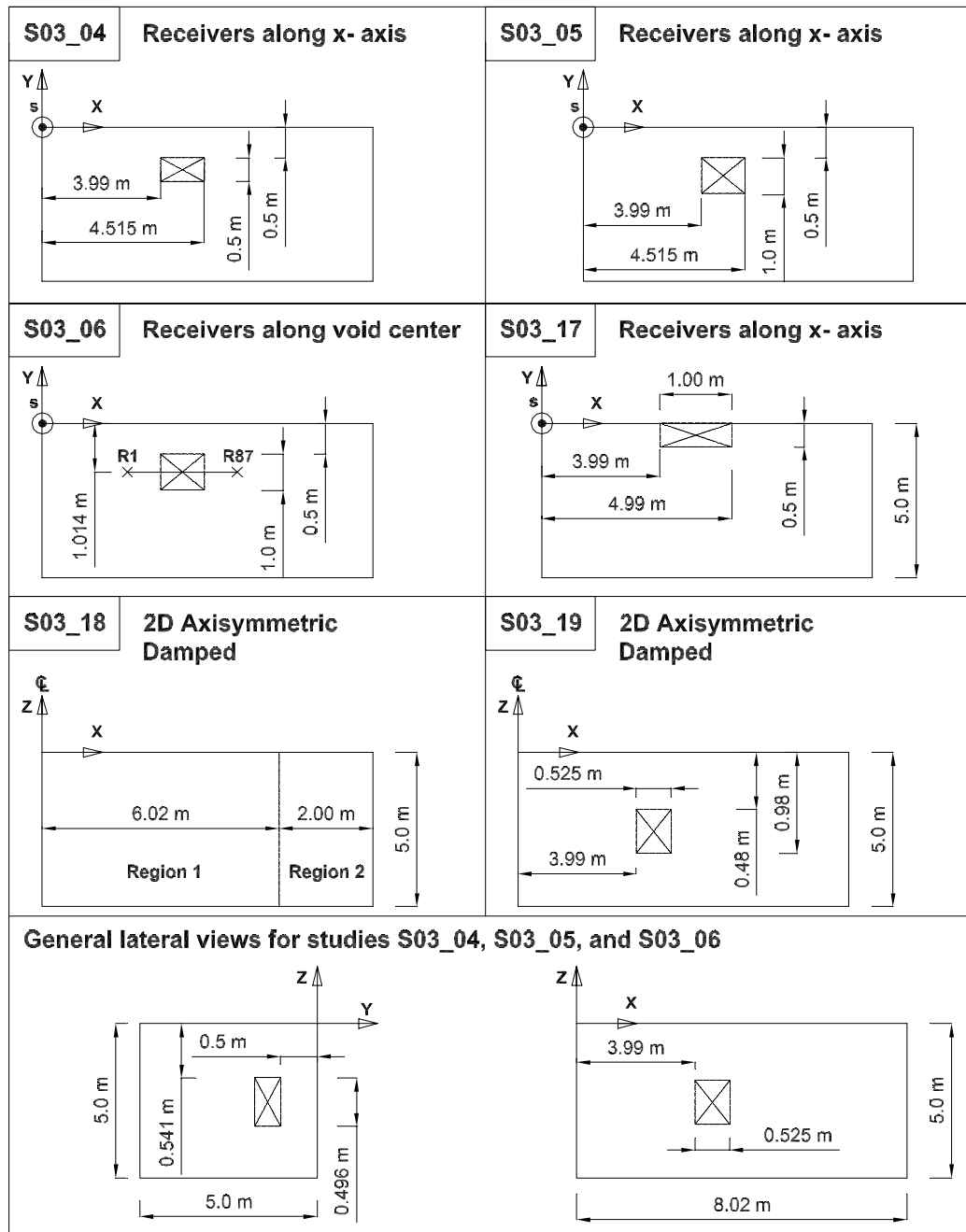


Figure 7-22: Description of 3D models developed in this study (Study S03). The basic model is S03\_00, which consists of two regions. Region 1 consists of uniform grids in x- direction and nonuniform grids in y- and z- directions. Region 2 has non uniform grids in all the three dimensions. The geometry of the voids considered in each study is presented in the associated figure. at the bottom of the figure views of the models in y-z and x-z plains are shown.

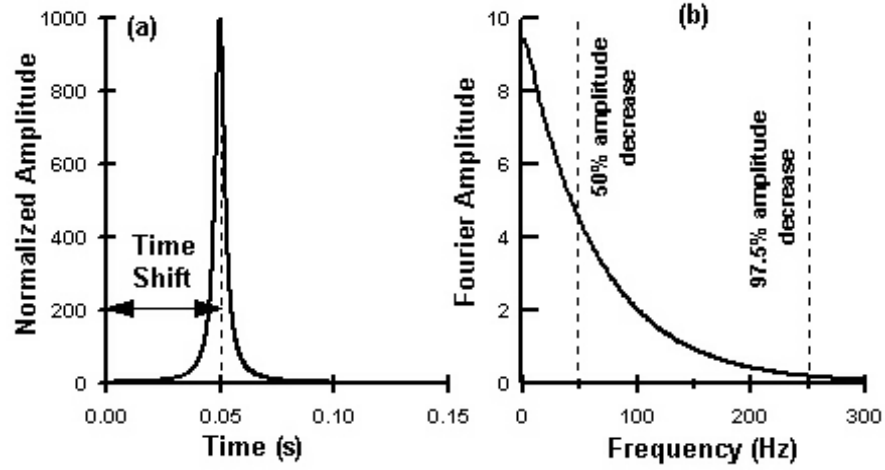


Figure 7-23: Representation of the source applied to model type S03. Plot (a) corresponds to time domain and plot (b) shows the same response in frequency domain. The frequencies at which 50% and 97.5 % decrease in frequency amplitudes occur are marked on plot (b).

Thus, the Nyquist frequency is  $10 \text{ kHz}$  ( $f_{Nyq} = 1/(2\delta t)$ ). The details of the referred calculations are presented in the mathgrams and calculation sheets in Appendix B. The maximum dynamic time for these studies is set to  $t_{max} = 0.26 \text{ s}$ . A Lamb source with  $\psi = 0.0025$  and maximum amplitude of  $1 \text{ kN}$  is applied at  $x = 0, y = 0, z = 0$  in the  $-z$  direction. Figure 7-23 shows the representation of the applied source in time and frequency domains. In 3D models the grid size is large with respect to the 2D models ( $ratio = \frac{0.035}{0.008} = 4.4$ ), thus the source in 3D models contain more energy in low frequency range. The frequencies corresponding to 50% and 97.5% amplitude decrease, are  $48 \text{ Hz}$  and  $250 \text{ Hz}$ , respectively.

In models S03\_01, S03\_02, and S03\_03 cubical voids are inserted as shown in figure 7-21. The void size in  $x$ - and  $z$ - directions are  $L_x = 0.525 \text{ m}$ , and  $L_z = 0.496 \text{ m}$ , and are kept constant. The void size in  $y$ - direction ( $L_y$ ) is  $0.1 \text{ m}$ ,  $0.5 \text{ m}$ , and  $2.5 \text{ m}$  in the mentioned models. As the  $x - z$  plain is a plain of symmetry the actual void size in  $y$ - direction is double of the stated values. The distance of the source and the near and far boundaries of the void in  $x$ - direction are  $3.99 \text{ m}$ , and  $4.515 \text{ m}$ , respectively. The embedment depth of the void (distance between the free surface and top of the void, in  $z$ - direction) is  $0.541 \text{ m}$ . 87 recording points at the surface (receivers) are chosen along the  $x$ - axis in plain  $y = 0$ , the distance between the

receivers is  $0.035\text{ m}$ , and the offset value and total array length is  $3.01\text{ m}$ . The objective of these models is to observe the effect of the out of plain size of the void on the surface responses. To comprehend the results, they are compared to the ones obtained from an axisymmetric model (S03\_19). The properties of the axisymmetric model is exactly the same as the ones that are explained for 3D models.

In models S03\_04, S03\_05 and S03\_06, the cubic void is located with an offset with respect to the plain  $y = 0$ . In these models, the distance between the nearest void boundary and the plain  $y = 0$  is  $0.5\text{ m}$  in  $y$ -direction. The void size in  $y$ -direction is  $L_y = 0.5\text{ m}$  in models S03\_04, and S03\_06, and is  $1.0\text{ m}$  in models S3\_05. The receiver array are deployed with an offset value of  $1.014\text{ m}$  in  $y$ -direction with respect to the source in model S03\_06. All other properties of the models are similar to ones explained before. Model S03\_17 is similar to S03\_02, with a larger void size in  $x$ - direction ( $L_x = 1.00\text{ m}$ ).

The 3D model without void (S03\_00) does not represent a half-space, because the boundaries are too close to the point of application of the source. Thus, it is not practical to compare its results with Lamb solution. Thus, to evaluate the accuracy of the responses the obtained surface displacements are compared to the corresponding responses obtained from an axisymmetric model with the same grid, source and material properties (model S03\_18). Figure 7-24 shows the comparison between the responses from 3D and 2D models with no void. Both displacements in  $x$ - and  $z$ - directions are depicted. In these plots event **A** shows the arrival of  $p$ -wave and event **B** corresponds to the arrival of main Rayleigh wave. Event **C** is associated to the reflection of the energy from bottom boundary of the model. The responses are normalized to the maximum of responses of model S03\_00. In both  $x$ - and  $z$ - displacements a good match is observed between the maximum positive responses. Though, slight differences are observed between the negative amplitudes of the responses. This difference is more observable in the displacements in  $z$ - direction. This difference could occur due to differences in the formulation of Rayleigh damping in FLAC2D and FLAC3D. Though, the exact reason for this difference is not clear. Figure 7-25 shows the frequency spectra of the same responses. To avoid the observed discrepancy in the amplitudes, the responses in each plot is normalized with respect to itself. Thus, the maximum amplitude in each figure is equal to 1. The frequency ranges and the trends show good agreement. The highs and lows in the plots are associated to the

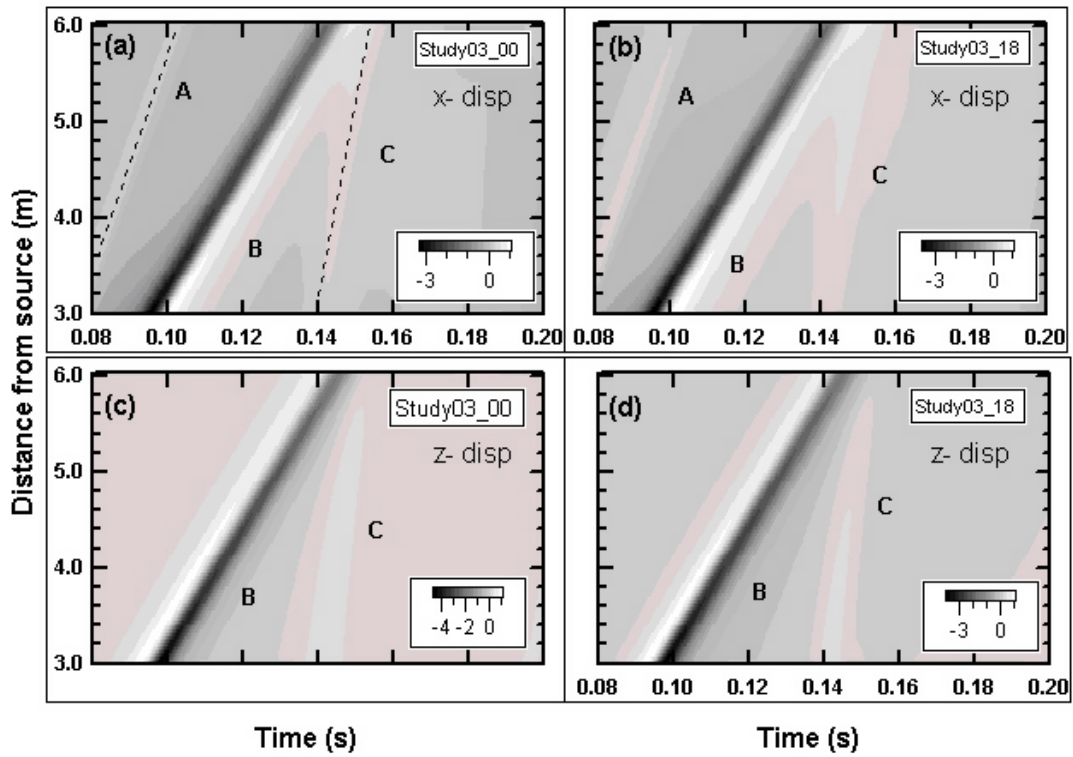


Figure 7-24: Comparison between the time responses of 3D models and 2D axisymmetric models. Plots (a) and (b) correspond to displacements in x-direction and plots (c) and (d) correspond to responses in z- direction. Study S03\_00 is the 3D model without void, and Study S03\_18 is the 2D axisymmetric model with the same properties as model S03\_00.

reflections from boundaries.

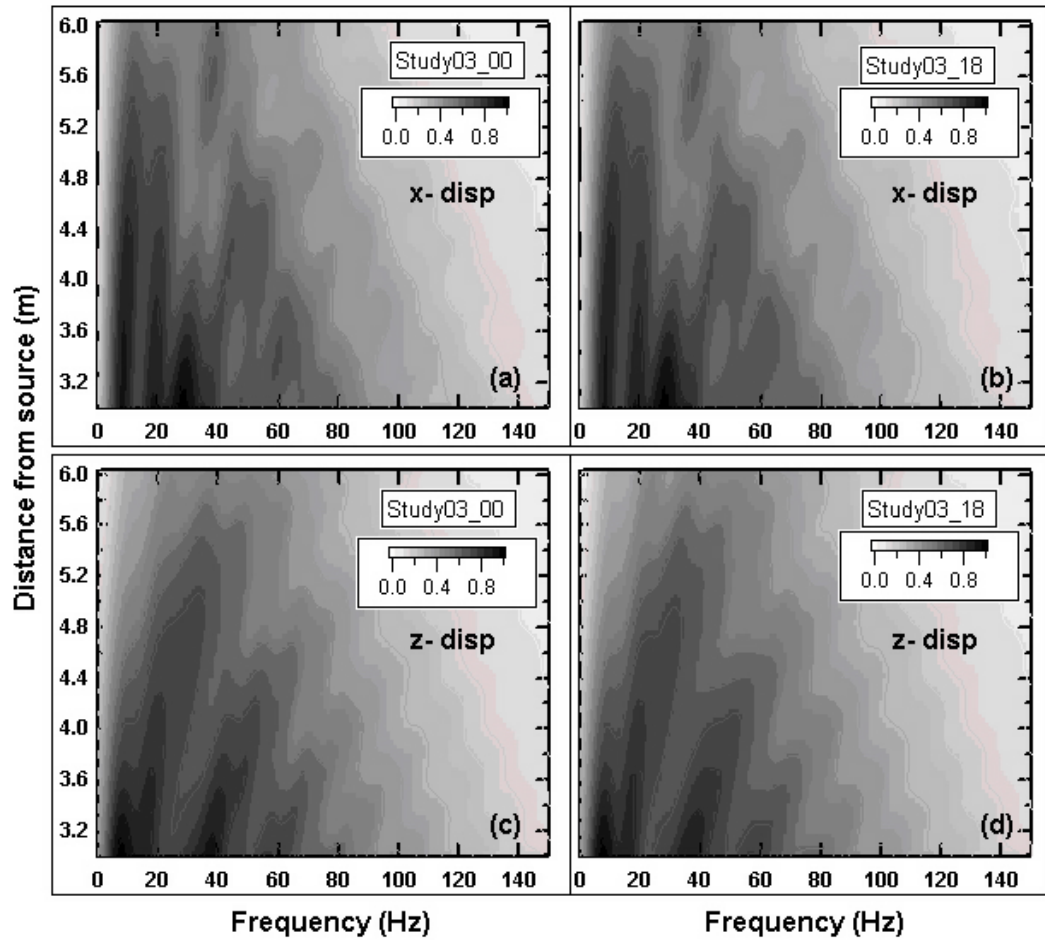


Figure 7-25: Comparison between the spectra of 3D models and 2D axisymmetric models. Plots (a) and (b) correspond to spectra of x displacements and plots (c) and (d) correspond z-displacement spectra. Study S03\_00 is the 3D model without void, and Study S03\_18 is the 2D axisymmetric model with the same properties as model S03\_00.

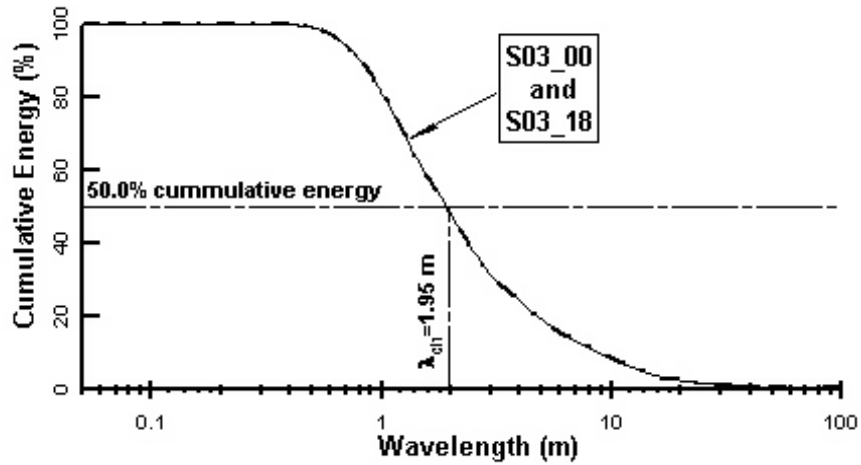


Figure 7-26: Cumulative energy versus wavelength in 3D models. The corresponding cumulative energy from model S03\_18 (2D axisymmetric model) is also depicted in the figure, but the difference between the two graphs is negligible. The measured characteristic wavelength is  $\lambda_{ch} = 1.95 \text{ m}$ .

Figure 7-26 shows the cumulative energy versus wavelength, calculated from the records of the first receiver of models S03\_00, and S0318. The two graphs match well and are almost identical. The graph starts with a horizontal branch that continues to wavelengths of about 0.5 or 0.6 m, which indicates that short wavelengths carry small amounts of energy. The characteristic wavelength, as defined in Chapter 6, is  $\lambda_{ch} = 1.95 \text{ m}$ , for 3D models.

The following sections present the obtained results along with the discussions.

### 7.6.2 Effect of out of plain dimension of the void on surface responses

To evaluate the effect of out of plain dimension of the void ( $L_y$ ) at the surface, the responses of models S03\_01, S03\_02, and S03\_03 are compared to the responses of axisymmetric model in the presence of void (S03\_19). The corresponding contour plots in time and frequency domains are presented in figures 7-27 and 7-28, respectively. The responses of 3D models are normalized to the maximum of corresponding responses of model S03\_00, and the responses of 2D model (S03\_19) are normalized with respect to responses in model S03\_18.

The time responses of model S03\_01 (plot 'b' Figure 7-27) do not show the effect of the void at the surface, i.e. reflections from void boundaries. Similar observation is made in frequency domain (plot 'b' in Figure 7-28). As the out of plain dimension of the void increases, the effect of void is more observable in time and frequency domains (plots 'c' and 'd' in Figures 7-27 and 7-28). Clear reflections from void boundaries, larger surface amplitudes in both frequency and time domains, and energy concentration in the vicinity of the near boundary of the void can be distinguished. These observations indicate that the surface responses are affected by all the three dimensions of the void. In other words, the surface responses reflect a three dimensional interaction of the incident energy and the cavity. In cases that out of plain dimension of the cavity is small with respect to the other dimensions and/or the available wavelengths in the incident wave, the void might not be detectable from surface responses. In the studied case (S03\_01) the out of plain dimension of the void is  $L_y = 0.2 \text{ m}$  (considering the plain of symmetry at  $y = 0$ ). As it was seen in figure 7-26, the incident wave does not carry a significant energy in the wavelengths close to this value of  $L_y$ . Thus, the wave traverse the medium almost without observing the cavity. By increasing  $L_y$  the trends of the responses get closer to the trends in the axisymmetric case. In the studied cases the effect of cavity is observable for  $L_y = 0.5 \text{ m}$  ( $\cong 0.25\lambda_{ch}$ ) and more. Thus when the the out of plain dimension of the void is larger than  $0.25\lambda_{ch}$  two dimensional or three dimensional models should give similar results.



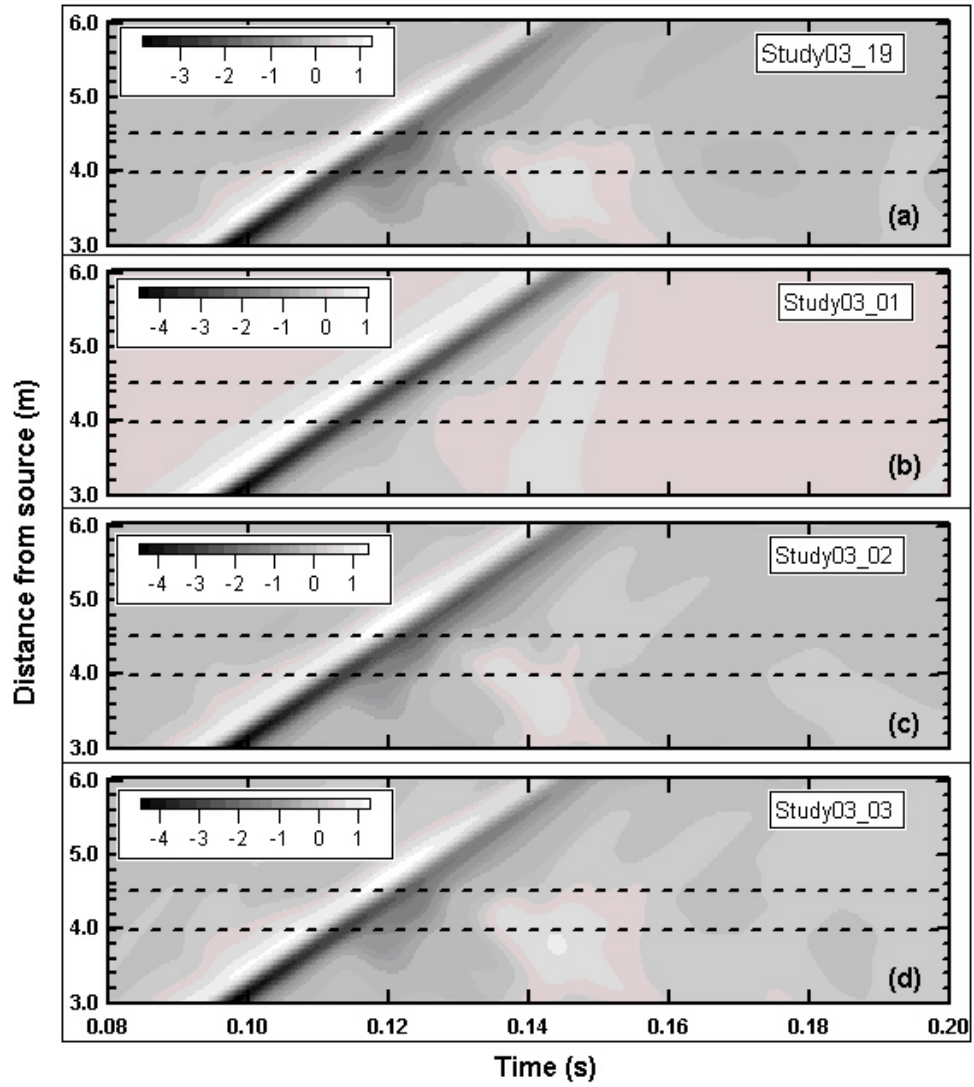


Figure 7-27: Effect of out of plain dimension of the void on surface responses in time domain. Plot (a) corresponds to the 2D axisymmetric model. The out of plain dimension of the void ( $L_y$ ) is 0.1 m, 0.5 m, and 2.5 m, in plots (b), (c), and (d), respectively.

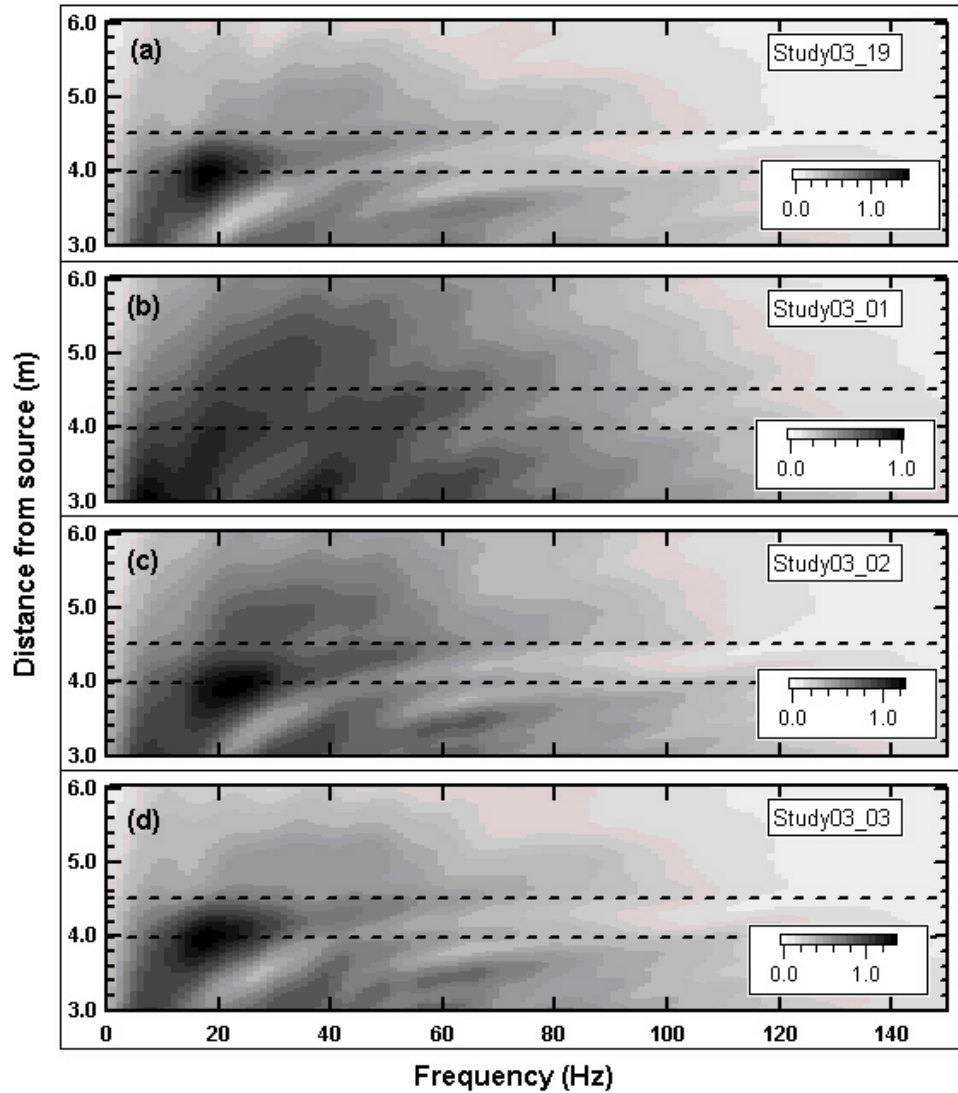


Figure 7-28: Effect of out of plain dimension of the void on surface responses in frequency domain. Plot (a) corresponds to the 2D axisymmetric model. The out of plain dimension of the void ( $L_y$ ) is 0.1 m, 0.5 m, and 2.5 m, in plots (b), (c), and (d), respectively. The dashed lines show the projected boundaries of the void to the surface.

### 7.6.3 Effect of void offset on the surface responses

So far, the assumption in the conducted numerical studies was that the source, the receivers array, and the void are aligned. The literature review in chapter 4, also shows that this assumption was made in all the reviewed works. Due to the unknown location of the void in the field, the alignment of void with the receiver array is not always possible. Thus, it is very probable that an MASW test be performed in the vicinity of a void, and not over the top of it. Further, in some cases it is possible that the source is not aligned with the receivers array. This case might happen when passive sources (such as ambient noise) are used in the MASW test. The latter problems are investigated by the aid of 3D modelling of the MASW test, and the results are presented in this section. Chapter 9 compares the discussed numerical results with field and laboratory scale results.

As explained in the previous sections, in models S03\_04, S03\_05, and S03\_06, the void is placed with an offset in the  $y$ - direction with respect to plain  $y = 0$ . In S03\_04, and S03\_05 the source and the receivers array are aligned, and in model S03\_06 the receivers array is aligned with the void center, and the source has an offset (Figure 7-22). The contour plots in Figure 7-29 compares the results in time domain. All the presented responses are normalized with respect to the maximum of model S03\_00. Plot 'b' shows that an offset equal to the size of the void ( $0.5 m$  or  $\cong 0.25\lambda_{ch}$ ) causes a significant decrease in the amount of the observed reflections. Reflections with small amplitudes are observed from near boundary, and the reflections from far boundary are not seen. A comparison between plots 'b' and 'a' (in which the void is aligned with the receivers array and source) shows that the maximum amplitudes are less in the, when the void has an offset. Plot 'c' shows the contour plot of responses in study S03\_05, where the void dimension in  $y$ - direction is doubled with respect to S03\_04 ( $L_y = 1.0 m \cong 0.5\lambda_{ch}$ ) and the offset in  $y$ - direction is kept constant. As it is seen, even doubling the out of plain size of the void can not compensate for the mitigating effect of the void offset with respect to the receivers array line. In plot 'd' the trends of the responses are more similar to the ones in plot 'a'. In both plots the receivers are aligned with the void center, but in 'd' the source is not in the same alignment. Reflections from both sides of the void, and amplitude increase with respect to the responses in S03\_00 are observed.

Figure 7-30 shows the same responses in frequency domain. All the responses are normalized

with respect to the corresponding values of study S03\_00. In plots 'b' and 'c' the effect of void is observed as energy concentration close to the near boundary of the void. This effect is observed as localized energy, without a significant amplitude amplification, as opposed to the case without any void offset (plot 'a'). The obtained spectrum show significant differences (in trends) in compare to the no void case (plot 'b' figure 7-28), but the effect of the void is not as conspicuous as it is when there is no void offset (plot 'a' figure 7-30). This observation confirms that responses in frequency domain are more sensitive to the existence of a void than time domain responses. Plot 'd' shows the spectrum when receivers array and the void center line are aligned and the void is applied with an offset in  $y$ - direction (Study S03\_06). The effect of void is seen as energy concentration close to the near boundary of the void, and as amplitude amplification. The amplification is slightly less than the ones observed in the reference study S03\_02.

Generally, the set of studies, presented in this section, indicate that void detection is very susceptible to the alignment of the receivers array and the void center line. Even small misalignments (in the order of the size of the void) can overshadow the effect of the void in the time and frequency responses. Frequency responses are more prone to the effect of the void, as observed in the previous sections and chapters. The detection of a cavity from surface responses is feasible, when the source is not in the same alignment with the void and receivers array. Therefore, sources such as ambient noise can be used for void detection.

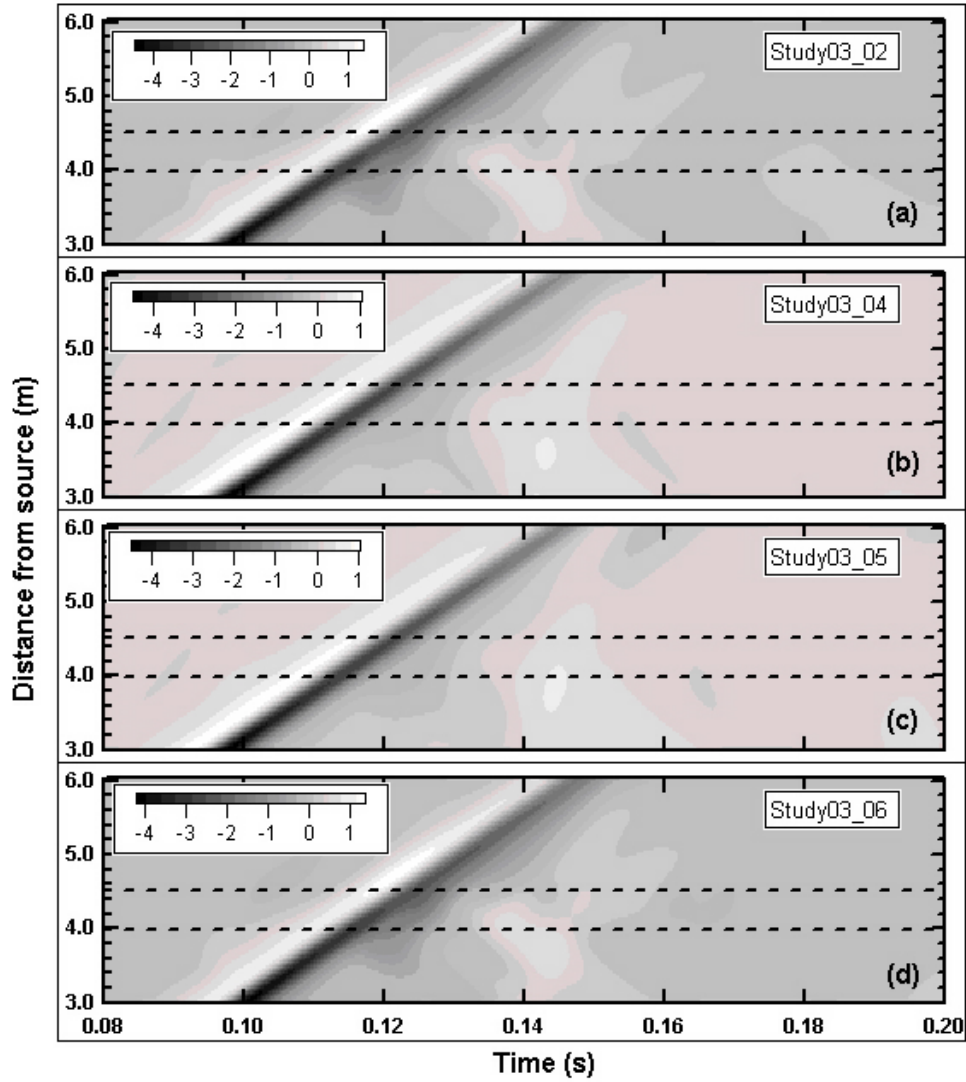


Figure 7-29: Effect of void offset in time domain. Plot (a) correspond to the case that the void, receivers array, and the source are in aligned. Plots (b) and (c) show that void offset from the receivers array has a strong influence on the observed responses at surface. Plot (d) shows that when the void is aligned with the receivers array, the void can be detected even when the source is offset.

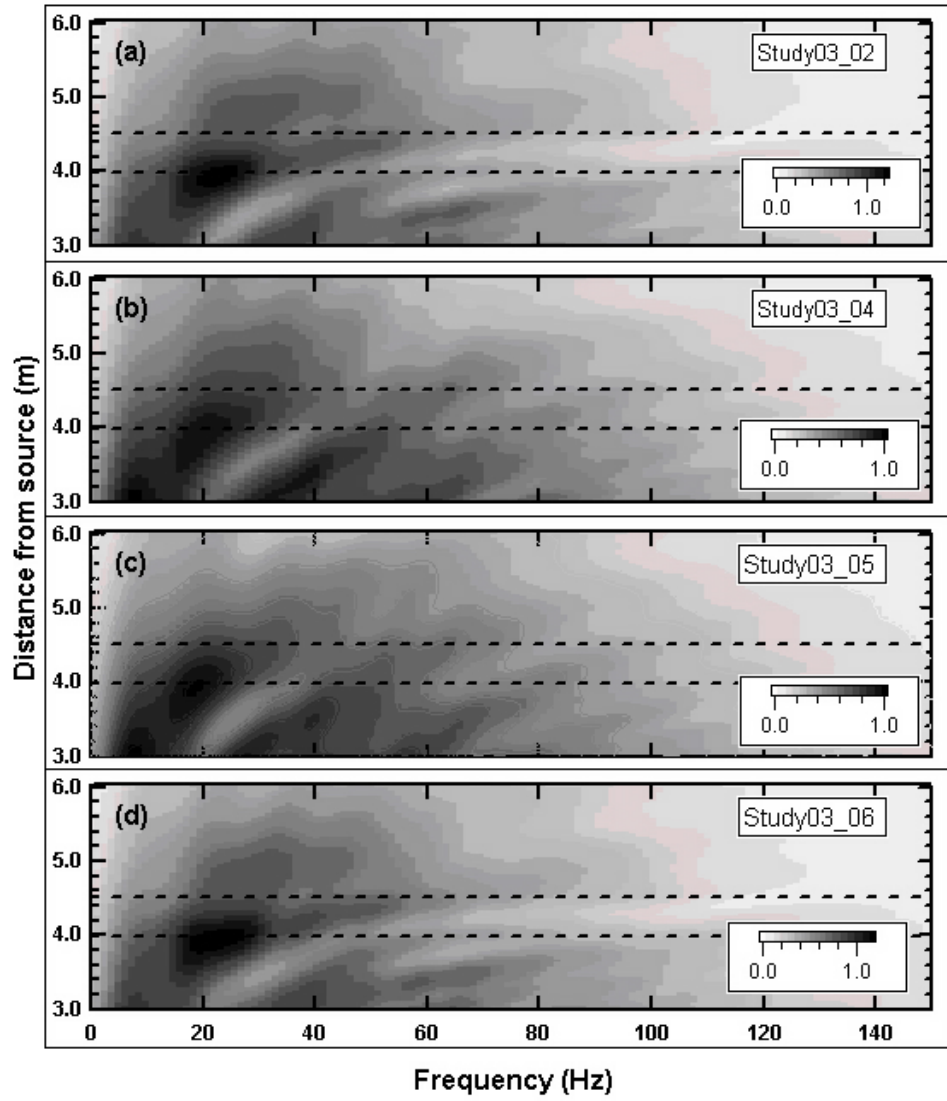


Figure 7-30: Effect of void offset in frequency domain. The effect of void is observed as energy concentration in the vicinity of void in the spectrum.

## 7.7 Summary of the conclusions

Chapter 7 presented the studies that were conducted to investigate the effect of different void characteristics on the surface responses. The effect of width and depth of the void, and the combined effect of void and natural and inverse layering of the medium were investigated. The effect of out of plain dimensions of the void on the surface responses were examined, through 3D modelling of the void and medium.

The width of the void has a significant effect on the observed responses at the surface. As the width increases more energy is trapped in the void region. The trapped energy is associated to the excitation of antisymmetric Lamb waves. In frequency domain, the trapped energy is seen as a region with energy concentration. When the width of the void is small in compare to the main wavelengths of the incident wave, most of the interaction is in the form of reflections. When the width of the void and the main incident wavelengths are comparable, most of the interaction is in the form of trapped energy. Therefore, in the latter case the width of the region with concentrated energy is comparable to the width of the void; whereas, in the former case the width of this region is much larger than the width of the void.

The surface responses are very sensitive to the embedment depth of the void. It is found that the combined effect of void size, embedment depth and the energy content of the incident wave determines the detectability of the void. The frequency range that the void interacts with, has a lower and upper bound. The lower limit is influenced by the void size, and the upper limit is susceptible to the void depth. The concept of cut off frequency is introduced that can be used to estimate the embedment depth of the void.

The effect of layered medium on the propagating energy reassembles to a high pass filter. This filtering effect can overshadow the interactions of the void with the propagating energy. The results confirmed that different sides of the void interact with different frequencies.

The three dimensional analyses showed that the size of the out of plain dimension of the void has an observable effect on the surface responses. Hence, very narrow cavities are not detectable by investigating their effect on the surface responses. Further, it was shown that the alignment of the receivers array with the void is an important parameter in the detection of the void.

## Chapter 8

# Attenuation Analysis of Rayleigh Waves Method

### 8.1 Introduction

In Chapters 6 and 7, the behavior of Rayleigh waves in the presence of voids was studied in detail. It was revealed that the void starts to vibrate with the medium when it is excited by Rayleigh waves. Due to this interaction, part of the incident energy is reflected, part of it is transformed into body waves, another part is trapped by the void, and the rest of the energy is transmitted. At the surface, these effects are seen as ripples and energy concentrations in the vicinity of the region that contains the void. Similar behavior was observed in the models with two layers and in three dimensional models. All these observations imply that the transmitted energy should be significantly attenuated with respect to the incident wave. Consequently, an analysis technique is developed based on the evaluation of the attenuation of Rayleigh waves at the surface. The technique is called Attenuation Analysis of Rayleigh Waves (AARW). The objective of AARW method is to determine the location and embedment depth of a void using the surface responses. The following sections describe the basic concepts of the method and the details of the procedure. The procedure is applied to several numerical models and the results are presented. To verify the AARW method, it is applied to the responses recorded at the surface of a prototype (Chapter 9). The results show that AARW is a promising tool for detecting underground cavities and estimating their extents.



## 8.2 Development of the method

Figures 8-1 to 8-4 show the displacement fields in a media with two layers and a void (model S02\_14). The displacements are due to the transmission of energy in the form of Rayleigh waves. As explained in the previous chapters the interaction of p- and s-wave fronts with the void are not significant in compare with Rayleigh waves, thus their effect are neglected. The R-wave velocity in the upper layer is  $C_R = 102.7 \frac{m}{s}$ . The distance between the near and far boundaries of the void and the source are 5.496 m, and 6.496 m, respectively. Therefore the arrival time of the main R-wave event to the near ( $t_{near}$ ) and far ( $t_{far}$ ) boundaries of the void are:

$$t_{near} = \frac{5.496 \text{ m}}{102.7 \frac{m}{s}} + 0.015 \text{ s} = 0.0685 \text{ s} \quad (8.1a)$$

$$t_{far} = \frac{6.496 \text{ m}}{102.7 \frac{m}{s}} + 0.015 \text{ s} = 0.07825 \text{ s} \quad (8.1b)$$

in the above calculations the 0.015 s is the time delay between the maximum amplitude of the source and the start of the excitation.

Plot 'a' shows the displacement field at time  $t = 0.030s$ . The body wave fronts are developed and surface waves are generated. Plot 'b' ( $t = 0.060s$ ) shows that the R-wave front advanced toward the void. As the R-wave goes farther from the source lower frequencies are developed fully, and the R-waves penetrates deeper into the medium. The main R-wave event, corresponding the peak of the source, is observed as vectors projected outward from the surface. Plots 'c' and 'd' show the displacement fields just before the arrival of main R-wave energy to the void ( $t = 0.065s$  and  $t = 0.0675s$ , respectively). The surface displacements are observed as vectors projecting out of the surface. The arrival of the initial fronts of the R-waves do not introduce any significant interaction with the wave. Plots 'e' and 'f' show the interaction of main R-wave front with the near boundary of the void. The void boundaries start to vibrate, that reflects back part of the incident energy, and scatters another part into the medium. Plots 'g' and 'h' show the interaction of the R-wave front with the far boundary of the void. Again, energy scattering and reflecting occurs. The plots in figure are adopted from the movies provided in

Appendix CD-Chapter8.

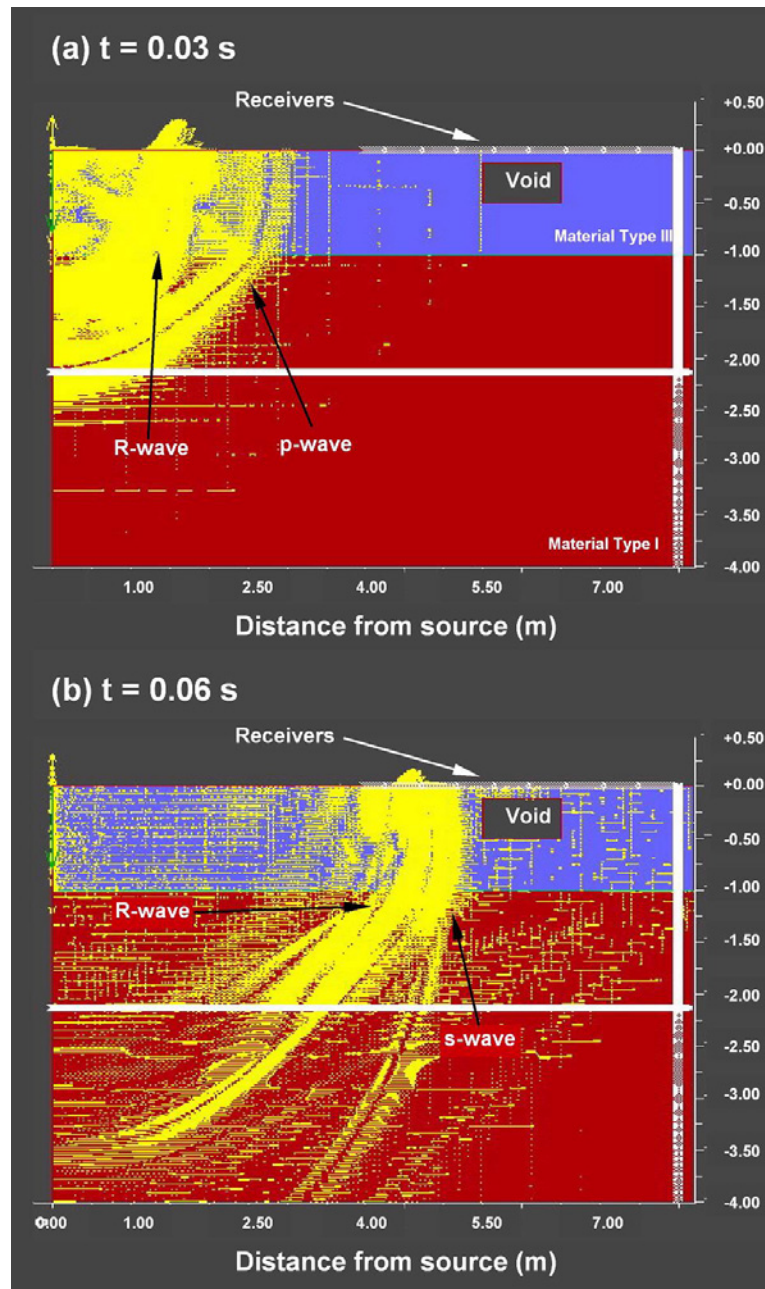


Figure 8-1: Displacement field in a two layered medium, and a void at different times. Due to interaction of the main R-wave event with the void, energy partitioning occurs. Thus, the transmitted energy is attenuated.

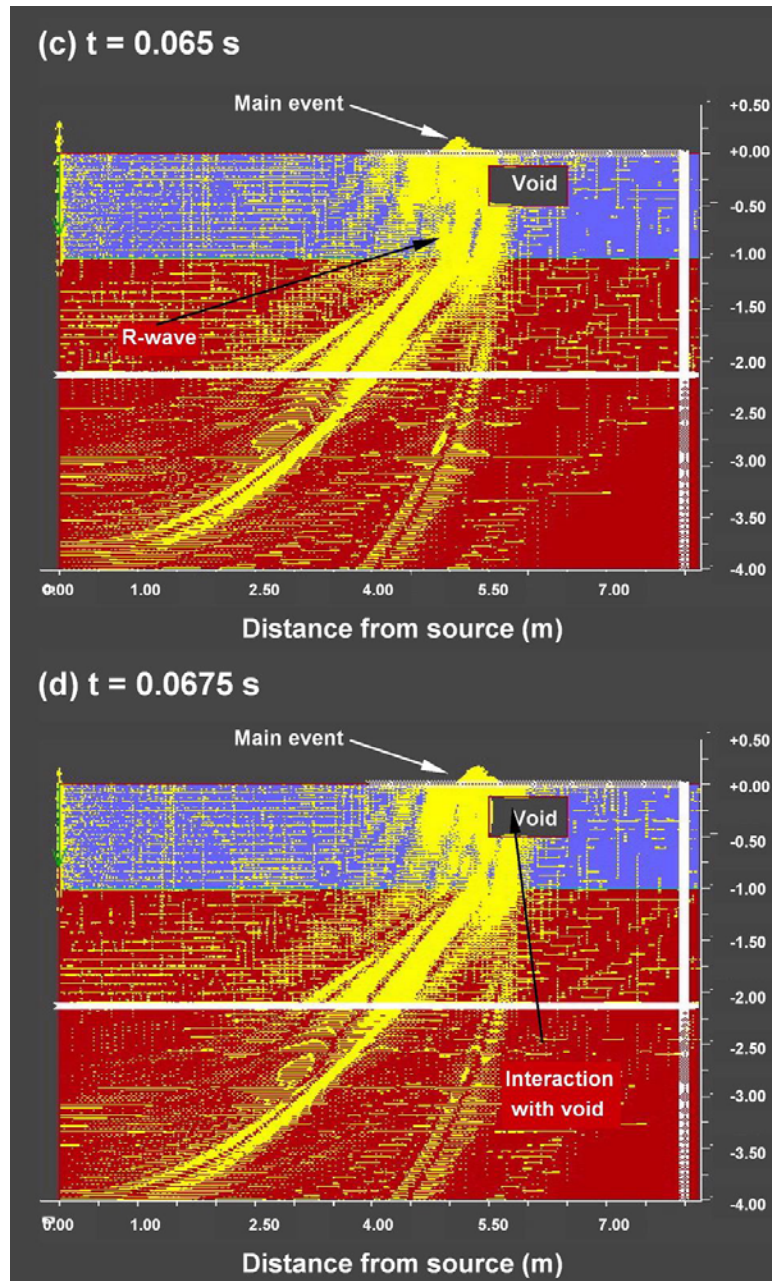


Figure 8-2: Displacement field in a two layered medium, and a void at different times. Due to interaction of the main R-wave event with the void, energy partitioning occurs. Thus, the transmitted energy is attenuated.

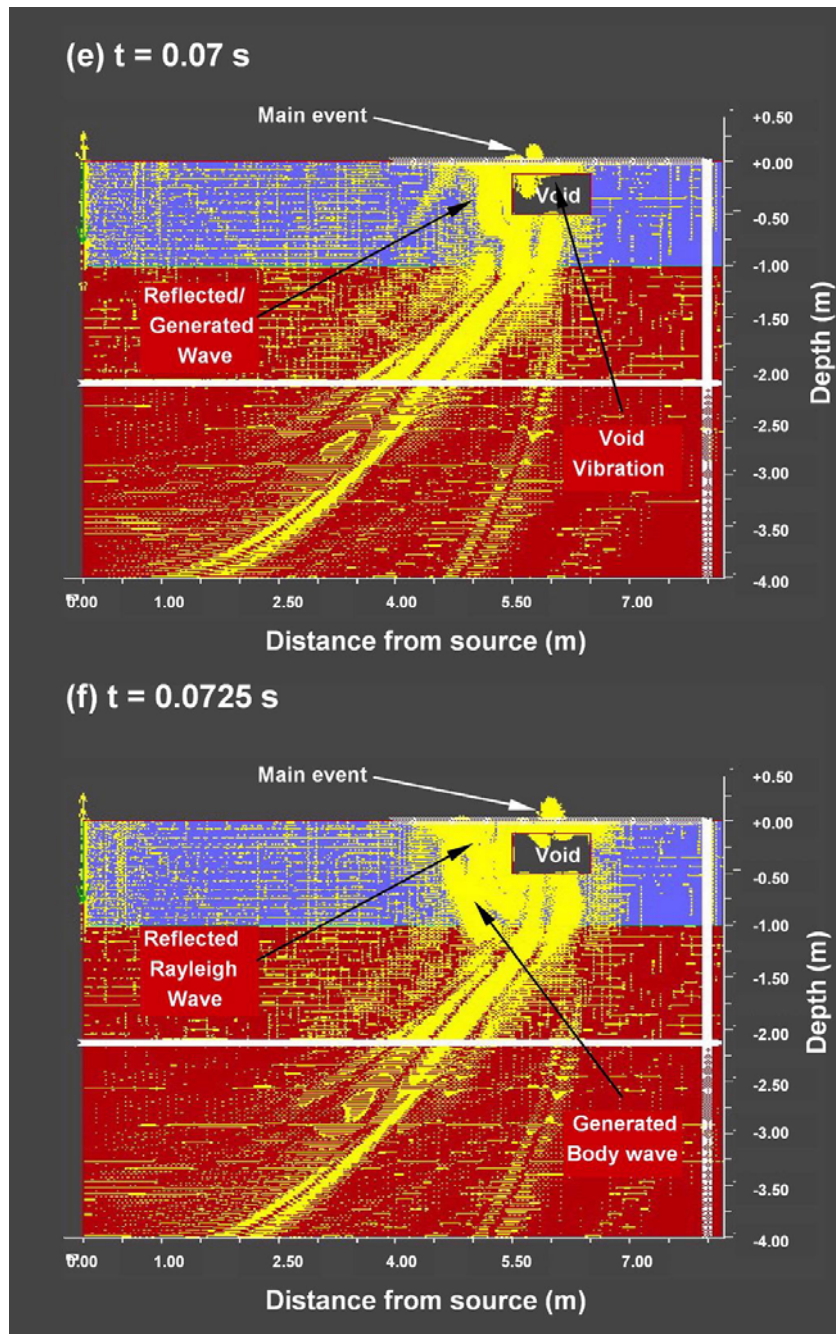


Figure 8-3: Displacement field in a two layered medium, and a void at different times. Due to interaction of the main R-wave event with the void, energy partitioning occurs. Thus, the transmitted energy is attenuated.

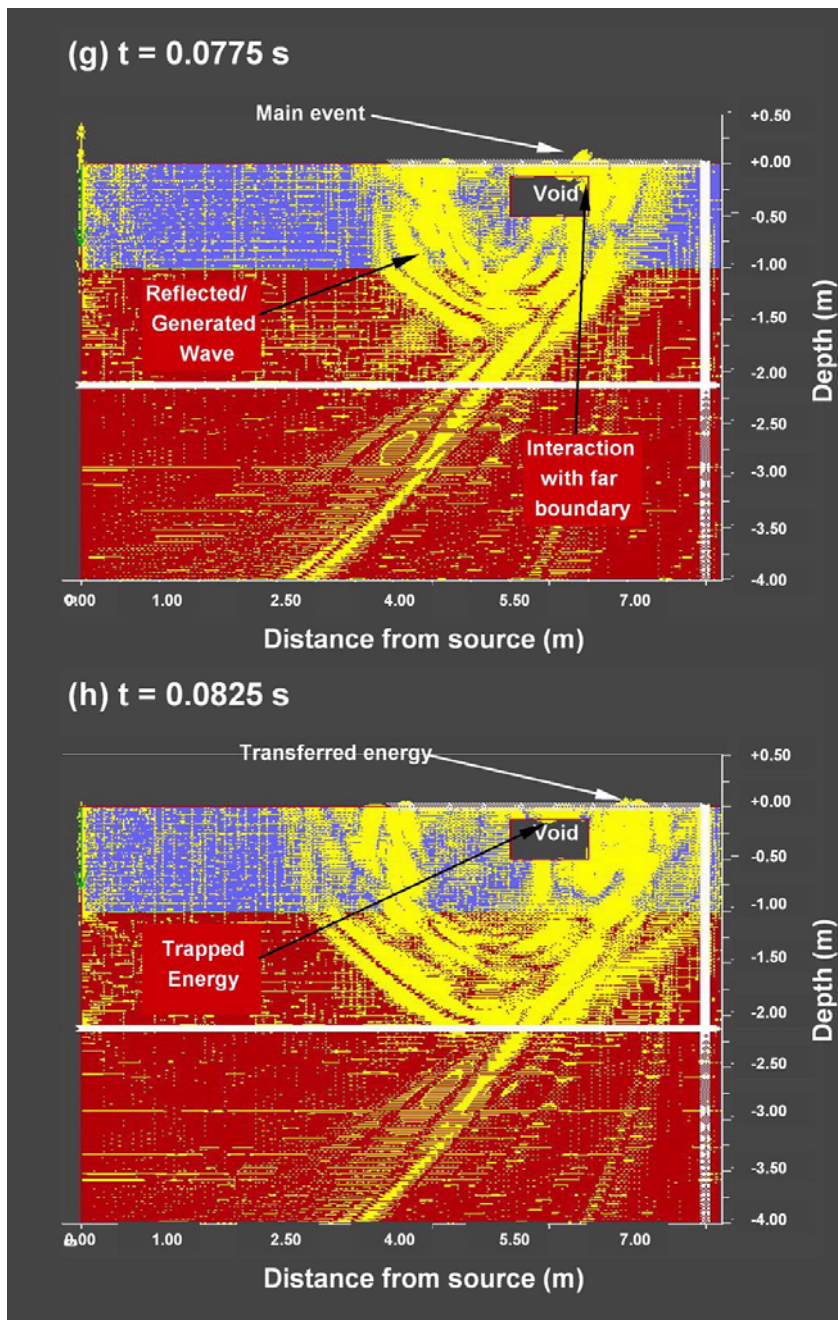


Figure 8-4: Displacement field in a two layered medium, and a void at different times. Due to interaction of the main R-wave event with the void, energy partitioning occurs. Thus, the transmitted energy is attenuated.

## Attenuation analysis

The previous analyses in the time and frequency domains show clearly that voids affect the attenuation characteristics of the recorded signals. In the presence of a void, wave attenuation accounts for reflections, refractions, and mode conversion of the wave fronts at void boundaries. Furthermore, the trends of the frequency contour plots imply that this apparent attenuation varies with frequency. The contour plots in figure 8-5 show representative spectrum of two different models. After the void, a region with highly attenuated amplitudes can be distinguished in both plots (region 'C'). Further, the region 'C' continues up to a frequency that is named cut-off frequency ( $f_{cu}$ ). Experiments with different models, show that the wavelength of the cut-off frequency is very close to the embedment depth of the void. In models S00\_07 and S00\_12 (figure 8-5a and b) the embedment depths of the voids are 0.16 m and 0.32 m, respectively. The cut-off frequencies measured from plots 'a' and 'b' are 368 Hz and 193 Hz with a corresponding wavelength of 0.17 m and 0.33 m, respectively. This trend is observed for voids with embedment depths of up to  $1.5\lambda_{ch}$  ( $\lambda_{ch} = 0.36m$ ) .

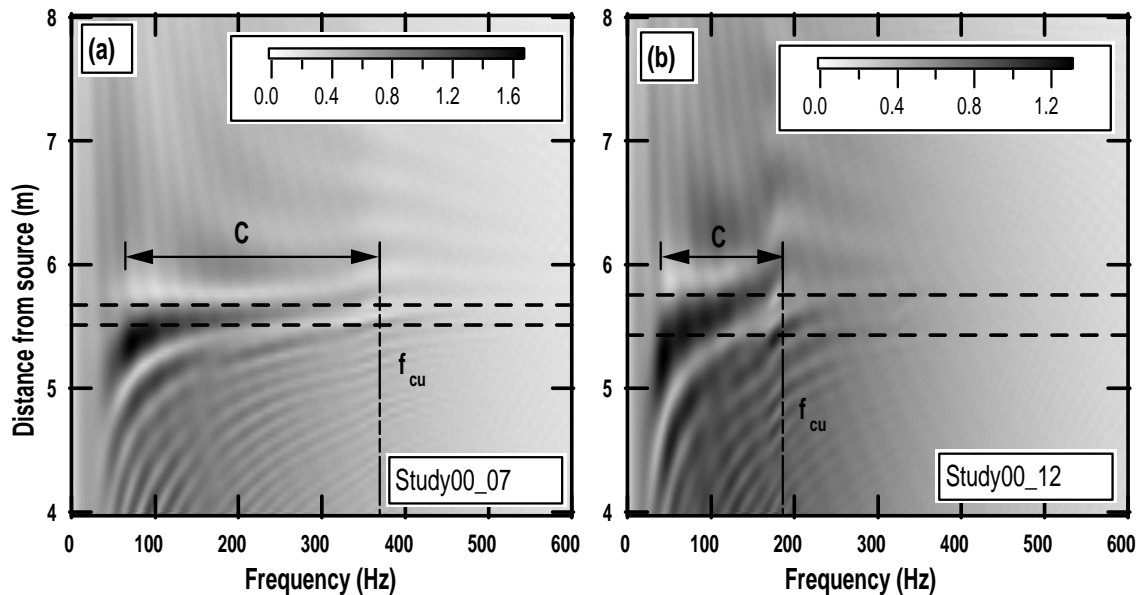


Figure 8-5: Frequency responses at the surface of two models (x displacements). The attenuated region (region C) and the cut off frequency ( $f_{cu}$ ) are marked on the figures.

In general, scattering and reflecting of the wave cause the energy to be spread in a larger volume. Thus, a significant attenuation of surface responses is expected at the location of near and far boundaries of the void. To evaluate the attenuation of waves different formulations are defined and used ([18]). In this study the following three formulations are assessed for their potential use in the AARW technique.

$$\Delta = \ln \left| \frac{u_i}{u_{i+1}} \right| \quad (8.2a)$$

$$\alpha = \frac{\Delta}{\lambda} \quad (8.2b)$$

$$\xi = \frac{1}{2\pi} \Delta \quad (8.2c)$$

in equation 8.2,  $u_i$  and  $u_{i+1}$  are any two successive peaks in time responses or frequency spectra,  $\lambda$  is wavelength,  $\Delta$  is logarithmic decrement,  $\alpha$  is attenuation coefficient, and  $\xi$  is damping ratio. The above definitions are vastly used in soil dynamics [135]. Among the above definitions, the logarithmic decrement (LD) is relatively easy to measure in practice, and showed to have sufficient accuracy for the purpose of this study. Thus, it is used in the development of AARW method. To account for the variation of the spectrum amplitudes with distance and frequency the following form of LD values is used in this study:

$$LD = Ln \left[ \frac{U_{j,z}}{U_{j,z+1}} \right] \quad (8.3)$$

where  $U_{i,z}$ , and  $U_{i,z+1}$  are the spectrum values at frequency  $f_j$  and receivers  $z$  and  $z + 1$ , respectively. Equation 8.3 evaluates the attenuation of the amplitudes of a single frequency with distance. Based on the above definition, a positive  $LD$  value indicates that the ratio  $\frac{U_{j,z}}{U_{j,z+1}}$  is larger than 1, thus implies attenuation. Conversely, an  $LD$  value of less than 1 is an indication of amplification.

Figure 8-6 shows the LD values for the horizontal component of the surface displacements for two different locations and different models. The time corresponding responses are multiplied by a gain function to eliminate the effect of geometrical damping. Figure 8-6 'a' and 'b' show the results for the model S00\_01 (homogeneous half space); where the logarithmic decrement should



be zero (no material damping or geometrical attenuation). The small fluctuations in these plots are due to the reflections from the model boundaries. In the presence of a void (models S00\_07 and S00\_09), the measured values of attenuation or amplification before the void ( $d = 4.352m$ ) are significantly larger than the values for the model S00\_01; this indicates that the reflected frequencies interact with the propagating front either constructively or destructively before the void. Although, the LD values after the void ( $d = 6.752m$ ) fluctuate more than the corresponding values in the model without void, the relative change are smaller than the changes before the void.

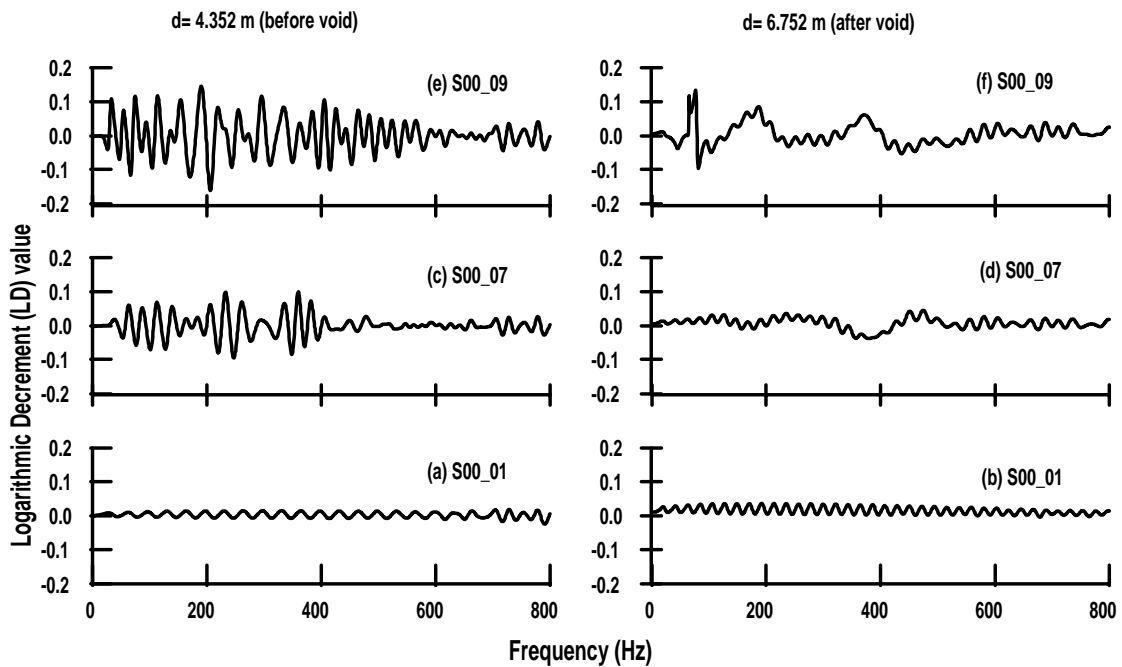


Figure 8-6: Calculated LD values for three different models, and two different locations. The signals are multiplied by a gain function to remove the effect of geometrical damping. plots 'a' and 'b' correspond to model S00\_01 (model with no void). The other plots correspond to two different models with void. Strong fluctuation are observed in the LD values in the presence of void.

The contour plot in figure 8-7 illustrates the LD values for model S00\_09. In the presence of a shallow void (embedding depth  $h \leq 1.5\lambda_{CH}$ ), the LD values change significantly with distance and frequency. Before the void, lower frequencies are magnified as the distance from the void

increases, whereas higher frequencies are magnified closer to the void. A possible explanation for this behavior is that larger wavelengths need larger distances to develop completely; thus, the influence of the reflected low-frequency components (larger wavelengths) are visible at farther distances from the void. Consequently, the maximum magnification/attenuation curves are bent asymptotically before the void. On the other hand, after the void the maximum attenuation is almost parallel to the void boundary because the void attenuates all frequency components. In front of the void, the waves are first magnified and then attenuated, whereas after the void they are attenuated first and then magnified. This characteristic of the LD plots can be utilized readily to locate an underground void. The LD values oscillate up to a cut-off frequency then they tend to remain constant. Experiments with different embedment depths and void sizes reveal that the wavelength of the cut-off frequency is close to the embedment depth of the void. The physical interpretation is that a void interacts with the waves whose wavelengths are close to or larger than its embedment depth. Consequently, smaller wavelengths propagate without recognizing the inhomogeneities. As the embedment depth of the void increases, the pattern of the LD values remains the same but the cut off frequency decreases. Therefore, the cut-off frequency is a quantitative parameter that can be used for estimating the embedment depth of a void.

### 8.3 Proposed method for detecting a void

It is concluded from the above observations that the energy content of the surface responses is different before and after the void. Specifically, the surface responses recorded before the void carry more energy than the ones after void. Part of this attenuation is due to geometrical damping, and part of it is due to scattering/reflecting of the wave by the void. As explained in Chapter 2, geometrical damping is frequency independent, and is conversely related to the distance from source. Thus, to remove the effect of geometrical damping the signals in space domain are multiplied by the following gain function:

$$g_z = \sqrt{\frac{d_z}{d_1}} \quad (8.4)$$

where  $g_z$  is the value of gain function at the location of receiver  $z$ , and  $d_z$  and  $d_1$  are the

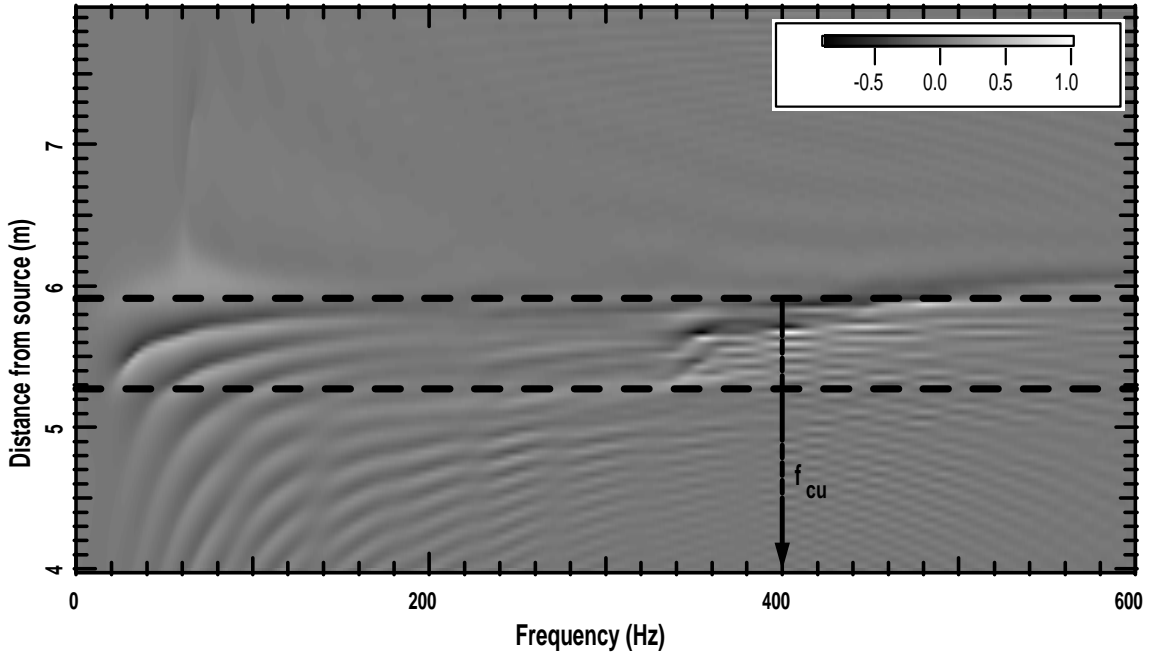


Figure 8-7: Logarithmic decrement (LD) contour for model S00\_09. Attenuation or amplification occurs up to a cut off frequency, the corresponding wavelength is close to the embedment depth of the void.

distances of receivers no  $z$  and 1 from the source, respectively. Figure 8-8 shows the gain function and its effect on a typical response. As it is seen, the effect of the defined gain function is to magnify the signal amplitudes. The magnification is more observable at larger distances from source. As the gain function is defined in the space domain, it can be either applied to time responses or frequency spectrum.

As the effect of amplification and attenuation is more observable in frequency domain responses (Chapter 6), the energy calculations are performed in the frequency domain. The energy is a function of signals amplitude, thus the signal energy ( $E_z$ ) at each receiver location is estimated by:

$$E_z = \sum_f |A_{f,z}|^2 \quad (8.5)$$

where  $|A_{f,z}|$  is the amplitude of the spectrum at frequency  $f$  for receiver number  $z$ . The

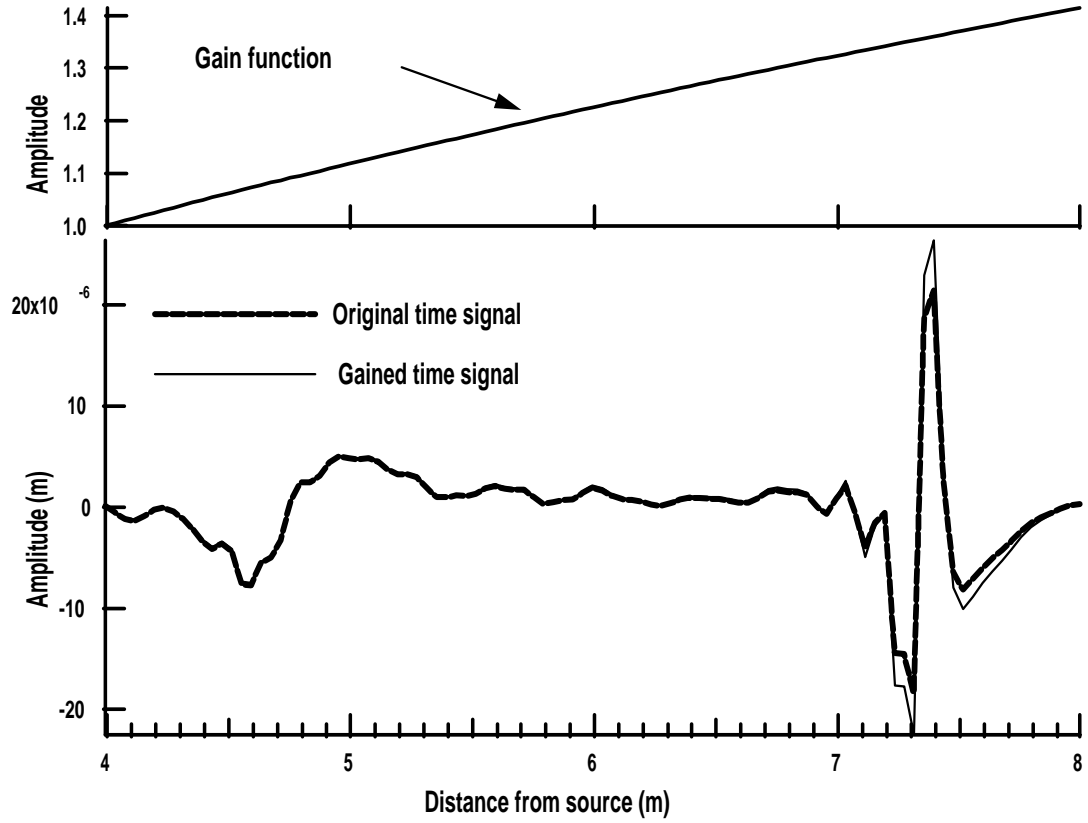


Figure 8-8: Representation of the gain function (top), original signal and the signal magnified by the gain function (bottom). The signal corresponds to the surface responses of model S00\_09 at time  $t = 0.15$  s.

summation is performed over the reliable frequency range, which depends on the geometry of the recording array, background noise, and etc. Physically, the parameter  $E_z$  is an indication of the cumulative energy at the location of each receiver.

The normalized energy-distance parameter ( $NED$ ) is defined as the cumulative spectrum energy normalized to the maximum energy across the array:

$$NED_z = \frac{E_z}{\max(E_z)} \quad (8.6)$$

equation 8.6 indicates that  $0 \leq NED_z \leq 1$  and is a dimensionless parameter. The variation of  $NED$  values with distance show the location of the void.

To illustrate the application of  $NED$  parameters for the detection of cavities, the calculated  $NED$  values for five different models are depicted in figure 8-9. The solid lines correspond to horizontal displacements and the dashed lines correspond to vertical displacements. In all cases, the responses are multiplied by the gain function in the space domain to eliminate the effect of geometrical damping, and  $\alpha = 4$ . For the homogeneous medium without void (model S00\_01, figure 8-9a) the calculated values for vertical and horizontal components are equal to one at all the locations. Small variations in the values are due to the existing noise. In model S00\_01, the only source of energy attenuation was geometrical damping, and its effect was removed by the application of gain function. Thus, in this case the  $NED$  values show that there is no variation of energy with distance. In the other four cases the  $NED$  value increases to its maximum ( $NED = 1$ ) and then drops to a minimum, and again rises to another high. In all the cases the maximum  $NED$  value occurs in the vicinity of near boundary of the void. The second high in the  $NED$  values occurs in proximity of the far boundary of the void. The plots in figure 8-9 show that the  $NED$  values obtained from horizontal displacements better reveal the location of the void. When the width of the void is small in compare to the distance between the receivers ('c'), the highs and lows might not be distinguishable. In such cases, the location of near and far boundaries of the void can not be estimated. This technique works even in the presence of different layers with different impedances (plots 'c' and 'd'). With the increase in the embedment depth of the void, the technique loses its accuracy, and it is estimated that after a depth of about  $1.5\lambda_{ch}$  the method is not applicable.

## 8.4 Proposed method for estimating the embedment depth of a void

As mentioned in the previous sections, a simple method to quantify the attenuation in the presence of a void is to calculate the logarithmic decrement parameter which is commonly used in engineering applications. In this section a procedure is defined to estimate the embedment depth of a void. The new procedure is based on equation 8.3. Two new parameters are introduced: the amplified logarithmic decrement (ALD) and its normalized cumulative summation (CALD):

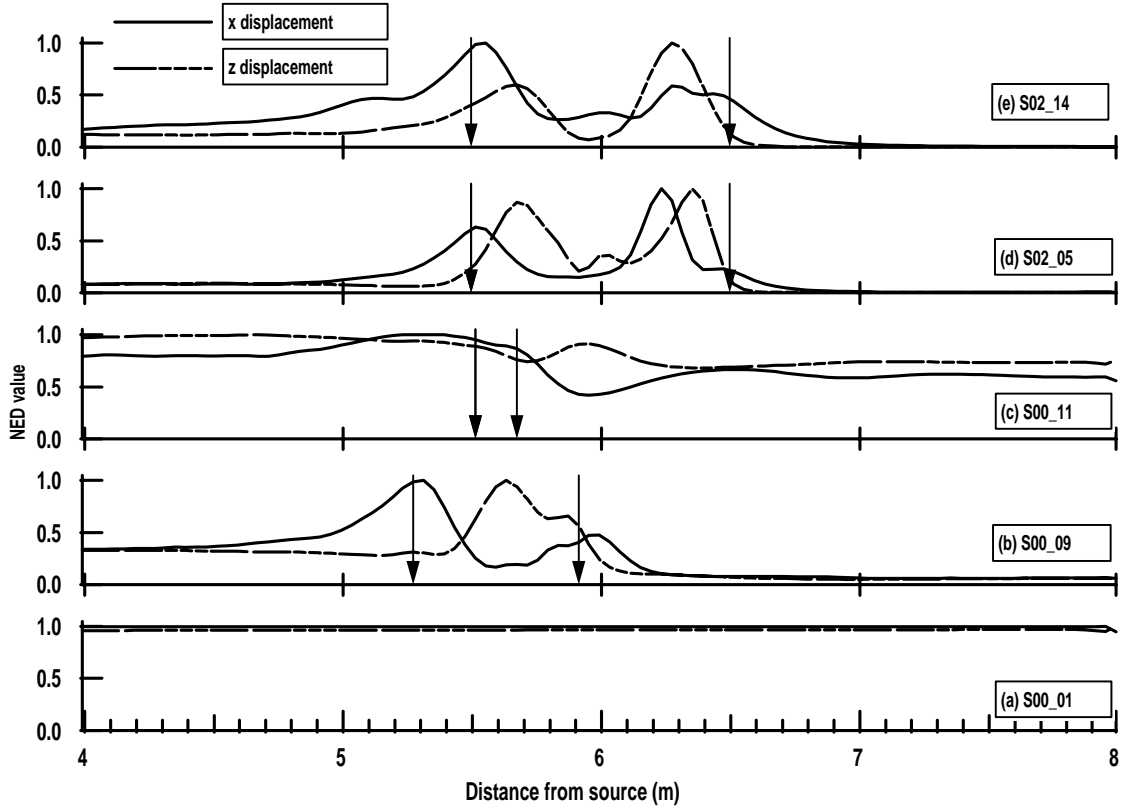


Figure 8-9: Variation of NED parameter with distance from source for five different cases. The solid and dashed lines correspond to horizontal and vertical component of surface displacements, respectively. The arrows show the near and far boundaries of the void, projected to the surface. High and low in the NED values show are indication of void.

$$ALD_j = \sum_{z=1}^{z_{\max}-1} \left[ \text{Ln} \left( \frac{U_{j,z} + \alpha}{U_{j,z+1} + \alpha} \right) \right]^\beta \quad (8.7a)$$

$$CALD_j = \frac{1}{T_{ot}} \sum_{jj=1}^j (ALD_{jj}) \quad (8.7b)$$

$$\text{and } T_{ot} = \sum_j ALD_j \quad (8.7c)$$

where  $f_j$  refers to the  $j$ th frequency,  $z_{\max}$  is the maximum number of receivers,  $U_{j,z}$  and  $U_{j,z+1}$  are the Fourier spectrum amplitudes at frequency  $f_j$  for two consecutive receivers num-

bered  $z$  and  $z+1$ . Two experimental constants are added to equation 8.7 to reduce the effect of noise (parameter  $\alpha$ ) and to enhance the peaks (parameter  $\beta$ ). The standard definition of logarithmic decrement (equation 8.3) is sensitive to low values of the term  $U_{j,z+1}$ , and large  $LD$  values can exist when the spectral amplitude tends to zero. To diminish this effect, the constant  $\alpha$  is added to the equation. The summation over the distance in equation (8.7a) is used to obtain the average fluctuation of the amplifications or attenuations over the reliable frequency range. When the values of  $U_{j,z}$  and  $U_{j,z+1}$  are small, the ratio in equation (8.7a) tend to 1; hence, the contribution to the  $ALD$  value tends to zero.  $\beta$  is an empirical even number to magnify the peaks and to keep the  $ALD$  values positive. For this study,  $b = 4$  and  $\alpha = 0.5\%$  of the maximum value of the spectrum magnitude. The value  $Tot$  is the summation of  $ALD$  values over the reliable frequency range. The  $CALD_j$  parameter is the cumulative value of  $ALD_j$  and is function of frequency or wavelength. The  $CALD$  parameter varies between 0 and 1.

Numerical simulation results for different models show that the plot of the  $CALD$  parameter versus wavelength is a useful tool to estimate the embedment depth of the void. The use of the  $CALD$  parameter is justified by the experimental and numerical evidence showing that an underground void produces surface amplifications at certain frequencies. Figure 15 presents typical results for the variation of the  $CALD$  parameter as function of wavelength for different models; the dashed lines show the top and bottom boundaries of the void. For comparison the plot obtained for model without void (S00\_01) is also included. The discontinuities in the plots happen between the top and bottom boundaries of the void and the corresponding wavelength gives a good estimation for the average depth of the void. Experiments with different void sizes and embedment depths confirm this result. For shallow voids (models S00\_07 and S00\_09), the estimated embedment depth has an error of 1.5%; however, the error increases with increasing depth; for embedment depths larger than  $1.5\lambda_{CH}$ , the error could be as large as 50%.

The particle displacements of R-waves show that the wave carries almost no energy after the depth of one wavelength. Therefore, frequencies with wavelengths smaller than the embedment depth of the void are almost unaffected; whereas, frequencies with larger wavelengths interact with the void. The strongest interactions with the void occur at frequencies for which the wavelengths are close to the embedment depth of the void, and the corresponding attenuation

or magnification is more conspicuous.

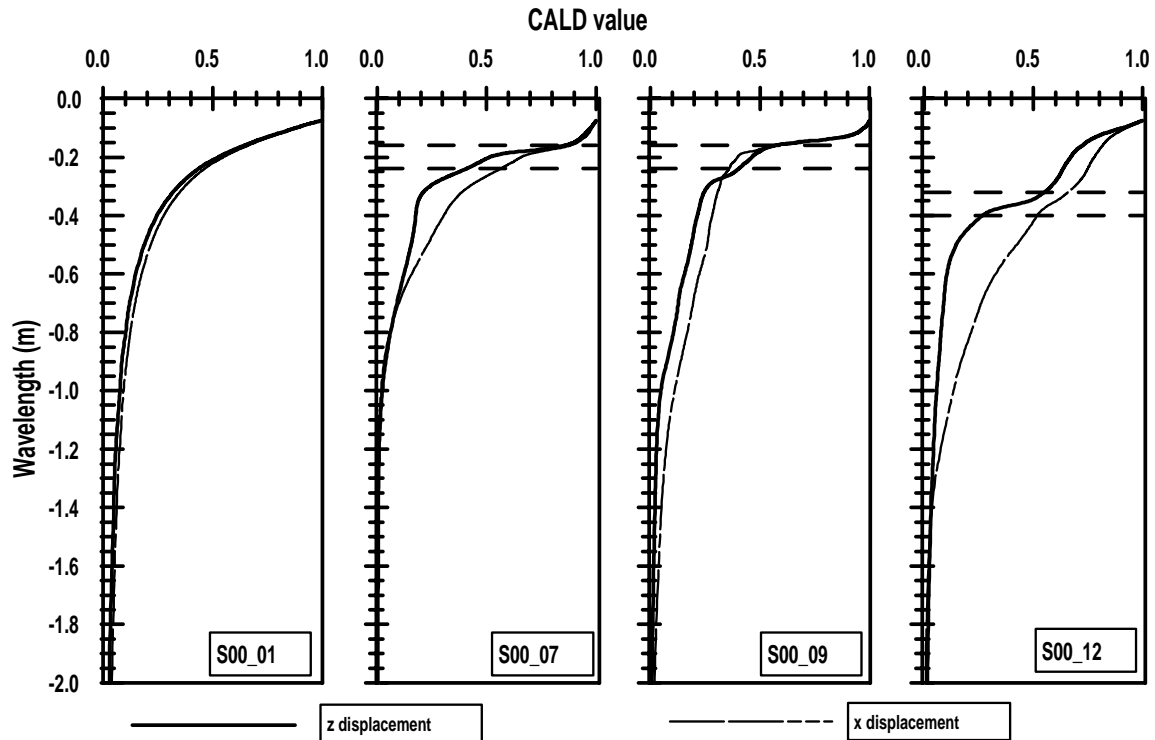


Figure 8-10: CALD values obtained from vertical and horizontal components of the surface responses. The vertical axis shows the wavelength. The horizontal dashed lines show the top and bottom boundaries of the void in each case. The discontinuities in the plots occur up to a wavelength which is close to the embedment depth of the void.

## 8.5 Summary of the Attenuation Analysis of Rayleigh Waves (AARW)

The *NED* and *CALD* parameters represent a promising tool for detecting a void and estimating its embedment depth. The following procedure is proposed:

- Design of the MASW test. The general guidelines set by Hiltunen and Woods [52] and Al-Hunaidi [101] can be used to select the spacing and source-transducer configuration. A priori estimation of the size and embedment depth of the void will reduce the fieldwork



significantly.

- Data collection. It is recommended that both the vertical and horizontal components of the surface displacement should be collected. In addition, more accurate estimations of the location and embedment depth of the void can be obtained by carrying out tests from both sides of the array of transducers.
- Time domain analysis. From the time domain data, the group velocity of the main event is calculated. This velocity is used to ensure that the main event corresponds to surface waves without strong contamination from body waves.
- Plot of the normalized energy distance parameter (*NED*). The maximum peak in the *NED*-distance plot corresponds to the location of the near boundary of the void. The results are valid only for voids with an embedment depth smaller than  $1.5\lambda_{\max}$ .
- Plot of the normalized cumulative logarithmic decrement values (*CALD*) verse wavelength. This plot gives an estimation of the embedment depth of the void. The discontinuities in the plot occur generally at a wavelength close to the embedment depth of the void. The deeper the void is the smaller the accuracy of the procedure. For embedment depths larger than  $1.5\lambda_{\max}$ , errors larger than 50% are expected.

## Chapter 9

# Verification of the results with experimental data

### 9.1 Introduction

This chapter explains the results MASW field tests conducted over 2 crown pillars in Sudbary, Ontario. Further, it explains the results of laboratory scale MASW tests performed on a sand box prototype. The objective is to verify the numerical results by comparing them to the practical data. The discussions provided in previous chapters are used to explain the field and laboratory observations. The test results are utilized to verify the numerical observations, explained in Chapters 6, 7 and 8. The experiments consist of

### 9.2 Abandoned mine detection at INCO mine site

#### 9.2.1 Site description

Crown pillars are horizontal pillars of rock and soil left above underground stopes mined near the ground surface. These pillars may fail, sometimes suddenly and catastrophically, leaving a hole through to the ground surface [136]. To maintain the stability, crown pillars are usually backfilled with sand. Schematic of a typical crown pillar is depicted in figure 9-1. Failure or collapse of crown pillars might cause surface subsidence or failure. Figure 9-2 shows a catastrophic failure of crown pillars in Crawford Mountains, Crawford, Utah [137]. Thus,

detection of the crown pillars and delineation of their extents are crucial for industry.

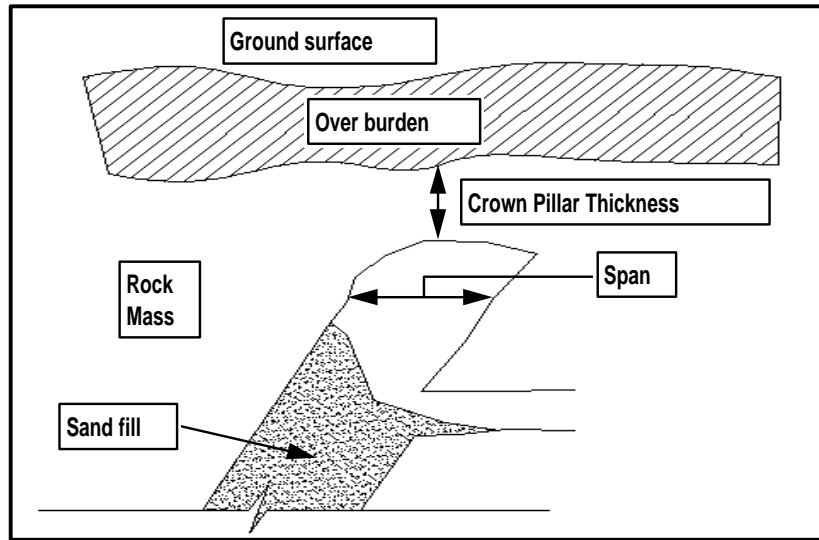


Figure 9-1: Schematic of a typical crown pillar.

MASW tests were performed over two near-surface mine workings to determine if geophysical methods could be used to accurately locate crown pillars, and assess the condition of the overlying geological medium [129]. The copper-nickel mine site is contained within a steeply dipping shear system ( $60^\circ$  to  $80^\circ$ ) consisting of felsic and mafic norite, meta sediments, and greenstone. The sulphide deposit was first developed in the early 1900's and has been mined intermittently. Mining is still active in the deposit. The studied crown pillars were developed in the 1940's. Due to the incompetence of the rock in the hanging wall, caving failures were observed during mining of one of the two investigated workings, which was backfilled later with hydraulic sand to provide support and minimize further collapse. Glaciofluvial deposits, consisting of sand and silt, overlie the bedrock in the area to a depth of approximately 20 m. Figure 9-3 shows an aerial map of the investigated mine site. Directly above the crown pillar 2, there is an old railway that runs adjacent to the mine property. The surface condition over this crown pillar consists of a combination of slag rock, and mine waste rock from the creation of a mine road adjacent to the site. Relatively, the presence of the mine did not affect the surface conditions over crown pillar 1, which consists of a sand/soil overburden supporting small trees



Figure 9-2: Crown pillar failure in Crawford Mountains, Rich County, Utah.

and brush. The minimum depth to void is 50 *m* for both crown pillars. The width of crown pillar 1 is approximately 30 *m* and the width of crown pillar 2 is about 15 *m*. These crown pillars have known location, geometry, and surface conditions. Phillips et. al. [130] summarizes the results from seismic and resistivity surveys over crown pillar 1. This study uses the results obtained over the two crown pillars to verify the conducted numerical studies.

### 9.2.2 Experimental methodology

MASW tests were performed along three lines over each crown pillar, one to either side and one directly above the crown pillar. The instrumentation consisted of a 24-channel seismograph and 8 *Hz* geophones. The geophone to geophone distance is 5 meters, for a total geophone spread length of 115 meters. Tests with different source types showed that with the available equipment, the only source that can provide enough energy in the low frequency range is passive source. Conventionally, in an MASW test, the R-waves travel parallel to the survey line. Moreover, it is better to know the location of the source to estimate the maximum reliable wavelengths available in the recorded spectra. Therefore, as passive source does not always satisfy these conditions, the use of passive energy is not always feasible. On the other side, passive seismic

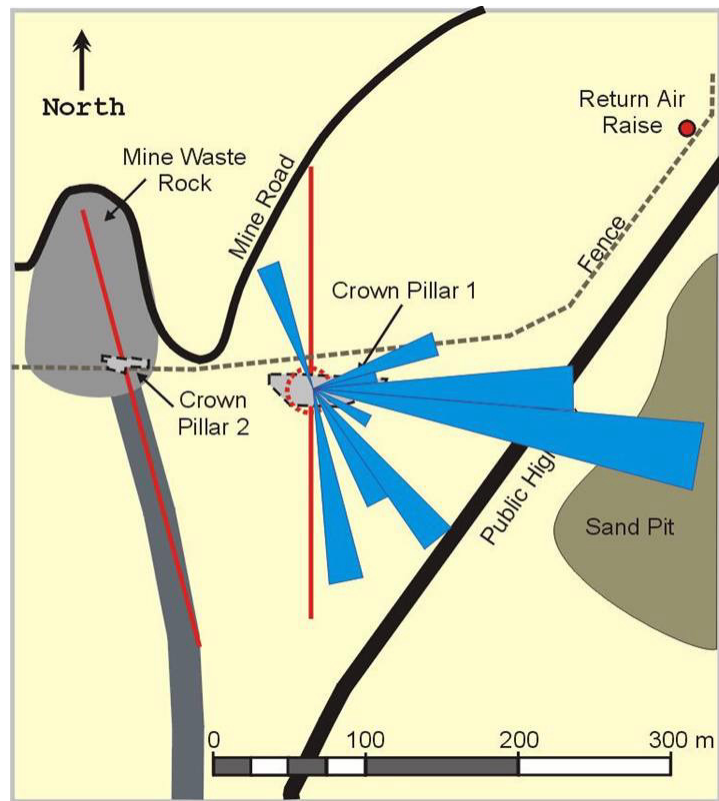


Figure 9-3: Aerial map of the investigated mine site. The testing lines are shown by solid lines over the crown pillars. The rose diagram shows the direction and relative intensity of observed passive seismic energy sources ([129]).

source, if present, often contains significant low frequency energy. Passive seismic sources were present at the study site, in the form of a well traveled highway and active gravel pit, to the east of the site, and an active mine site to the north-west. To determine the direction from which the passive seismic energy was traveling, a 60 m diameter circle of geophones was setup and passive seismic energy was measured 30 times (figure 9-3). A total of 47 separate seismic events were identified from the collected seismic traces. The measurement shows that the majority of the passive seismic energy is coming from the east, and it is a combination of gravel pit operations and highway traffic. Only four events were identified as coming from within the mine site. This is because the seismic surveys were performed during a period of time in which the mine was shut down, and these events were attributed to maintenance operations that were being performed near the geophysical testing site. Measurements along the survey lines show

that the majority of the passive source energy is in the frequency range of 12 to 18  $Hz$ . The active energy results show that the Rayleigh wave velocity in the overburden sand deposit is about  $240 \frac{m}{s}$ . No information is available about the wave velocities in the underlying sand layers and the rock mass.

### 9.2.3 Experimental results

The surface responses at the site, due to passive source, are collected in time domain. Figures 9-4 and 9-5 show typical time responses recorded along the survey line over crown pillars 1 and 2. The total length of the survey line is 235 *m*, and the distance between the beginning of the survey line and the center of cavity is  $x = 150$  *m*. The total recording time is 0.25 *s*, and the sampling time and frequency are:

$$\delta t = \text{Sampling time} = 0.25 \text{ ms} \quad \text{and} \quad \delta f = \text{Sampling frequency} = \frac{1}{\delta t} = 4 \text{ kHz} \quad (9.1)$$

Plot 'a' (figures 9-4 and 9-5) shows typical time traces at different distances from the beginning of the survey line ( $d$ ), and plot 'b' shows typical contours of the recorded responses. All the responses are normalized with respect to the maximum of the matrix. Thus, the maximum contour value is 1. The continuous lines show the limits of the boundaries of the crown pillar projected to the surface. The time traces recorded over the cavity have relatively larger amplitudes than other records (amplitudes at  $x = 150$  *m*, Figures 9-4 and 9-5). Magnified amplitudes can be distinguished over the void and the nearby region. Because of the complex nature of ambient vibrations, no distinct event is visible in the time traces; thus, the apparent velocity cannot be calculated from the data.

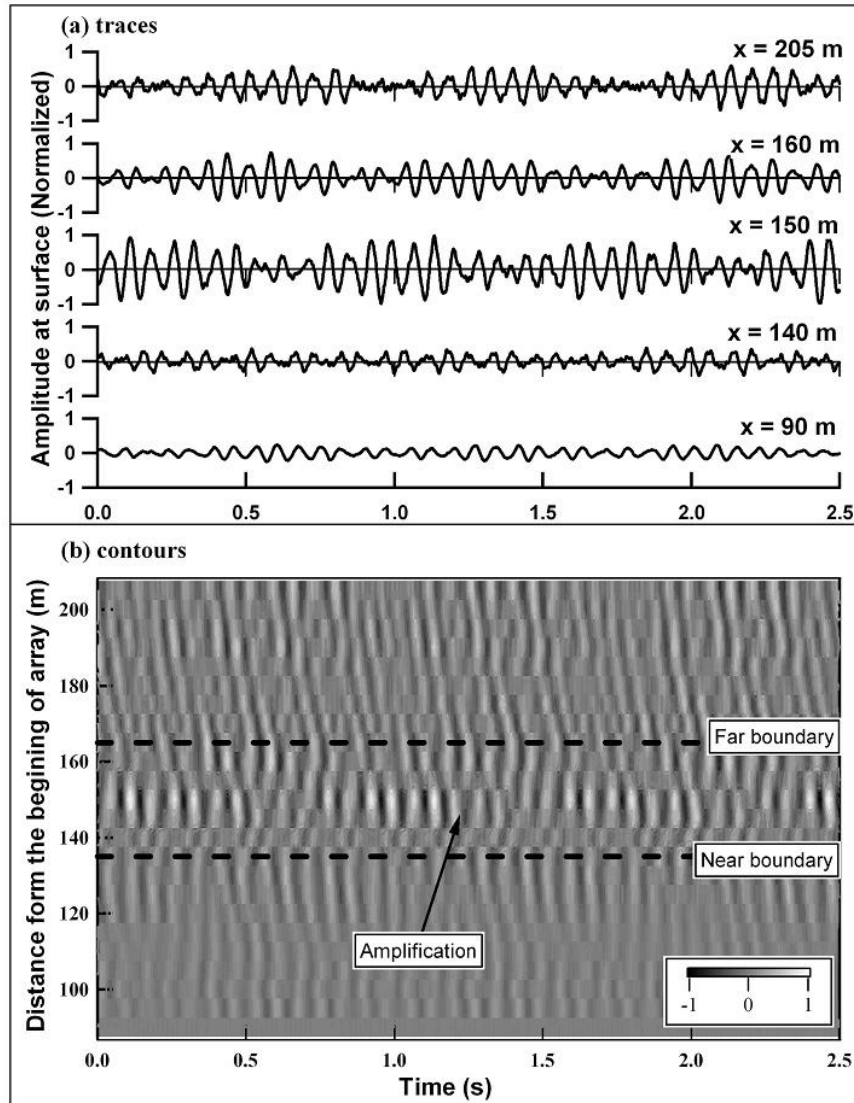


Figure 9-4: Recorded responses over crown pillar 1. Plot (a) shows typical traces recorded at different distances from the beginning of the array ( $d$ ). Plot (b) shows the same responses in contour form. The known center of crown pillar is at  $150\text{ m}$  from the beginning of the array. The cavity boundaries ( $\approx 30\text{ m}$ ) are shown by solid lines in plot (b).



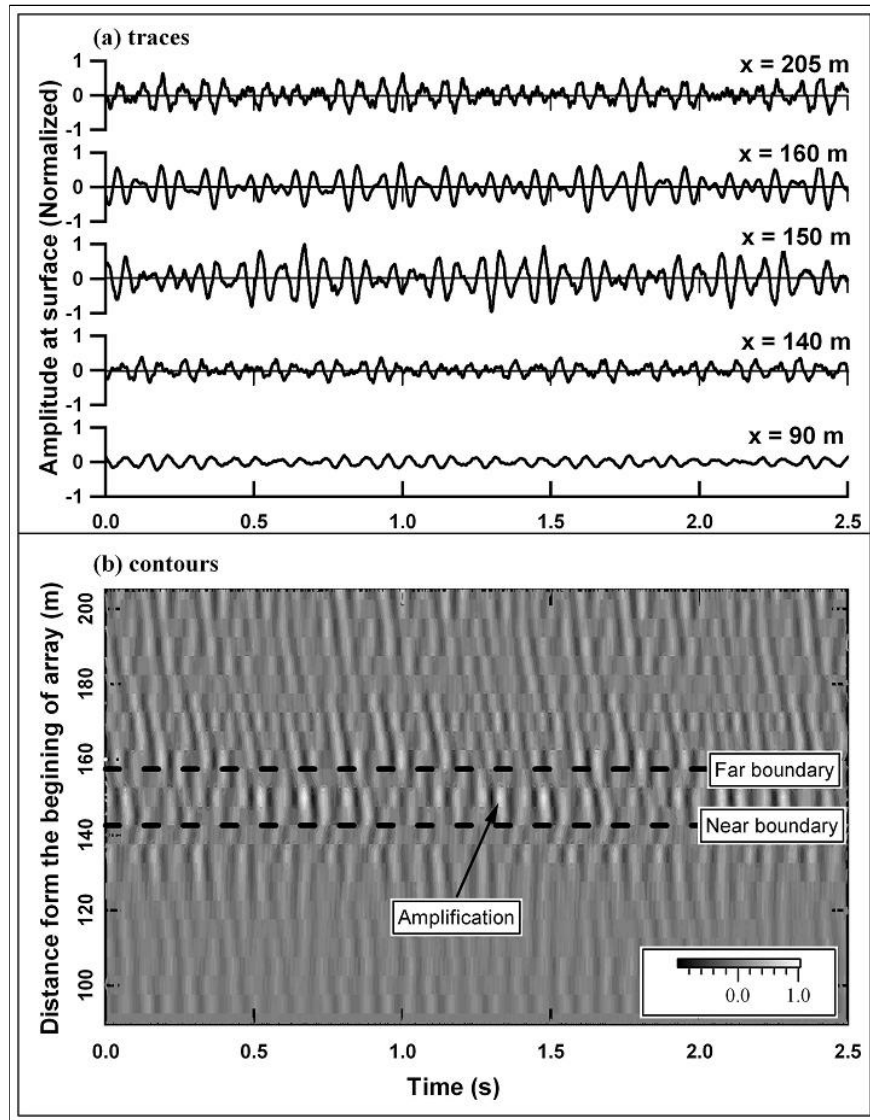


Figure 9-5: Recorded responses over crown pillar 2. Plot (a) shows typical traces recorded at different distances from the beginning of the array ( $d$ ). Plot (b) shows the same responses in contour form. The known center of crown pillar is at  $150\text{ m}$  from the beginning of the array. The cavity boundaries ( $\approx 30\text{ m}$ ) are shown by solid lines in plot (b).

Figure 9-6 shows the frequency spectrum for the passive source test over crown pillars 1 and 2. A significant high-energy region at frequencies close to 15  $Hz$  is visible, centered at  $x = 150$  meters along the survey line, which is the known location of the center of the mine working. Amplifications occur at some of the frequencies that carry significant amount of energy (15  $Hz$  is the estimated central frequency of the ambient sources [129]). The width of the zone that shows significant energy amplification is approximately  $w = 35\ m$  in plot 'a', which is comparable to the width of crown pillar 1. However, in plot 'b' the width of the zone is about  $w = 40\ m$ , which is significantly greater than the known width of the void ( $w = 15\ m$ ). Another region with energy concentration is seen close to the void boundaries but after the void at  $f = 20\ Hz$ . Various passive tests on crown pillars 1 and 2 show that the width of the energy concentration region gives a good estimation of the width of the cavity; however, it is not always the case.

The above observations are in good agreement with the numerical observations, explained in Chapters 6 and 7. The void traps some energy, thus amplitude amplifications in the time domain data, and energy concentration in the frequency spectrum are observed. The trends of the frequency spectrum are comparable to the ones presented in figures . Energy concentration is observed at different frequencies, corresponding to different modes of vibrations and interactions of the energy with different sides of the void.

The previous chapters concluded that in frequency domain, the trapped waves produce a region of high energy concentration. If the width of the void is larger than the main wavelengths present in the incoming R-waves, the void traps more energy and generates more conspicuous amplifications in the frequency domain. The width of the amplification region can be used to estimate the width of the void. If the void size is relatively small with respect to the main wavelengths of the excitation, the frequency spectra show amplifications before the void because of the reflected R-waves. In this case, the width of the void is difficult to estimate from the measurements. The above conclusion explains the reason that the width of crown pillar 1 could be estimated with reasonable accuracy from the recorded data. In the case of crown pillar 2, the width of the cavity is smaller than the wavelength of the main energy. Therefore,

Figure 9-7 shows the application of AARW technique to two sets of data recorded over crown pillar 1. The figure shows the variation of NED values with distance from the beginning of the survey line. Location of void boundaries are depicted by arrows. The peak of the graph

occurs over the void, with smaller peaks at the two sides of the void. As the source was not in-line with the receivers array, the variation of geometrical damping with distance is not a simple function, as discussed in chapter 8. Thus, the sets of data are not multiplied by a gain function. This observation, shows the applicability of the proposed method for detection of the void. The reason that the peak does not occur at the beginning of the void, as observed in chapter 8, is associated to the difference in the geometry of the cavity than the ones assumed in the numerical models, and the source-receiver array offset. The depth estimation based on the proposed method is not possible with the available set of data. The source-receivers array offset imposes a complicated pattern of attenuation that is different than the one used for calculation CALD values. Thus, the method is not applicable to this case. These results confirm that the MASW test associated with AARW technique is a promising tool for locating a void.

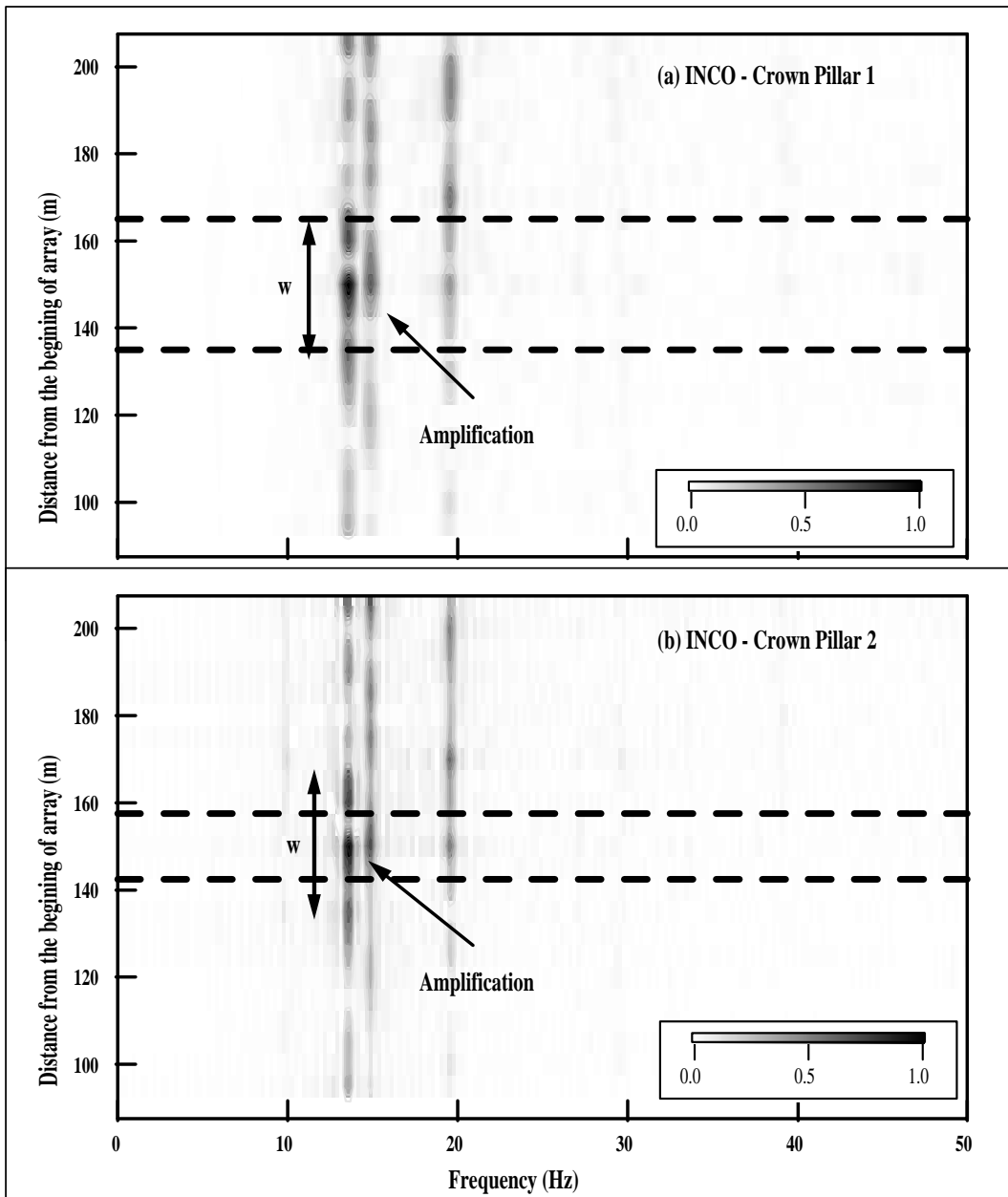


Figure 9-6: Spectrum of the responses over crown pillars. Plots (a) and (b) show the contours over crown pillars 1 and 2, respectively. The known center of crown pillar is at  $x = 150\text{ m}$  from the beginning of the survey line. The cavity boundaries are shown by dashed lines in the plots.

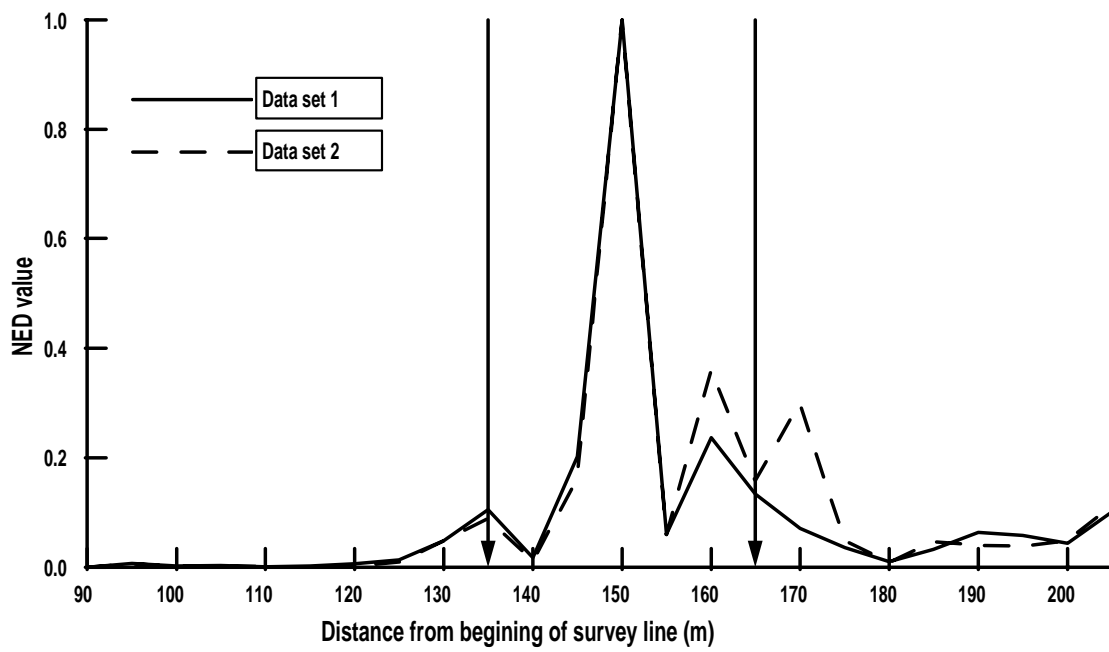


Figure 9-7: Variation of NED with distance, over crown pillar 1. The arrows show the location of the cavity boundaries.

## 9.3 Sandbox prototype

### 9.3.1 Prototype description

Laboratory scale MASW tests were carried out on a sand box prototype (Fig. 9-8). The sand box was filled with fine sand with mean grain size  $D_{50} = 0.15 \text{ mm}$ , to a height of about  $55.0 \text{ cm}$  above the bottom of sand box. The bottom sand layer was overlain by about  $23.0 \text{ cm}$  of cemented sand. The Rayleigh wave velocity of the underlying sand layer is estimated to be  $240.0 \frac{\text{m}}{\text{s}}$  [129]. The cemented sand consisted of fine sand mixed with about 10% cement. Resonant column tests on this material showed that the Rayleigh wave velocity of the material is about  $1000 \frac{\text{m}}{\text{s}}$  Khan2004. During the placement of material in the sandbox, an inflated balloon was placed at the middle of the sandbox in the cemented sand layer to introduce an air filled cavity beneath the surface. The walls of the sand box are covered with a layer Styrofoam, about  $6.0 \text{ cm}$  thick, to reduce reflections from the boundaries. Figure 9-9 shows the geometry of the sand box and the location of the void [138].

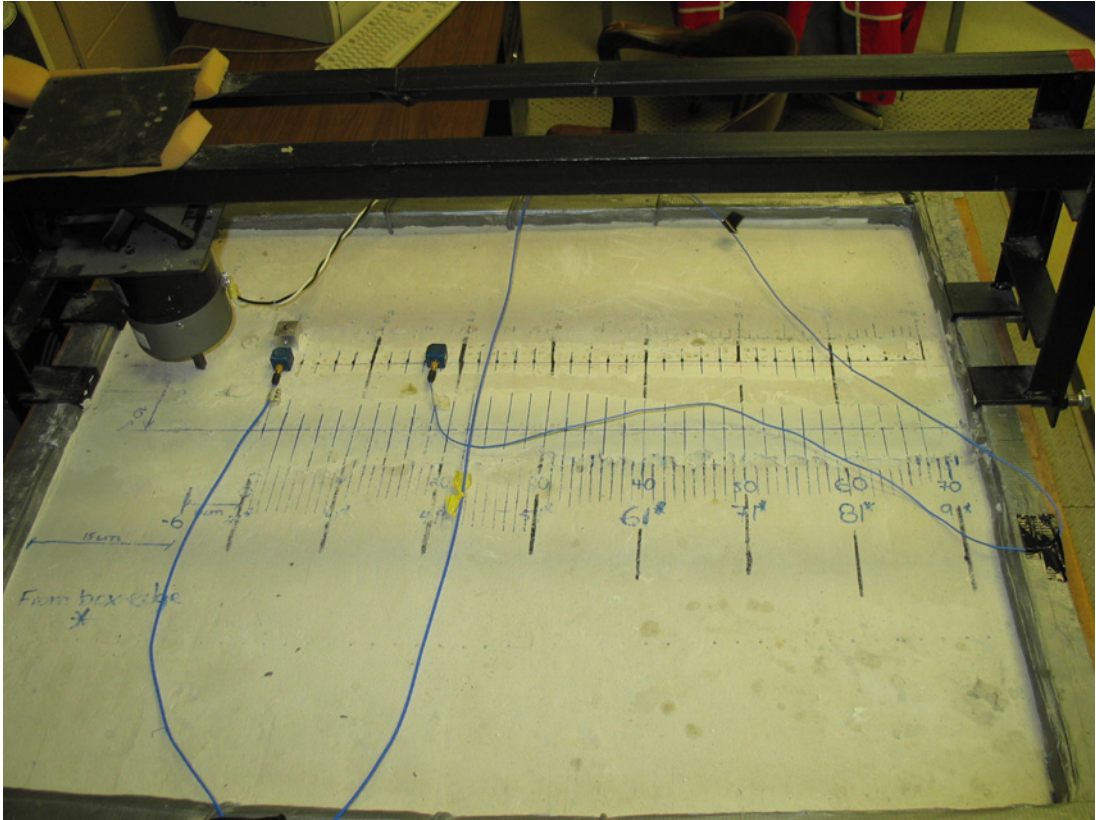
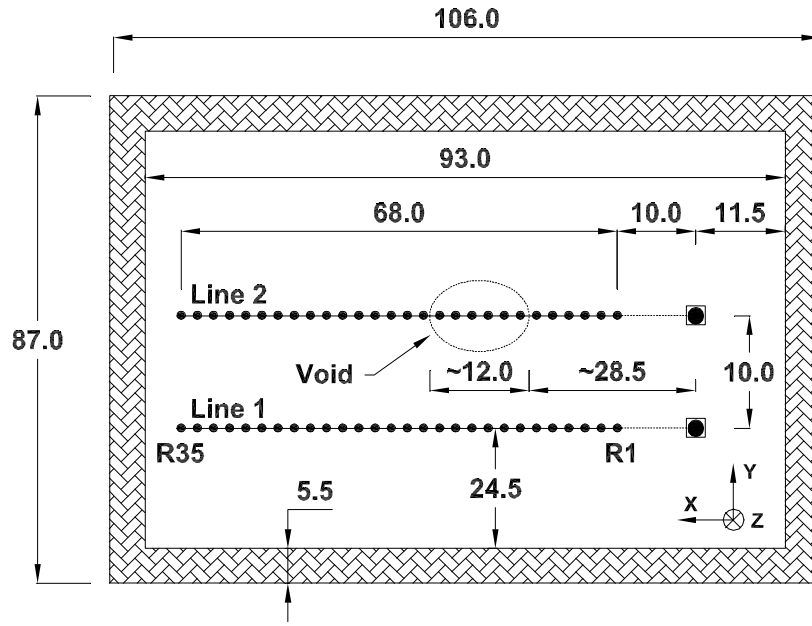
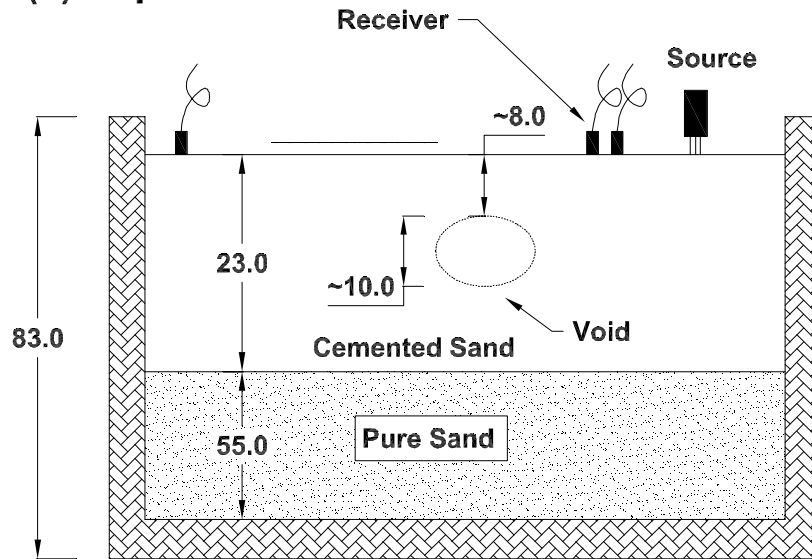


Figure 9-8: Picture of the sandbox used for the test.



**(a) Top view**



**(b) Section view**

Figure 9-9: Sketch of the sand box prototype and the corresponding dimensions. Plot (a) shows the plan view, and plot (b) depicts a section of the prototype. The location of the void, receivers array, and the source are shown in the sketch.



### 9.3.2 Experimental methodology

In this experiment surface responses were collected along two survey lines parallel to the length of the sand box. Survey line 1 was located between the void and sandbox boundary, and survey line 2 was located along the center line of the void. The laboratory test set up is depicted in figure 9-9. The distance between the two survey lines was about 10.0 *cm*. A Hewlett Packard 33120A function/waveform generator was used to trigger a signal pulse of 1 *Hz* that was transferred to the medium through a shaker type source mounted on a 5.0 *cm* diameter cylindrical metal base. Accelerometers (PCB 356B08) with a linear frequency response between 0.5 *Hz* to 5.0 *kHz*, were used to measure surface accelerations in three dimensions. The distance between the source and the first receiver (offset value) was 10.0 *cm*, the distance between the consecutive receivers was 2.0 *cm*, and a total of 35 recording points were chosen along each survey line. The total receivers array length was 68 *cm*. The measurements were performed with three accelerometers. For each measurement along the the survey lines, the first and last receivers were fixed in their locations and the middle receiver was moved along the survey line. The fixed receivers were used to assure that the signals recorded at different locations are coherent.

The sampling time ( $\delta t$ ) and sampling frequency ( $\delta f$ ) was:

$$\delta t = 9 \times 10^{-6} s \quad \text{thus} \quad \delta f = 111 \text{ kHz} \quad (9.2)$$

The trace length was 4096 points in time. The experiments at each location were repeated 9 times, and the results were averaged to reduce the effect of random noise. The response at the location of receiver 1 is used to calculate the critical wavelength ( $\lambda_{ch}$ ). Figure 9-10 shows the variation of cumulative energy with wavelength. The measured critical wavelength is  $\lambda_{ch} = 0.22$  *m*, which is very close to the depth of the top layer.

### 9.3.3 Experimental results

Figure 9-11 shows the contours of the vertical responses recorded along lines 1 and 2 (plots 'a' and 'b', respectively), at the sand box surface. The main event correspond to Rayleigh wave, with a measured velocity of 1080  $\frac{m}{s}$ , which matches well with the reported values for cemented

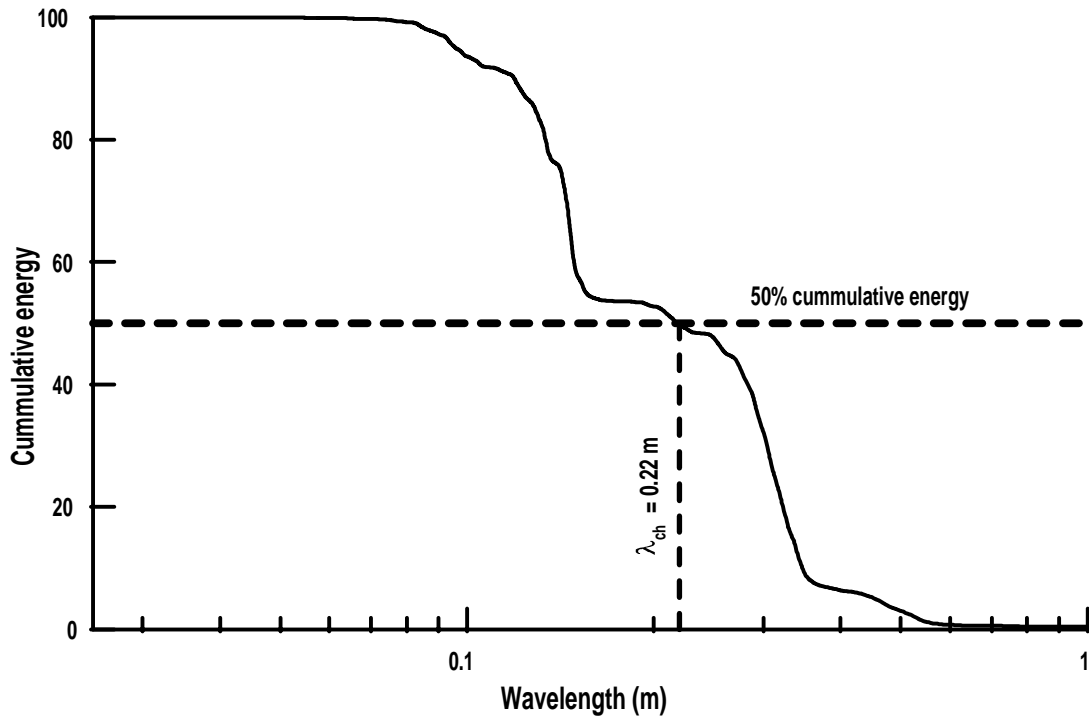


Figure 9-10: Cumulative energy at the location of first receiver along line 2 at the surface of sand box. The critical wavelength, wavelength that corresponds to 50% of cumulative energy, is 0.22 m.

sand [139]. Reflections from the sand box boundary are observed in both plots (event **A**). The reflections are stronger along line 1, because it is closer to the longitudinal boundary of the sand box. In plot 'b' the projected boundaries of the cavity are depicted by dashed lines. Some reflections, and minor amplifications can be distinguished in the vicinity of the void (event **B**), though they are not very strong events.

Figure 9-12 shows the spectrum of the sand box responses. The spectrum are multiplied by a gain function in distance, to enhance the peak values (Chapter 8). Both plots are normalized to the maximum of responses along line 1. Thus the maximum of plot (a) is 1. Event **A** in both plots correspond to the reflections from boundaries, which is stronger along line 1. Event **B** shows amplifications over the cavity and along its boundaries. The amplitude of the spectrum along line 2 is about 20% larger than the amplitudes along line 1.

Figure 9-13 shows the application of AARW technique to the data obtained along line 2 (over the void). Plot 'a' shows the variation of NED value with distance, and the arrows show the location of the cavity. The maximum of the NED value occurs at the beginning of the void, and a local peak is observed around the center of the void. The peaks at farther distances correspond to the high energies due to reflections. Plot 'b' shows the variation of CALD value with wavelength. The plot does not show any significant discontinuity, thus the CALD calculation fails to estimate the embedment depth of the void in this case. This observation can be explained by recalling that the embedment depth of the void is about 0.08  $m$ , corresponding to a frequency of  $f = \frac{1080}{0.08} = 13500 \text{ Hz}$ . The latter frequency is beyond the linear range of the used accelerometers, thus they could not be detected accurately. Further, in this test acceleration at the surface was recorded, and the CALD value was developed based on displacement records. Thus, it is expected to encounter larger cut off frequencies in the acceleration records, which is again beyond the linear range of the used accelerometers.

In general, the sand box results are in good agreement with the results obtained from numerical models. It was shown in Chapter 7 that the behavior of void in a medium with inverse layering is similar to one in a half space, which is verified by the sand box test. Although, the shape of the cavity in the sand box test was different than the ones considered in the numerical models, energy concentration was observed in the vicinity of the void. This observation, confirms that due to the interaction of the void with Rayleigh wave, energy partitioning occurs, and part of the energy is trapped on the void region. The 3D modeling showed that when the void is not in-line with the receivers array, the effect of the void is not observed in the recorded responses. The records along line 1, which was not in the same alignment with void, confirm the latter observation. The AARW technique showed to be a powerful technique to detect a void. Though, due to limitations in the collected frequency ranges, the applicability of the AARW method for estimating the embedment depth of the void could not be verified, with the sand box test.

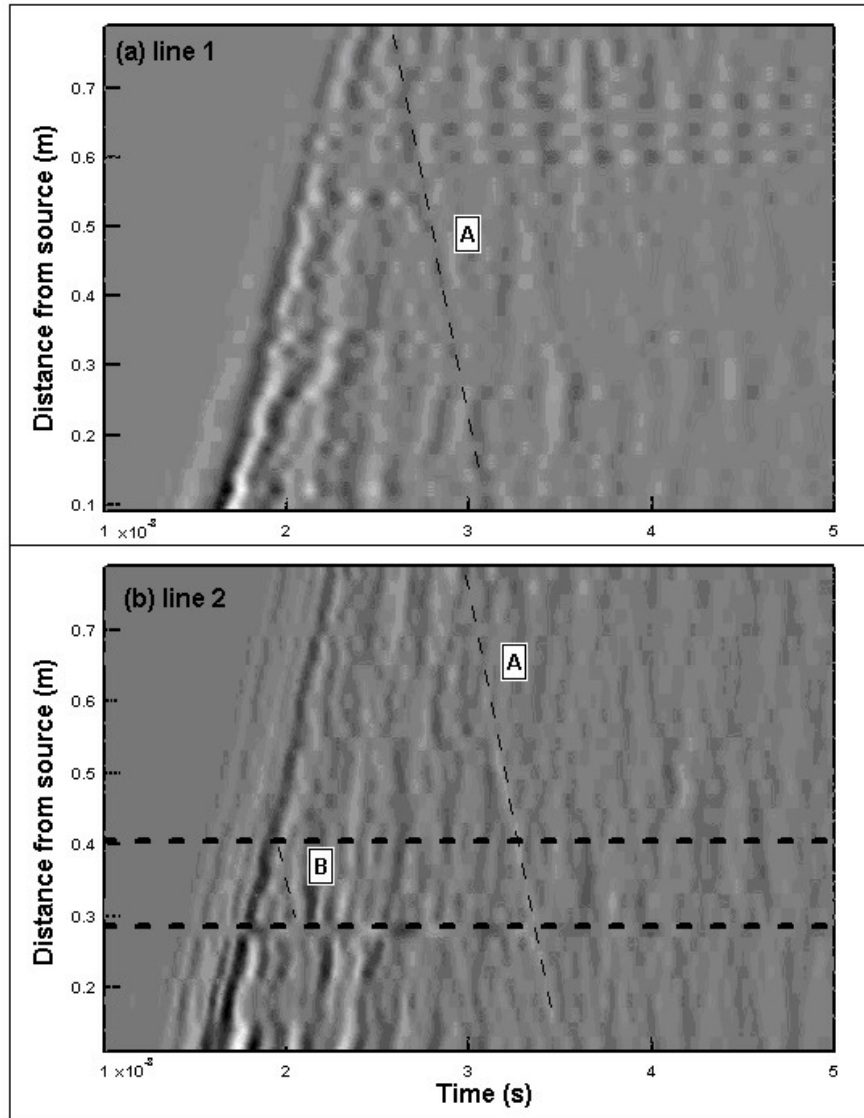


Figure 9-11: Contours of the surface responses of the sand box. Plots (a) and (b) correspond to lines 1 and 2, respectively. The dashed lines in plot (b) show the boundaries of the cavity projected to the surface.

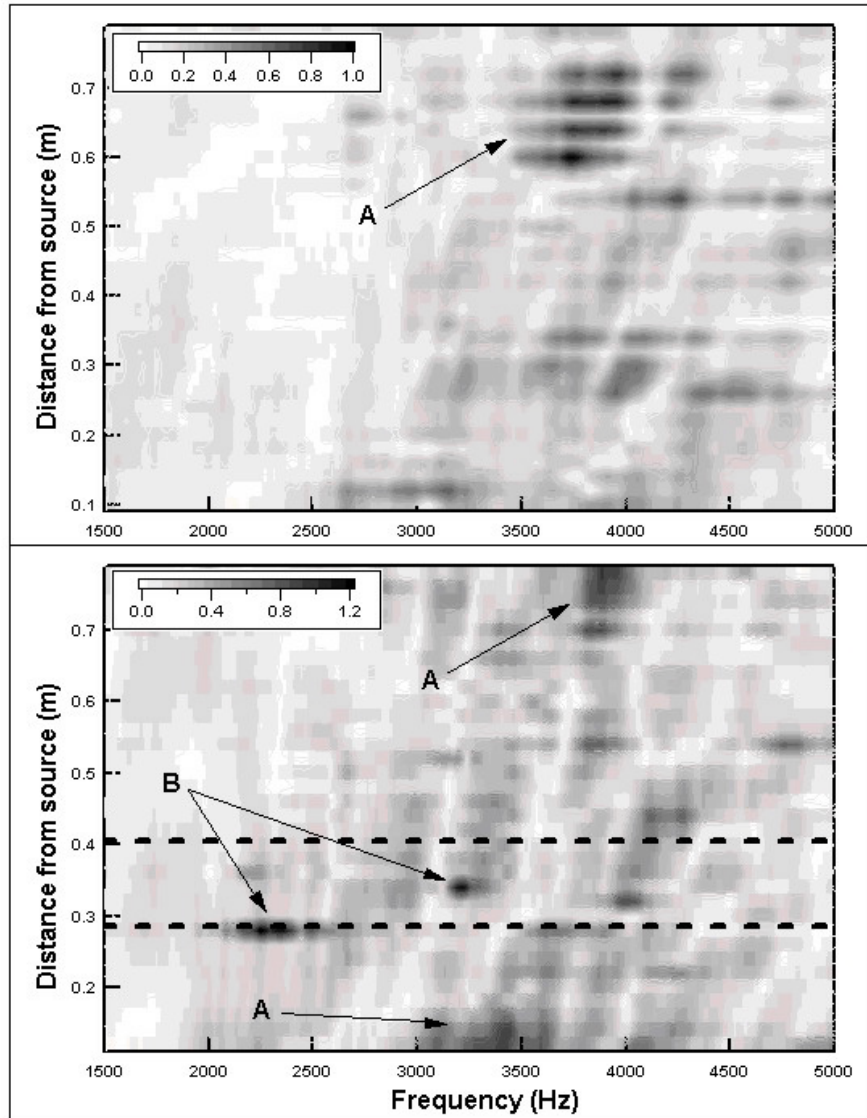


Figure 9-12: Spectrum of the surface responses of the sand box. Plots (a) and (b) correspond to lines 1 and 2, respectively. The dashed lines in plot (b) show the boundaries of the cavity projected to the surface.

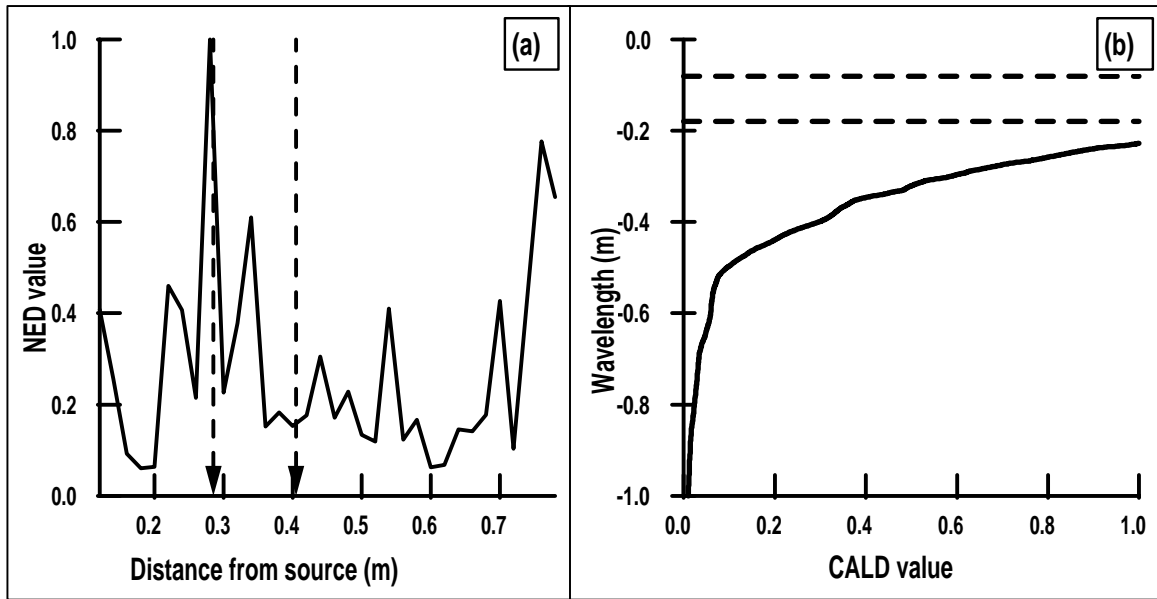


Figure 9-13: Application of AARW method to the sand box data. Plot (a) shows the variation of NED value with distance. Plot (b) shows the variation of CALD value with wavelength.

## 9.4 Summary and conclusions

This chapter explained the procedures that were followed to verify the conducted studies in this research. The data collected over two known crown pillars were presented and investigated in time and frequency domains. Further, the results of a series of tests that were performed on a sand box prototype were discussed. The field and laboratory data showed to be in good agreement with the numerical results. Energy concentration was observed in the vicinity of the cavities both in time and frequency domains. It was shown that the width of the region with energy concentration can be used to estimate the extents of the cavity, in some cases. The concept of characteristic wavelength ( $\lambda_{ch}$ ) was used to evaluate the energy content of the data. AARW technique was applied to the data to detect the cavities. It was shown that AARW provides good results for the detection of void. The applicability of the AARW technique to estimate the embedment depth of the void could not be demonstrated, by the available data.

# Chapter 10

## Conclusions and Recommendations

### 10.1 Conclusions

The major conclusions and contributions of this study are summarized as follows:

1. Two and three dimensional numerical models were developed to investigate the behavior of Rayleigh waves in the presence of lateral (void) and vertical (layers) anomalies.
2. The void interacts with the incident Rayleigh wave. Due to this interaction energy partitioning happens. Part of the incident energy is reflected back, part of it is transformed into other types of waves (mode conversion), part of it is entrapped in the void region, and part of it is transmitted.
3. The majority of reflected wave is in the form of Rayleigh wave. Reflection occurs from both the near and far boundaries of the void (The near boundary is defined as the one which is closer to the source).
4. Due to the interaction of void and the Rayleigh wave part of the energy is transformed into body waves, most of which is in the form of p-wave. The generated p-wave is observed in the regions before and after the void, and inside the medium.
5. Part of the incident energy is entrapped in the void region. This entrapped energy excites antisymmetric Lamb waves, which are observed in the traces over the void. This part of the entrapped energy bounces back and forth between the void boundaries until it totally

attenuates due to geometric damping, scattering and other existing damping mechanisms. The measured velocities of the anti symmetric Lamb waves are less than the Rayleigh wave velocity of the medium.

6. Part of the entrapped energy causes the void to vibrate. This void vibration lasts much longer than the surface vibrations due to the main event. Therefore, late energy emissions from the void are observed. These late energy emissions can be measured at the surface, though due to their small amplitudes
7. Due to reflection, mode conversion, scattering, and entrapment of incident energy, the amplitudes of the responses in the regions after the void are attenuated.
8. The measured group velocities in the presence of a void are slightly smaller than the Rayleigh wave velocity of the medium. The measured differences in difference cases is about 2% to 3%. Therefore, a delay is observed in the transmitted waves.
9. The reflections from the far boundary of the void are delayed in compare to the theoretical arrival times. Therefore, the measurement of void size based on the time delay between the reflected waves from near and far boundaries of the void results in larger void size than the actual void size.
10. The concept of characteristic wavelength ( $\lambda_{ch}$ ) is defined. Characteristic wavelength is defined as the wavelength that 50% of the wave energy is concentrated at wavelengths smaller than that, and is calculated based on the recorded amplitudes at the first receiver. Characteristic wavelength can be measured in the field, and can be used to quantify the wave properties.
11. The entrapped energy is observed as regions with concentrated energies over the void, in frequency domain. The interaction of the void with the Rayleigh wave occurs in a certain frequency bandwidth. In cases that the embedment depth of the void is less than or equal to the embedment depth of the void the lower boundary is defined by the width of the void (excited Lamb wave modes), and the upper boundary is defined by embedment depth of the void.



12. Cut off frequency is defined as the frequency with a wavelength equal to the depth of the void. The interaction of the void with the incident energy occurs to a frequency close to the cut off frequency.
13. Cavities with larger widths trap more energy. Therefore, in frequency domain energy concentration is observed over the void, and the width of this region is comparable to the width of the void. This phenomena is observed for cavities with widths larger than  $\lambda_{ch}$ .
14. In frequency domain a region with highly attenuated amplitudes is observed after the void region.
15. It is found that the average penetration depth of the source energy is about  $2.5\lambda_{ch}$ .
16. Investigation of 2D Fourier transforms showed that the presence of a void does not excite higher modes of Rayleigh wave.
17. 2D Fourier transforms show some dispersions in the presence of void. Thus, it is proved that the medium is dispersive in the presence of a void.
18. The effect of void on the surface decreases with the increase of on the embedment depth of the void. It is estimated that after a depth of about  $1.3$  to  $1.5\lambda_{ch}$  the amplification effect on the surface is not observed and void effect on the surface is not significant.
19. The presence of underlying stiff layers, close to the bottom boundary of the void, overshadows the effect of the void at the surface.
20. The effects void in the surface responses are observed as reflections and energy concentration; whereas, the effect of horizontal layers with different mechanical properties are observed as higher modes of vibration. Therefore, 2D Fourier transforms can be utilized to distinguish between the two effects.
21. Three dimensional (3D) models of a medium with cavity were developed. The 3D models allowed to investigate the effect of out of plain dimension of the void, and the effect of misalignment of the void-receivers array on the surface responses.

22. The out of plain dimension of the void has a significant effect on the surface responses. For out of plain dimensions larger than  $0.25\lambda_{ch}$ , the results of 2D axisymmetric models and 3D models are similar.
23. The alignment of the cavity with the receivers array is a crucial limitation that determines the success of MASW test in void detection.
24. The Attenuation Analysis of Rayleigh Wave Method (AARW) was developed. AARW is an analysis technique to detect underground cavities and estimating their extents and embedment depths.
25. The results of this study were verified by investigating the recorded responses over two crown pillars. The location of crown pillars were observed as regions with energy concentration in the frequency domain data. The width of the region was comparable to the width of the cavity in one case and it was larger than the width of the cavity in the second case. These observations were explained using the concepts of entrapped energy and characteristic wavelength.
26. The results obtained from a laboratory sandbox prototype were investigated. The responses verified the existence of regions with energy concentration in the vicinity of the void.

## 10.2 Recommendations for future works

This study showed that the MASW test is a promising tool for detecting underground cavities. For further improvement of the technique and continuation of this study the following recommendations are made:

- Designing and conducting more field and laboratory scale tests to investigate the limitations of the observations made in this work and the applicability of the AARW method for void detection;
- Studying the effect of the shape of the cavity on the surface responses;

- Investigating the effect of surface topography on the recorded responses in the presence of a cavity;
- Quantifying and generalizing the application of 2D Fourier transforms for detecting underground cavities;
- Continuing the studies with more advanced 3D numerical models;
- Understanding the effect of source-receiver and receiver-receiver distances, void size, and total array size on the delectability of the void by MASW method;
- Investigating the application of MASW test in detection of underground anomalies such as boulders; and
- Developing a software to analyze the collected data based on AARW and PSD methods.

# Bibliography

- [1] John M. Reynolds, *An introduction to applied and environmental geophysics*, John Wiley and Sons, West Sussex, England, 1997.
- [2] D. M. Boore, “Finite difference methods for seismic wave propagation in heterogeneous materials,” *Methods in computational Physics*, vol. 11, pp. 1, 1972.
- [3] J. Lysmer and R. Kuhlemeyer, “Finite dynamic model for infinite media,” *Journal of Engineering Mechanics Division*, p. 859.
- [4] Itasca, *FLAC: fast Lagrangian analysis of continua users guide*, Itasca consulting group Inc., Minneapolis, Minnesota, 2000.
- [5] J. E. Turney, “Subsidence above inactive coal mines: information for homeowner,” [www.mines.edu](http://www.mines.edu), 1985, Accessed 26 November 2004.
- [6] J. Vlcko, “Engineering geological failures on historic structures and historic sites,” [www.fns.uniba.sk](http://www.fns.uniba.sk), 1985, Accessed 26 November 2004.
- [7] Lu Yaoru and A.H. Cooper, “Gypsum karst geohazards in china,” in *The engineering geology and hydrogeology of karst terranes*, B. F. Beck and B. Stephenson, Eds., pp. 117–126. A.A.Balkema, Brookfield, Rotherdam, 1997.
- [8] D.J. Hutchinson, C. Phillips, and G. Cascante, “Risk considerations fro crown pillar stability assessment for mine closure planning,” *Journal of geotechnical and geological engineering*, vol. 20, no. 1, pp. 41–64, 2002.
- [9] B. F. Beck and B. Stephenson, Eds., *The engineering geology and hydrogeology of karst terranes*, A.A.Balkema, Rotterdam, Brookefield, 1997.

- [10] H. Kolsky, *Stress waves in solids*, Dover Publications Inc., New York, 1963.
- [11] Adel S. Saada, *Elasticity theory and application*, Pergamon Press Inc., New York, 1974.
- [12] Karl F. Graff, *Wave motion in elastic solids*, Dover Publications, New York, 1975.
- [13] J. D. Achenbach, *Wave propagation in elastic solids*, North-Holland Publishing Company, New York, second edition, 1976.
- [14] A. E. H. Love, *A treatise on the mathematical theory of elasticity*, Dover Publications Inc., New York, 1st edition, 1944.
- [15] J.W.S. Rayleigh, “On waves propagated along the plane surface of an elastic solid,” in *Proceedings of the London Mathematical Society*, 1885, vol. 17, pp. 4–11.
- [16] I. A. Viktorov, *Rayleigh and Lamb waves*, Plenum Press, New York, 1967.
- [17] Seth Stein and Michael Wysession, *An introduction to seismology, earthquakes, and earth structure*, Blackwell Publishing, Malden, MA, USA, 2003.
- [18] J. Carlos Santamarina, Katherine A. Lein, and Moheb A. Fam, *Soils and waves*, John Wiley and Sons, LTD, England, 2001.
- [19] Huch Doyle, *Seismology*, John Wiley and Sons, New York, 1995.
- [20] Love A.E.H., *Some problems of geodynamics*, Cambridge university press, Cambridge, 1911.
- [21] L. Knopoff, “Attenuation of elastic waves in the earth,” in *Physical Acoustics*, W. P. Mason, Ed., pp. 287–324. Academic press, 1965.
- [22] Ray W. Clough and Joseph Penzien, *Dynamics of structures*, McGraw-Hill Inc., Singapore, 2nd edition, 1993.
- [23] Einar Kjartansson, “Constant q-wave propagation and attenuation,” *Journal of geophysical research*, vol. 84, pp. 4737–4748, 1979.
- [24] Steven L. Kramer, *Geotechnical earthquake engineering*, Prentice Hall, Upper Saddle River, New Jersey, 1996.

- [25] Bobby O. Hardin, “The nature of damping in sands,” *Journal of the soil mechanics and foundations division*, vol. 91, no. SM1, pp. 63–97, January 1965.
- [26] H. Lamb, “On the propagation of tremors over the surface of an elastic solid,” in *Philosophical transactions of the Royal society of London*, A203. 1904.
- [27] W.M. Ewing, W.S. Jardetzky, and F. Press, *Elastic waves in layered media*, McGraw-Hill, New York, 1957.
- [28] J. Carlos Santamarina and Dante Fratta, *Introduction to discrete signals and inverse problems in civil engineering*, ASCE Press, Reston, Virginia, 2001.
- [29] Mark Cartwright, *Fourier methods for mathematicians, scientists and engineers*, Ellis Horwood limited, GT Britain, 1990.
- [30] James S. Walker, *Fast Fourier transforms*, CRC-press, 2nd edition, 1996.
- [31] Hwei P. Hsu, *Shaum’s outline of theory and problems in signals and systems*, McGRAW-HILL, New York, 1995.
- [32] Ervin Kreyszig, *Advanced engineering mathematics*, John Wiley and Sons, New York, NY, 2nd edition, 1967.
- [33] L.G. Peardon, “Fk techniques in seismic processing,” in *Geophysical signal processing*, E.A. Robinson and T.S. Durrani, Eds., pp. 388–474. Prentice-Hall Inc., Englewood Cliffs, New Jersey, 1986.
- [34] Dan E. Dudgeon and Russel M. Mersereau, *Multidimensional digital signal processing*, Prentice-Hall Inc., Englewood Cliffs, NJ, 1984.
- [35] W. Niblack, *Introduction to digital image processing*, Prentice-Hall International, Englewood Cliffs, N.J., 1986.
- [36] R.C. Gonzalez and R.C. Woods, *digital image processing*, Addison-Wesley, Mass., 1992.
- [37] R.D. Costley Jr. and Y.H. Berthelot, “Dispersion curve analysis of laser generated lamb waves,” *Ultrasonics*, vol. 32, no. 4, pp. 249–253, 1994.

- [38] John P. Greenhouse, “Environmental geophysics: It’s about time,” *The Leading Edge*, vol. 10, no. 1, pp. 32–34, 1991.
- [39] Don W. Steeples, “Engineering and environmental geophysics at the millennium,” *Geophysics*, vol. 66, no. 1, pp. 31–35, January 2001.
- [40] B.W. Darracott and D. M. McCann, “Planning engineering geophysical surveys,” in *Site investigation practice: Assessing BS5930*, A.B. Hawkins, Ed., pp. 14–18. Geological Society Engineering, Geology Special Publication n. 2, 1986.
- [41] Philip Kearey, Michael Brooks, and Ian Hill, *An introduction to geophysical exploration*, Blackwell Science Ltd., GT Britain, 3rd edition, 2002.
- [42] T.G. Baker and J.L. Stevens, “Shallow shear wave velocity and q structures in the el centro strong motion accelerograph array,” *Geophysical research letters*, vol. 10, no. 9, pp. 853–856, 1983.
- [43] G.M. Habberjam, *Apparent resistivity and the use of square array techniques*, Gebrüder Borntraeger, Berlin, 1979.
- [44] O. Koefoed, *Geosounding principles, 1-resistivity sounding measurements*, Elsevier, Amsterdam, 1979.
- [45] A. A. R. Zohdy, “A new method for the automatic interpretation of schlumberger and wenner sounding curves,” *Geophysics*, vol. 54, no. 2, pp. 245–253, 1989.
- [46] Justin Anning, ,” <http://members.iinet.net.au/anningj/resistivity2.jpg>, Accessed 28 July 2005 2000, Accessed 28 July 2005.
- [47] J.M. Reynolds and D.I. Taylor, “The use of geophysical surveys during the planning, construction and remediation of landfills,” in *Engineering geology of waste storage and disposal*, S. Bentley, Ed., pp. 93–98. Geological society special publication no. 11, 1995.
- [48] A.M. Ebraheem, M.W. Hamburger, E.R. Bayless, and N.C. Krothe, “A study of acid mine drainage using earth resistivity measurements,” *Grounwater*, vol. 28, pp. 361–368, 1990.

- [49] R.D. Barker, “Electrical imaging and its application in engineering investigations,” in *Modern geophysics in engineering geology*, D.M. McCann, M. Eddlestone, P.J. Fenning, and G.M. Reeves, Eds., pp. 37–43. Geological Society Engineering, Geology Special Publication n. 12, 1997.
- [50] J.E. Prentice and P. McDowell, “Geological and geophysical methods in the location and design of services,” *Underground Services*, vol. 4, pp. 15–18, 1976.
- [51] T.E. Osterkamp and R.W. Jurick, “Detecting massive ground ice in permafrost by geophysical methods,” *Northern Engineer*, vol. 12, no. 4, pp. 27–30, 1980.
- [52] D.R. Hiltunen and R.D. Woods, “Influence of source and receiver geometry on the testing of pavements by the surface waves method,” in *Nondestructive testing of pavements and backcalculation of moduli*, A.J. BushIII and G.Y. Baladi, Eds., ASTM STP 1026, pp. 138–153. American society for testing and materials, Philadelphia, 1989.
- [53] G.F. Miller and H. Pursey, “On the partition of energy between elastic waves in a semi-infinite solid,” in *Proceedings of Royal society of London*, 1955, vol. 233 of A, pp. 55–59.
- [54] R.D. Woods, “Screening of surface waves in soils,” *Journal of the soil mechanics and foundations division*, vol. 94, no. SM4, pp. 951–979, July 1968.
- [55] L.V. Socco and C. Strobbia, “Surface-wave method for near surface characterization a tutorial,” *Near surface geophysics*, vol. 2, no. 4, pp. 165–185, January 2004.
- [56] Choon B. Park, Richard D. Miller, and Jianghai Xia, “Multichannel analysis of surface waves,” *Geophysics*, vol. 64, no. 3, pp. 800–808, 1999.
- [57] Degebo, *Deutsche gesellschaft fur bodenmechanik*, vol. 4, Springer, Berlin, 1938.
- [58] S.G. Bergstrom and S. Linderholm, “Dynamisk metod att utrona ultiga marklagers genomsnittliga elasticitetsegens kaper,” *Handlinger 4, Svenska Forsknings-institutent for cement och betong vid. kungl., Tekniska, Hogskolan*, 1946.
- [59] L.W. Nijober and C. Van der Poel, “A study of vibration phenomena in asphaltic road construction,” in *Proceedings. Association of asphaltic pavement technology*, 1953, pp. 197–231.



- [60] R. Jones, “In-situ measurement of the dynamic properties of soil by vibration method,” *Geotechnique*, vol. VIII, pp. 1–21, 1958.
- [61] R.F. Ballard Jr., “Determination of soil shear moduli at depths by in situ vibratory techniques,” Miscellaneous paper 4-691, U.S. Army engineer waterways experiment station, Vicksburg, MS, 1964.
- [62] J.S. Heisy, K.H. Stokoe II, W.R. Hudson, and A.H. Meyer, “Determination of in-situ shear wave velocities from spectral analysis of surface waves,” Research report 256-2, Center for transportation research, The university of Texas at Austin, December 1982.
- [63] W. Heukelom and J.G. Klomp, “Dynamic testing as a means of controlling pavements during and after construction,” in *Proceedings, international conference on structural design of asphalt pavements*, Ann Arbor, MI, 1962, pp. 495–510.
- [64] Freeman Gilbert and George E. Backus, “Propagator matrices in elastic wave and vibration problems,” *Geophysics*, vol. 31, no. 2, pp. 326–332, 1966.
- [65] William T. Thomson, “Transmission of elastic waves through a stratified solid medium,” *Journal of Applied Physics*, vol. 21, no. 2, pp. 89–93, 1950.
- [66] C.P. Abbis, “Shear wave measurements of the elasticity of the ground,” *Geotechnique*, vol. 31, pp. 91 – 104, 1981.
- [67] R.W. Cunny and Z.B. Fry, “Vibratory in situ and laboratory soil moduli compared,” *Journal of the soil mechanics and foundations division*, vol. 99, no. SM12, pp. 1055–1076, 1973.
- [68] G.T. Baird, “Wave propagation method of pavement evaluation,” Tech. Rep., New Mexico engineering research institute, university of New Mexico, Albuquerque, 1982.
- [69] J. S. Watkins, R. H. Godson, and K. Watson, “seismic detection of near surface cavities,” Contribution to astrogeology, Geological survey profesional paper 599-A, National aeronautics and space administration, U.S. department of the interior, U.S. government printing office, Washington, D.C., 1967.

- [70] R.D. Rechten and D.M. Stewart, "A seismic investigation over a near-surface cavern," *Geoexploration*, vol. 13, pp. 235 – 246, 1975.
- [71] George A. McMechan and Mathew J. Yedlin, "Analysis of dispersive waves by wave field transformation," *Geophysics*, vol. 46, no. 6, pp. 869–874, 1981.
- [72] L. Knopoff, "Observation and inversion of surface wave dispersion," *Tectonophysics*, vol. 13, no. 1-4, pp. 497–519, 1972.
- [73] G. Nolet and G.F. Panza, "Array analysis of seismic surface waves: limits and possibilities," *Pure and applied geophysics*, vol. 114, pp. 776–790, 1976.
- [74] S. Nazarian, *In situ determination of elastic moduli of soil deposits and pavement systems by spectral-analysis-of-surface-waves method*, PhD dissertation, The university of Texas at Austin, 1984.
- [75] K.H. Stokoe II and S. Nazarian, "Determination of moduli and thickness of five pavement sections, mcdrill airforce base, florida by different insitu seismic tests," Tech. Rep., geotechnical engineering center, The university of Texas, Austin, 1984.
- [76] M. Horike, "Inversion of phase velocity of long period microtremors to the s-wave velocity structure down to the basement in urbanized areas," *Journal of physics of the earth*, vol. 33, pp. 59–96, 1985.
- [77] K. Takimatsu, K. Shinzawa, and S. Kuwayama, "Use of short period micro tremors for vs profiling," *Journal of geotechnical engineering, American society of civil engineers*, vol. 118, no. 10, pp. 1544–1558, 1991.
- [78] P. Gabriels, r. Snieder, and G. Nolet, "In situ measurement of shear-wave velocity in sediments with higher mode rayleigh waves," *Geophysical prospecting*, vol. 35, pp. 187–196, 1987.
- [79] K.O. Addo and P.K. Robertson, "Shear-wave velocity measurements using rayleigh waves," *Canadian geotechnical journal*, vol. 29, no. 4, pp. 558–568, 1992.

- [80] M.M. Hossain and V.P. Drnevich, “Numerical and optimization techniques applied to surface waves for back-calculation of layer moduli,” in *Nondestructive testing of pavements and backcalculation of moduli*, A.J. BushIII and G.Y. Baladi, Eds., ASTM STP 1026, pp. 649–669. American society for testing and materials, Philadelphia, 1989.
- [81] R.B. Hermann and G.I. Al-Eqabi, “Surface wave inversion for shear velocity,” in *Shear waves in marine sediments*, J.M. Hoven, Ed., pp. 545–556. Kluwer academic publishers, 1991.
- [82] D. Yuan and S. Nazarian, “Automated surface waves method: Inversion technique,” *Journal of geotechnical engineering*, vol. 119, no. 7, pp. 1112–1126, July 1993.
- [83] K. H. Stokoe II, S. Nazarian, G. J. Rix, I. Sanchez-Salinero, J.C. Sheu, and Y.J. Mok, “In situ seismic testing of hard to sample soils by surface wave methods,” in *Earthquake engineering and soil dynamics II- recent advances in ground-motion evaluation*, J.L. Von Thun, Ed., Geotechnical special publication no. 20, pp. 264–278. ASCE, New York, NY, 1988.
- [84] D. Jongmans and d. Demanet, “The importance of surface waves in vibration study and the use of rayleigh waves for estimating the dynamic characteristics of soils,” *Engineering geology*, vol. 34, pp. 105–113, 1993.
- [85] V. Ganji, N. Gucunski, and S. Nazarian, “Automated inversion procedure for spectral analysis of surface waves,” *Journal of geotechnical and geoenvironmental engineering*, vol. 124, no. 8, pp. 757–770, 1998.
- [86] M.D. Martinez, X. Lana, J. Olarte, J. Badal, and J.A. Canas, “Inversion of rayleigh wave phase and group velocities by simulated annealing,” *Physics of the earth and planetary interiors*, vol. 122, pp. 3 – 17, 2000.
- [87] N. Ryden, C.B. Park, P. Ulriksen, and R.D. Miller, “Multimodal approach to seismic pavement testing,” *Journal of geotechnical and geoenvironmental engineering*, vol. 130, no. 6, pp. 636 – 645, June 2004.

- [88] N. Ryden and C.B. Park, "Surface waves in inversely dispersive media," *Near surface geophysics*, vol. 2, no. 4, pp. 187 – 197, November 2004.
- [89] D. Kim and H.C. Park, "Determination of dispersive phase velocities for sasw method using harmonic wavelet transform," *Soil dynamics and earthquake engineering*, vol. 22, pp. 675 – 684, 2002.
- [90] N. Gucunski and P. Shokouhi, "Sasw dispersion curve generation by wavelet transform," in *Proceedings of the Symposium on the Application of Geophysics to Engineering and Environmental Problems*, Colorado springs, Colorado, 2004, pp. 1532–1543, SEG.
- [91] Glenn J. Rix, Carlo G. Lai, and A. Wesley Spang Jr., "In situ measurement of damping ratio using surface waves," *Journal of Geotechnical and Geoenvironmental Engineering*, vol. 126, no. 5, pp. 472–480, 2000.
- [92] s. Foti, "Using transfer function for estimating dissipative properties of soils from surface-wave data," *Near surface geophysics*, vol. 2, no. 4, pp. 231 – 240, 2004.
- [93] V. Ganji, N. Gucunski, and A. Maher, "Detection of underground obstacles by sasw method - numerical aspects," *Journal of geotechnical and geoenvironmental engineering*, vol. 123, no. 3, pp. 212 – 219, March 1997.
- [94] N. Gucunski, V. Ganji, and M.H. Maher, "Effects of obstacles on rayleigh wave dispersion obtained from the sasw test," *Soil dynamics and earthquake engineering*, vol. 15, no. 4, pp. 223 – 231, 1996.
- [95] N. Gucunski, V. Krstic, and M.H. Maher, "Experimental procedures for detection of underground objects by the sasw test," in *Geotechnical site characterization*, Robertson and Mayne, Eds., pp. 469 – 472. Balkeme, Rotterdam, 1998.
- [96] P. Shokouhi and N. Gucunski, "Application of wavelet transform in detection of shallow cavities by surface waves," in *Proceedings of the Symposium on the Application of Geophysics to Engineering and Environmental Problems*, San Antonio, Texas, 2003, pp. 1582–1600, SEG.

- [97] C. Phillips, A. Nasser-Moghaddam, T. Moore, G. Cascante, and D.J. Hutchinson, “A simple automated method of sasw analysis using multiple receivers,” in *Proceedings of the Symposium on the Application of Geophysics to Engineering and Environmental Problems*, San Antonio, Texas, 2003, pp. 1582–1600, SEG.
- [98] N. Gucunski and P. Shokouhi, “Detection and characterization of cavities under the airfield pavements by wavelet analysis of surface waves,” in *2004 FAA worldwide airport technology transfer conference*, Atlantic City, New Jersey, 2004, pp. 1532–1543.
- [99] A. Nasser-Moghaddam, G. Cascante, C. Phillips, and D.J. Hutchinson, “A new quantitative procedure to determine the location and embedment depth of a void using surface waves,” *Journal of environmental and engineering geophysics*, vol. 10, no. 1, pp. 51 – 64, 2005.
- [100] Kenneth H. Stokoe II, Stephen G. Wright, James A. Bay, and José M. Roësset, “Characterization of geotechnical sites by sasw method,” in *Geophysical characterization of sites*, Richard D. Woods, Ed., pp. 15–25. International science publisher, New York, 1994.
- [101] M.O. Al-Hunaidi, “Insights on the sasw nondestructive testing method,” *Canadian journal of civil engineering*, vol. 20, pp. 940–950, 1993.
- [102] D.R. Hiltunen and R.D. Woods, “variables affecting the testing of pavements by the surface wave method,” *Transportation research record*, , no. 1260, pp. 45–52, 1990.
- [103] I. Sanchez-Salinerio, J.M. Roësset, K.Y. Shao, K.H. Stokoe II, and G.J. Rix, “Analytical evaluation of variables affecting surface wave testing of pavements,” *Transportation research record*, , no. 1136, pp. 86–95, 1987.
- [104] S. Nazarian and M.R. Desai, “Automated surface wave method: Field testing,” *Journal of geotechnical engineering*, vol. 119, no. 7, pp. 1094–1111, 1993.
- [105] A. P. Shalito, “Seismic phase unwrapping: methods, results, problems,” *Geophysical prospecting*, vol. 40, pp. 211–225, 1992.
- [106] F.E. Ricahrt, Jr J.R. Hall, and R.D. Woods, *Vibration of soils and foundations*, Prentice-Hall, Inc., Englewood Cliffs, New Jersey, 1970.

- [107] E. Kausel and J.M. Roësset, “Stiffness matrices for layered soils,” *Bulletin of the seismological society of America*, vol. 71, no. 6, pp. 1743–1761, 1981.
- [108] Alterman and R. Z. Burridge, “The elastic radiation from an expanding spherical cavity,” *Geophys. J. R. astr.*, vol. 30, pp. 451, 1972.
- [109] L. D. Bertholf, ,” *J.Appl.Mech.*, vol. 34, pp. 725, 1967.
- [110] A. G. Petschek and M. E. Hanson, ,” *J.Comp.Phys.*, vol. 3, pp. 307, 1968.
- [111] K. Aki and K. L. Larner, ,” *J.Geophys. Res.*, vol. 75, pp. 933, 1970.
- [112] J. C. Strikwerda, *Finite Difference Schemes and Partial Differential Equations*, Wadsworth and Brooks, Pacific Grove, California, 1989.
- [113] W. J. Lick, *Difference equations from Differential Equations (Lecture Notes in Engineering)*, Springer-Verlag, Berlin, Germany, 1989.
- [114] G. D. Smith, *Numerical solution of partial differential equations, Finite difference methods*, Clarendon Press, OXFORD.
- [115] A. R. Mitchell, *Computational Methods in Partial Differential Equations*, Wiley, New York, New York, 1969.
- [116] A. S. Alterman, J. Aboudi, and F. C. Karal, “Pulse propagation in a laterally heterogeneous solid elastic sphere,” *Geophys. J. R. astr.*, vol. 21, pp. 243, 1970.
- [117] E. H. Saenger, N. Gold, and S. A. Shapiro, “Modeling the propagation of elastic waves using a modified finite-difference grid,” *Wave - Motion*, vol. 31, pp. 77.
- [118] R. A. Stephen, “A comparison of finite difference and reflectivity seismograms for marine models,” *Geophys. J. R. astr. Soc.*, vol. 72, pp. 39, 1983.
- [119] J. R. H. Otter, A. C. Cassel, and R. E. Hobbs, “Dynamic relaxation(paper no. 6986),” *Proc. Inst. Civil Eng.*, vol. 355, pp. 633, 1966.
- [120] J. Virieux, “P - sv wave propagation in heterogeneous media: Velocity- stress finite difference method,” *Geophysics*, vol. 51, 1986.

- [121] O. Holberg, “Computational aspects of the choice of operator and sampling interval for numerical differentiation in large-scale simulation of wave propagation,” *Geophysical prospecting*, vol. 35, pp. 629, 1987.
- [122] A. Zerwer, G. Cascante, and J. Hutchinson, “Parameter estimation in finite element simulations of rayleigh waves,” *Journal of geotechnical and geoenvironmental engineering*, pp. 250 – 261, March 2002.
- [123] M. L. Wilkins, “Calculation of elastic-plastic flow,” *Methods in computational Physics advances in research and applications*, vol. 3, pp. 211, 1964.
- [124] L. Malvern, *Introduction to the Mechanics of a Continuous Medium*, Prentice-Hall, Englewood Cliffs, N.J., 1969.
- [125] N. A. Haskell, “The dispersion of surface waves on multilayered media,” *Bull. Seismol. Soc. Am.*, vol. 54, no. 2, pp. 627–679, 1953.
- [126] C. Phillips, G. Cascante, and J. Hutchinson, “Evaluation of lateral homogeneity with the distance analysis of surface waves,” *Canadian Geotechnical Journal*, vol. 41, no. 2, pp. 212–226, 2004.
- [127] N. Gucunski and R. D. Woods, “Numerical simulation of the sasw test,” *Soil dynamics and earthquake engineering*, vol. 11, no. 4, pp. 213–227, 1992.
- [128] Donattene Leparoux, Arnand Bitri, and Gilles Grandjean, “Underground cavity detection: a new method based on seismic rayleigh waves,” *European Journal of Environmental and Engineering Geophysics*, vol. 5, pp. 33 – 53, 2000.
- [129] C. Phillips, G. Cascante, and D.J. Hutchinson, “Numerical simulation of seismic surface waves,” in *Proceedings of the 54th Canadian geotechnical conference*, Calgary, Alberta, September 2001, pp. 1538–1545, Canadian Geotechnical Society.
- [130] C. Phillips, G. Cascante, and D.J. Hutchinson, “The innovative use of surface waves for void detection and material characterization,” in *Proceedings of the Symposium on the Application of Geophysics to Engineering and Environmental Problems*, Las Vegas, Nevada, 2002, SEG.

- [131] J.C. Sheu, K. H. StokoeII, and J.M. Roesset, “Effect of reflected waves in sasw testing of pavements,” Research record N. 1196, Transportation research board, National research council, Washington, D.C., 1988.
- [132] G. Hevin, O. Abraham, and H.A. Pederson nad M. Campillo, “Characterization of surface cracks with rayleigh waves: a numerical model,” *NDT and E International*, vol. 31, no. 4, pp. 289–297, 1998.
- [133] E.A. Robinson and T.S. Durrani, *Geophysical signal processing*, Prentice-Hall, Inc., Englewood Cliffs, New Jersey, 1986.
- [134] B. L. N. Kennett, *Seismic wave propagation in stratified media*, Cambridge University Press, Cambridge, GT Britain, ist edition, 1983.
- [135] Sharma Prakash, *Soil dynamics*, McGraw-Hill, Inc., New York, NY, 1981.
- [136] D. J. Hutchinson, ,” [http://geol.queensu.ca/people/jhutchin/cur\\_research.html](http://geol.queensu.ca/people/jhutchin/cur_research.html), February 2006, Accessed 1 February 2006.
- [137] L. A. Amodt and M. R. Mesch, “Crawford mountains reclamation project,” in *2003 National association of abandoned mine programs conference*, 2003.
- [138] K.L.M. Solvason, *Underground void detection using 3D spectral analysis of surface waves SASW*, Bsc, University of Waterloo, 2001.
- [139] Z. Khan, A. Majid, and G. Cascante, “Measurement of ultrasonic wave velocities,” Quebec city, Quebec, Canada, October 2004, Canadian Geotechnical Society.



# Appendix A

## Selected closed form solutions

This appendix contains a selection of the closed formed solutions derived by different researchers for the propagation of mechanical waves in an elastic half space. These formulations are adopted from Graff [12], Lamb [26], and Miller & Pursey [53]. Table A.1 defines the parameters in the other two tables. Table A.2 defines the loading and medium conditions for the cases shown in table A.3.

Table A.1: Definition of the parameters used in the closed form solutions

$J_n(x) = x^n \sum_{m=0}^{\infty} \frac{(-1)^m x^{2m}}{2^{2m+n} m!(m+n)!}$
$H = -\frac{\xi(2\xi^2 - k^2 - 8\alpha_1\beta_1)}{F'(\xi)} \text{ and } K = -\frac{k^2\alpha_1}{F'(\xi)}$
$\alpha_1 = \sqrt{\xi^2 - h^2}, \beta_1 = \sqrt{\xi^2 - k^2}, \xi^2 = \frac{\omega^2}{C_R^2}, h^2 = \frac{\omega^2}{C_p^2}, k^2 = \frac{\omega^2}{C_s^2}$
$F(\xi) = (2\xi^2 - k^2)^2 - 4\xi^2\alpha\beta$
$F'(\xi) = 8\xi \left[ (2\xi^2 - k^2) - \sqrt{\xi^2 - h^2}\sqrt{\xi^2 - k^2} - \frac{\xi^2}{2} \left( \sqrt{\frac{\xi^2 - k^2}{\xi^2 - h^2}} + \sqrt{\frac{\xi^2 - h^2}{\xi^2 - k^2}} \right) \right]$
$v = a \tan\left(\frac{t-cr}{\tau}\right) \text{ where } t \text{ is time in second, } c \text{ is the corresponding velocity,}$ $r \text{ is the distance from source, and } \tau \text{ is the time factor}$
$\bar{Q}, Q, Z, \text{ and } P \text{ are load amplification factors}$

Table A.2: Model properties and loading conditions for the studied cases

Case No.	Properties of the medium	Loading conditions	Loading	
			$\sigma_{zz}$	$\sigma_{zx}$
1	Semi infinite, Elastic	at plain $z=0$	$H, DL:$ $Z e^{i\xi x} e^{i\omega t}$	0
2	Semi infinite, Elastic, Large $x$	at line $z=x=0$ , inward	$H, LL :$ $-Q \left( \int_{-\infty}^{+\infty} \frac{e^{i\xi x}}{2\pi} d\xi \right) e^{i\omega t}$	0
3	Semi infinite, Elastic	at plain $z=0$	0	$H, DL:$ $Z e^{i\xi x} e^{i\omega t}$
4	Semi infinite, Elastic, Large $x$	at line $z=x=0$ , inward	0	$H, LL :$ $-P \left( \int_{-\infty}^{+\infty} \frac{e^{i\xi x}}{2\pi} d\xi \right) e^{i\omega t}$
5	Semi infinite, Elastic	at plain $z=0$ , Inward, 3D axisym.	$H, DL:$ $Z J_0(\xi r)$	0
6	Semi infinite, Elastic	at point $x=y=z=0$ , Inward, 3D axisym.	$H, PL:$ Amplitude $-Q$	0
7	Semi infinite, Elastic	at point $x=y=z=0$ , Inward, 3D axisym.	$PL$ $\frac{\bar{Q}}{\pi} \frac{\tau}{\tau^2+t^2}$	0

Table A.3: Surface displacements for the studied cases

Case No.	Surface displacements	
	Vertical ( $u_{3,0} = v_0$ )	Horizontal ( $u_{1,0} = u_0$ )
1	$\frac{k^2 \alpha}{F(\xi)} \frac{Z}{\mu} e^{i(\xi x + \omega t)}$	$\frac{i\xi(2\xi^2 - k^2 - 2\alpha\beta)}{F(\xi)} \frac{Z}{\mu} e^{i(\xi x + \omega t)}$
2	$-\frac{iQ}{\mu} K e^{i(\omega t - \kappa x)} +$ $\frac{2Q}{\mu} \sqrt{\frac{2}{\pi}} \sqrt{1 - \left(\frac{h}{k}\right)^2} \frac{e^{i(\omega t - kx - \frac{\pi}{4})}}{(kx)^{\frac{3}{2}}} +$ $\frac{Q}{2\mu} \sqrt{\frac{2}{\pi}} \frac{h^2 k^2}{(k^2 - 2h^2)^2} \frac{e^{i(\omega t - kx - \frac{\pi}{4})}}{(hx)^{\frac{3}{2}}}$	$-\frac{Q}{\mu} H e^{i(\omega t - \kappa x)} +$ $\frac{Q}{2\mu} \sqrt{\frac{2}{\pi}} \sqrt{1 - \left(\frac{h}{k}\right)^2} \frac{e^{i(\omega t - kx - \frac{\pi}{4})}}{(kx)^{\frac{3}{2}}} -$ $\frac{Q}{\mu} \sqrt{\frac{2}{\pi}} \frac{h^3 k^2 \sqrt{h^2 - k^3}}{(k^2 - 2h^2)^3} \frac{e^{i(\omega t - kx - \frac{\pi}{4})}}{(hx)^{\frac{3}{2}}}$
3	$\frac{-i\xi(2\xi^2 - k^2 - 2\alpha\beta)}{F(\xi)} \frac{X}{\mu} e^{i(\xi x + \omega t)}$	$\frac{k^2 \beta X}{F(\xi) \mu} e^{i(\xi x + \omega t)}$
4	$-\frac{P}{\mu} H e^{i(\omega t - \kappa x)} +$ $\frac{P}{\mu} \sqrt{\frac{2}{\pi}} \sqrt{1 - \left(\frac{h}{k}\right)^2} \frac{e^{i(\omega t - kx - \frac{\pi}{4})}}{(kx)^{\frac{3}{2}}} -$ $\frac{P}{\mu} \sqrt{\frac{2}{\pi}} \frac{h^3 k^2 \sqrt{k^2 - h^2}}{(k^2 - 2h^2)^3} \frac{e^{i(\omega t - kx - \frac{\pi}{4})}}{(hx)^{\frac{3}{2}}}$	$-\frac{iP}{\mu} K e^{i(\omega t - \kappa x)} +$ $\frac{2Q}{\mu} \sqrt{\frac{2}{\pi}} \sqrt{1 - \left(\frac{h}{k}\right)^2} \frac{e^{i(\omega t - kx - \frac{\pi}{4})}}{(kx)^{\frac{3}{2}}} +$ $\frac{Q}{2\mu} \sqrt{\frac{2}{\pi}} \frac{h^2 k^2}{(k^2 - 2h^2)^2} \frac{e^{i(\omega t - kx - \frac{\pi}{4})}}{(hx)^{\frac{3}{2}}}$
5	$\frac{k^2 \alpha}{F(\xi)} J_0(\xi r) \frac{Z}{\mu} e^{i\omega t}$	$\frac{\xi(2\xi^2 - k^2 - 2\alpha\beta)}{F(\xi)} J_1(\xi r) \frac{Z}{\mu} e^{i\omega t}$
6	Rayleigh : $f\left(\frac{1}{r}\right)$ $p$ and $s$ waves : $f\left(\frac{1}{r^2}\right)$	
7	$\frac{K\bar{Q}C_R}{4\pi\mu\tau^2} \sqrt{\frac{2\tau}{C_{Rr}}} \cos\left(\frac{\pi}{4} - \frac{3}{2}v\right) \cos^{\frac{3}{2}}(v)$ $\frac{\bar{Q}}{\pi} \frac{\tau}{\tau^2+t^2}$	$-\frac{H\bar{Q}C_R}{4\pi\mu\tau^2} \sqrt{\frac{2\tau}{C_{Rr}}} \sin\left(\frac{\pi}{4} - \frac{3}{2}v\right) \cos^{\frac{3}{2}}(v)$

## Appendix B

# Developed MathCAD<sup>®</sup> work sheets

This appendix contains the developed MathCAD<sup>®</sup> work sheets that were used for the calculations.

Mathgram 2-1: shows the Lamb solution and calculates the corresponding displacements

Mathgram 3-1: Shows the method used for calculating the 2D Fourier transforms

Mathgram 6-1: Shows the followed procedure for checking the stability of the numerical models

## Mathgram 2-1:

### Lamb Solution

References: Kramer (1996) , Bath (1984)

ORIGIN:= 1

#### Functions:

Function F -3:

$$\text{Do\_FFT}(x) := \begin{cases} \text{for } j \in 1.. \text{cols}(x) \\ \text{Out}^{(j)} \leftarrow \text{FFT}(x^{(j)}) \\ \text{Out} \end{cases}$$

#### Input Data:

Material properties:

Poisson ratio:  $\nu := 0.2$  Elastic modulus:  $E := 19$  MPa Bulk density:  $\rho := 1600$  Kg/m<sup>3</sup>

Time parameters :

Number of points in time:  $N_t := 2^8$   $i := 1.. N_t$   $\Delta t := 2.5 \cdot 10^{-4}$   $t_i := (i - 1) \cdot \Delta t$

Frequency parameters:

Number of points in frequency :  $N_f := \frac{N_t}{2} + 1$   $j := 1.. N_f$   $\Delta f := \frac{1}{N_t \cdot \Delta t}$   $\Delta f = 15.625$

$f_j := (j - 1) \cdot \Delta f$   $f_{nyq} := \frac{1}{2 \cdot \Delta t}$   $f_{nyq} = 2000$  Hz

Maximum meaningful frequency:  $f_{max} := 5$

#### Computations:

Shear modulus:  $G := \frac{E}{2 \cdot (1 + \nu)}$  Constraint modulus:  $M := \frac{1 - \nu}{(1 + \nu) \cdot (1 - 2 \cdot \nu)} \cdot E$

Bulk modulus:  $K := \frac{E}{3 \cdot (1 - 2 \cdot \nu)}$  P-wave velocity:  $C_p := \sqrt{\frac{M \cdot 10^6}{\rho}}$

S-wave velocity:  $C_s := \sqrt{\frac{G \cdot 10^6}{\rho}}$  Rayleigh wave velocity:  $C_R := \frac{0.87 + 1.12 \cdot \nu}{1 + \nu} \cdot C_s$

$G = 7.917$  Mpa  $M = 21.111$  Mpa  $K = 10.556$  Mpa

$C_p = 114.867$  m/s  $C_s = 70.341$  m/s  $C_R = 64.128$  m/s

**Lamb source and solution - Axisymmetric - 3D :**

Parameters : Source amplitude: Qbar := 1000 Source f content:  $\tau := 0.00075$

$$a := \frac{1}{C_p} \quad b := \frac{1}{C_s} \quad c := \frac{1}{C_R} \quad \text{Wave slowness}$$

$\omega_{\max} := 2 \cdot \pi \cdot f_{\max}$   $h := \omega_{\max} \cdot a$   $k := \omega_{\max} \cdot b$   $\chi := \omega_{\max} \cdot c$  Wave numbers

$$\alpha_1 := \sqrt{\chi^2 - h^2} \quad \beta_1 := \sqrt{\chi^2 - k^2}$$

Derivative of Rayleigh equation: 
$$F(\zeta) := 8 \cdot \zeta \cdot \left[ (2 \cdot \zeta^2 - k^2) - \sqrt{\zeta^2 - h^2} \cdot \sqrt{\zeta^2 - k^2} - \frac{\zeta^2}{2} \cdot \frac{\sqrt{\zeta^2 - k^2}}{\sqrt{\zeta^2 - h^2}} - \frac{\zeta^2}{2} \cdot \frac{\sqrt{\zeta^2 - h^2}}{\sqrt{\zeta^2 - k^2}} \right]$$

$$v(x,t) := \text{atan}\left(\frac{t - c \cdot x}{\tau}\right) \quad K := \frac{-k^2 \cdot \alpha_1}{F(\chi)} \quad H := \frac{-\chi \cdot (2 \cdot \chi^2 - k^2 - 2 \cdot \alpha_1 \cdot \beta_1)}{F(\chi)}$$

Source function:

$$Q(t) := \frac{Qbar \cdot \tau}{\pi \cdot (t^2 + \tau^2)^2}$$

Delay := 750 Δt

$$q_i := Q(t_i - \text{Delay})$$

Vertical surface displacement far from source:

$$u3_0(x,t) := \frac{K \cdot Qbar \cdot c}{4 \cdot \pi \cdot G \cdot \tau^2} \cdot \sqrt{\frac{2 \cdot \tau}{c \cdot x}} \cdot \cos\left(\frac{\pi}{4} - \frac{3}{2} \cdot v(x,t)\right) \cdot \cos(v(x,t))^2$$

Horizontal surface displacement far from source:

$$u1_0(x,t) := \frac{H \cdot Qbar \cdot c}{4 \cdot \pi \cdot G \cdot \tau^2} \cdot \sqrt{\frac{2 \cdot \tau}{c \cdot x}} \cdot \sin\left(\frac{\pi}{4} - \frac{3}{2} \cdot v(x,t)\right) \cdot \cos(v(x,t))^2$$

Fourier transform of the source:

$$FQ := \text{Do\_FFT}(q) \quad \text{AmpFQ}_j := |FQ_j|$$

Distance from source (m):

$$Di := 1..3 \quad d_1 := 0.75 \cdot d_2 := 1.125 \quad d_3 := 1.5$$

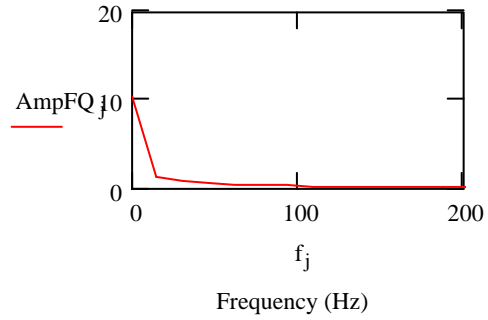
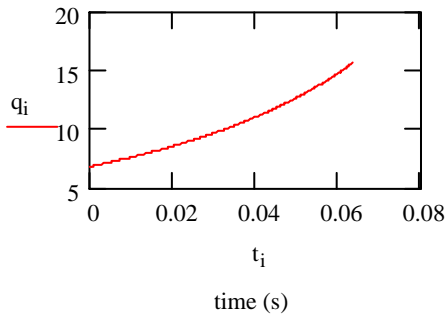
Discretized displacements:

$$Du3_{0,i,Di} := u3_0(d_{Di}, t_i) \quad Du1_{0,i,Di} := u1_0(d_{Di}, t_i)$$

Saving Displacements:

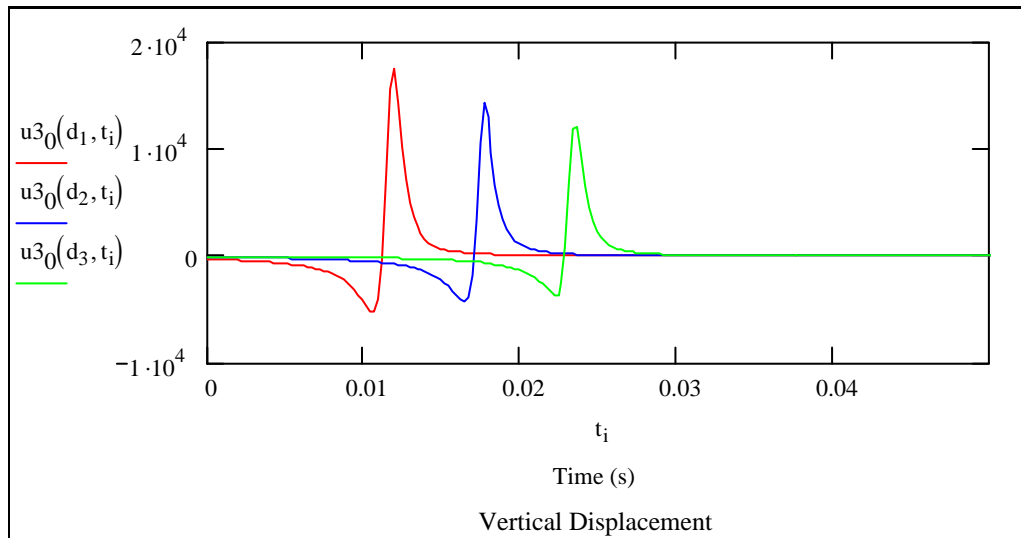
$$\text{out}^{\langle 1 \rangle} := t \quad \text{out}^{\langle Di+1 \rangle} := Du3_0^{\langle Di \rangle} \quad \text{out}^{\langle Di+4 \rangle} := Du1_0^{\langle Di \rangle}$$

## Graphs:

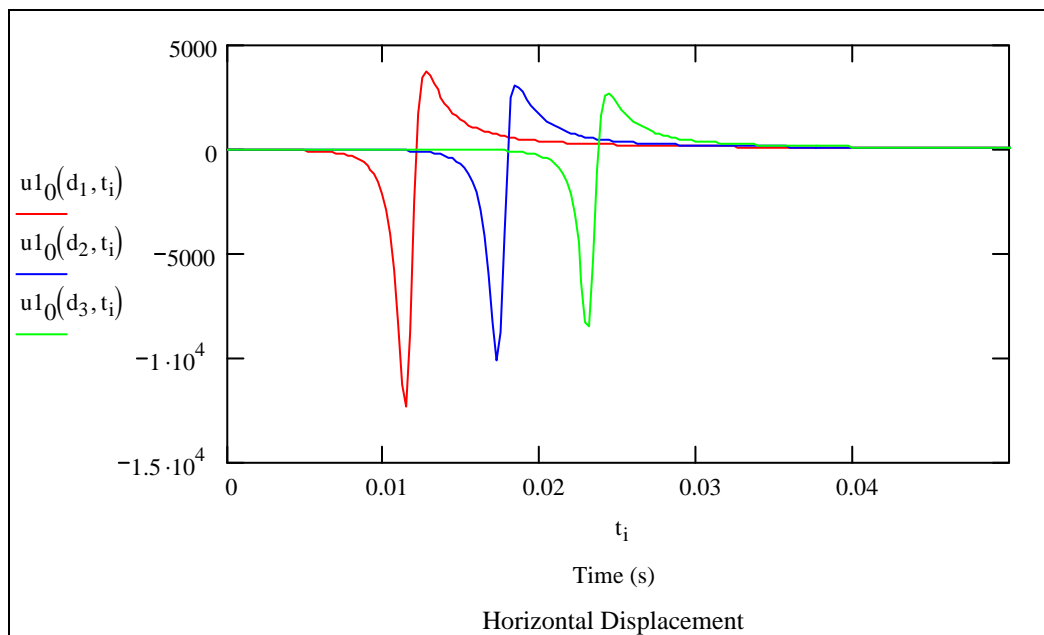


Lamb Source

Lamb Source



Vertical Displacement



Horizontal Displacement

## MathGram 3-1:

### 2D Fourier calculation

References: Kramer (1996) , Bath (1984)

ORIGIN:= 1

#### Functions :

Function F -36:

```
ZeroPadd_2D(x, N, M) :=
  for i ∈ 1.. N
    for j ∈ 1.. M
      outi, j ← 0
    for i ∈ 1.. rows(x)
      for j ∈ 1.. cols(x)
        outi, j ← xi, j
  out
```

Function F -34:

```
Hanning(tmax, Δt) :=
  E ←  $\frac{tmax}{\Delta t} + 1$ 
  M ← 0.5·E
  for i ∈ 1.. E
    outi ←  $\begin{cases} 0.5 + 0.5 \cdot \cos\left[\frac{2\pi}{E} \cdot (i - M)\right] & \text{if } |i - M| \leq \frac{E}{2} \\ 0 & \text{otherwise} \end{cases}$ 
  out
```

#### Input Data and defined indices:

##### Defined indices

$N_t := 10$        $N_{t_{tot}} := 2^{N_t}$       Total number of points after zero padding

Number of points in frequency :  $N_{f_{tot}} := N_{t_{tot}}$        $j_f := 1.. N_{f_{tot}}$

$N_d := 30$        $N_{d_{tot}} := N_d$       Total number of spatial points after zero padding

Number of points in wavenumber :  $N_{k_{tot}} := N_{d_{tot}}$        $j_k := 1.. N_{k_{tot}}$

$i := 1.. N_{t_{tot}}$        $k := 1.. N_{d_{tot}}$

Max no. of receivers:      Receiver\_max :=  $N_{d_{tot}}$

$$z := 1.. \text{Receiver\_max} \quad zz := 1.. \text{Receiver\_max} - 1$$

Assumed frequency:  $\omega := 100 \quad \frac{\text{rad}}{\text{s}}$

Assumed wavelength:  $\lambda := 1 \quad \text{m}$

$$f := \frac{\omega}{2 \cdot \pi} \quad f = 15.915 \quad \text{Hz} \quad T := \frac{1}{f} \quad T = 0.063 \quad \text{s} \quad \Delta t := \frac{T}{10} \quad \Delta x := \frac{\lambda}{10}$$

Temporal sampling rate:  $\Delta t = 0.006283$       Spatial sampling rate:  $\Delta x = 0.1$

**Time parameters :**

Original number of points in time for numerical solution:  $t_i := (i - 1) \cdot \Delta t$

**Frequency parameters:**

$$\Delta f := \frac{1}{N t_{\text{tot}} \cdot \Delta t} \quad \Delta f = \quad f_{j f} := (j f - 1) \cdot \Delta f \quad F_{\text{nyq}} := \frac{1}{2 \cdot \Delta t} \quad F_{\text{nyq}} = \quad \text{Hz}$$

$$\omega_{\text{nyq}} := 2 \cdot \pi \cdot F_{\text{nyq}} \quad \omega_{\text{nyq}} = \quad \frac{\text{rad}}{\text{s}}$$

**Wave-number parameters:**

$$\Delta k := \frac{1}{N d_{\text{tot}} \cdot \Delta x} \quad \Delta k = \quad N d_{\text{tot}} = \quad k_{j k} := (j k - 1) \cdot \Delta k \quad k_{\text{nyq}} := \frac{1}{2 \cdot \Delta x}$$

$$k_{\text{nyq}} = \quad 1/m \quad \max(k) =$$

**Spatial parameters:**

$$\text{Receiver\_max} = \quad \text{mid} := 0.5 \cdot (\text{Receiver\_max} - \text{mod}(\text{Receiver\_max}, 2)) + 1$$

$$x_z := (z - 1) \cdot \Delta x \quad \max(x) =$$



**Generated signals:**

$$SData_{i,z} := \begin{cases} 0 & \text{if } t_i < 2 \cdot T \\ 10 \sin(\omega \cdot t_i) & \text{if } 2 \cdot T \leq t_i \leq 7 \cdot T \\ 0 & \text{otherwise} \end{cases}$$

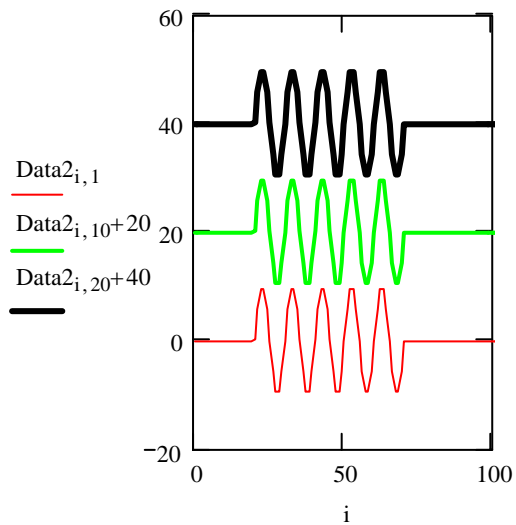
Synthetic data: a sinusoid with 5 cycles

**Final Signals:**

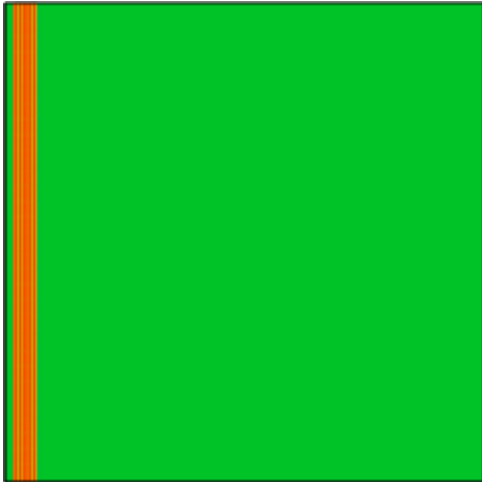
Data1 := SData

Data2 := SData

**Plot of the synthetic data**



Wiggle plot of the synthetic data



Contour plot of the synthetic data

Data1

### **Computations:**

#### **Generating Hanning window in temporal and spatial domain:**

$$\text{maxt} := \max(t) \quad \text{maxx} := \max(x) \quad \text{wt} := \text{Hanning}(\text{maxt}, \Delta t) \quad \text{wd} := \text{Hanning}(\text{maxx}, \Delta x)$$

$$\text{win}_{i,z} := \text{wt}_i \cdot \text{wd}_z$$

#### **Windowing the signals in time and space:**

$$\text{wData1}_{i,z} := \text{win}_{i,z} \cdot \text{Data1}_{i,z} \quad \text{wData2}_{i,z} := \text{win}_{i,z} \cdot \text{Data2}_{i,z}$$

#### **Optical transformation of the Data1:**

$$\text{owData1}_{i,z} := (-1)^{i+z} \cdot \text{wData1}_{i,z}$$

#### **Zero padding the signals in time and spatial domain:**

$$\text{zowData1} := \text{ZeroPadd\_2D}(\text{owData1}, N_{t_{\text{tot}}}, N_{d_{\text{tot}}})$$

$$\text{zowData2} := \text{ZeroPadd\_2D}(\text{wData2}, N_{t_{\text{tot}}}, N_{d_{\text{tot}}})$$

**Frequency computations :**

$$fzowData1 := \text{cfft}(zowData1)^T \quad fzowData2 := \text{cfft}(zwData2)^T$$

**Calculating the magnitudes:**

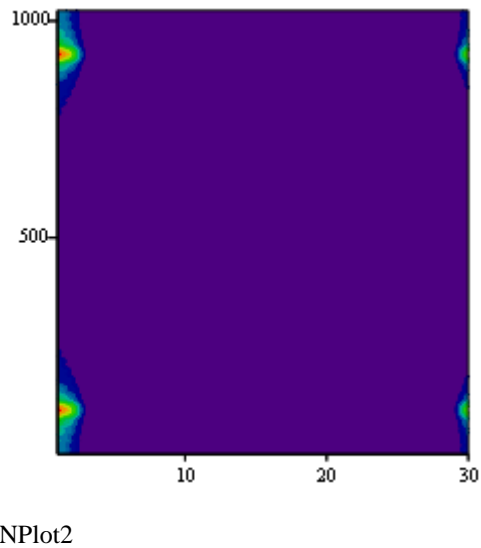
$$MData1_{jk, jf} := \left| fzowData1_{Nk_{tot}-jk+1, jf} \right| \quad MData2_{jk, jf} := \left| fzowData2_{jk, jf} \right|$$

**Plotting the data:**

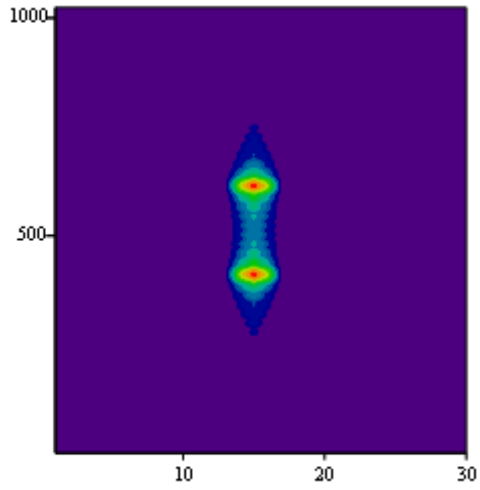
$$\begin{aligned} \text{Amp} &:= 10 & \alpha &:= 10 \cdot 10^{-2} & \text{lim1} &:= 1 & \text{lim2} &:= Nf_{tot} \\ \text{qmin} &:= \alpha \cdot \max(MData1) \\ \text{Dum1} &:= \text{submatrix}(MData1, 1, Nk_{tot}, \text{lim1}, \text{lim2}) & \text{Plot1} &:= \text{Amp} \cdot \log(\text{qmin} + \text{Dum1}) \\ \text{qmin} &:= \alpha \cdot \max(MData2) \\ \text{Dum1} &:= \text{submatrix}(MData2, 1, Nk_{tot}, \text{lim1}, \text{lim2}) & \text{Plot2} &:= \text{Amp} \cdot \log(\text{qmin} + \text{Dum1}) \end{aligned}$$

**Normalizing the data:**

$$\begin{aligned} \text{MAX1} &:= \max(|\max(\text{Plot1})|, |\min(\text{Plot1})|) & \text{MAX2} &:= \max(|\max(\text{Plot2})|, |\min(\text{Plot2})|) \\ \text{NPlot1} &:= \frac{\text{Plot1}}{\text{MAX1}} & \text{NPlot2} &:= \frac{\text{Plot2}}{\text{MAX2}} \end{aligned}$$



FK transform of the data **without** optical transformation



FK transform of the data *with*  
optical transformation

NPlot1

**Mathgram 6-1:**  
**Stability conditions for the numerical models:**

References: Kramer (1996), Comprehensive Proposal (Ali)

ORIGIN:= 1

**Input Data:**

**Material Properties: Material Type III (Medium Sand)**

Description: Material type I : Loose sand

Poisson ratio:  $\nu := 0.2$  Elastic modulus:  $E := 61$  MPa Bulk density:  $\rho := 2000$  Kg/m<sup>3</sup>

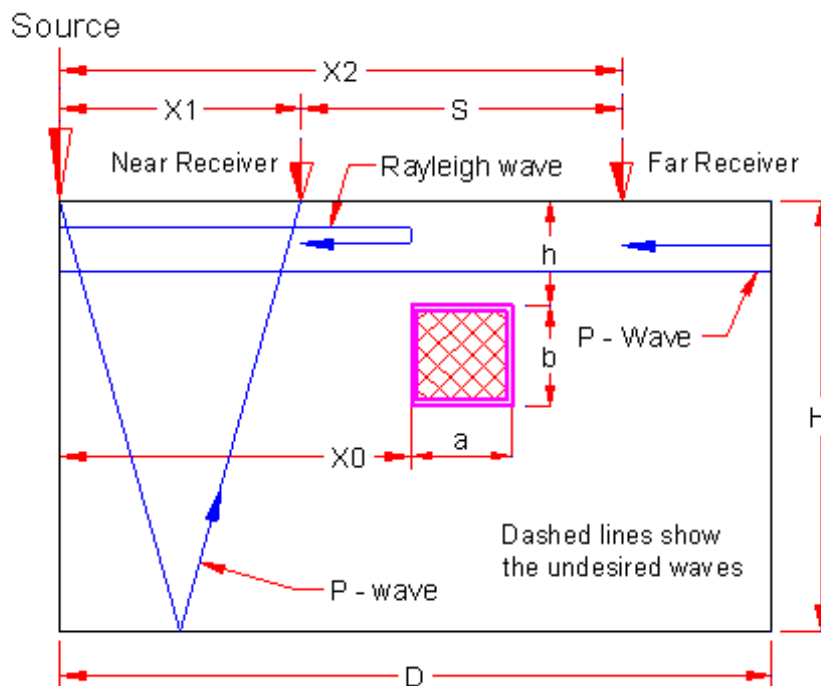
**Model Geometry:**

Overall model dimensions  $D := 20$  m  $H := 20$  m

Dimensions of the uniform part of the model  $D1 := 8$  m  $H1 := 8$  m

Location of receivers and anomalies:  $x_0 := 3.992$  m  $x_1 := 4$  m  $S := 3$  m

No. of grid points in uniform grid:  $NG := 1000$  Total No. of grid points:  $TNG := 600$



"J:\Ali\Thesis20060124\Figures\Chapter6\Model-Sizing.bmp"

## Calculations:

### Material Properties:

Shear modulus:  $G := \frac{E}{2 \cdot (1 + \nu)}$       Constraint modulus:  $M := \frac{1 - \nu}{(1 + \nu) \cdot (1 - 2 \cdot \nu)} \cdot E$

Bulk modulus:  $K := \frac{E}{3 \cdot (1 - 2 \cdot \nu)}$       P-wave velocity:  $C_p := \sqrt{\frac{M \cdot 10^6}{\rho}}$

S-wave velocity:  $C_s := \sqrt{\frac{G \cdot 10^6}{\rho}}$

### Rayleigh wave velocity:

$C_R := \frac{0.87 + 1.12 \cdot \nu}{1 + \nu} \cdot C_s$       Approximate value used for the guess value  $C_R = 102.773$

$C_{min} := 0.95 \cdot C_R$        $C_{max} := 1.05 \cdot C_R$       Max and min of guessed values

Calculation of the Rayleigh wave velocity from the exact equation:

$$F(C) := \left[ 2 - \left( \frac{C}{C_s} \right)^2 \right]^2 - 4 \cdot \sqrt{\left[ 1 - \left( \frac{C}{C_p} \right)^2 \right] \cdot \left[ 1 - \left( \frac{C}{C_s} \right)^2 \right]} \quad C_R := \text{root}(F(C), C, C_{min}, C_{max})$$

Final Results for the material properties:

$G = 25.417$	Mpa	$M = 67.778$	Mpa	$K = 33.889$	Mpa
$C_p = 184.089$	m/s	$C_s = 112.731$	m/s	$C_R = 102.698$	m/s

## Model parameters Calculations:

Grid distance in uniform part:

$$\Delta s := \frac{D1}{NG} \quad \Delta s = 0.008 \quad \text{m}$$

Time increment according to stability condition:  $\Delta t_{\max} := \frac{\Delta s}{4 \cdot \sqrt{2} \cdot C_p}$   $\Delta t_{\max} = 7.682 \times 10^{-6} \text{ s}$

Chosen time increment:

$$\Delta t := 5 \times 10^{-6} \text{ s}$$

Lower limit for Dynamic time :  $t_{\min} := \max \left( \left( \frac{2 \cdot x_0 - x_1}{C_R} \right), \left( \frac{x_1 + S}{C_R} \right) \right)$   $t_{\min} = 0.068 \text{ s}$

Upper limit for Dynamic time :  $t_{\max} := \min \left( \left( \frac{2 \cdot D - x_1 - S}{C_R} \right), \left( \frac{2 \cdot x_0 + x_1}{C_R} \right), \left( \frac{\sqrt{4 \cdot H^2 + x_1^2}}{C_R} \right) \right)$   $t_{\max} = 0.11669 \text{ s}$

Note: This condition for  $t_{\max}$  can be overwritten by using absorbing boundaries.

Chosen dynamic time:

$$t := 0.21 \text{ s}$$

**Required No. of time dynamic steps:**

$$Nt := \frac{t}{\Delta t} \quad Nt = 42000$$

Near field effects:

$$\lambda_{\max} := \frac{x_1}{2} \quad \lambda_{\max} = 2 \text{ m}$$

Minimum frequency that can be extracted:

$$f_{\min} := \max \left( \left( \frac{C_R}{\lambda_{\max}} \right), \left( \frac{1}{t} \right) \right) \quad f_{\min} = 51.349 \text{ Hz}$$

Minimum wavelength which is not affected by numerical dispersion:  $\lambda_{\min} := 10 \Delta s$

$$\lambda_{\min} = 0.08 \text{ m}$$

Maximum frequency that can be extracted:  $f_{\max} := \min \left( \left( \frac{1}{2 \cdot \Delta t} \right), \left( \frac{C_R}{\lambda_{\min}} \right) \right) f_{\max} = 1283.7 \text{ Hz}$

### Summary of the Results:

$$\Delta t = 5 \times 10^{-6} \text{ s} \quad \Delta s = 0.008 \text{ m} \quad t = 0.21 \text{ s}$$

$$t_{\max} = 0.117 \text{ s} \quad f_{\min} = 51.3 \text{ Hz}$$

$$t_{\min} = 0.068 \text{ s} \quad f_{\max} = 1283.7 \text{ Hz}$$



# Appendix C

## Selected FLAC<sup>®</sup> input files

### C.1 FLAC input file for model S00\_02:

(Two dimensional model)

```
#####  
;#  
;# Objective:  
;#  
;# Investigating the effect of a void in a half space  
;# Effect of void on the responses along vertical lines  
;#  
;# Revision date: August 25, 2005  
;#  
;# Formulation References :  
;#  
;# PHD comprehensive proposal (Ali)  
;#  
;# Units: m , s & N  
;#  
;# Material type I: Loose sand
```

```

;#
;# Poisson Ratio= 0.2, E = 19 MPa,
;# Density= 1600 kg/m3, G= 7.92 MPa
;# Bulk Modulus= 10.556 MPa
;#
;# Cp=114.87 m/s, Cs=70.34 m/s, CR= 64.13 m/s
;#
;# Damping not activated, void size: 0.08 x 0.08m, h=0.08 m
;#
;#
;#####
new
config axisymmetry Dynamic
grid 1150,416
model elastic
gen 0,-20 0,-2.12 8,-2.12 8,-20 &
rat=1,0.986 i=1,1001 j=1,151
gen 0,-2.12 0,0 8,0 8,-2.12 &
rat=1,1 i=1,1001 j=151,417
gen 8,-20 8,-2.12 20,-2.12 20,-20 &
rat=1.0143,0.986 i=1001,1151 j=1,151
gen 8,-2.12 8,0 20,0 20,-2.12 &
rat=1.0143,1 i=1001,1151 j=151,417
; # properties:
prop dens=1600 bulk=10.6e6 shear=7.92e6 i=1,1151 j=1,417
fix x i 1
apply xquiet yquiet i 1151
apply xquiet yquiet j 1
; ++++++ Fish Functions ++++++
;*** FISH Function to Define Model Running Loop

```

```

def run_model
  Initialize_Data
  command
  apply yforce -1 hist inpwave i=1 j=417
  end_command
  loop n (1,1)
  command
  step 32000
  end_command
end_loop
end

def run_model_movie
  Initialize_Data
  command
  apply yforce -1 hist inpwave i=1 j 417
  end_command
  loop n (1,moviesteps)
  command
  step moviesteps
  ; plot bou red vel yel apply green
  end_command
end_loop
end

##### Setting initial values
def Initialize_Data
  command
  Set dydt = 1e-5
  set dytime = 0
  history nstep=10
  history 6000 inpwave

```

```

history 5999 unbal
history 5998 dytime
end_command
moviesteps=1000
moviesteps=32
SetupDispHistories
end
;*** Setup Displacement Histories
Def SetupDispHistories
; ***** Displacements along Vertical line @ d=3.992 m
;# Y diaplacement histories
loop ii (1,51)
jjval = 167+5*(ii-1)
command
history ydisp i 500 j jjval
mark j=jjval i=500
endcommand
end_loop
;# Y diaplacement histories
loop ii (1,51)
jjval = 167+5*(ii-1)
command
history ydisp i 600 j jjval
mark j=jjval i=600
endcommand
end_loop
;# Y diaplacement histories
loop ii (1,51)
jjval = 167+5*(ii-1)
command

```

```

history ydisp i 700 j jjval
mark j=jjval i=700
endcommand
end_loop
;# Y diaplacement histories
loop ii (1,51)
jjval = 167+5*(ii-1)
command
history ydisp i 800 j jjval
mark j=jjval i=800
endcommand
end_loop
;# Y diaplacement histories
loop ii (1,51)
jjval = 167+5*(ii-1)
command
history ydisp i 900 j jjval
mark j=jjval i=900
endcommand
end_loop
;# ***** X Displacement histories *****s
;# x diaplacement histories
loop ii (1,51)
jjval = 167+5*(ii-1)
command
history xdisp i 500 j jjval
mark j=jjval i=500
endcommand
end_loop
;# x diaplacement histories

```

```

loop ii (1,51)
jjval = 167+5*(ii-1)
command
history xdisp i 600 j jjval
mark j=jjval i=600
endcommand
end_loop
;# X diaplacement histories
loop ii (1,51)
jjval = 167+5*(ii-1)
command
history xdisp i 700 j jjval
mark j=jjval i=700
endcommand
end_loop
;# X diaplacement histories
loop ii (1,51)
jjval = 167+5*(ii-1)
command
history xdisp i 800 j jjval
mark j=jjval i=800
endcommand
end_loop
;# X diaplacement histories
loop ii (1,51)
jjval = 167+5*(ii-1)
command
history xdisp i 900 j jjval
mark j=jjval i=900
endcommand

```

```

end_loop
; ***** Displacements along the surface
;# Y diaplacement histories
loop ii (1,101)
iival = 500+5*(ii-1)
command
history ydisp i iival j 417
mark i=iival j=417
endcommand
end_loop
;# x diaplacement histories
loop ii (1,101)
iival = 500+5*(ii-1)
command
history xdisp i iival j 417
endcommand
end_loop
end
; ##### Saving Displacements
def History_save
loop ii (h1,h2)
command
history write ii
end_command
end_loop
end
;*** defining Lamb source
def inpwave
deltat=1e-5
sai=0.00075

```

```

Fb=1000
tf=dytime-3600*deltat
inpwave=(Fb*sai/(3.1415*(tf^2+sai^2)))
end
save e:\flac\dum.sav
; ##### End of functions
model null j=397,406 i=695,704
run_model
; Y displacements along Vertical lines
set hisfile e:\flac\Y_V1.txt
set h1=1
set h2=51
History_save
set hisfile e:\flac\Y_V2.txt
set h1=52
set h2=102
History_save
set hisfile e:\flac\Y_V3.txt
set h1=103
set h2=153
History_save
set hisfile e:\flac\Y_V4.txt
set h1=154
set h2=204
History_save
set hisfile e:\flac\Y_V5.txt
set h1=205
set h2=255
History_save
; X displacements along Vertical lines

```



```
set hisfile e:\flac\X_V1.txt
set h1=256
set h2=306
History_save
set hisfile e:\flac\X_V2.txt
set h1=307
set h2=357
History_save
set hisfile e:\flac\X_V3.txt
set h1=358
set h2=408
History_save
set hisfile e:\flac\X_V4.txt
set h1=409
set h2=459
History_save
set hisfile e:\flac\X_V5.txt
set h1=460
set h2=510
History_save
; Along the surface
set hisfile e:\flac\SurfY.txt
set h1=511
set h2=611
History_save
set hisfile e:\flac\SurfX.txt
set h1=612
set h2=712
History_save
save e:\flac\s00.sav
```

## C.2 FLAC input file for model S03\_01 (Three dimensional model):

```
*****
; 3D model of a semi infinite medium
;
; Prepared by: Ali Nasser-Moghaddam
; ***** Date: 04 May 2005 *****
; Material properties: Model elastic
;
; Material properties:  $\nu=0.2$ ,  $E=19$  MPa,  $\rho=1600$  kg/m3
; Wave velocities:  $C_p=114.87$  m/s,  $C_s=70.34$  m/s,  $C_R=64.08$  m/s
;
; Units: m, s, kg
;
; Damping not activated
;
; *****
;
New
Config dynamic
; ***** Defining the geometry
;
;
set directory e:\flac3d
; Defining model size
Gen zone brick &
P0 0 0 0 p1 6.02 0 0 p2 0 -5 0 p3 0 0 -5 &
Size 172 68 68 &
Rat 1 1.01 1.01
```

```

Gen zone brick &
p0 6.02 0 0 p1 8.02 0 0 p2 6.02 -5 0 p3 6.02 0 -5 &
Size 33 68 68 &
Rat 1.032 1.01 1.01
;*** Assigning range names
;
Range name=fine x=-0.005,6.02 y=-5.0,0.005 z=-5.0,0.005
Range name=coarse fine not
Range name=Origin x=0 y=0 z=0
; Assigning range names to boundary planes
;
Range name=joint x=6.01,6.03
Range name=Xstart x=0,0
Range name=Xend x=8.02,8.02
Range name=Ystart y=-5.0,-5.0
Range name=Yend y=0,0
Range name=Zstart z=-5.0,-5.0
Range name=Zend z=0,0
; Assigning void range
Range name=void x=4,4.5 y=-0.1,0 z=-1,-0.5
attach face range=joint
;*** Assigning material properties
;
M e
Prop dens=1600 bulk=10.6e6 shear=7.9e6
;*** Assigning boundary conditions
;
Fix x range=Xstart ; Symmetry condition at x=0
Fix y range=Yend ; Symmetry condition at y=0
Fix z range=Zstart ; Base of the model fixed in vertical direction

```

```

Apply dquiet squiet nquiet range=Xend
Apply dquiet squiet nquiet range=Ystart
;*** Defining Lamb source
;
def inpwave
deltat=5e-5
sai=0.0025
Fb=-1000*3.1415*sai
tf=dytime-1000*deltat
inpwave=(Fb*sai/(3.1415*(tf^2+sai^2)))
end
;*** Defining histories
;
hist id=3000 inpwave
hist id=3001 unbal
hist id=3002 dytime
;*** Z displacement histories @ y=0 and z=0
def Zdisp_history
loop ii (1,87)
xval = 2.975+(ii)*0.035
his_id=ii
command
history id=his_id nstep=1 gp zdisp xval,0,0
endcommand
end_loop
end
;*** X displacement histories
def Xdisp_history
loop ii (1,87)
xval = 2.975+(ii)*0.035

```

```

his_id=200+ii
command
history id= his_id nstep=1 gp xdisp xval,0,0
endcommand
end_loop
end
;*** z displacement histories around the void
def VZdisp_history
loop ii (1,16)
GPNumber = 215125+(ii-1)*2
his_id=1000+(ii-1)
command
history id= his_id nstep=1 gp zdisp id=GPNumber
endcommand
end_loop
loop ii (1,8)
GPNumber = 203216-(ii-1)*11937
his_id=1016+(ii-1)
command
history id= his_id nstep=1 gp zdisp id=GPNumber
endcommand
end_loop
loop ii (1,16)
GPNumber = 107662+(ii-1)*2
his_id=1024+(ii-1)
command
history id= his_id nstep=1 gp zdisp id=GPNumber
endcommand
end_loop
loop ii (1,8)

```

```

GPNumber = 119629+(ii-1)*11937
his_id=1040+(ii-1)
command
history id= his_id nstep=1 gp zdisp id=GPNumber
endcommand
end_loop
end
def VXdisp_history
loop ii (1,16)
GPNumber = 215125+(ii-1)*2
his_id=2000+(ii-1)
command
history id= his_id nstep=1 gp xdisp id=GPNumber
endcommand
end_loop
loop ii (1,8)
GPNumber = 203216-(ii-1)*11937
his_id=2016+(ii-1)
command
history id= his_id nstep=1 gp xdisp id=GPNumber
endcommand
end_loop
loop ii (1,16)
GPNumber = 107662+(ii-1)*2
his_id=2024+(ii-1)
command
history id= his_id nstep=1 gp xdisp id=GPNumber
endcommand
end_loop
loop ii (1,8)

```

```

GPNumber = 119629+(ii-1)*11937
his_id=2040+(ii-1)
command
history id= his_id nstep=1 gp xdisp id=GPNumber
endcommand
end_loop
end
save e:\flac3d\dum.sav
,*****
,
,*****
,
;*** Model t8: model with 2% mass damping at f=100 Hz
,*****
,
,*****
,
; *** Function for saving historieess
def ZHistory_save
command
history write 1 2 3 4 5 6 7 8 9 vs 3002 &
fi=e:\flac3d\t11zdisp01.txt
history write 10 11 12 13 14 15 16 17 18 19 &
fi=e:\flac3d\t11zdisp02.txt
history write 20 21 22 23 24 25 26 27 28 29 &
fi=e:\flac3d\t11zdisp03.txt
history write 30 31 32 33 34 35 36 37 38 39 &
fi=e:\flac3d\t11zdisp04.txt
history write 40 41 42 43 44 45 46 47 48 49 &
fi=e:\flac3d\t11zdisp05.txt
history write 50 51 52 53 54 55 56 57 58 59 &
fi=e:\flac3d\t11zdisp06.txt
history write 60 61 62 63 64 65 66 67 68 69 &
fi=e:\flac3d\t11zdisp07.txt

```

```

history write 70 71 72 73 74 75 76 77 78 79 &
fi=e:\flac3d\t11zdisp08.txt
history write 80 81 82 83 84 85 86 87 &
fi=e:\flac3d\t11zdisp09.txt
end_command
end
def XHistory_save
command
history write 201 202 203 204 205 206 207 208 209 vs 3002 &
fi=e:\flac3d\t11xdisp01.txt
history write 210 211 212 213 214 215 216 217 218 219 &
fi=e:\flac3d\t11xdisp02.txt
history write 220 221 222 223 224 225 226 227 228 229 &
fi=e:\flac3d\t11xdisp03.txt
history write 230 231 232 233 234 235 236 237 238 239 &
fi=e:\flac3d\t11xdisp04.txt
history write 240 241 242 243 244 245 246 247 248 249 &
fi=e:\flac3d\t11xdisp05.txt
history write 250 251 252 253 254 255 256 257 258 259 &
fi=e:\flac3d\t11xdisp06.txt
history write 260 261 262 263 264 265 266 267 268 269 &
fi=e:\flac3d\t11xdisp07.txt
history write 270 271 272 273 274 275 276 277 278 279 &
fi=e:\flac3d\t11xdisp08.txt
history write 280 281 282 283 284 285 286 287 &
fi=e:\flac3d\t11xdisp09.txt
end_command
end
def VZHistory_save
command

```



```

history write 1000 1001 1002 1003 1004 1005 1006 1007 1008 1009 vs 3002 &
fi=e:\flac3d\t11Vzdisp01.txt
history write 1010 1011 1012 1013 1014 1015 1016 1017 1018 1019 vs 3002 &
fi=e:\flac3d\t11Vzdisp02.txt
history write 1020 1021 1022 1023 1024 1025 1026 1027 1028 1029 vs 3002 &
fi=e:\flac3d\t11Vzdisp03.txt
history write 1030 1031 1032 1033 1034 1035 1036 1037 1038 1039 vs 3002 &
fi=e:\flac3d\t11Vzdisp04.txt
history write 1040 1041 1042 1043 1044 1045 1046 1047 vs 3002 &
fi=e:\flac3d\t11Vzdisp05.txt
end_command
end
def VXHistory_save
command
history write 2000 2001 2002 2003 2004 2005 2006 2007 2008 2009 vs 3002 &
fi=e:\flac3d\t11Vxdisp01.txt
history write 2010 2011 2012 2013 2014 2015 2016 2017 2018 2019 vs 3002 &
fi=e:\flac3d\t11Vxdisp02.txt
history write 2020 2021 2022 2023 2024 2025 2026 2027 2028 2029 vs 3002 &
fi=e:\flac3d\t11Vxdisp03.txt
history write 2030 2031 2032 2033 2034 2035 2036 2037 2038 2039 vs 3002 &
fi=e:\flac3d\t11Vxdisp04.txt
history write 2040 2041 2042 2043 2044 2045 2046 2047 vs 3002 &
fi=e:\flac3d\t11Vxdisp05.txt
end_command
end
; **** printing grid positions around the void
def Print_Position
loop ii (1,16)
GPNumber = 215125+(ii-1)*2

```

```

command
print gp pos range id=GPNumber
endcommand
end_loop
loop ii (1,8)
GPNumber = 203216-(ii-1)*119377
command
print gp pos range id=GPNumber
endcommand
end_loop
loop ii (1,16)
GPNumber = 107662+(ii-1)*2
command
print gp pos range id=GPNumber
endcommand
end_loop
loop ii (1,8)
GPNumber = 119629+(ii-1)*11937
command
print gp pos range id=GPNumber
endcommand
end_loop
end
;*** Model t11_1: Running the model
set dyn damp rayleigh 0.02 100
m n range=void
set log on logfile=e:\flac3d\pos.txt
Print_Position
set log off
set dynamic dt=5e-5

```

```
set grav 0 0 0
apply zforce 1 h=inpwave range x=0 y=0 z=0
Zdisp_history
Xdisp_history
VZdisp_history
VXdisp_history
plot his 1, 30, 65 vs 3002
solve age=0.26
Save e:\flac3d\t11_1.sav
ZHistory_save
XHistory_save
VZHistory_save
VXHistory_save
```